Radio studies of relativistic outflows from black hole transients

Joe Bright

Corpus Christi College

University of Oxford

A thesis submitted for the degree of

Doctor of Philosophy

Michaelmas 2020

Statement of Originality

The work presented in this thesis was completed during a Doctor of Philosophy (DPhil) degree at the University of Oxford, funded by a Science and Technology Facilities Council Studentship through the Science and Technology Facilities Council. This degree was completed between October 2016 and July 2020.

The chapters of this thesis are based on works published in peer reviewed academic journals, or from works in preparation to be submitted to peer reviewed academic journals, as indicated at the beginning of each chapter.

I assert that the work contained in this thesis is my own, and that any results used to supplement my research that are not my own have been properly cited. None of the work in this thesis has been submitted as part of another degree at the University of Oxford, or any other university.

To Mum and Dad

Acknowledgements

I am very grateful for the support of my supervisor, Professor Rob Fender, during the completion of my DPhil. My time at Oxford has been both enjoyable and engaging, in no small part due to the working environment fostered in our research group.

I would like to thank my parents for their boundless support during the writing of this thesis, and throughout the entirety of my time as a student. Without them I surely would not have got this far.

Special thanks to Doctor Sara Motta for her guidance and friendship throughout my time at Oxford. My understanding of a whole host of subjects would be poorer without her help, and I will always have fond memories of the not modest amount of time we spent drinking coffee, talking science, and gossiping together. I owe a similar thanks to Doctor Ian Heywood, who has had endless patience for my equally endless questions, and has always been up for talking astronomy and interferometry, be it at work, online, or at the pub.

Completing this thesis would have been significantly harder without Allison Matthews. Her advice and support throughout the process, especially these final months, has made it much more bearable. Some of my most productive time was spent in Charlottesville together with her, and I'm extremely excited about my upcoming move to the USA.

A big thank you to my fellow DPhil students at Oxford, especially Lauren, Sam, Catherine, Sergio, Paul, Naomi, and Marius. Also thank you to my friends from back home and from Warwick, Charlotte, Jess, Georgia, Ollie, Pete, Jack, Heard, Fudge, and Charlie. Thank you to Steve and Ingrid for always showing interest in talking about my work. A big thank you to Monty.

Finally I want to acknowledge the support of Professor Boris Gänsicke and Professor Danny Steeghs who helped encourage me to study astronomy.

Abstract

In this thesis I will present observational studies of transient systems that produce mildly to extremely relativistic outflows through a coupling to an accretion flow. I will focus on the analysis of data taken from three source classes: black hole X-ray binaries (BHXRBs; particularly the system MAXI J1820+070), gamma-ray bursts (GRBs; particularly the system GRB 171010A), and tidal disruption events (TDEs; particularly the systems ASASSN-14li and Swift J1644+57).

I will present an extensive radio monitoring campaign on MAXI J1820+070 utilising five different interferometers, along with extensive X-ray observations, during the system's 2018 outburst. Together these data allowed me to probe the coupling between accretion and jet production throughout an entire outburst cycle, as well as during multiple hard accretion state only re-brightenings, tracked over a two year time frame. As MAXI J1820+070 transitioned from the hard to soft accretion state, contemporaneous time-series indicators of the launch of bipolar relativistic ejections were observed at both radio and X-ray frequencies (manifesting as a radio flare and an evolving quasi-period oscillation, respectively). I then confirmed the presence of these ejecta utilising multiple interferometers, and was able to track the evolution of both the approaching and receding ejecta for over ~ 150 d. Through utilising interferometers sensitive to very different angular scales, I was able to infer the internal energy of the ejection, and found it to be much larger than the value implied from the state transition radio flare. This is strong evidence for ongoing particle acceleration as ejections interact with the surrounding interstellar medium. In addition to the study of MAXI J1820+070, I will also present a broader population study of state transition radio flares from black hole X-ray binaries, and demonstrate that commonly employed models (which attribute flares to an optical depth evolution from an expanding region) are not appropriate for the majority of flares in the sample studied. I describe the ability of extended periods of particle

acceleration to explain the flare profiles.

GRB 171010A was a luminous and nearby long GRB detected at early times by the Arcminute Microkelvin Imager Large Array interferometer, as well as with the *Swift* X-ray telescope. Long GRBs produce highly relativistic outflows that are best studied through their interaction with the circumburst material. This interaction produced a broadband synchrotron afterglow. I present a study of the radio through X-ray afterglow of GRB 171010A in the context of the fireball model (which details the interaction of the jet and interstellar medium). By fitting the time evolving spectra, the values and evolution of the characteristic synchrotron frequencies can be inferred. GRB 171010A is one of the most energetic GRBs detected below $z \sim 0.5$, allowing for our theoretical understanding of afterglows to be investigated. While I find general agreement with the canonical models (particularly the spectral indices either side of the minimum energy frequency) a number of deviations are seen. I discuss possible solutions to these deviations, which likely include the addition of a second spectral component resulting from a reverse shock.

Finally, I will present late time radio and X-ray observations of the thermal TDE ASASSN-14li, and late time radio only observations of the relativistic TDE Swift J1644+57. Tidal disruption events occur when a star passes too close to a supermassive black hole and is torn apart by tidal forces. Approximately half of the stellar material is accreted and the rest is unbound. ASASSN-14li is a radio bright thermal TDE, and the origin of this radio emission is disputed. I will show that the late time radio properties are now consistent with background AGN activity, but that while the TDE was the dominant radio component, the radio emission was correlated with the X-ray emission. This provides evidence that thermal TDEs produce jets. It is not disputed that the relativistic TDE Swift J1644+57 produced a jet, and said jet's radio emission has now been monitored for ~ 10 yrs. I will present the most recent monitoring of Swift J1644+57 in the context of previously proposed jet models for the source. I will additionally discuss the up-to-date population of radio loud TDEs.

My conclusions contain a comparison of the outflows produced by these sources, and how they are analysed in different frameworks.

Contents

List of Figures

Chapter 1

Introduction

1.1 Black holes

The concept of a black hole, although not yet given that name, was first discussed by John Michell in 1784 where he proposed that a sufficiently massive star would, if light followed Newtons corpuscular theory of light, force the light it emitted to return back towards it [1]. A similar idea was proposed soon after by Laplace, but the apparent impossibility to prove the result experimentally, and limited understanding of the phenomenon of gravity at the time, prevented the idea from becoming widely accepted. It was only when Einstein developed his theory of general relativity, which explains gravity as resulting from a curvature of space-time which itself is curved by matter and energy responding to said curvature ("Space tells matter how to move. Matter tells space how to curve" - John Wheeler), that significant progress was made in the understanding of gravity [2]. A year after the field equations of general relativity were published, they were solved by Schwarzschild for a non-rotating point mass [3]. The space-time metric in such a configuration, as presented by Schwarzschild, contained two apparent singularities. One at the location of the point mass, and one at a radial distance $r_{sch} = 2GM/c^2$ from the point mass (the Schwarzschild radius). Singularities in a metric do not necessarily imply singularities in the space time they describe, but instead can result from the choice of coordinate system. In fact the metric singularity at the location of the point mass is indeed a physical one, whereas the singularity at the Schwarzschild radius is a coordinate one, and could be traversed freely without any indication that this point in space was special. To a distant observer however, the Schwarzschild radius would indeed appear to be special. It is the radius at which, in order to escape from the mass at the coordinate centre, an object must move away at the speed of light. At radii within the Schwarzschild radius objects would necessarily fall towards the location of the attracting mass, and even light would not be able to escape. Once matter or light has passed beyond the Schwarzschild radius, it is completely cut off from

larger radii, and a distant observer could not communicate in any way with an object within the Schwarzschild radius. This would make a black hole appear dark to an observer, with the surface defined by the Schwarzschild radius known as the event horizon. Once matter or light is beyond the event horizon it is inevitable that it will end up at the singularity, as all future light cones intersect the singularity. The timescale for this to occur is linear with black hole mass. For stellar mass black holes said timescale is of the order milliseconds or less, whereas for SMBHs the in-fall can take hours or days. The location of the event horizon can also be derived by simply considering the escape velocity from an object. The velocity required for an object to 'escape' from a body of mass M to infinity can be written $v_{\rm esc} = \sqrt{2GM/r}$, where G is the universal gravitational constant, and r is the separation that the escaping object is initially at from the gravitationally attracting body. Setting $v_{\rm esc} = c$ leads to a critical radius, the Schwarzschild radius, $r_{\rm sch} = 2GM/c^2$. It took until 1963 for the the space-time metric for a rotating mass to be derived, but the solutions to the field equations in this configuration also included a singularity at the location of the spinning mass, as well as an event horizon [4]. For a non rotating black hole (or Schwarzschild black hole) the event horizon is spherically symmetric whereas for a rotating (or Kerr) black hole the event horizon is elongated in the rotational plane and contracted orthogonal to it. In addition to the event horizon, spinning black holes possess another critical surface called the ergosurface, bounding the ergoregion. Within the ergoregion particles can still escape the hole, as the escape velocity is still less than the speed of light, however the effect of frame dragging in this region is so strong that within it a particle must co-rotate with the central object. Frame dragging also occurs outside of the ergoregion, and causes precession in the orbit of a body. The existence of the ergoregion implies the possibility that spin energy can be extracted from the black hole. This is discussed later in this chapter.

While these mathematical descriptions were compelling it was not proof that black holes existed in nature. It was not known if a massive body could compress within its event horizon and form such a singularity. Proving the existence of black holes through the presence of event horizons is still one of the fundamental goals of high energy astrophysics. In 1931 Chandrasekhar calculated the maximum mass that a white dwarf (WD; a compact star supported by electron degeneracy pressure) could support before continuing its collapse (the Chandrasekhar limit), having a modern value of $\sim 1.44\,M_\odot$ [5, 6]. Soon after (and quickly following the discovery of the neutron) it was proposed that a new form of matter, supported by neutron degeneracy pressure, could halt the collapse of a super-Chandrasekhar white dwarf – forming a neutron star (NS). Such a configuration has a maximum mass, known as the Tolman-Oppenheimer-Volkov (TOV) limit, of 2 to $3\,M_\odot$ [7, 8]. Once a

NS exceeds the TOV limit it will continue its collapse, and there is currently no known mechanism that would prevent it collapsing completely into a single point – a singularity – forming a black hole defined entirely by its mass, charge, and angular momentum [9, 10, 11].

1.1.1 Observational evidence of black holes

Despite the considerations in the previous section, there is no concrete evidence of the existence of event horizons or singularities in nature (although the cosmic censorship hypothesis postulates that naked singularities do not occur, despite them being valid solutions in certain space-time metrics [10]). There is a wealth of indirect evidence suggesting that black holes are present over a range of masses throughout the universe, a collection that is continually being added to, and the overwhelming consensus is that black holes do indeed occur in nature. I will highlight some of the most compelling and high profile pieces of observational evidence, roughly chronologically, but will not attempt to be completely exhaustive.

One of the earliest pieces of evidence for the existence of black holes came from the discovery of quasars - objects that appeared stellar in nature (compact optical sources) but were determined to be at distances well beyond our Galaxy [12]. It was suggested that the extreme luminosities associated with quasars could be explained via gas accretion onto a compact object, in particular a supermasive black hole [13, 14, 15].

Additional early evidence for black holes came from observing binary systems within the Galaxy. A significant number of stars are known to exist in binary configurations, orbiting around their common centre of mass. The individual stars in the binary therefore have a periodic variation in their radial velocity with respect to Earth and as such the centroid position of lines in their spectra will oscillate sinusoidally. The periodicity and amplitude (K) of the radial velocity (the former of which corresponds to the binary period $P_{\rm orb}$) can be related, via Kepler's third law, to the masses of the binary constituents and the inclination of the binary through the mass function. Supposing a system consists of an observable object of mass M_1 for which the spectrum is well known, and a secondary object of mass M_2 then the mass function is $f = M_2^3 \sin i^3/(M_1 + M_2)^2 = P_{\rm orb}K^3/2\pi G$. The mass function can be considered in two limits. In the case that $M_1 >> M_2$ it follows that $M_2 \geq f^{1/3}M_1^{2/3}$. Therefore if M_1 can be estimated, e.g. through spectral modelling, then a lower limit on the secondary can be found. The other case, which is more applicable for binary systems containing a compact object, is that $M_1 << M_2$. Here $M_2 \geq f$, and no information on the companion mass is needed for a lower limit on the hidden object mass to be found. In

general the mass of the hidden object is greater than the maximum of these two cases, but will always be greater than the mass function. The first system with a so called 'dynamically confirmed' black hole was the galactic high mass X-ray binary Cygnus X-1 which consists of a high mass B star in a binary with an unseen companion with a lower limit to its mass of $\sim 3\,M_{\odot}$, above the TOV mass limit [16, 17] (resolving the long standing Hawking-Thorne bet). More recently the black hole in the low mass X-ray binary V404 Cygni was found to have a dynamical mass of at least $\sim 9\,M_{\odot}$, well above the TOV limit [18]. Since then many more galactic binaries have been found where one of the constituents has a mass consistent with having to have formed a black hole [19, 20, 21, 22].

Further evidence for the existence of supermassive black holes ($M >> M_{\odot}$) came through studying the motion of individual stars at the centre of our Galaxy, which can be individually resolved with high angular resolution infrared telescopes [23, 24]. It was found that those stars closest to Sgr A* (within $1''$ of the compact radio source at the centre of the Galaxy) were orbiting the galactic centre on highly elliptical orbits which have since been tracked in exquisite detail for over 20 years. Modelling the orbits of these stars gives information on the object that the stars are orbiting, as well as a constraint on the objects physical extent. These observations show that a dark (not seen in visible light) mass of $\sim 10^6\,M_{\odot}$ is contained within a region of radius $\sim 100\,\mathrm{AU}$. While this is outside of the Schwarzschild radius of such a massive black hole, the high density and 'dark' nature of the central mass suggested it was a strong candidate to be a black hole. Similar analyses can be performed using water masers orbiting local AGN, with NGC 4258 having the most well measured mass, based on the rotation curve of the masers it hosts, of $\sim 4 \times 10^7\,M_{\odot}$ within a region less than a parsec across [25].

Within the past 5 years two exciting avenues to probe the existence of black holes have opened up. Firstly, the LIGO-Virgo gravitational wave interferometer has begun detecting compact object mergers, which include objects with pre- and post-merger masses of 10s of $M_{\odot}$. To date the LIGO-Virgo collaboration has published data from over 10 compact binary mergers, and is probing a region of compact object space that appears distinct from the lower mass stellar mass black holes found in galactic binaries [26] (see Figure 1.1). Secondly the Event Horizon Telescope has obtained observations of the central object in the nearby galaxy M87 at an unprecedented angular resolution (utilising global mm interferometry). Such observations probe angular scales corresponding to just a few Schwarzschild radii at the distance of M87, and have revealed the 'shadow' cast by the light bending of the supermassive black hole which appears to agree well with the predictions of light bending

from general relativity [27].

Interestingly, while there are compelling lines of evidence for both stellar and super massive black holes, there is a distinct lack of strong black hole candidates with $\sim 100\,M_\odot < M < 10^6\,M_\odot$, the intermediate mass black hole population. Despite the black hole population spanning 9 orders of magnitude in mass they are all thought to be completely described by only three parameter, their masses, angular momenta (spins), and charges. It is therefore expected that there is some degree of commonality to astrophysical processes associated with them (although occurring on very different timescales). Figure 1.1 shows the currently known black hole and neutron stars with masses $M < 100\,M_\odot$.

Finally, it has been suggested that the presence of an event horizon could be inferred through a comparison of the accretion luminosity between neutron star and black hole systems, although this has so far remained inconclusive, mostly due to the difficulty of finding 'apples to apples' systems to compare as the comparison is only valid for identical accretion rates [28, 29, 30, 31, 32]. The reasons for the difference will be discussed in the following section.

1.2 Accretion

Accretion, in the most general sense, is the process of the accumulation of matter onto a body via a gravitational interaction. It occurs in a host of phenomena on a range of size scales, from the formation of rain drops, to the accumulation of material in protoplanetery disks, to disks around Galactic and supermassive BHs. As accreting material falls onto a gravitationally attracting object it loses gravitational potential energy, which it gains as kinetic energy. For an object of mass m falling in the gravitational potential of a body of mass M the liberated energy is as large as $(1/2)mc^2(r_{\rm sch}/r)$ where r here is the final radius of the falling body. For a neutron star of radius 10 km and the same mass as our sun the liberated energy is $\sim 0.15mc^2$, a significant fraction of the rest mass of the accreting material (or an accretion efficiency of 15%). For a Schwarzschild black hole (and for black holes in general) there is no solid surface to accrete on to and past the event horizon material will be lost and its thermal energy with it (in either case the rest mass energy of the accreting material is not released). In fact the innermost stable circular orbit (ISCO) is $3r_{sch}$ for a Schwarzschild black hole which implies an accretion efficiency of 17% but, for black holes with high spin, can reach as high as 42%! If the rate of mass transfer on to an object is $\dot{m}$ then the luminosity of the accreting material can be as high as $L = (1/2)\dot{m}c^2(r_{\rm sch}/r) = (GM/R)\dot{m}$.

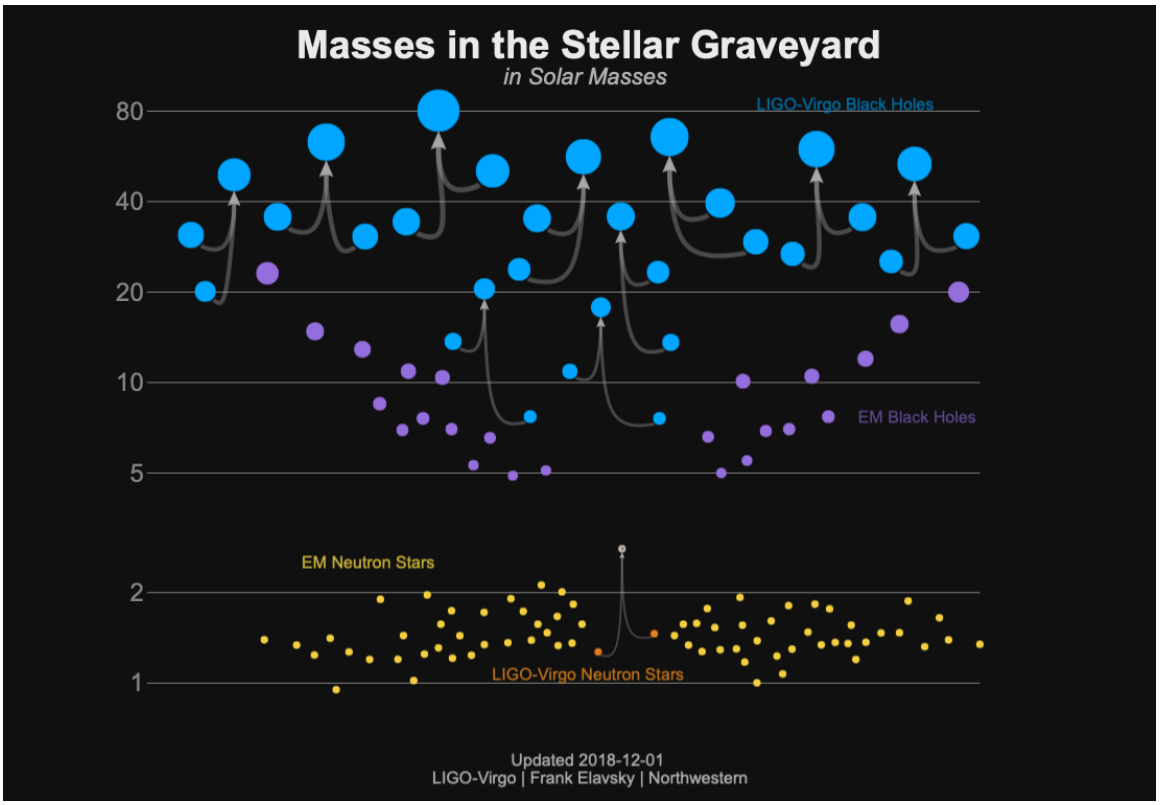

Figure 1.1: Masses of stellar mass black holes and neutron stars. Blue points show the constituents and product of binary black hole mergers observed with LIGO-Virgo, with the arrows demonstrating the evolution channel. Purple points shows stellar mass black holes discovered electromagnetically (e.g. Cygnus X-1). The single pair of orange points shows the so far only observed neutron star merger with an unknown end product (sitting in the mass gap) by LIGO-Virgo. Yellow points shown neutron stars discovered electromagnetically. The radii are scaled in accordance to the mass. Credit: Visualization: LIGO/Frank Elavsky/Northwestern | Non-LIGO Data Sources: Neutron Stars: `http://xtreme.as.arizona.edu/NeutronStars/data/pulsar_masses.dat` Black Holes: `https://stellarcollapse.org/sites/default/files/table.pdf`| LIGO-Virgo Data: `https://www.gw-openscience.org/events/`.

The maximum accretion rate is fundamentally capped at the Eddington limit, where radiation pressure becomes sufficient to halt the flow of material towards the compact object. The Eddington limit is applicable for symmetrical accretion, which most accretion is not, and so super-Eddington accretion is neither unprecedented or unexpected (see e.g. ultra-luminous X-ray sources which accrete at rates over 100 times that of the Eddington rate, although see [33]). The Eddington luminosity and the Eddington accretion rate are given in Equations (1.1) and (1.2). The numerical constant in Equation (1.2) hints at the extreme efficiency of accretion, with only a billionth of a solar mass per year required to sustain accretion at the Eddington rate for a stellar mass object.

$$L_{\mathrm{Edd}} = \frac{4\pi GMcm_p}{\sigma_T} \approx 1.3 \times 10^{38} (M/M_\odot)\,\mathrm{erg\,s^{-1}} \tag{1.1}$$

$$\dot{M}_{\mathrm{Edd}} = \frac{4\pi GMm_p}{\epsilon c \sigma_T} \approx 2.2 \times 10^{-9} (M/M_\odot)\,M_\odot\,\mathrm{yr^{-1}} \tag{1.2}$$

In the majority of astrophysical systems accreting material has significant angular momentum, which must be conserved during the accretion process. This prevents matter from falling directly onto the black hole, instead it settles into approximately Keplarian orbits at radii appropriate for the material's angular momentum. The accreting material will possess a range of specific angular momenta and thus orbit at different radii (in fact the material will quickly settle into a plane perpendicular to the average angular momentum vector possessed by the accreting material). This differential rotation causes 'friction' between material at different radii and allows for the viscous transport of material and angular momentum through the rings. This process leads to radial spreading of the accreting material and the formation of an accretion disk, allowing for the liberation of gravitational potential as material moves through the disk which is converted to kinetic energy and radiated [34]. It can be shown that molecular viscosity in accretion disks is not sufficient to transfer material through the disk at a sufficient rate to explain observations of systems thought to contain accretion disks (see below) and instead turbulent mechanisms are required. Although there is currently no consensus on the exact mechanism at work, it is widely accepted that a magnetic instability is responsible for the turbulence [35, 36].

An important yet still open question in accretion physics is that of how efficiently a disk is able to radiate away its energy (the accretion efficiency, introduced previously, is given as $\eta = L/\dot{m}c^2$). For systems when the accreting body contains a physical surface

(any body other than a black hole) even if the disk itself is not radiating efficiently material will eventually strike the surface and release any energy not radiated in the disk. This is not the case for black holes, where, once material passes the event horizon, any energy associated with it (and, of course, its rest mass energy) is lost. For an object with a surface the maximum efficiency is still $\sim 15\%$ as stated previously.

1.2.1 Radiatively efficient accretion flows

The thin disk accretion disk model of Shakura & Sunyaev 1973 represented a step change in the understanding of accretion disks. This model assumes that an accretion disk is thin (the height is significantly less than the radius, $H << R$), radiatively efficient (the radiation loss rate is equal to the heating rate at every point in the disk), steady state (accretion rate is constant), and assumes Keplarian orbits [37]. Such a disk is geometrically thin and optically thick, and as such each disk annulus emits thermal (black body) radiation at a single temperature. Most important to the progression of accretion disk understanding was through the introduction of the α-ansatz, which prescribes the disk viscosity to be $\alpha c_s H$ where c_s and H are the disk sound speed and height, respectively. This was motivated by the fact that turbulent regions are necessarily limited by the height of the disk. The requirement of radiative efficiency is only satisfied when the accretion rate is $\sim 0.01\dot{m}_{Edd} \lesssim \dot{m} \lesssim \dot{m}_{Edd}$, and outside of these ranges cooling is not efficient enough to balance the input of accretion energy, resulting in the formation of an advection dominated accretion flow (ADAF).

1.2.2 Advection dominated accretion flows

Above and below $\sim \dot{m}_{Edd}$ and $\sim 0.01\dot{m}_{Edd}$, respectively, a different type of accretion flow is formed which in both cases is dominated by advection. For an advection dominated accretion flow either the radiative mechanisms at work in a thin disk are not efficient enough to balance the gravitational potential energy being liberated through viscous coupling (for $\lesssim 0.01\dot{m}_{Edd}$) [38], or photons scatter out of the flow on a timescale longer than the inflow timescale (for $\gtrsim \dot{m}_{Edd}$), and significant amounts of energy can be advected across the event horizon, and advective cooling dominates radiative cooling. These two cases are known as super-critical and two-temperature flows, respectively [39].

In the case of a super critical flow, where the accretion rate is at, or significantly larger than, the Eddington rate, there is a critical accretion disk radius within which material is advected across the horizon faster than it can radiate (the inflow timescale is smaller than the radiative timescale). This results in the accretion disk puffing up (caused by the over-dense

accretion flow having a large optical depth, effectively trapping the radiation, heating, and expanding), and the thin disk approximation becoming invalid. Super-critical ADAFs can therefore emit significantly sub-Eddington luminosities even for super-Eddington accretion rates [40].

At much lower accretion rates and disk densities, below around $1\%\dot{m}_{Edd}$, a second type of advection dominated accretion flow can form (sometimes called a two-temperature flow). For a two-temperature flow, occurring below $\sim 1\%$ of the Eddington rate, the density of the accreting material drops significantly. The protons in the accretion flow are preferentially heated by viscous processes but radiate less efficiently than the electron population (due to their significantly larger mass). Due to the low density in the accretion flow, Coulomb interactions occur between the protons and electrons on a longer timescale than the accretion timescale. This results in the electrons and protons being out of equilibrium (at different temperatures) and the protons advecting a significant amount of the thermal energy liberated by accrection across the event horizon [41].

Both of these mechanisms result in a hotter accretion disk which will puff up and no longer be geometrically thin. While the thin disk has a modified black body spectrum (the sum of disk anulii, each having a single temperature, plus general relativistic corrections especially important for the inner disk) ADAFs show an additional spectral component manifesting as a power law with spectral indices of ~ 0.5 to 1.5 in AGN [42, 43] and ~ 0.5 in BHXRBs (e.g. [44, 45, 46] and references therein). This is the result of hot ($\sim 100\,\mathrm{keV}$ in BHXRBs, and similar in AGN [47, 48]) thermal electrons (the corona) Compton up-scattering cooler disk photons. The power-law component peaks at approximately the electron temperature and then falls off rapidly. Accretion disks can exhibit spectral features of both an ADAF and a radiatively efficient flow (e.g. hard state BHXRBs), with the power-law component dominating at higher energies. So called 'disk-corona' models have been invoked to explain these, where a thin outer disk truncates at some radius and transitions to a hot gas pressure dominated thick disk [49, 38] with similar properties to the later introduced ADAFs. The luminosities of ADAFs and thin disks have different dependencies on the accretion rate. For a slim disk $L \propto \dot{m}$ whereas for an ADAF $L \propto \dot{m}^{\sim 2}$. Consequently, ADAFs are significantly underluminous for their accretion rate when compared to systems with a radiatively efficient disk.

While accretion disks are the most common geometry for accreting material, accretion can also be highly collimated (in e.g. magnetically dominated systems [50]) or, for Bondi-

Hoyle accretion, gravitationally focused for an object moving through a cloud of gas with low specific angular momentum [51].

1.2.3 Observations of accretion disks

Disk structures are ubiquitously observed in astrophysical systems, and can be directly seen in many cases without the use of cutting edge instrumentation. Standing outside on a clear night away from terrestrial light sources you can clearly see that the galaxy is planar, having similar structure to local disk galaxies that can be observed at a variety of orientations with modest optical telescopes. Similarly, objects in our solar system lie in a plane, and the planets likely formed from a disk of material around the young Sun. Images of the centres of nearby AGN by the Hubble Space Telescope (HST) have revealed disks of dust roughly perpendicular to the system's jets, strong evidence for an accretion disk [52, 53]. Observations of AGN accretion disks have recently been pushed to the extreme through the use of global sub-mm VLBI, enabling physical resolution on the scale of the event horizon for the nearby AGN M87 [27, 54]. These observations revealed an asymmetric (in brightness) ring with a central dark region. This configuration matches the predicted observational signature of light bending around a spinning supermassive black hole, and photon capture at its event horizon, where the emitting material is hot plasma orbiting the black hole - part of an accretion flow [27, 55]. HST has also directly imaged disks on smaller scales, around young stars (the Herbig-Haro objects) that are also seen to launch jets perpendicular to the plane of accretion [56].

More recent evidence for naturally occurring accretion disks in stellar systems comes from observations of proto-stellar objects with sub-mm interferometers, specifically with the Atacarma Large (sub-)millimeter Array (ALMA) due to its high angular resolution [57, 58]. These observations have directly resolved disk structures accreting onto young stars in great detail, leaving little doubt about the formation of accretion disks in nature.

More indirect, yet relevant to the study of transients, evidence is optical through X-ray observations of CVs, NSXRBs, and BHXRBs. In certain accretion states the optical/UV/X-ray (depending on the object) spectra of these accreting systems are very well described by modified black body templates, indicating the presence of a thin accretion disk. Although the accretion disks in such systems have angular extents unresolvable by any current instruments, they can be mapped out through modelling the movement of emission lines in their spectra in a process called Doppler tomography [59].

1.3 Jets and ejections

Intrinsically linked to the process of accretion is the formation of outflows - material ejected from an accreting system. Outflows, like accretion, are ubiquitous and occur in a range of configurations. The slowest forms of outflow seen are winds, which are significantly sub-relativistic ($\sim$ 100s to $\sim$ 1000s $\mathrm{km s^{-1}}$, with the slowest outflows occurring in young stellar objects e.g. [60]) and are usually associated with an outflow from the accretion disk itself, driven by radiation pressure. Such outflows also provides another mechanism for the accretion disk to lose angular momentum, in addition to viscous processes.

A more well known signature of accretion, and one for which the formation process is not well understood, is the production of jets. These differ from accretion disk winds in that they are anywhere from mildly ($\Gamma = 1/\sqrt{1-\beta^2} \sim 2$ in e.g BHXRBs [61, 62]) where β is the bulk velocity of the outflow, to moderately ($\Gamma \sim 30$, typically, in e.g. AGN [63, 64]), to extremely ($\Gamma \gtrsim 100$ e.g. in GRBs [65]) relativistic, where Γ is the bulk Lorentz factor of the outflow. Also unlike disk winds, which are expelled from systems over a wide angle, jets are highly collimated outflows (with an opening angle $\theta \lesssim 10^\circ$ in most cases [66, 62, 67]) which are launched approximately perpendicular to the accretion disk plane in two anti-parallel directions. As well as the launching mechanism for jets not being well understood, neither are their make-ups or structures. These properties are most easily probed in nearby AGN (see Figure 1.2) in which the jets can be directly resolved from radio all the way to X-ray frequencies, revealing their collimated structure. AGN jets are seen to extend well beyond the galaxy that hosts the black hole producing them, and appear to expand almost spherically in lobes formed where the jets shock the intergalactic medium. The extended lobes have a spectral index (and polarisation) consistent with being produced by optically thin synchrotron radiation, a realisation which lead to the inference of the internal energy of the lobes being a significant fraction of the time integrated accretion power [68]. Jets therefore are able to influence scales larger than an entire galaxy, whilst being fed from a region comparable in size to the Solar System, and are thought to mediate the growth of the galaxies that host them. Simulations suggest that the majority of radio emission from jets comes from synchrotron emitting electrons in a sheath (i.e. jets are continually less dense towards their central axis [69]), but the question of baryon loading and the presence of positrons in jets is still an open one.

The origin point of the jet, at the centre of the galaxy, reveals a compact radio source with a flat spectrum (see Chapter 2 for more detail) which is consistent with synchrotron

radiation from a superposition of different temperature electron populations at different separations from the black hole [70]. Electrons are accelerated into a power law distribution either by shocks internal to the jet or through jet – ISM/IGM interactions.

Jet formation is evidently linked to accretion (originating in the same compact regions) but does not require a black hole. Jets have been observed from stellar systems, white dwarfs, and Neutron stars, as well as from black holes both of approximately stellar mass and supermassive [71, 72, 73]. While accretion and jet production are clearly linked phenomena, jet-like outflows have also been observed from non-accreting but rapidly rotating objects, such as pulsars or massive stars [74]. As mentioned previously, the exact mechanism responsible for the launching of jets is not well understood, however there are a range of theoretical prescriptions describing the process, as well as sophisticated simulations demonstrating the ability of accretion disks to launch jets. The predominant mechanisms to explain jet launching invoke a coupling between magnetic fields and the rotational energy of some element of the accreting system (the disk or the compact object itself). I will briefly mention two of the most commonly invoked ideas:

- **Black hole spin powered:** This scenario, commonly called the Blandford & Znajek (BZ) scenario, discusses the affect of a spinning black hole with an event horizon threaded by magnetic fields, allowing for the extraction of the rotational energy of the black hole [75]. The rest mass of a black hole can be written as $M = M_{\rm irr} + M_{\rm red}$ where $M_{\rm irr}$ is the irreducible mass of the black hole, and $M_{\rm red}$ is its reducible mass [76]. For a non-rotating (Schwarzschild) black hole $M = M_{\rm irr}$ and the rest mass of the black hole is a quantity that is only ever increased by classical processes (e.g. through accretion). Hawking radiation can, oxymoronically, reduce the irreducible mass of a black hole but it is a negligible affect for black holes of stellar masses and above (and it is a quantum mechanical process, not a classical one). For a rotating black hole some of hole's mass is associated with its spin and $M_{\rm red} > 0$, which is mass that can be extracted. In the ergoregion of spinning black holes there exists negative energy orbits which were shown to allow for the extraction of the reducible mass by particle pairs - one falling into the hole and one escaping to infinity [10]. This process (the Penrose process) is not thought to be efficient enough to account for the production of jets. However, under the assumption of ideal magnetohydrodynamics, magnetic flux in the accretion disk is frozen into the accreting material and is therefore amplified at the inner disk. As the material is lost across the event horizon the magnetic field lines are anchored to it, coiling them up, enhancing the toroidal component of the magnetic

field, and creating large magnetic field gradients and therefore pressure forces in the direction of the spin axis. However the field lines, coiled by frame dragging, are not coiled 'for free' but rather are done so by the black hole doing work on the field lines. The process therefore taps the spin energy of the black hole (analogously to the Penrose process). It has been claimed that a correlation between black hole spin and jet power has been observed in galactic black hole binaries [77], which would be strong evidence for the operation of the BZ mechanism (which is more efficient for higher spin) but this result is disputed [78]. A similar relation between spin and jet power has also been invoked to explain the radio-loudness of AGN [79]. The BZ mechanism cannot operate in systems that do not contain an event horizon.

- **Accretion disk powered**: This scenario, commonly called the Blandford & Payne (BP) scenario, instead invokes the rotation of the accretion disk to produce jets, and therefore does not require an event horizon [80]. In the BP model, as for the BZ model, there is the assumption that poloidal magnetic field lines are 'frozen in' to the disk and so co-rotate with it, while extending outwards from the disk. Plasma is guided by these field lines (not moving radially away from them) but can be moved along them. This is analogous to the motion of a bead threaded by a rotating wire [81]. It was shown that the angle the poloidal field lines make with the plane of the disk (as they exit the disk) influences the stability of the plasma threaded by the field lines upon perturbation. Under the assumption of ideal MHD, the Lorentz force can be decomposed into two components, a magnetic pressure (a force directed from regions of large magnetic field density to low) and tension (acting to straighten field lines). As the field lines twist up due to the rotation of the disk a strong toroidal component is created near the disk which is weaker in the direction of the disk rotation axis, and so the pressure gradient drives plasma up the disk rotation axis, while the tension force collimates the outflow. This only occurs if the angle made by the poloidal to the plane of the accretion disk is smaller than 60°, otherwise perturbations are restored by gravitational forces. This mechanism can operate in any astrophysical system with an accretion disk, making it an attractive 'universal' solution to jet production. At some distance from the disk the plasma will have significant thermal energy and will no longer be bound to the field lines and the acceleration will cease.

Given that jets are seen in non-black hole systems it is likely that the accretion disk is the common mediator for jet production, but it could be that black hole jets are produced via a different mechanism to e.g. those in neutron star systems, or that multiple processes

work in concert (e.g. black hole spin could augment the disc-only jet power).

I will also take this opportunity to distinguish what I will call 'discrete ejections' from jets. These are observed to be launched from BHXRB systems during particular reconfigurations of the accretion flow (discussed in more detail in Chapters 4 and 5). These differ from jets in that they are not a constantly replenished outflow (and as such don't have the classic conical jet morphology) instead being apparently spatially unconnected to the black hole (although there is observational evidence of energy exchange between the core jet and discrete ejections in a handful of cases [82, 83, 84]). They are still relativistic outflows, and are observed to move to much larger separations than the head of the compact core jet, and represent an additional feedback mechanism in BHXRBs, which may also be applicable in AGN but on much longer timescales [85]. The launching mechanism for discrete ejections is not understood but is likely related to the one producing the core jet switching off (as they are seen to launch during state transitions as the core jet quenches). Despite the apparent differences between discrete ejections and the compact core jet it could be that they are e.g. bright spots embedded in a fainter continuous flow as in the FR II AGN.

1.4 The transient universe at radio frequencies

The above sections motivate the question - what kind of astrophysical systems produce transient astrophysical jets? Significant changes to the processes of accretion and jet production in AGN happen on vast timescales compared to those in galactic systems (despite the dynamical timescale at the event horizon being only of the order hours), and while the structure of jets is more easily probed in nearby AGN, their formation and evolution are much harder to study. This is not the case in transient systems, where changes in the accretion properties of a system (driven by a host of mechanisms for different source classes) occur rapidly and can lead to the production of jets, winds, and ejections. Additionally, due to the variety of progenitors to radio transients, outflows are produced with a diverse range of properties (bulk Lorentz factors, masses, opening angles, total energy) and interact with regions with diverse properties (from ISM regions polluted by the eruptive mass loss from giant stars, to pristine cavities evacuated by constant jet action).

The field of astrophysical transients is in perhaps the most exciting position it has ever been in. There is a vast breadth of phenomena to be studied, all of which provide new and exciting information on a range of physical processes, from the properties of compact objects

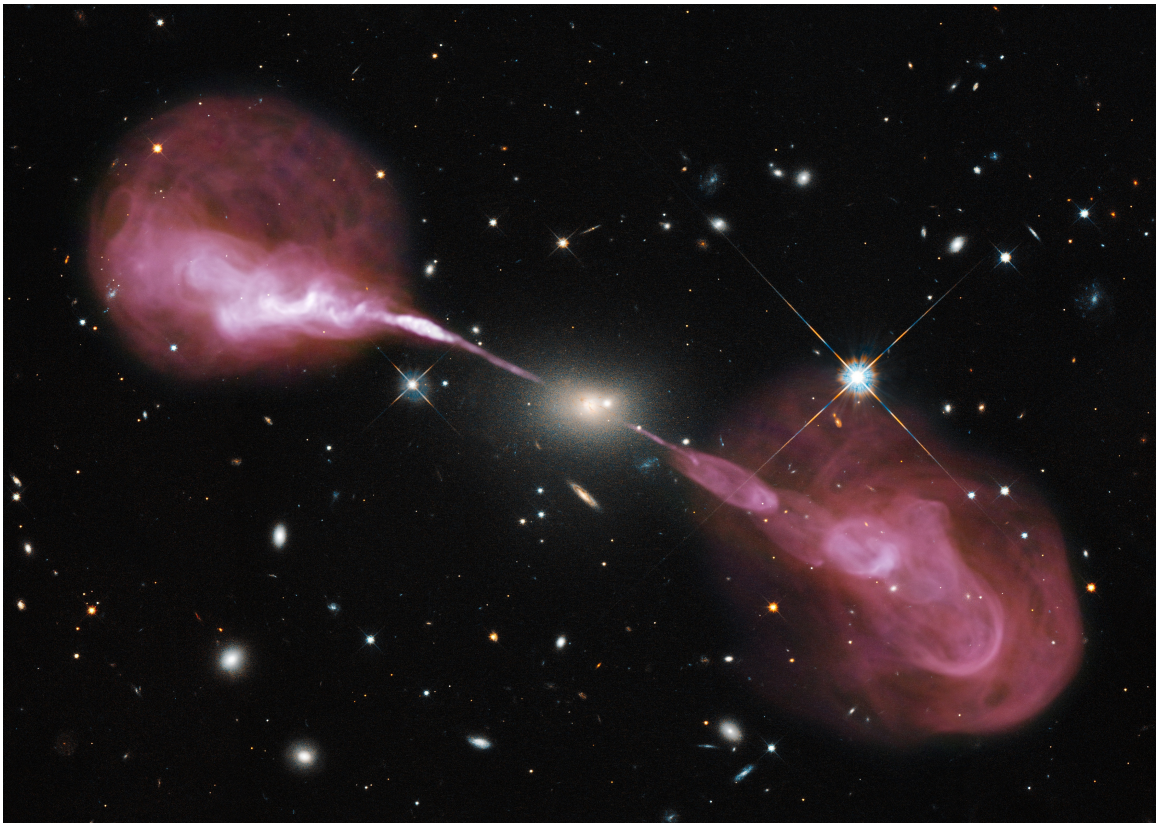

Figure 1.2: Multiwavelength image of Hercules A made with the the Hubble Space Telescope and the Karl G. Jansky Very Large Array. The central extended object in white is the optical galaxy which hosts a $\sim 10^9\, M_\odot$ black hole. Huge, initially collimated, radio jets are seen to be launched from the galaxy. Image credit: ESO.

within our Galaxy to the death mechanisms of massive stars in the very early universe. A common theme in such transient systems (especially those showing radio emission) is that of accretion and the subsequent production of outflows. Here I will briefly highlight key observations of jets in transient systems, demonstrating the diversity of systems producing jets. I will also try to briefly highlight the key physical inferences gained from such observations. Through my thesis I will discuss a number of these source classes in more depth and so will not go into great detail here.

1.4.1 Fast transients

Fast radio transients are typically not studied in the image plane as they vary on timescales significantly less than the usual correlator dump time employed for standard imaging observations (typically a few seconds). In order to study such transients the raw correlator voltages as a function of time are studied instead, allowing for temporal and spectral structure of these transients to be probed in greater detail.

The most well studied and well known class of fast transients are the radio pulsars, the first of which was discovered in the late 1960s as a 'rapidly pulsating radio source' at the Mullard Radio Astronomy Observatory at the University of Cambridge [86]. The regularity of the source led to its classification as a rapidly rotating neutron star, a classification which has since been widely accepted and adopted to explain the large number of pulsars known today. It is thought that pulsars emit beams of radiation (in addition to their particle outflows [74]) which we only see when they are pointed towards the Earth, and due to their steady rotation we see periodic radio emission. The exact mechanism causing the emission is not known (although it is likely that it requires a coupling between the large angular velocity and strong magnetic field in a Neutron star), but it is a 'coherent' radio process, where emitting particles do so dependent on one another with a fixed phase relation (as apposed to an incoherent process, i.e. synchrotron, where particles emit independently). Pulsar periods are in the approximate range 10^{-3} to 10 s and are clustered into two groups [87]. The millisecond, or recycled, pulsars have periods between 10^{-3} to 0.1 s whereas the 'normal' pulsars rotate with periods between 0.1 to 10 s. The recycled pulsars are thought to have been spun up by the transfer of angular momentum from material accreted from a binary companion. Pulsar studies help to probe the interior properties of neutron stars themselves, as well as the properties of material in large magnetic fields and strong gravity. Due to their extreme regularity pulsars essentially act as accurate clocks operating in strong gravitational potentials, and as such they have also been used as tests of general relativity [88, 89].

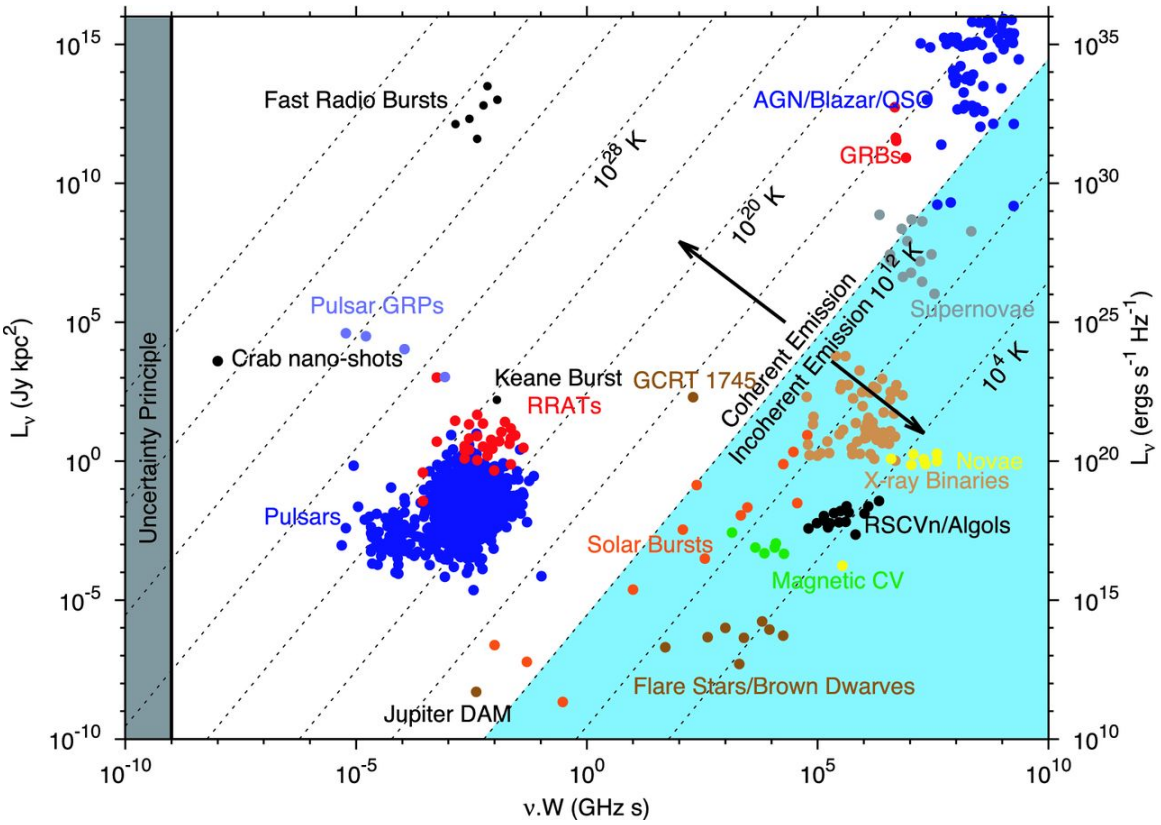

Figure 1.3: Luminosities and rise times of fast (coherent) and synchrotron transients with source classes labelled on the figure. Dotted lines denoted constant brightness temperature. The diversity in timescales and peak energetics of transient events is evident. Note that the coherent transients are not bound by the $\sim 10^{12}$ brightness limit imposed by Compton cooling, which bounds the incoherent transient region (where incoherent events with apparently higher brightness temperatures are likely beamed). The timescales for incoherent transients are shown in more detail in Figure 1.8. Figure reproduced from [94].

A relatively new class of fast radio transients are the Fast Radio Bursts (FRBs) which are pulses of high ($\gtrsim 1$ Jy) amplitude radio emission lasting $\lesssim 50$ ms (once de-dispersed to account for frequency dependent propagation affects that occur as radiation travels through the IGM) [90]. FRBs differ from pulsars in that they are not periodic, with the majority of the population recorded as isolated events (and those that do repeat do not appear to do so with any periodicity). They also have very large dispersion measures, which indicate they are extra-galactic in nature (confirmed through several FRB host galaxies now having localisations [91, 92]). FRBs were discovered in 2007 by the Parkes Radio Telescope and have sparked a resurgence in the implementation of low frequency transient search instruments [93, 90]. The study of FRBs is still in its infancy, with the class of sources emitting them still unknown. The typical timescales and luminosities of FRBs, Pulsars, as well as a number of other transient types showing coherent emission are demonstrated in Figure 1.3.

1.4.2 Synchrotron Transients

Transients associated with the synchrotron emission mechanism (which produced incoherent radiation) evolve on timescales longer than a few seconds, typically facilitating their study in the image plane using radio observations (see Chapter 3 for details).

Black hole and neutron star X-ray binaries (BHXRBs and NSXRBs, respectively) are compact objects accreting from a main sequence companion. They are separated into two further categories, depending on the mass of the companion, as either high mass (HMXRBs) or low mass (LMXRBs). HMXRBs transfer matter onto the compact object via a radiation driven wind, whereas the stellar companions in LMXRBs fill their Roche lobe and transfer matter through the primary Lagrange point (see Chapter 4 for details). X-ray binaries are alternatively called 'microquasars' due to having an analogous structure (albeit significantly scaled down in mass and size) to accreting and jet producing supermassive black hole at the centre of active galaxies. I will not refer to the high/low mass distinction again as, despite the different feeding mechanisms, both types of system accrete via a disk and can produce jets - thus being appropriately labelled as microquasars. BHXRBs are among the best systems to study the coupling between accretion and the production of outflows, as the accretion state of these systems can evolve on timescales easily accessible within a human lifetime (or, in the case of Chapter 4, within the lifetime of a PhD studentship). Resolving jets launched from systems within our galaxy is more challenging than those from AGN, and it has only been achieved for the core jet in two black hole X-ray binaries [95, 96]. In addition to the standard compact jet, LMXRBs also expel discrete ejections to larger angular separations which are more easily resolved at radio and X-ray frequencies [97, 98, 99, 100]. Tracking the velocity of these ejecta provides vital information on the geometric properties of XRBs, and in some cases the distance, black hole mass, and jet angle of such systems are very well constrained [100, 101, 20]. Additionally there are multiple systems (SS433, V404-Cygni, Circinus-X1) that show indisputable evidence for core jet precession [102, 103, 104], which subsequently informs us about the properties of the inner accretion disk (which may well precess along with it). Also evident in some XRB systems (SS433, Circinus-X1) is the presence of large scale nebula structures which are being shaped by the kinetic feedback from jets and ejections. Again, through analogy to AGN, this may provide valuable information on the mechanisms by which outflows from supermassive black holes can influence their surroundings, especially given that it can be shown that jet power is related to accretion in a common way across black holes of all masses [105]. I will discuss the accretion and outflow properties of BHXRBs in greater detail in Chapters 4 and 5.

Cataclysmic variables (CVs) are, in many ways, similar to XRBs but contain a white dwarf as the degenerate binary partner. Their outbursts are well modelled by instabilities in the accretion flow driven by the ionisation of hydrogen. As material builds up in the disk it will eventually reach a temperature sufficient to ionise hydrogen, which results in a sudden increase in the viscous coupling in the disk, and therefore accretion rate, until the disk is drained. A similar mechanism is thought to operate in XRBs, although without modification it cannot explain the entirety of outbursts from these systems [106]. While their accretion properties are well characterised, CVs are weak radio sources and therefore the coupling between accretion and outflows is hard to probe [72]. Core jets are inferred in CVs due to their flat radio spectrum, but are never resolved, and are mostly too weak to study in detail in the time domain. Discrete ejections have not been seen from CVs. Some radio loud CVs have shown circular polarisation consistent with 100% which precludes the presence of a jet, where the magnetic field is turbulent [107].

There are plenty of non-compact object stellar systems showing variable radio emission (e.g. [108, 109, 110]) likely due to magnetic reconnection events. The work in this thesis focuses primarily on transient sources with outflows powered by accretion, so I will not go into any more detail on these systems.

Gamma-ray bursts (GRBs) were discovered in the 1960s by satellites designed to detect the signatures of nuclear weapon tests. They instead detected flashes of astrophysical γ-ray emission lasting between a few and a few hundred seconds, and located isotropically across the sky [111] (meaning the progenitor mechanism must be occurring on scales much smaller than or much larger than the scale of the Galaxy). The isotropic equivalent energy inferred from the γ-ray emission and estimates of the source distances lead researchers to initially prefer the former (a population of local objects) and an array of theories were produced to explain the phenomena [112, 113]. Although a cosmological origin was also considered it required isotropic energy outputs comparable to the entire rest mass energy of the Sun. The initially poor localisation provided by early γ-ray observatories made associations with multi-wavelength counterparts challenging, and precluded e.g. redshift measurements for distance determination. As localisations improved the γ-ray sources were identified with host galaxies, and their distances could then be determined, showing that they were indeed cosmological [114]. In addition to the short timescale γ-ray emission, GRBs also produce afterglows which last from weeks to years after the initial γ-ray detection and are observed at radio through X-ray frequencies. There appear to be two populations of GRBs, motivated by the observed bi-modality in the event duration, with the prompt emission from short

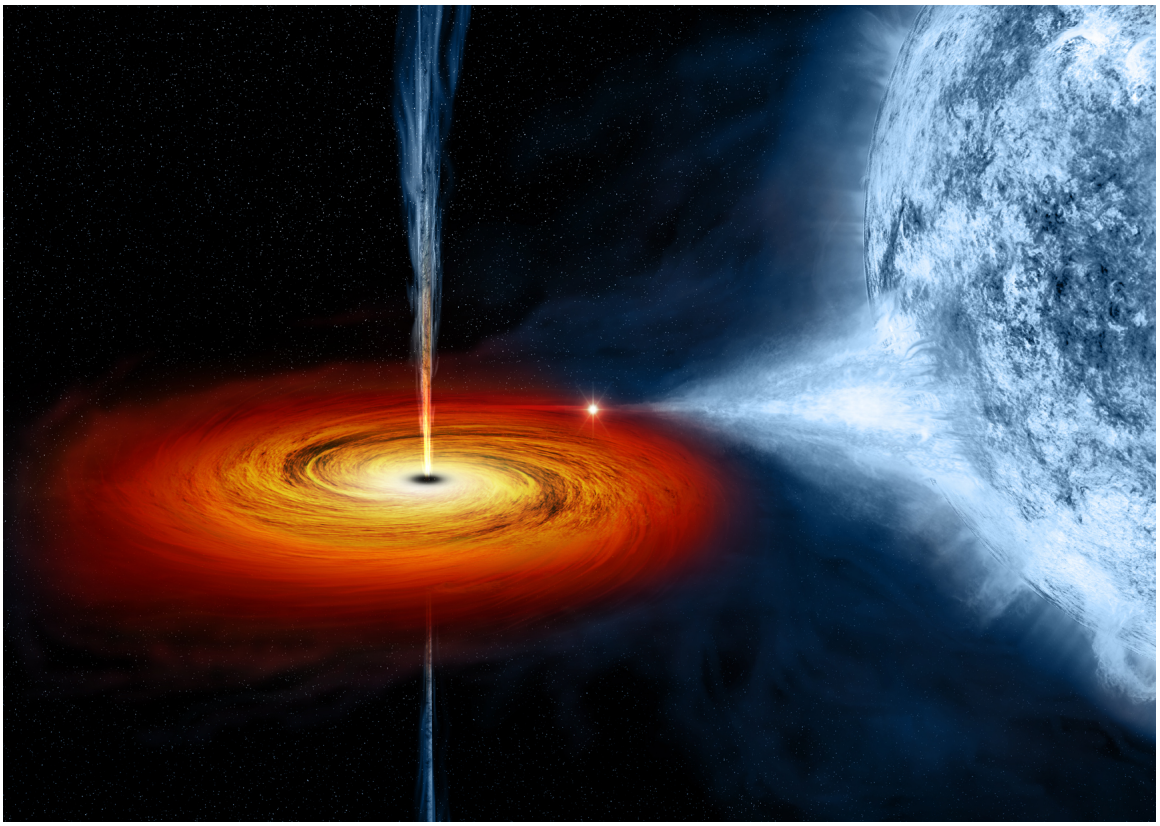

Figure 1.4: An artistic impression of a black hole X-ray binary. Material is accreted onto the black hole from its stellar companion through the first Lagrange point and then via an accretion disk which is primarily visible at optical in X-ray frequencies. The black hole is launching bipolar streams of collimated material, a jet, which is visible primarily at radio frequencies. Image credit: NASA.

GRBs lasting < 2 s and long GRBs > 2 s [115, 116]. These differences are though to be motivated by different progenitor systems although both produce similar afterglows. Long GRBs are thought to be produced by the death mechanism of massive stars as they collapse and form a black hole. This process results in the expulsion of a shell of material as well as extreme accretion rates on to the black hole of up to $\sim 1\,M_{\odot}\,\mathrm{s}^{-1}$, driving the production of an extremely relativistic jet (with bulk $\Gamma > 100$, or $v_{\rm jet} > 0.99995c$). Due to relativistic effects such a fast outflow is beamed into an extremely small angle ($\theta \sim 1/\Gamma$) and we only observe GRBs where the jet axis points at or close to our line of sight. This beaming also solved the so-called 'compactness problem' where, without beaming, the observed high energy from GRBs would mean their optical depth to pair production would be too large for us to observe γ-rays (this is discussed in more detail in Chapter 6). Amazingly, detailed VLBI studies of gamma-ray bursts have also lead to direct evidence of jets in the form of apparently superluminally moving (or expanding) radio sources [117, 118]. Figure 1.5 shows an artistic/schematic demonstration of the outflow produced by a GRB. In Chapter 6 I will present a radio and X-ray study of GRB 171010A where I will discuss the properties of GRB outflows in more detail.

Short GRBs are thought to originate from a different progenitor channel compared to long GRBs. It has long been conjectured that short GRBs result from the merger of binary neutron star systems, after gravitational wave radiation extracts appropriate angular momentum to bring the stars into contact. Gravitational wave radiation had been invoked to explain the decreasing orbital separation of the Hulse-Taylor binary pulsar, although this was only an indirect inference of its existence [88, 119]. In 2017 the LIGO-VIRGO interferometer directly detected gravitational waves from a binary merger with constituent objects of masses consistent with both being neutron stars (and has been detecting gravitational waves from binary black hole mergers since 2015 [120, 121]). There was an extensive search for the associated electromegnetic counterpart which was successfully located at radio, sub-mm, IR, optical, UV, X-ray, and γ-ray frequencies by a range of facilities [121]. This set of observations effectively confirmed the link between neutron star mergers and short GRBs (although this was a significantly sub-luminous SGRB) and provided an independent method to cross-check gravitational wave sources detected by LIGO-Virgo. These multiwavelength studies have led to a number of exciting results, including the confirmation that NS mergers can distribute heavy elements into their environment [122]. Radio studies of this source, named GW170817, have revealed the properties of the outflow it produced to be a relativistic jet, further strengthening the connection to SGRBs [123, 118]. To date GW170817 is the only electromagnetic counterpart to a gravitational wave source (likely

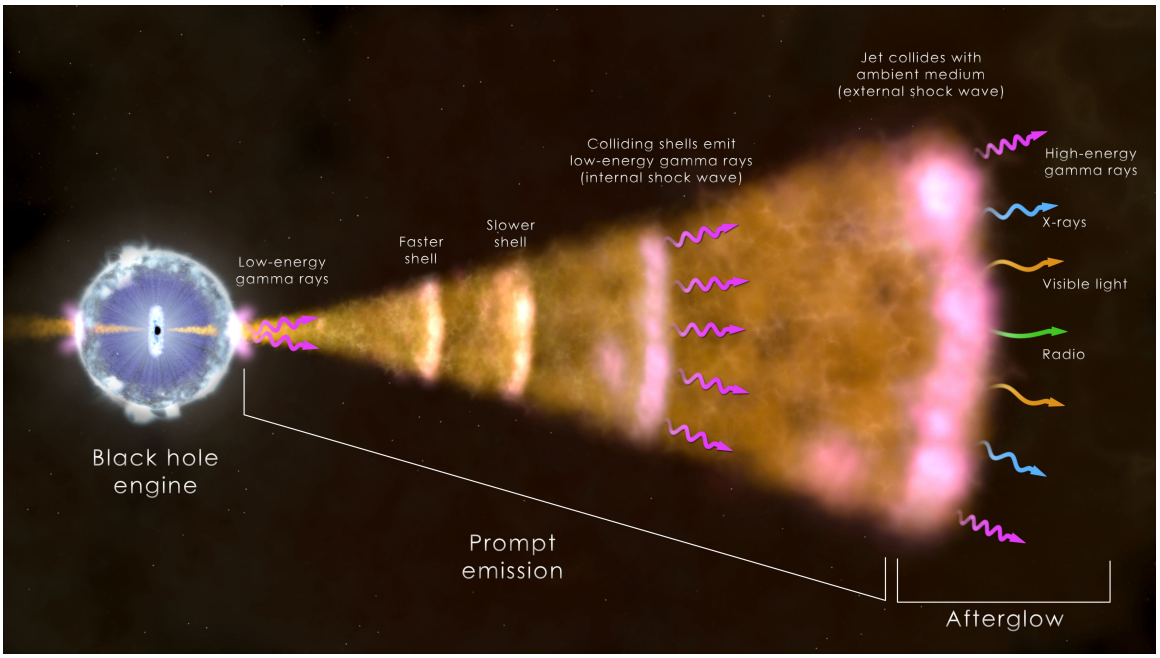

Figure 1.5: An artistic impression of a gamma-ray burst, highlight some of the key processes associated with the event. Although the details of the central engine powering GRBs is not completely understood, although merging neutron stars and the collapse of massive stars are likely progenitors. Rapid accretion occurs in such events, resulting in the formation of extremely relativistic jet which shock internally to produce prompt γ-rays. The long lived afterglow is the result of this jet ploughing into, and shocking, the circumburst material. Image credit: NASA.

due to its relative proximity to Earth), but new triggers (including those with one or more black hole constituent) are extensively followed up and it seems likely that new events will soon be detected with both gravitational wave and electromagnetic facilities. Short GRBs, along with LGRBs, produce afterglows which are studied in the same framework, which I discuss in Chapter 6 in the context of the long GRB 171010A.

While accretion onto AGN via a standard accretion disk is a slowly evolving process, supermassive black holes are still involved in transient events. Stars that stray too close to a supermassive black hole can be tidally disrupted and a fraction of its mass is accreted onto the black hole [124]. Such events are known as tidal disruption events (TDEs) or tidal disruption flares (TDFs). Observing TDEs gives a unique opportunity to study the onset of accretion, as well as the formation of accretion disks (which can be initially significantly inclined to the spin axis of the black hole) which is not probed in e.g. galactic binaries where the accretion disk is well established and the onset of increased accretion occurs due to instabilities in the disk. Observations of TDEs have provided a unique method to probe the structure of galaxies on the small scales around the central supermassive black hole, both in terms of the stellar distribution (through studies of event rates) and the host density

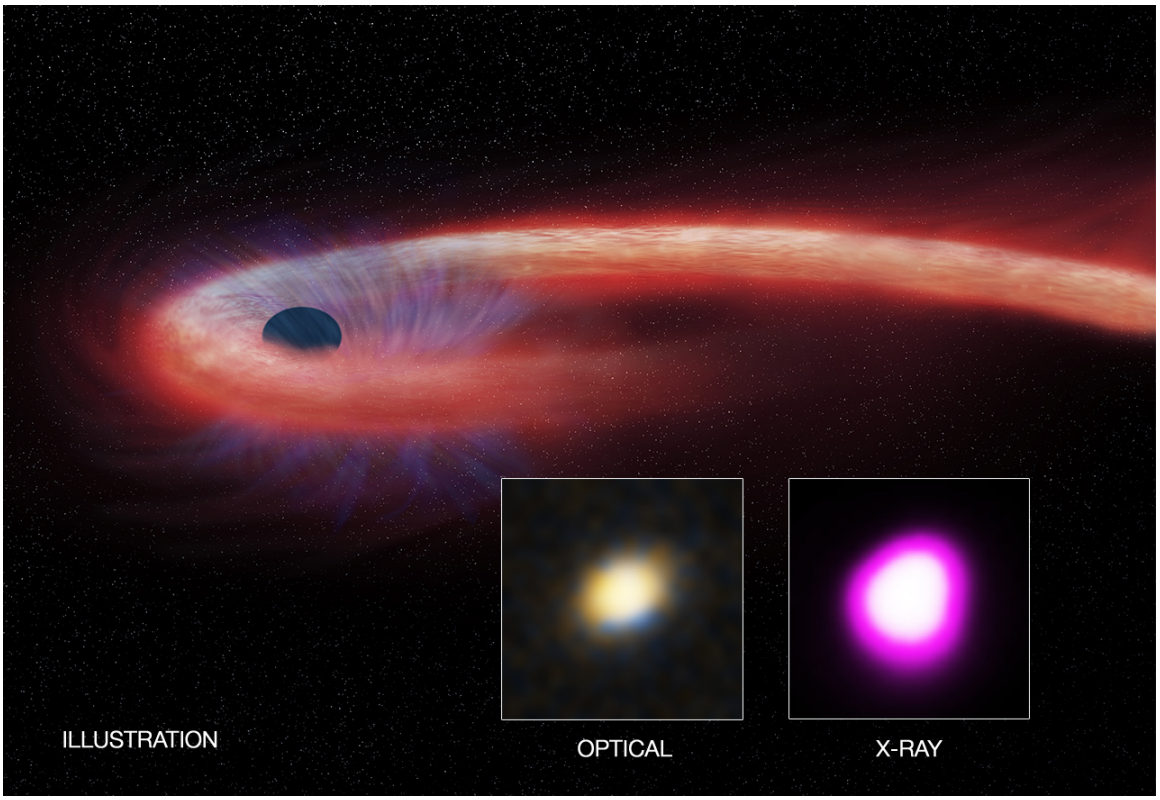

Figure 1.6: An artistic impression of a tidal disruption event, showing a stream of material which is the remnant of a star that has passed within the tidal radius of the supermassive black hole. Image credit: NASA.

environment through a study of how their outflows evolve at radio frequencies. The outflows from TDEs initially appeared to come in two classes, either a relativistic jet (from the so called relativistic TDEs [125, 126]) or a lower velocity outflow (from the so called thermal TDEs [127, 128]). The multiwavelength properties of these two classes vary, as does their energy budget, with the relativistic TDEs being significantly more energetic and their multiwavelength properties consistent with coming from a jet. More recent observational studies have cast doubt on the non-jetted/jetted paradigm, with evidence suggesting even the thermal population might produce jets (although with lower velocities and energies, see Chapter 7 for more details). The optical through X-ray observations of the thermal TDEs are consistent with coming from a multicomponent black body which is likely the accretion disk. TDEs are still predominantly studied at optical through X-ray frequencies, and the number of TDE candidates with a radio counterpart remains limited. I will present a study of the thermal TDE ASASSN-14li, as well as updated observations of the relativistic TDE Swift J1644+57, in Chapter 7.

Perhaps the most abundant class of optical transients are the supernova (SNe) which

have seen a rapid increase in their discovery rate with the onset of next generation wide field optical transient surveys (e.g. the Zwicky Transient Facility [129]). There are a host of supernova classes which are distinguished based upon a number of factors, including their progenitor system (from core collapse to thermonuclear detonation of white dwarfs) and optical spectral lines. Certain classes of SNe (those involving the death of massive stars) are intrinsically linked to long GRBs, and any radio emission is attributed to the approximately symmetric expulsion of stellar material from the system – a process distinct from the relativistic jet that drives long GRB afterglows [130]. The optical emission from supernovae is driven by radioactive decay of heavy elements. Supernova outflows are not typically jetted, they are approximately spherical and have typical velocities of order $\lesssim 1000\,\mathrm{kms}^{-1}$. Radio emission is still predominantly from the synchrotron process, driven by the outflow shocking the ISM. Some of the more exotic supernova classes show outflow velocities (and collimation) more akin to those associated with jets, up to $\sim 0.7c$, indicating the possible presence of a 'central engine' (accreting compact object) in such systems. The search continues for radio emission from the class of superluminous supernovae [131].

A new class of transients which were originally classified as supernova are the fast blue optical transients (FBOTs), demonstrating optical rises under $\sim 10\,\mathrm{d}$, blue (hot) featureless spectra, and large optical luminosities ($\sim 10^{44}\,\mathrm{erg\,s}^{-1}$ at peak) making them hard to reconcile with any class of supernova [132]. A handful of the population (only 10s of sources in total at this time) have also shown radio emission. This radio emission is comparable in luminosity to the sub-energetic GRBs and significantly larger than for normal supernovae [133, 134]. Radio studies of these sources have revealed that the outflow is both mildly relativistic (see Figure 1.7), collimated, and carries a large mass (greater than $0.01 M_{\odot}$), with X-ray observations suggesting that a central engine (a magnetar or black hole) is powering the outflow [135]. FBOTs are an exciting class of object that seems to possess properties intermediate to those of GRBs and supernovae.

A comparison of the outflow velocities and energetics from explosive compact object transients is shown in Figure 1.7, demonstrating the continuum of outflow speeds and their corresponding kinetic energy. The timescales and peak luminosities of both explosive and recurrent coherent radio transients are demonstrated in Figure 1.8, showing (exponential) rise times and peak luminosities spanning 6 and 22 orders of magnitude, respectively. Such studies demonstrate a general relationship between the quantities and indicate the potential power of using these simple observables to provide object classifications [94].

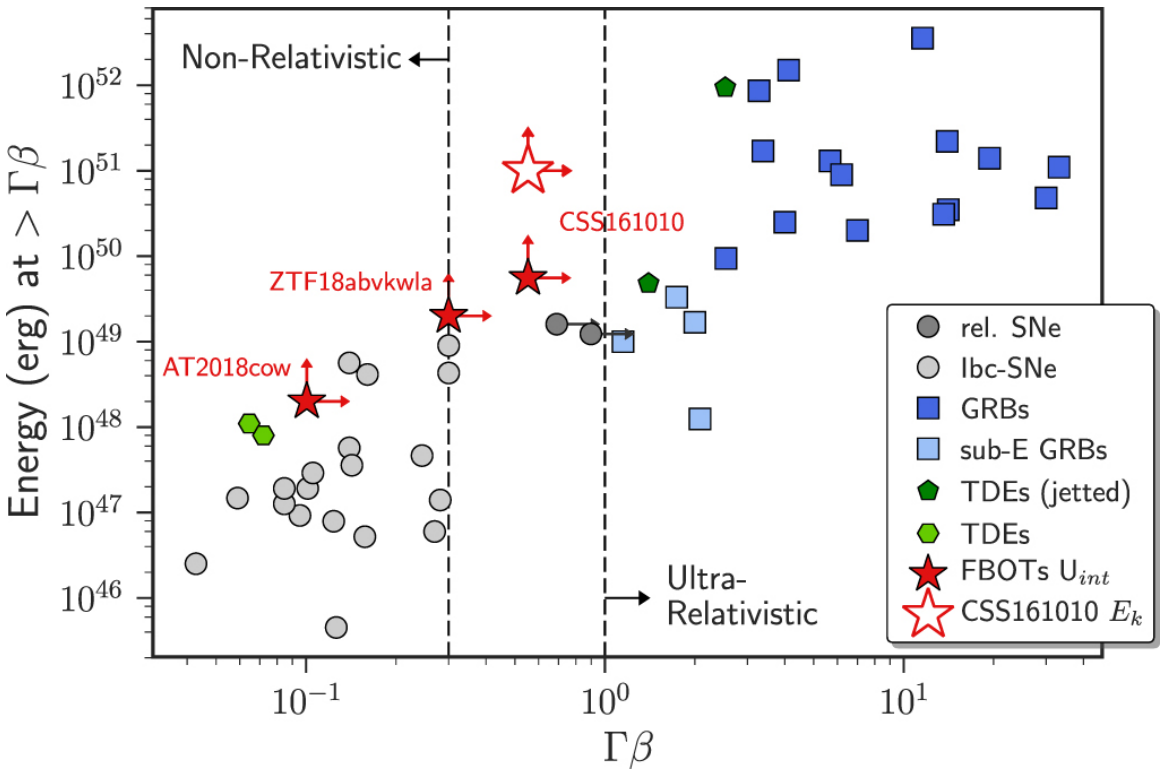

Figure 1.7: Outflow energy as a function of velocity (parameterised as $\Gamma\beta$, which is approximately equal to β for $\beta \ll 1$ and approximately equal to Γ for $\beta \gg 1$) for SNe, GRBs, GRBs, TDEs, and FBOTs. There is a clear continuum of outflow velocities, with faster outflows possessing larger amounts of energy. Standard GRBs are significantly relativistic, whereas standard SNe are non-relativistic. FBOTs seem to produce a range of outflow velocities, although for all source classes deceleration may occur and the initial velocities could be larger. Figure reproduced from [133].

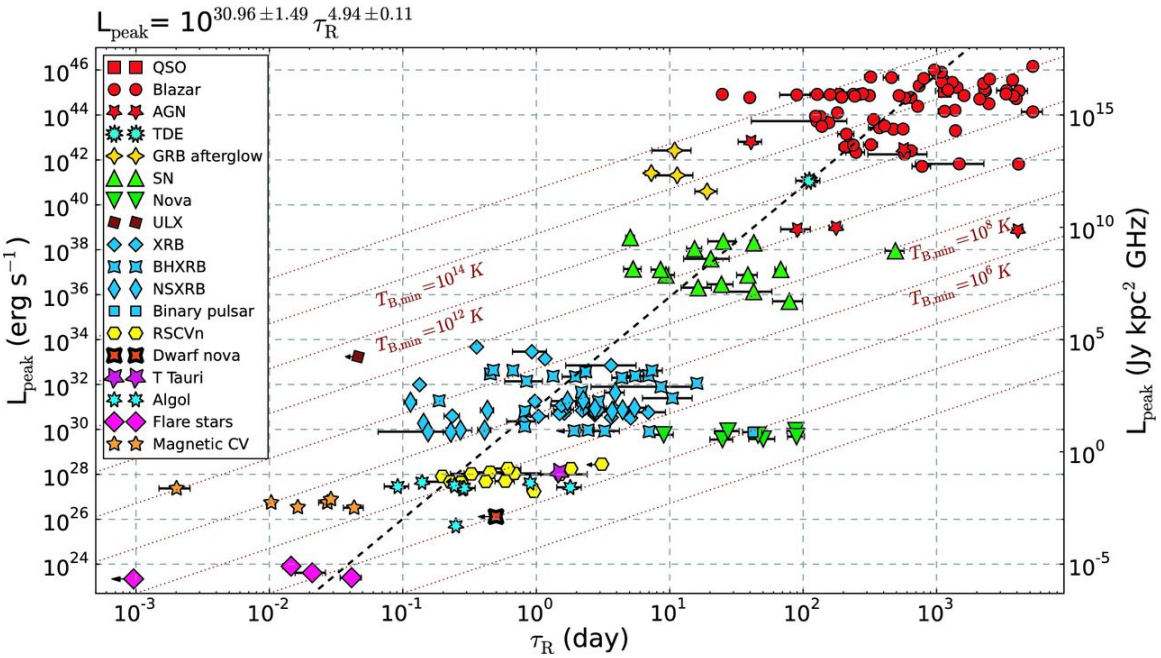

Figure 1.8: Exponential rise times and peak luminosities for incoherent transient events from stars to supermassive black holes. Lines of constant brightness temperature are marked in red. An emprical relationship between the peak luminosity and rise time is demonstrated by the black dotted line, with the functional form shown above the plot. Note the fitted slope being significantly steeper than the one expected under the assumption of all sources obeying the same relation between variability timescale and physical size [94]. Figure reproduced from [94].

I have described a range of transient phenomena that are studied at radio frequencies and contain a form of outflow, predominantly focusing on jets. Studying the systems in their own right has provided a wealth of information on a range of fundamental physics, and even more can be learned when considering population statistics studies and novel ways of utilising transient sources to probe seemingly unrelated phenomena, such as the expanding universe revealed with type 1a supernova, or the sub-parsec properties of the centre of galaxies probed by TDEs.

1.5 Thesis structure

In this thesis I will present data on a number of transient events, within three source classes - black hole X-ray binaries (BHXRBs), Gamma-ray bursts (GRBs), and tidal disruption events (TDEs). In Chapters 2 and 3 I will discuss relevant radiative processes and observational techniques, respectively. In Chapter 4 I will present an extensive observing campaign on the BHXRB MAXI J1820+070. Chapter 5 contains an analysis of radio flaring from BHXRBs as they transition between accretion states. In Chapters 6 and 7 I will present

radio observations of GRB 171010A and the TDE ASASSN-14li, respectively. Finally, in Chapter 8 I will present my conclusions and a discussion of the similarities and differences in the radio properties of the range of transient sources studied as part of this thesis.

Chapter 2

Radiation processes

In this Chapter I will give a brief account of the various radiation mechanisms referred to during this thesis. The following discussions are adapted from [136, 137], where more extensive treatments of these topics can be found.

2.1 Synchrotron radiation

2.1.1 Synchrotron power

As charged particles interact with magnetic fields they are accelerated and emit radiation. The interaction is characterised by the Lorentz force $\vec{F} = q(\vec{E} + \frac{\vec{v}}{c} \times \vec{B})$ where $\vec{F}$ is the force on a test particle of charge q, $\vec{v}$ is the particle's 3-velocity, and $\vec{E}$ and $\vec{B}$ are an electric and magnetic field, respectively. Considering only a uniform magnetic field, we may write

$$\vec{F} = m_0 \frac{\mathrm{d}(\gamma\vec{v})}{\mathrm{d}t} = m_0 \left(\gamma \frac{\mathrm{d}\vec{v}}{\mathrm{d}t} + \vec{v} \frac{\mathrm{d}\gamma}{\mathrm{d}t} \right) = m_0 \left(\gamma \frac{\mathrm{d}\vec{v}}{\mathrm{d}t} + \gamma^3 \vec{v} \frac{\vec{a} \cdot \vec{v}}{c^2} \right) = q \left(\frac{\vec{v}}{c} \times \vec{B} \right) \tag{2.1}$$

where $\vec{a}$ is the particle's acceleration and, given that the Lorentz force is applied perpendicular to the velocity vector ($\vec{a} \cdot \vec{v} = 0$), we immediately see that

$$\frac{\mathrm{d}\vec{v}}{\mathrm{d}t} = \frac{q}{m_0 \gamma} \left(\frac{\vec{v}}{c} \times \vec{B} \right). \tag{2.2}$$

where γ is the Lorentz factor of the particle. If we then decompose the velocity vector as $\vec{v} = \vec{v}_{\parallel} + \vec{v}_{\perp}$ with respect to the direction of the magnetic field, we see that the velocity component along the field lines is unchanged (the force is proportional to the cross product of $\vec{B}$ and $\vec{v}$ so there is no acceleration in the direction of $\vec{B}$), and that

$$\frac{\mathrm{d}\vec{v}_{\perp}}{\mathrm{d}t} = \vec{a} = \frac{q\vec{v}_{\perp} B}{m_0 \gamma c} (\hat{i}_{v_{\perp}} \times \hat{i}_B). \tag{2.3}$$

A particle with no motion along a field line, but some velocity component perpendicular to the magnetic field, will execute uniform circular motion around the field line, at a frequency $\nu = qB/2\pi\gamma m_0 c = \nu_g/\gamma$m where $\nu_g = qB/2\pi m_0 c$ is the non relativistic gyrofrequency (or alternatively the cyclotron frequency). If the parallel velocity component is non-zero, then the particle will execute helical motion at a pitch angle θ, with $\tan\theta = \vec{v}_\perp/\vec{v}_\parallel$.

When accelerated, charged particles lose energy, emitting electromagnetic radiation. In the case of $\gamma \sim 1$ (non-relativistic charged particle motion) this is known as cyclotron radiation, and for $\gamma \gg 1$ it is called synchrotron radiation. Both limits occur in astronomical systems. Cyclotron radiation occurs in, for example, accreting systems with large magnetic fields (e.g. cyclotron lines seen in optical observations of magnetic CVs) whereas synchrotron radiation occurs where electrons are accelerated to large Lorentz factors across shock fronts (or by any other acceleration processes). The latter limit is the one most relevant when studying transient systems at radio frequencies, as sources of such emission are associated with relativistic outflows (which drive relativistic shocks), producing emission clearly consistent with both self absorbed and/or optically thin synchrotron radiation (with characteristic properties that I will discuss below). For non-relativistic charged particles the power of the emitted radiation is described by Larmor's formula:

$$P = \frac{2q^2a^2}{3c^3}, \tag{2.4}$$

Which can be extended to include relativistic motion, becoming

$$P_{\rm rel} = \gamma^4 P = \frac{2\gamma^2 q^4 B^2 v^2}{3c^3 m_0^2}\sin^2\theta \tag{2.5}$$

when substituting in Equation (2.3). From Equation (2.5) it can be seen that less massive particles are accelerated more efficiently, and thus electrons (and positrons) will radiate significantly more power than protons. I will therefore continue the discussion of synchrotron radiation implicitly referring to the acceleration of electrons, and thus substitute q for e, the charge of an electron, and m_0 for m_e, the mass of an electron. Time averaging over possible pitch angles and recasting the magnetic field in terms of the magnetic energy density, $U_B = B^2/8\pi$, and introducing the Thompson cross section $\sigma_T = 8\pi e^4/3m_e^2c^4$, we arrive at the final expression for synchrotron power from a relativistic electron:

$$P_{\rm rel} = \frac{4}{3}\sigma_T c U_B \left(\frac{v}{c}\right)^2 \gamma^2. \tag{2.6}$$

While the total power emitted from a single electron may not sound like a useful quantity, we will see later that it is useful when calculating the spectrum from a population of electrons with a realistic energy distribution.

2.1.2 The synchrotron spectrum of a single electron

The observed synchrotron radiation spectrum from a single electron depends on its kinetic energy (i.e. its velocity). In the case that $v \ll c$ and $\gamma \approx 1$ the cyclotron radiation emitted is sharply peaked around the frequency $\nu_g = eB/2\pi m_e c$ as beaming is negligible (the emission intensity is essentially sinusoidal). For electrons with moderate Lorentz factors, the radiation spectrum is distorted as beaming causes the emission intensity to be enhanced as the electron moves towards the observer and is otherwise suppressed (the beaming angle is $\sim 1/\gamma$). The Fourier transform of the intensity profile with time (the spectrum) now shows emission from harmonics of the relativistic gyrofrequency ($eB/2\pi\gamma m_e c = \nu_g/\gamma$) contributing more strongly (the power from each sequential harmonic is suppressed by a factor of approximately $(v/c)^2$) and are broadened (with width increasing for higher harmonics). For relativistic electrons the spectrum is in fact simpler, as the harmonics effectively 'merge' together. It is peaked at $0.29\nu_c$ ($\nu_c = (3/2)\gamma^2\nu_g$) and emission is suppressed exponentially above the peak. Below the peak the spectrum rises as as a power law with index $1/3$.

2.1.3 The synchrotron spectrum of a power law distribution of electron energies

While it is valuable to consider the spectral profile of a single emitting electron, in astrophysical systems they are found in huge numbers and often with non-thermal energy distributions. Shocks, forming as a flow of material strikes another and drives into it with a velocity greater than the local sound speed, act to accelerate electrons such that the ensemble population has an energy distribution of the form $N(E)dE = kE^{-p}dE$ (or equivalently $N(\gamma)d\gamma = k'\gamma^{-p}d\gamma$) where $N(E)dE$ ($N(\gamma)d\gamma$) is the number density of electrons with an energy in the range E to $E + dE$ (Lorentz factor in the range γ to $\gamma + d\gamma$), k (k') is a proportionality constant, and the power law index p can be measured directly from an optically thin synchrotron spectrum (as shown below) and is usually found to be in the range 2 to 2.5. This process is known as first order Fermi acceleration [138, 139, 140]. As the synchrotron spectrum of a single electron is sharply peaked at $\nu_c \approx \gamma^2\nu_g$, we can make the simplification that electrons with energies in the range E to $E + dE$ are responsible for

emission at frequencies in the range ν_c to $\nu_c + d\nu_c$. We can write the radiated energy within this range as

$$J(\nu_c)d\nu_c = P_{\rm rel}(\nu_c)N(E)dE = \frac{4}{3}\sigma_T c\frac{B^2}{8\pi}k\frac{\nu_c}{\nu_g}\left(\frac{\nu_c}{\nu_g}\right)^{-p/2}(m_e c^2)^{-p}dE \tag{2.7}$$

where $J(\nu_c)$ is the radiation spectrum and has units erg s^{-1} cm^{-3} Hz^{-1}, and then see that, as $E = \gamma m_e c^2$,

$$J(\nu_c) = \frac{\sigma_T c B^2 k}{12\pi}(m_e c^2)^{1-p}\left(\frac{\nu_c}{\nu_g}\right)^{-(p-1)/2}. \tag{2.8}$$

We identify $\alpha = -(p-1)/2$ and see that the spectrum goes as $J(\nu_c) \propto \nu_c^{-\alpha}$ where α is known as the spectral index. The spectrum also depends on k and B, with all other quantities being constant. This simplified analysis gives the same dependence on ν_c, k, and B as the full treatment. As we are no longer interested explicitly in the maximum of the spectrum of a single electron, I will drop the use of ν_c and instead just use ν. The full emission coefficient, calculated by integrating the contribution from electrons at all energies to emission at a single frequency, is

$$J(\nu) = \frac{\sqrt{3}e^3 Bk}{c^2 m_e}\left(\frac{3eB}{2\pi m_e^3 c^5}\right)^{(p-1)/2}a(p)\nu^{-(p-1)/2} \tag{2.9}$$

where $a(p)$ is a function with a weak dependence on p ($a(p) = 0.529$ and $a(p) = 0.269$ for $p = 2$ and $p = 3$, respectively).

2.1.4 Synchrotron self absorption

The spectral flux dependence identified in Section 2.1.3 must be extended to consider the effect of synchrotron self absorption - the opacity of a population of electrons to its own synchrotron radiation. The brightness temperature of an emitting region is defined as the temperature of a black body producing the same intensity (erg s^{-1} cm^{-2} Hz^{-1} sr^{-1}) as the observed intensity of the region. The intensity of black-body radiation, in the Rayleigh-Jeans limit, is $I_\nu \approx 2k_B T_B/\lambda^2$ where k_B is Boltzman's constant. Self absorption becomes relevant when the temperature of the electrons at a given frequency (which can still be defined despite their distinctly non-thermal distribution of temperatures preventing the population being described by a single value) becomes comparable to the brightness temperature of the photons emitted by electrons at said frequency. The effective temperature of the electrons is $T_e \approx (m_e c^3/3k_B)(\nu_c/\nu_g)^{1/2}$ which, when equated to the brightness temperatures in the

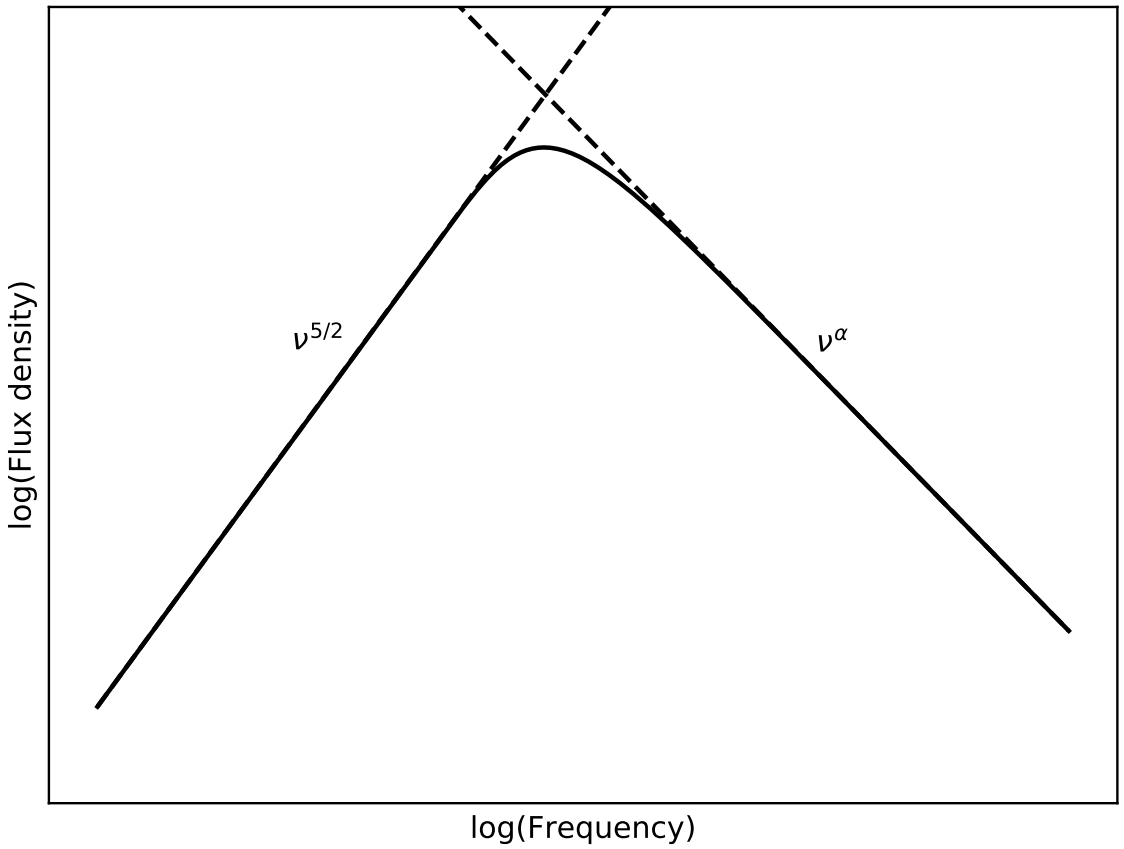

Figure 2.1: A schematic synchrotron spectrum for a non-thermal population of electrons. At low frequencies the spectrum is dominated by synchrotron self absorption and the spectrum is optically thick. Above the break frequency self absorption effects are negligible and the spectrum is inverted, or optically thin, with a power law index observed to be $\alpha = -(p-1)/2 \approx -0.6$.

Rayleigh-Jeans limit, gives the following for the flux density of self absorbed synchrotron radiations:

$$S_\nu = \frac{2m_e}{3\nu_g^{1/2}} \Omega \nu_c^{5/2} = \left(\frac{8\pi m_e^3}{9e}\right)^{1/2} \theta^2 B^{-1/2} \nu_c^{5/2} \tag{2.10}$$

where $\Omega \approx \theta^2$ is the solid angle subtended by the source and θ is its angular size. So, at lower frequencies, where the brightness temperature can become comparable with the electron temperature, the synchrotron spectrum is steep with a power law index $\alpha = 2.5$. A schematic spectrum for synchrotron radiation, including self absorption, is shown in Figure 2.1.

The absorption coefficient, which is used when calculating the specific intensity through

the source function (as well as the optical depth), is

$$\chi_\nu = \frac{\sqrt{3}e^3}{2\pi m_e}\kappa B^{(p+2)/2}\left(\frac{3e}{2\pi m_e^3 c^5}\right)^{p/2} b(p)\nu^{-(p+4)/2} \tag{2.11}$$

which has units cm^{-1}. $b(p)$ is a function with weak dependence on p ($b(p) = 0.269$ and $b(p) = 0.233$ for $p = 2$ and $p = 3$, respectively).

2.1.5 A note on highly energetic phenomena and spectral evolution

The previous analysis in this section assumes that the synchrotron spectrum emits up and down to an arbitrarily large and small frequency, respectively, giving the spectrum shown in Figure 2.1. In reality, there is a frequency (ν_c) above which the cooling timescale of synchrotron emitting electrons is comparable to their emitting timescale, and electrons will quickly radiate away their energy until they are below this frequency. The synchrotron cooling timescale is $\tau_{\mathrm{sync}} = 3m_e c^2/4\sigma_T c U_{mag}\gamma \sim (25/B^2\gamma)$ years (when B is measured in Gauss). In some time t the electrons at the cooling frequency will radiate a significant fraction of their energy via synchrotron radiation, giving the condition $\gamma_c m_e c^2 = P(\gamma_c)t$ which implies $\gamma_c = (6\pi m_e c)/(\sigma_T B^2 t)$. Electrons with Lorentz factors above the critical cooling value will quickly cool down to it, radiating synchrotron radiation at frequency $\nu \propto \gamma^2$ as it does so. However the electron energy is also changing appreciably in this time, with $E \propto \gamma$, which effectively means that there are less electrons emitting at a given frequency above the cooling break than $N(E) = \kappa E^{-p} dE$ would imply. This modification takes the form $N(E) = \kappa E^{-p-1} dE$, where the additional factor of E comes from the synchrotron cooling timescale ($\tau_{sync} \propto \gamma^{-1} \propto E^{-1}$) which, when propagated into Equation (2.9), gives the condition $J(\nu > \nu_c > \nu_m) \propto \nu^{-p/2}$. Here I have introduced the minimum energy frequency ν_m, which is the synchrotron frequency at which the lowest energy electrons in the power-law distributed population. Below ν_m the synchrotron emission is dominated by the electrons emitting at ν_m, and the ensemble population emitting above ν_m has little effect. Considering the case where $\nu_m < \nu_{sa} < \nu_c$, I have already shown the spectral shape in all cases but below the minimum energy frequency. Below this frequency there are no more emitting electrons and we lose the temperature dependence on frequency (the temperature is simply constant) and we get the dependence $S(\nu) \propto \nu^2$ giving the final spectrum

$$S(\nu) \propto \begin{cases} \nu^2, & \nu < \nu_m \\ \nu^{5/2}, & \nu_m < \nu < \nu_{sa} \\ \nu^{\alpha}, & \nu_{sa} < \nu < \nu_c \\ \nu^{-p/2}, & \nu_c < \nu \end{cases} \tag{2.12}$$

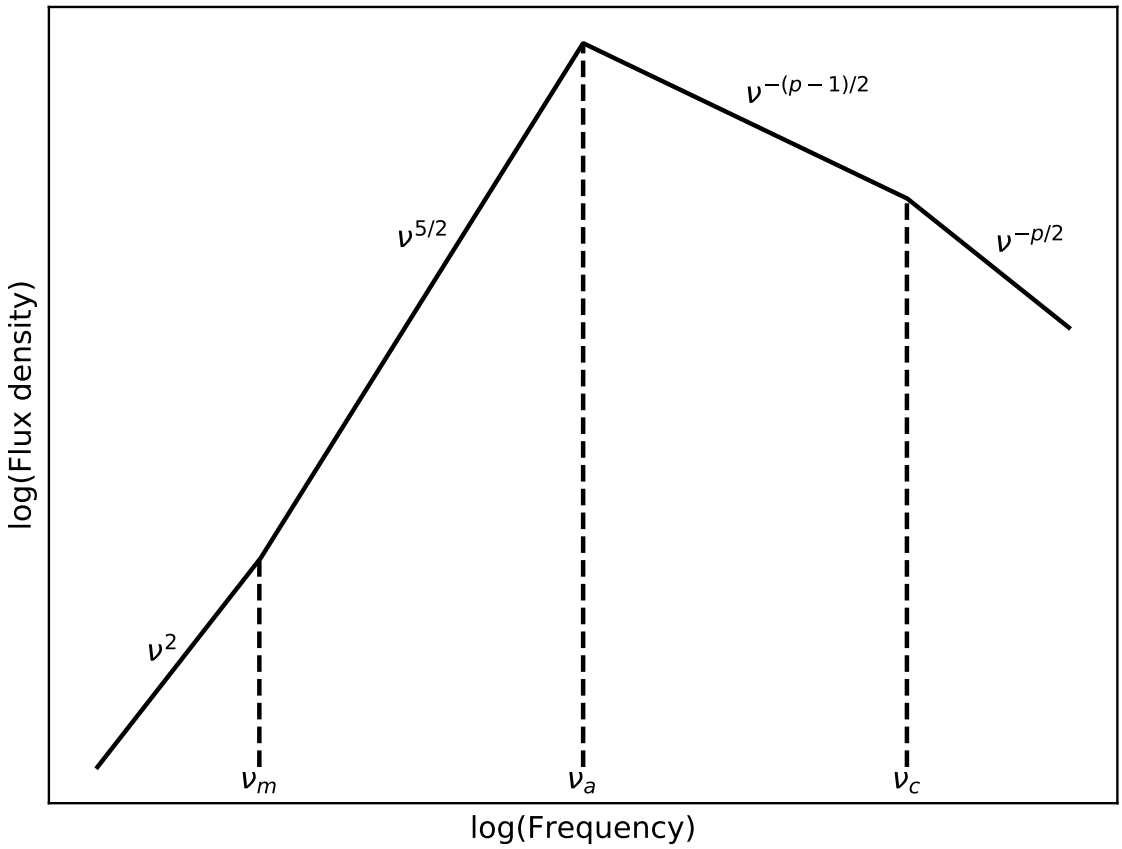

Figure 2.2: A schematic synchrotron spectrum for a non-thermal population of electrons demonstrating all the spectral breaks in the configuration $\nu_m < \nu_{sa} < \nu_c$. At low frequencies the spectrum is dominated by synchrotron self absorption and the spectrum is optically thick. Above the self absorption break frequency self absorption effects are negligible and the spectrum is inverted, or optically thin, with a power law index observed to be $\alpha = -(p-1)/2 \approx -0.6$. This becomes further inverted once the cooling break is reached.

which is shown schematically in Figure 2.2. Such a configuration of frequencies is found in transient systems that do not accelerate electrons to extreme Lorentz factors such as the transient ejections from BHXRBs, although ν_m is usually below the lowest frequencies BHXRBs are observed at so the transition from 2 to 5/2 is not seen.

For higher energy transients that more efficiently accelerate electrons (due to the higher shock velocities involved [141]) the spectrum is slightly modified such that

$$S(\nu) \propto \begin{cases} \nu^2, & \nu < \nu_{sa} \\ \nu^{1/3}, & \nu_{sa} < \nu < \nu_m \\ \nu^{\alpha}, & \nu_m < \nu < \nu_c \\ \nu^{-p/2}, & \nu_c < \nu \end{cases} \tag{2.13}$$

where in the range $\nu_{sa} < \nu < \nu_m$ we see the low energy tail of the lowest energy electrons

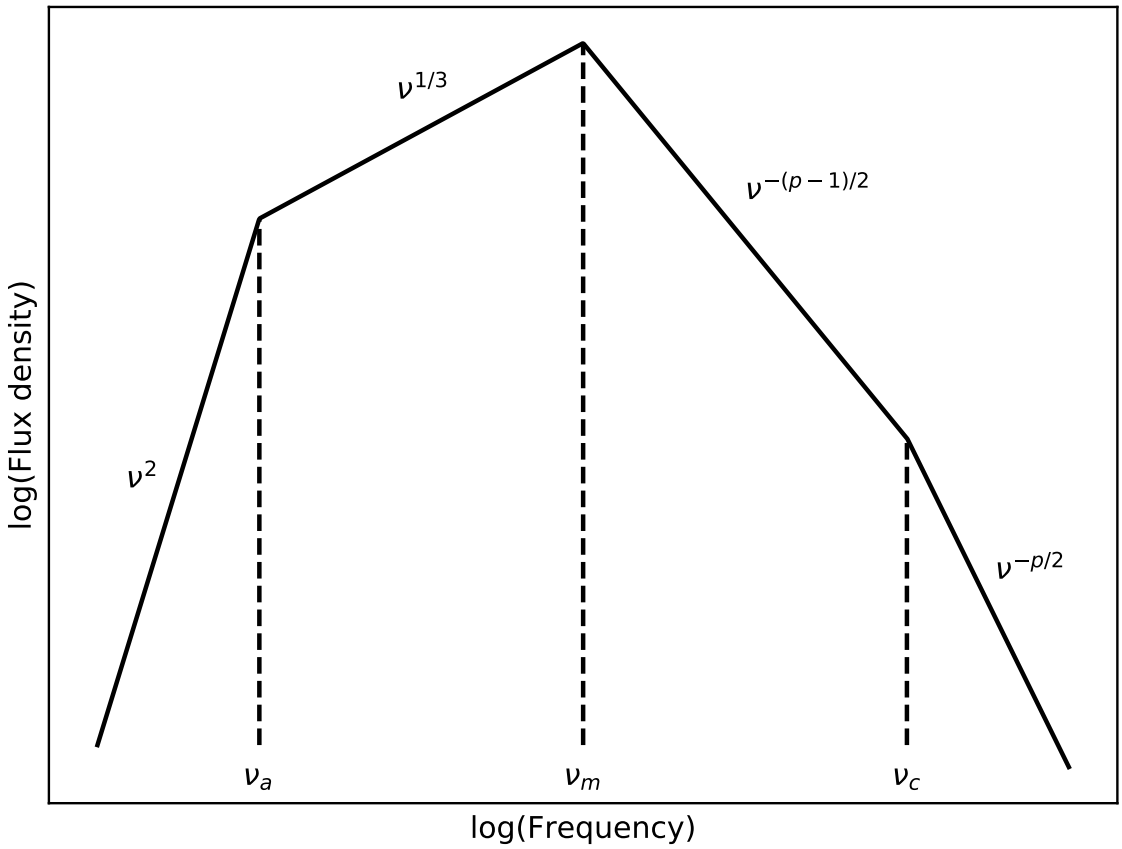

Figure 2.3: A schematic synchrotron spectrum for a non-thermal population of electrons in the slow cooling configuration $\nu_{sa} < \nu_m < \nu_c$. At low frequencies the spectrum is dominated by synchrotron self absorption of the slow cooling electrons at the lowest energy in the power-law distribution and the spectrum is optically thick. Above the self absorption break frequency self absorption effects are negligible and we see the spectral tail of the lowest energy electrons. Above the minimum energy break the spectrum is inverted with a power law index observed to be $\alpha = -(p-1)/2 \approx -0.6$. This becomes further inverted once the cooling break is reached.

un-obscured by self absorption. This spectrum is known as the slow cooling one as the majority of the electron population is below the cooling break and are not cooling significantly via synchrotron radiation. This configuration is is demonstrated schematically in Figure 2.3.

For the most energetic transients, at early times, the entire electron population is accelerated to emit at frequencies above the cooling frequency. We then have an additional case for the range $\nu_c < \nu < \nu_m$ where we see the whole electron population contributing as they cool on the dynamic timescale [142]. The electrons have energy $\sim \gamma$ and radiate at a typical frequency γ^2 and so the flux density goes as $\gamma^{-1} \propto \nu^{-1/2}$. This is known as the fast cooling

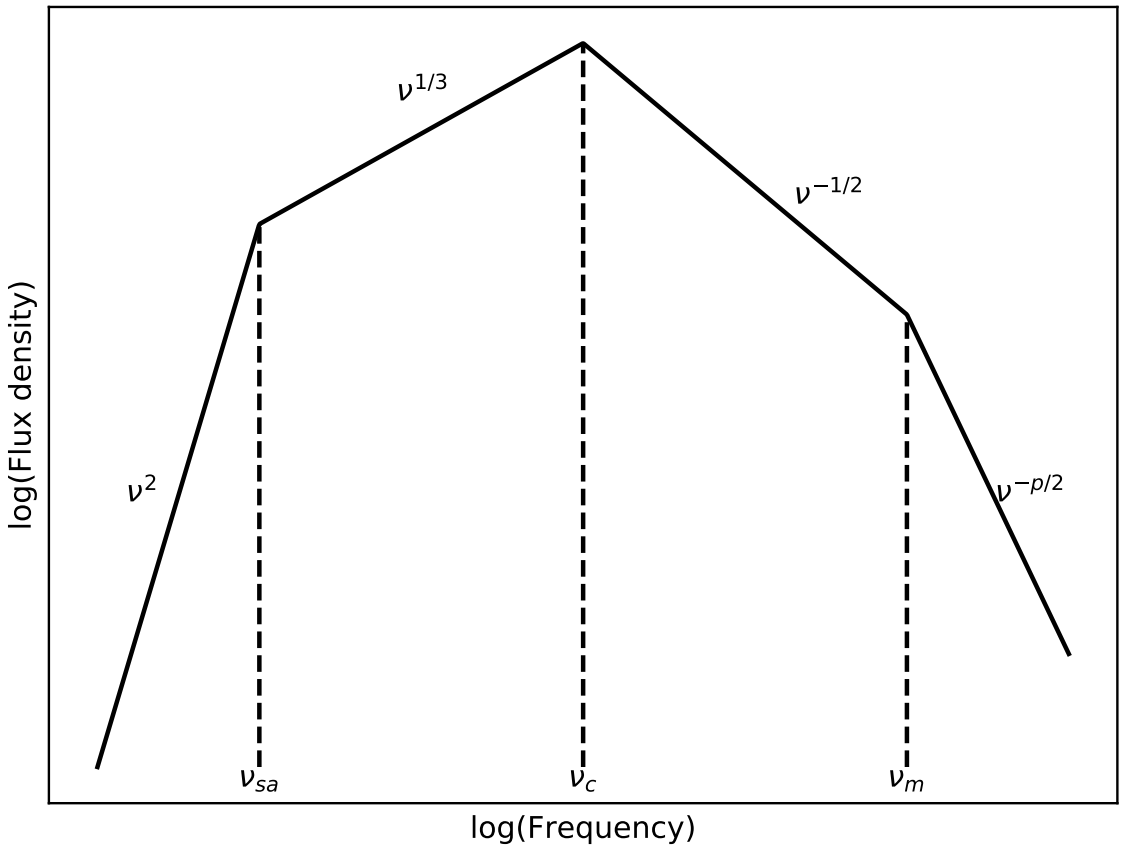

Figure 2.4: A schematic synchrotron spectrum for a non-thermal population of electrons in the configuration $\nu_{sa} < \nu_c < \nu_m$. At low frequencies the spectrum is dominated by synchrotron self absorption and the spectrum is optically thick. Above the self absorption break frequency self absorption effects are negligible and we see the spectral tail of the lowest energy electrons. Between the cooling and minimum energy break we see the entire electron population fast cooling. This becomes further inverted once the cooling break is reached.

case, shown in Figure 2.4 and the spectrum takes the form

$$S(\nu) \propto \begin{cases} \nu^2, & \nu < \nu_{sa} \\ \nu^{1/3}, & \nu_{sa} < \nu < \nu_c \\ \nu^{-1/2}, & \nu_c < \nu < \nu_m \\ \nu^{-p/2}, & \nu_m < \nu \end{cases} . \tag{2.14}$$

The three characteristic break frequencies, ν_m, ν_c and ν_{sa}, are not static, and will evolve with time depending on the dynamics and physical properties of the emitting region. This is also the case for the flux density associated with the segments of the spectrum (defined as the regions of frequency space between two breaks). As the segments of the spectrum depend on the break frequencies defining the segment, the shape of the spectrum will also evolve with time. Most notable is the transition between the fast cooling case and the slow

cooling case, as the population of electrons quickly cools down such that $\nu_m < \nu_c$, which is thought to occur at early times in GRB afterglows. GRB afterglows are also the primary systems in which the cooling break can be observed (even in the slow cooling case) due to the synchrotron spectra being visible up to X-ray frequencies (where the cooling break is expected to be) [143, 144, 145]. Breaks can be detected directly through broadband spectral modelling, or through observations at a single frequency as a change in decay rate in the light curve. I will discuss the movement of spectral breaks in more detail in Chapter 6 where I used radio and X-ray observations to characterise the afterglow of the long GRB 171010A. The cooling break can also be used to age sources that have produced a population of synchrotron emitting electrons [146].

The spectrum shown in Figure 2.2 is the one commonly seen from discrete ejections associated with X-ray binaries, but only above ν_m. The compact jet in those systems (and also in the compact component of the FR I class of radio galaxies [147]) has a flat spectrum over a wide range of frequencies which is inconsistent with any of the previously discussed spectra from a single physical component with a power law population of electrons.

2.1.6 Core/compact jet spectra

The radio emission from astrophysical jets themselves is not caused by a single population of electrons accelerated into some non-thermal distribution, as discussed previously (as is the case when a jet interacts with the ISM). Instead they are constantly replenished collimated conical/parabolic (a transition from parabolic to conical has been seen in e.g. M87 [148], I will refer to the structure as conical as the exact shape will not majorly influence the following discussion) structures where electrons are continuously accelerated and cool as they move away from the object powering the jet. A comprehensive treatment of the broadband SED of jets from AGN and BHXRBS (or microquasars due to the similarity in their properties) can be found in e.g. [70, 149]. Imagine slicing the conical jet into small segments of size $\pi r^2 dz$ at each z with the properties of the electrons and the magnetic field also being functions of the distance down the jet. Under the assumptions $B(r) \propto r^{-1}$, a populations of electrons with $N(\gamma) \propto \gamma^{-2}$, and electron re-acceleration to account for adiabatic cooling, each segment of the self-similar conical jet emits a characteristic synchrotron spectrum as in Figure 2.1. However, due to the magnetic field variation, populations closer to the base of the jet will emit a synchrotron spectrum peaking at a higher energy. For the specified variation of B, and for electron populations having $p = 2$, the composite spectrum (made up of the superposition of spectra at different z) is flat over a wide range of frequencies. At low frequencies a cutoff will occur where the lowest energy electrons in the population at

the head of the jet becomes self absorbed. Two high frequency breaks occur. The first of these is due to the electron populations closest to the jet base, where the conical jet stops being self similar and the high energy tail of these electrons dominates the emission (shown in Figure 2.5). The second break is the cooling one from this same population, where the spectrum will steepen (Figures 2.3 and 2.4). A schematic core jet spectrum is shown in Figure 2.5.

2.1.7 Relativistic considerations and apparent superluminal motion

In addition to the electrons themselves having relativistic velocities, it is common that the emitting region itself is moving at a significant fraction of the speed of light (e.g. $1 \lesssim \Gamma \lesssim 30$, typically, in AGN jets, although some sources show significantly higher values inferred from variability studies [64]), where Γ is the bulk Lorentz factor. This motion causes additional aberrations to the observable properties of a synchrotron source in the observers frame when compared to the inertial frame associated with the bulk motion of the jet. If the motion of the emitting region has a bulk Lorentz factor Γ, then the relativistic Doppler factor is defined as

$$D_{\mathrm{app,rec}} = \frac{1}{\Gamma(1 \mp \beta_j \cos\theta_{obs})}, \tag{2.15}$$

where β_j is the speed of the jet in units of the speed of light, and θ_{obs} is the angle between the jet propagation direction and the observer's line of sight. The minus and plus sign refers to a jet travelling towards (app) and away from (rec) an observer, respectively. This Doppler factor is used to convert to and from quantities seen by the observer or in the rest frame of the jet in the form shown in Equation (2.16).

$$L_{\nu,obs}(\nu_{obs}) = D^2 L_\nu(\nu_{obs}/D) \tag{2.16a}$$

$$\nu_s = \nu_{s,obs}/D \tag{2.16b}$$

$$\sin\theta = D\sin\theta_{obs} \tag{2.16c}$$

It is worth noting that the luminosity conversion in Equation (2.16a) is different for an expanding spherical region (as opposed to a conical jet) and the scaling becomes $L_{\nu,obs}(\nu_{obs}) = D^3 L_\nu(\nu_{obs}/D)$. This difference is the result of a steady conical outflow occupying a stationary solid angle in the observer's frame of reference (effectively the motion is not 'seen'), and therefore the volume of the emitting region is not boosted by a factor D as in the case of a moving sphere. These formulae allow for the conversion of the

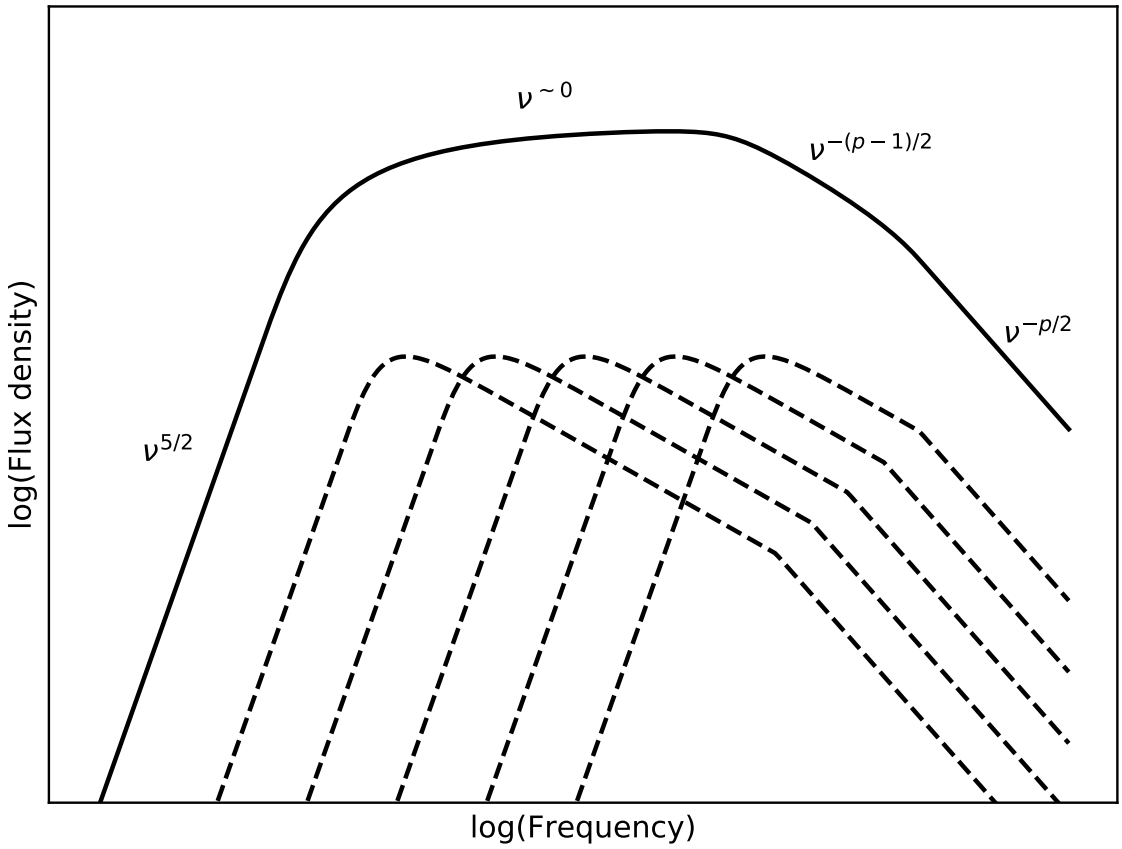

Figure 2.5: A schematic compact core jet spectrum, shown by the solid line, is the sum of spectra from power law electron populations at different radii along the jet axis (with populations further down the jet peaking at lower frequencies due to the reduction in magnetic field strength), five such spectra are shown as dotted lines and have the same form as the one shown in Figure 2.1 but with the addition of a cooling break in each spectrum above which the slow steepens to $-p/2$ as the electrons radiate on a timescale shorter than the dynamical timescale. At the lowest frequencies the total jet spectrum will be self absorption from the least energetic population of electrons. The jet spectrum is then roughly flat topped due to the superposition of synchrotron spectra from the individual components (depending on how the magnetic field evolves down the the). Above some frequency all of the individual spectra are optically thin, and so is the composite spectrum. Similarly the spectrum breaks again above some frequency there the individual spectra are all fast cooling.

quantities discussed in this Chapter into an observers frame of reference.

Due to the high bulk Lorentz factors of GRB jets, the radiation they emit can be beamed into an angle that is smaller than the opening angle of the jet itself ($\Gamma^{-1} < \phi_j$). As the jet interacts with the circumburst material it will decelerate and at some point the beaming angle will be larger than the opening angle. If a GRB was initially observable then, at the time when $\Gamma^{-1} \sim \phi_j$, the observed flux decay rate will increase at all frequencies simultaneously (jet breaks are achromatic). Additionally this affect can lead to GRBs that are not initially beamed into our line of sight becoming visible after the jet break condition is reached. These are known as orphan afterglows as they are not detected by their γ-ray emission directly after the progenitor event as the emission is highly beamed along the jet axis.

Some jetted sources display apparent superluminal motion (both within [97, 100] and outside of [150] our Galaxy). Nothing can move faster than the speed of light, and so observing motion that apparently violates this fact must be caused by geometric effects. In fact superluminal motion is the result of emitting material travelling with a radial velocity component that is a significant fraction of c. The conditions for superluminal motion can be derived simply through considering an emitting region moving at an angle θ relative to the observer with a rest frame velocity $\beta = v/c$. The emitting region emits radiation at a time t and then again at time t' and therefore the difference in arrival time to the observer from those two photons is $(t' - t)(1 - \beta\cos\theta)$ and therefore the apparent transverse velocity is $\beta_{\rm app} = \beta\sin\theta/(1 - \beta\cos\theta)$. So, for example, if the emitting region is moving at an angle $\theta = \pi/4$ to the line of sight then it will appear to move superluminally for $\beta > 2^{-1/2}$. In fact the maximum apparent transverse velocity occurs when $\cos\theta = \beta$ and for this angle superluminal motion occurs if $\beta\gamma > 1$ (which is almost equivalent to $\gamma > 1$ for significantly relativistic motion). Examples of the apparent transverse velocity, as a function of angle to the observer's line of sight, are shown for a number of intrinsic velocities in Figure 2.6. Observations of superluminal motion of sources provides constraints on their distance from the observer as well as the angle to the line of sight, this will be discussed in detail in Chapter 4.

2.2 Thermal radiation

Synchrotron radiation is often referred to as non-thermal radiation, as the broad band spectrum arises from a non-Maxwellian distribution of electrons. However this is only the case

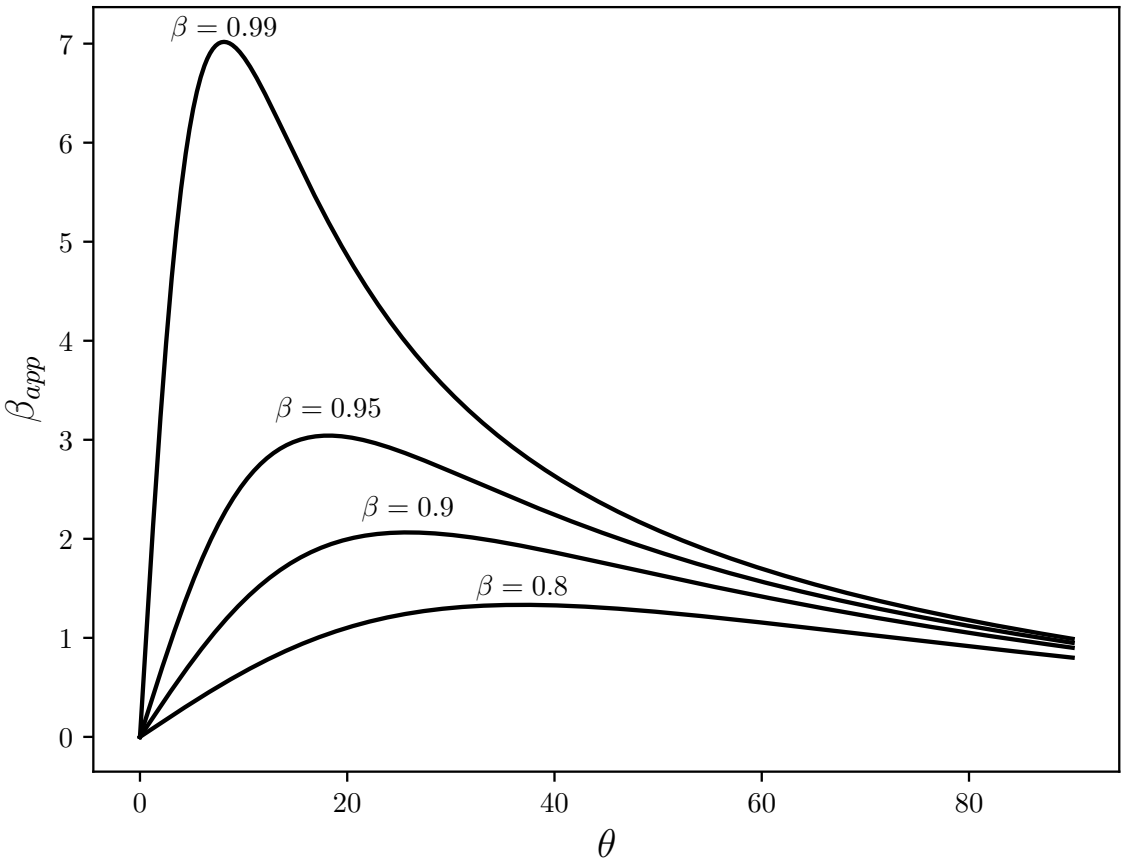

Figure 2.6: The apparent transverse velocity of a relativistic source as a function of the angle the source's direction of motion makes to the observer's line of sight, shown for four different intrinsic velocities. The maximum apparent transverse velocity occurs when $\cos\theta = \beta$. Highly relativistic sources can be near face on and yet still appear to move superluminally.

if the electrons have been accelerated into a power law energy distribution. If the electrons instead have a relativistic Maxwellian distribution then they emit *thermal* synchrotron radiation which may be of interest in e.g. GRB afterglows where the non-thermal electron population can contribute to and interact with the emission from the accelerated population [151]. Due to the association between shock acceleration, which results in a power-law (non-Maxwellian) distribution of electrons, it is usually appropriate to refer to synchrotron radiation as a non-thermal process.

Thermal emission is invoked to explain the observed spectra of XRBs in the soft accretion state, where emission from a modified black body (the sum of black body spectra from accretion disk anulii at different radii) fits the observations well (see e.g. [152] for examples). In the hard accretion state the X-ray spectrum peaks at higher energies, which thought to be the result of a thermal population of hot ($\sim$ 100 keV) thermal electrons Compton up-scattering seed photons from the accretion disk [153]. Similar coronae are also observed in AGN and are explained in the same framework [154].

2.3 Inverse Compton radiation

The Shakura & Sunyaev 1973 [37] disk model precisely predicts the radial temperature profile of a geometrically thin and optically thick accretion disk. This prediction is well supported by observational evidence of accretion disks, e.g. in CVs, which show multi-component black body spectra and whose outbursts can be well reproduced with an accretion disk instability model [155, 156]. Similarly, while in certain accretion states, BHXRBs show spectra consistent with multi-component black bodies peaking at a few keV. Applying the disk instability model to XRBs has proved more challenging. While the model does appear to correctly predict if XRB systems are persistent (with a stable accretion disk) or transient (with an accretion disk undergoing an instability due to hydrogen ionisation), based on their accretion rate and orbital period, the detailed evolution through an outburst cannot be reproduced with the instability model. In other accretion states, however, BHXRBs show a spectrum clearly not from a classical Shakura & Sunyaev accretion disk, having a power-law component and peaking at closer to 100 keV. This led to the development of two-component accretion disk models to explain X-ray emission from accreting systems, where a hot population of electrons (sometimes called a corona) is located close to the accreting compact object [157, 158]. Coronae are also observed in AGN [158]. This electron population is thought to up-scatter 'cool' photons from the accretion disk via the inverse Compton process (in the Compton process photons *lose* energy through their

interaction with an electron), resulting in the high energy power law tail seen in systems with accretion disks [152]. The inverse Compton process increases the frequency of radiation by a factor γ^2 (where γ is the Lorentz factor of the electron causing the scattering) and so, for sufficiently relativistic electrons, inverse Compton scattering can drastically alter the photon energy. While the inverse Compton process is efficient in up-scattering photons to higher energies, a seed photon population is required. Transient systems are not sources of significant microwave radiation (with thermal and synchrotron processes both having steep spectra towards lower frequencies) and so there is no source of low energy photons to up-scatter into the radio band. Therefore inverse Compton radiation is not considered as a contributor of radio emission and hence I won't discuss it in much more detail, as the previous paragraph will be sufficient to understand the accretion states BHXRBs can show. It is, however, worth mentioning the phenomena of synchrotron self Compton (SSC, or synchro-Compton) radiation. Highly energetic electrons produce low energy (radio) photons via the synchrotron process, as discussed previously in this Chapter. If there is a sufficient density of low energy photons then the relativistic electrons that produced them can interact via the inverse Compton process, causing potentially significant energy loss for the electrons, as they continuously (once the electron energy loss rate via inverse Compton is greater than the synchrotron loss rate the continuously higher energy photons drain energy from the electrons in a feedback loop) scatter the photons to higher energies. This condition is satisfied for brightness temperatures above $\sim 10^{12}$ K, which therefore should not be violated for compact radio sources in order to avoid catastrophic energy losses from the source's electrons.

Chapter 3

Observational techniques

3.1 Radio interferometry

The breadth and depth of the field of aperture synthesis are both vast, and giving a complete treatment of the process in this thesis is not possible. It is, however, important that the subject is motivated and described in some detail, especially certain intricacies related to the data presented in this work. There are plenty of excellent books presenting all aspects of interferometry, including, but in no way limited to, [159, 137, 160].

The fundamental goal of interferometry is to use physically separated antennae to replicate the performance of a totally filled aperture of the same diameter as the distance separating them. Why is this necessary? Consider that the angular resolution of a telescope, θ, scales as $\theta \propto \lambda/D$ where λ is the wavelength of the radiation observed and D the diameter of the telescope's collecting aperture. For visible light (say at $\lambda = 600\,\mathrm{nm}$) observed with a current state of the art optical telescope, with a primary mirror of diameter $D = 10\,\mathrm{m}$, a diffraction limited resolution of $\theta \sim 6 \times 10^{-8}\,\mathrm{rad} \sim 0.01''$ is achievable (although in practice this will be limited by atmospheric seeing conditions unless adaptive optics techniques are employed). If an observer was interested in probing structure on similar angular scales emitting at $\lambda = 0.21\,\mathrm{m}$ (to e.g. map neutral hydrogen via its hyperfine transition) an aperture with $D = 3500\,\mathrm{km}$ would be required, or roughly one third of the diameter of Earth. Building a single structure of this size, or even 1% of this size, is completely infeasible (the single biggest steerable telescope ever operated is the Green Bank Telescope with $D = 100\,\mathrm{m}$) and so at first glance it may appear that angular resolutions better than a few minutes of arc are not achievable when observing in the GHz regime. This limit was overcome when it was realised that a partially filled version of a large aperture could be synthesised using pairs (or multiple pairs) of antennae by correlating the signals they

received [161].

It is helpful to first consider on axis emission incident on a single parabolic dish with a receiver sensitive to radio emission at its focal point. Imagine that this completely filled dish is constructed of N area elements, the sum of which equals that of the total dish area. The total power at the receiver is the sum of the power received from each (inclusive) pair of elements and is given as

$$\langle P \rangle = \sum \langle \Delta V_i^2 \rangle + \sum_{i \neq j} \langle \Delta V_i \Delta V_j \rangle. \tag{3.1}$$

Here ΔV_i is the voltage of the i^{th} element of the dish. The first term in this expression is called the auto-correlation term and the second is called the cross-correlation term. Equation (3.1) contains terms that depend only on a pair of antennae and – as long as the voltage from each element pair is arriving in phase (a condition met as we are currently only considering plain waves incident on a parabolic aperture) – there is no need for the elements to be physically connected. You can then imagine, in the infinitesimal limit, replacing each of the N area elements with an antenna of the same area. Each of the cross-correlation terms can be measured with two of these distinct antennae at locations i and j and the total power can be recovered. If a source is unchanging in time, then components of the total power can be sampled non-simultaneously. Of course, to avoid the previously discussed downsides of building an impossibly large structure, we should be able to replace some subset of the N area elements with antennae and recreate the resolving power of a totally filled dish with a diameter above that which we can build if it is fully filled. It is not clear from Equation (3.1) that removing terms from either the auto- or cross-correlations (corresponding to those from antennae elements you have decided to not include) will reproduce the total power, but I will show that, under certain assumptions and with certain limitations, such a simplification is possible.

Instead of focusing on the performance of N elements, instead now consider the operation of a single pair of antenna, demonstrated schematically in Figure 3.1. Understanding a simple two element system is sufficient to characterise the properties of arrays with $N > 2$ antennae, as these can be considered as $N(N-1)/2$ pairs of this simple set-up. The two elements are placed separated by a distance $|b|$ (called the baseline length) and are pointed away from zenith at an angle θ (in the direction $\vec{s}_0$) towards a source of radiation (with a sky brightness distribution $I(l, m)$), with their individual responses to incident radiation combined at a correlator that multiplies and averages the signals from the antennae pair.

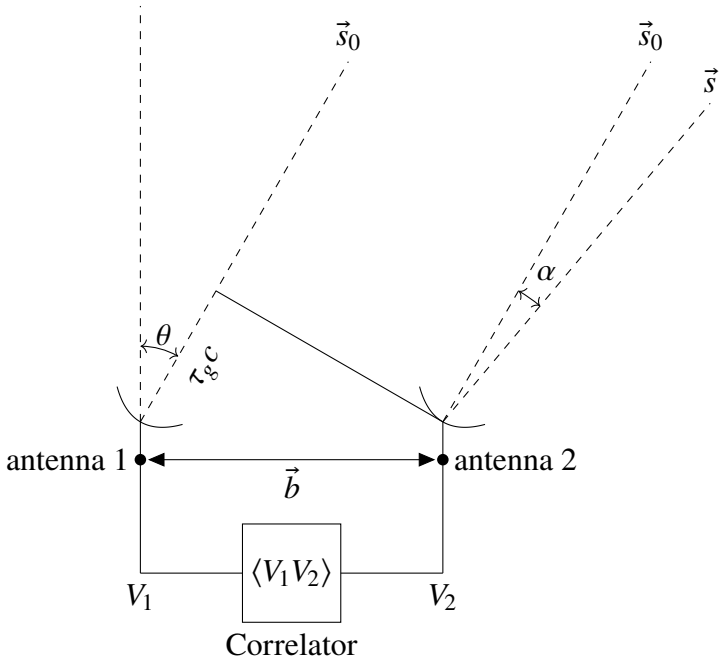

Figure 3.1: A schematic diagram of a two element interferometer.

Radiation arrive at antenna 1 delayed by $\tau_g = (\vec{b} \cdot \vec{s_0})/c$ compared to their arrival at antenna 2, and thus are no longer in phase. If $V_1 = V\cos\big(2\pi\nu(t - \tau_g)\big)$ and $V_2 = V\cos(2\pi\nu t)$ then the correlator measures $\langle V_1 V_2 \rangle = V^2\cos\big(2\pi\nu\tau_g\big)$, a quantity that varies sinusoidally as the Earth rotates and the baseline vector's orientation with respect to the source direction changes. Introduction of a delay before the correlation (which was previously achieved using variable cable length, but is now done on a software level) can account for the geometric delay of on-axis radiation, however such a delay will not phase-up radiation incident on the two antennae that is off-axis (the position on the sky with zero phase offset, s_0, is known as the phase centre). Before continuing it is convenient to define a coordinate systems for the baseline vector under the assumption that it is co-planar. It is conventional to let u be the projected baseline vector in the East-West direction and v be the projected baseline vector in the North-South direction, both measured in units of the observing wavelength for reasons that will become clear later. The correlator records the output of the antennae pair as a function of time and thus samples at different points on the (u, v) plane (which is demonstrated in Figure 3.2). Pairs of antennae trace out ellipses on the UV plane. For a purely East-West array (such as Westerbork) the maximum separation in the u direction is just the baseline length (measured in wavelengths) whereas the maximum in the v direction is shortened depending on the declination (for sources at the pole an East-West array traces out circles in the (u, v) plane). For an East-West array the ellipses are centred on the origin.

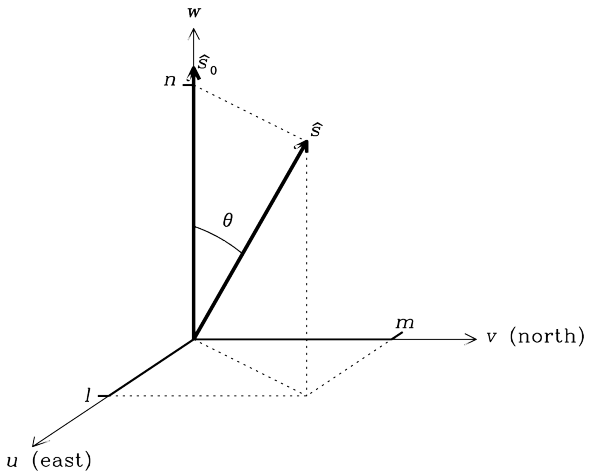

Figure 3.2: The (u, v, w) plane with the phase centre in direction $\hat{s}_0$ (which is also the w direction). $\hat{s}$ is an arbitrary unit vector, and l, m, and n are its projection onto the u, v, and w axes respectively.

Consider a plane on the sky such that $\vec{s}_0$ is normal to it, with off axis emission having a position (l, m) on the plane, with $l = \sin\alpha$ and $m = \sin\beta$. For simplicity you can imagine that the angle α is in the plane of the diagram in Figure 3.1 (as shown), and β is orthogonal to it (not shown). The arrival of radiation from position (l, m) at antenna 1 will be delayed by a path length $ul + vm$ with respect to its arrival at antenna 2 (where v is the projected baseline length in the direction orthogonal to the plane of Figure 3.1 and it is important to remember there is a electronic phase delay that phases up on-axis emission). This path length difference will manifest as a phase delay in the voltages received by antennas 1 and 2, such that $V_2 = V_1 e^{2\pi i(ul+vm)}$, with u and v both measured in units of the observing wavelength. We can now identify the output of the correlator as

$$\begin{aligned}\langle V_1 V_2 \rangle &= \langle \iint V_1(l,m)dldm \iint V_2(l,m)dldm \rangle \\ &= \iint \langle V_1(l,m)^2 \rangle e^{2\pi i(ul+vm)} dldm.\end{aligned} \tag{3.2}$$

Where I have made the assumptions that radiation from different parts of the sky is incoherent (e.g. emission from (l_1, m_1) and $(l_2 \neq l_1, m_2 \neq m_1)$ correlates to zero), and the integrals indicate that each antenna is receiving radiation from a continuous range of directions (l, m). Identifying that the voltage product in Equation (3.2) is proportional to the received power, which in turn is proportional to the source brightness, we see that the correlator measures a complex function known as the visibility

$$\mathcal{V}(u, v) = \iint I(l, m) e^{2\pi i(ul+vm)} dldm = Ae^{i\varphi}. \tag{3.3}$$

This is in the form of a Fourier transform, where u and v are spatial frequencies. Therefore the function measured through the correlation of signals received by distinct antennae is the Fourier transform of the sky brightness distribution, which we can recover through an inverse Fourier transform to be

$$I(l,m) = \iint \mathcal{V}(u,v) e^{-2\pi i(ul+vm)} du dv. \tag{3.4}$$

In practise it is impossible to sample the entire visibility function with a finite number of antennae sampling at discrete times over a finite interval, so antennae separated by $\vec{b}$ will sample the sky brightness distribution on spatial scales inversely proportional to the projected separation of the antennae (and measured in units of the wavelength of the emission being observed), and information on spatial scales not sampled is completely lost. An interferometer consisting of N elements samples $N(N-1)/2$ components of the visibility each time the correlator reads out. This is called a snapshot observation and, for simple source structures and large N arrays, such an observation may provide enough samples to produce an image. If such a snapshot image is not possible to make, then the rotation of the Earth can be used to provide additional samples of the visibility. As the Earth rotates the position of a source will change on the sky, and so will the projected baseline lengths (u and v). Sampling the correlation from pairs of antennae as the Earth rotates corresponds to sampling along ellipses in the (u,v) plane - providing better sampling of the complex visibility (and access to a wider range of angular scales). Up to now I have only considered observations at a single frequency. Modern interferometers are simultaneously sensitive to thousands of discrete frequencies across some bandwidth which allows for additional samples of the visibility to be measured. These correspond to radially distributed samples in the (u,v) plane, which is defined with respect to the central frequency of the bandwidth. Observations at higher frequencies are sensitive to structures on smaller spatial scales and therefore correspond to samples of the visibility function at larger (u,v) values (which can also be seen by considering that by definition we measure the baseline lengths in units of wavelength and so the Fourier transform implies long baselines sample small angular scales). Additional sampling of the (u,v) plane can also be achieved by observing sources with antennae in different location configurations (as is done with the VLA or ATCA). Examples of the ability of different arrays to observe structures on different angular scales is shown in Figure 3.3.

There are three important spatial scales to consider when utilising a radio interferometer. The resolution of the interferometer is limited by the longest baseline (which samples the highest spatial frequencies) to be $\theta_{min} \sim \lambda/b_{max}$ (the response to a point source is constant

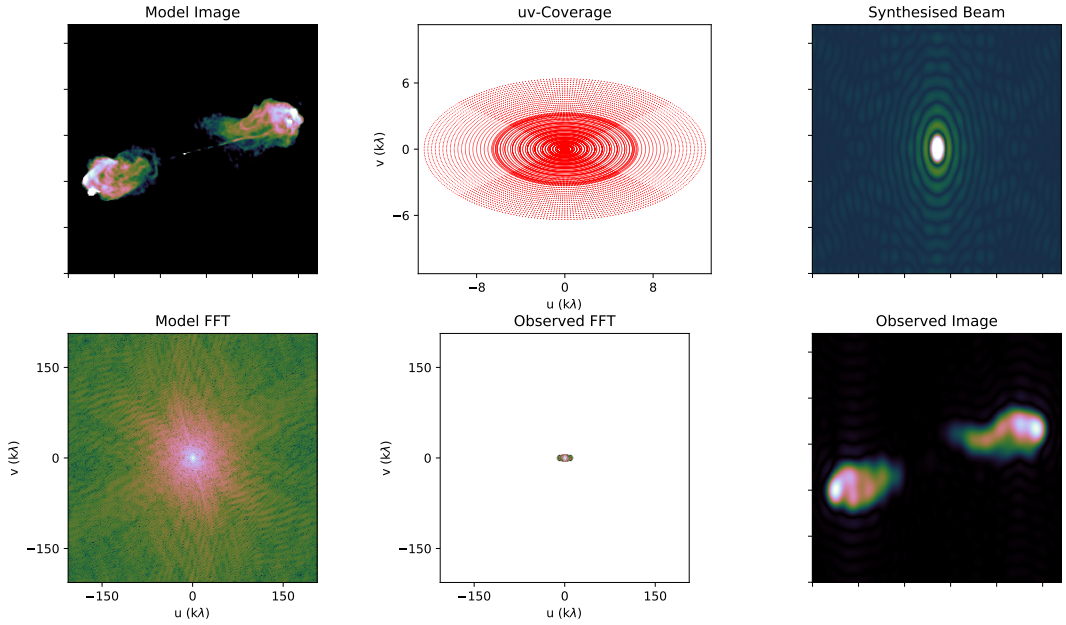

(a) Simulated Westerbork Synthesis Radio Telescope observations of the radio galaxy Cygnus A.

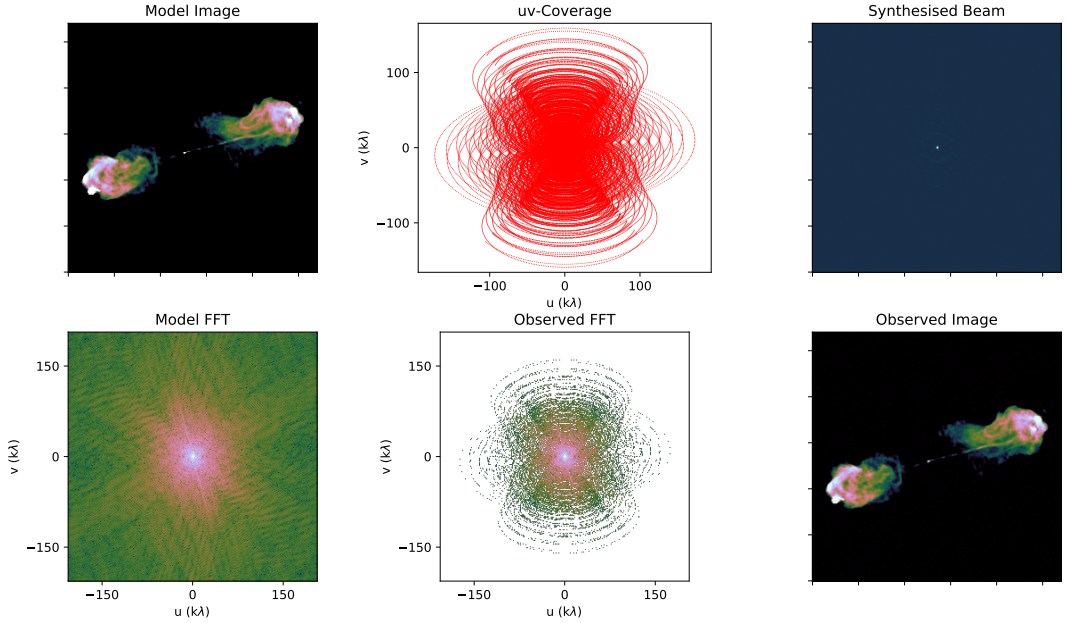

(b) Simulated VLA A-configuration observations of the radio galaxy Cygnus A.

Figure 3.3: Two simulated full track L-band observations of the radio galaxy Cygnus A with WSRT (Figure 3.3a) and the VLA in A-configuration (Figure 3.3b). Each panel demonstrates (from top left moving clockwise) the model image, the UV coverage of the source by the array (source at a declination of +30°), the synthesised beam (which is the Fourier transform of the (u, v) sampling function), the Fourier transform of the model image, the Fourier transform of the observed image, and the observed image. The VLA has significantly longer projected baselines and therefore recovers higher spatial frequencies, but its lack of short spacing means it recovers less flux on larger angular scales (shown by the observed FFT and observed image). These images were created using the Friendly Virtual Radio Interferometer software which can be found at `https://github.com/crpurcell/friendlyVRI`.

with baseline length so you do in fact recover the total flux of unresolved sources). The interferometer does not 'see' structure on scales limited by the shortest baseline (sampling the lowest spatial frequencies, note the hole in the centre of the observed image FFT in Figure 3.3b), on scales above $\theta_{max} \sim \lambda/b_{min}$. This leads to the so called 'total power' or 'zero spacing' problem, where the total power of an extended source can only be recovered with single dish measurements which provide autocorrelations (corresponding to zero spacing in the (u, v) plane). Finally the field of view of an interferometer is set by the size of its dishes, and is λ/D where D is the dish diameter.

There are two major modifications that must be made to equation (3.4) before it is in its final form. The first comes from the aforementioned fact that the visibility function is only sampled discretely. If we define the sampling function over all (u, v) space to be $S(u, v) = \sum_{k=1}^{N} \delta(u - u_k, v - v_k)$ i.e. unity at points where we measure a visibility and zero otherwise (although note that sampling is not instantaneous but is rather an average of a signal over a certain time frame), the sampled visibility function is $\mathcal{V}^S = S\mathcal{V}$ and the sampled brightness distribution is modified as

$$I^D = \mathcal{F}(\mathcal{V}^S) = \mathcal{F}(S\mathcal{V}) = \mathcal{F}(S) * \mathcal{F}(\mathcal{V}) = \mathcal{F}(S) * I \tag{3.5}$$

where $\mathcal{F}$ indicates a Fourier transform and $*$ a convolution, and we have used the convolution theorem to equate the Fourier transform of a product with the convolution of their Fourier transforms. I^D is usually referred to as the dirty image, and is the intrinsic sky brightness convolved with the sampling function. The second modification is due to the response of the antennas in the array, which vary depending on source position with off axis signals appearing weaker than those observed at the phase centre. We end up with the relation $I^D(l, m) = \mathcal{F}(S) * (I(l, m)A(l, m))$ where $A(l, m)$ is the response of the antenna. As well as sources of emission being convolved with the sampling function of the array, the measured flux in a dirty image will not be correct until it is divided through by the antenna response pattern. Sources away from the phase centre will appear fainter than they intrinsically are, as arrays are less sensitive to off axis emission. Sources at the phase centre are not altered by this as the antenna response is maximal at this point and data calibration (see below) will ensure the flux density at this point is 'correct'.

In theory, we now have all the tools necessary to produce images with an interferometer. Simply sample components of the complex visibility and Fourier transform them to recover the sky brightness distribution on angular scales to which your array is sensitive. There are, however, a number of issues that need to be addressed to complete this process.

Firstly data must be calibrated, allowing their interpretation in astronomically interesting units (such as flux and position) rather than those measured directly by the correlator (some voltage and phase). Additionally, performing a 2D Fourier transform is not trivial and certain approximations need to be made to perform the inversion. Finally, imaging the data requires deconvolving the sampling function and correcting for the primary beam (which sets the overall field of view of the interferometer and is the Fourier transform of an antenna aperture). In the following sections I will describe the process of going from raw (visibility amplitudes and phases directly from the interferometer) to calibrated data, followed by the process of imaging.

3.1.1 Data flagging

A certain percentage of the data recorded by an interferometer will be unavoidably corrupted by a number of processes. Foremost of these is radio frequency interference (RFI) from man-made sources (e.g. satellites) which are strong sources of radio emission that overwhelm any cosmic signals. Such signals are time variable, direction dependent, usually narrow band, and can affect different baselines to a variable degree. Data corrupted by RFI is unusable and must be removed (flagged) before the good data can be calibrated. Data corruption can also be caused by poor weather, antennae pointing errors, or by malfunctioning hardware or software. Incorrect removal of corrupted data can result in calibration failure or corrupted images. Due to the vast amount of data taken with an interferometer over the entire bandwidth with all baselines manual data removal is no longer a feasible option for most modern interferometers (especially as data averaging, which would speed up the task, suppresses narrow band RFI). Instead it is common to use autoflagging algorithms which fit the response of the interferometer in time and frequency space and search for significant deviations indicative of RFI. Care must be taken however as some astrophysical signals may appear similar in form to RFI (e.g. dispersed pulses from FRBs or pulsars).

3.1.2 Calibration

Once you have a flagged data set, the next task is to calibrate it. The amplitudes and phases of the components of the complex visibility that have been sampled need to be corrected so as to be meaningful (amplitudes converted to the correct flux density scale, and phases referenced to some known position system). Additionally, signals from sources will be corrupted from their true amplitudes and phases by effects along the signal path, be it during propagation or within the electronics systems once detected. In order to solve these

issues, sources with *a priori* known radio spectra, positions, and polarisation need to be measured. I will focus on sources with the first two of these characteristics as I have not utilised polarisation measurements as part of the work presented in this thesis. Following the formalism of [159] the measured visibilities ($\tilde{\mathcal{V}}$) between a baseline pair ij can be related to the 'true' source visibilities ($\mathcal{V}$) as

$$\tilde{\mathcal{V}}_{ij}(t) = \mathcal{G}_{ij}(t)\mathcal{V}_{ij}(t) + \epsilon_{ij}(t) + \eta_{ij}(t) \tag{3.6}$$

under the assumption of linearity and antennae pair independence. $\mathcal{G}_{ij}(t)$ is the complex gain of the antennae pair, $\epsilon_{ij}(t)$ is a complex offset for the antennae pair, and $\eta_{ij}(t)$ represents complex noise. The majority of signal corruption occurs before correlation (primarily due to atmospheric and weather effects) and as such the complex gain can be written as

$$\mathcal{G}_{ij}(t) = g_i(t)g_j^*(t) = a_i(t)a_j(t)e^{i(\phi_i(t)-\phi_j(t))}, \tag{3.7}$$

where $a_i(t)$ and $\phi_i(t)$ are the antenna-based amplitude and phase corrections, respectively. Calibration involves determining these correction terms through observations of sources with well known fluxes and positions. Typically two sources are observed in addition to the science target for this purpose. Firstly a primary flux and bandpass calibrator is observed, which should be compact with the array you are observing with (this is not possible for VLBI observations due to their exceptionally high angular resolution), have a well known position, and a well characterised radio spectrum (known flux in each frequency channel). Such a source is typically observed once at either the start or end of an observing run (but for long observations it can be observed more regularly to account for potential system instabilities over the observation) and is used to set the absolute flux scale as well as the amplitude of the complex gain corrections. Additionally a secondary (or phase) calibrator is observed at regular intervals interleaved with the science target. While the position of the primary flux calibrator on the sky is not important (as long as it is observable at a reasonable elevation by the array), the secondary calibrator should be as close to the source as possible whilst still being compact, bright, and with a reasonably characterised spectrum. Regular observations of the secondary throughout the observation allow, by interpolating solutions to source scans, for time dependent amplitude and phase corrections to be made. The secondary should be close to the source in position so that to a good approximation the same effects occur on the radio waves from both the calibrator and the science target (primarily these are due to the atmosphere/weather).

3.1.2.1 Self calibration

In addition to calibrating based on observations of well characterised radio sources, the observation of the science target field can be used to improve the quality of the calibration. While producing images of a field, a model of the sky is created (see below for details) which can be used as a reference to derive improved complex gains. At first glance this may seem circular, however as complex gain corrections are antenna based (and not baseline based), and each antenna is involved in $N-1$ measurements at each correlator dump, the calibration is sufficiently over-constrained to allow for self-calibration. This is especially the case for arrays with large N, such as MeerKAT or the VLA.

3.1.2.2 Fringe fitting

For very long baseline observations additional care must be taken when correcting for the delay between pairs of antennae, which is time varying and frequency dependant. The accuracy required for modelling this correction depends on the distance between the antennae, with higher order effects needing to be accounted for for VLBI experiments (such as the accuracy of the station clocks, and accounting for tidal affects [162]). The accuracy of these models makes VLBI instruments sensitive to even minute shifts in their positions, being able to track the motion of the Earth's tectonic plates. It is important to consider the 'fringe rate' of an interferometer containing long baselines. While it is possible to maintain the position of a source in an interferometers interference patterns at its phase centre, off axis sources will move through the pattern due to the rotation of the Earth. At the north celestial pole a source at the first null of the primary beam moves through a complete cycle of the interference pattern for an interferometer with dishes of diameter D and baseline length B in $t \approx D/(\omega_e B)$ s. Where $\omega_e = 7.3 \times 10^{-5}\,\mathrm{rad\,s^{-1}}$ is the Earth's rotation rate. The VLBA has a maximum baseline of ~ 8500 km and dishes of size 25 m, and so the fringe rate is $t^{-1} \sim 25$ Hz. This severely restricts the field of view of VLBI instruments and means imaging is only possible near the phase centre of a VLBI array.

3.1.2.3 Wide field imaging

There was an implicit assumption made in the derivation of Equation (3.3), that the path difference between two antennae is entirely due to their planar separation. Formally, the phase delay should be written as $ul+vm+wn$, where we are accounting for phase delays from a non-coplanar array. In the already defined coordinate system we can write $l^2+m^2+n^2 = 1$

and we rewrite Equation (3.3) as

$$\mathcal{V}(u,v) = \iint I(l,m) e^{2\pi i(ul+vm+w(\sqrt{1-l^2-m^2}-1))} \frac{dldm}{\sqrt{1-l^2-m^2}} \tag{3.8}$$

which reduces to Equation (3.3) in the case that l and m are small, i.e. we are imaging close to the phase centre. The coplanar assumption is often violated by modern interferometers and the w direction must be considered when performing imaging. Wide field imaging also presents additional calibration challenges, as the phase calibrator no longer well represents the atmospheric effects experienced by radio waves away from the phase centre and the model of the phase calibrator field will no longer be that of a single point source. To account for this, direction dependant self calibration can be used, where gain solutions are derived in 'facets' on the sky (sub-regions of the image containing significant enough flux to provide gain solutions). Such techniques are especially required if bright off-axis sources corrupt the image at the phase centre with uncorrected calibration artefacts.

3.1.3 Making images

Finally, after flagging and calibration, we are (to a good approximation) at the stage of Equation (3.3), where we now know the correct set of visibilities that correspond to the Fourier transform of the sky brightness distribution. Inverting the visibilities (usually through gridding and then a fast Fourier transform) will produce the sky brightness distribution convolved with the sampling function and modified by the antenna response function (i.e. a dirty image; Equation (3.5)). One important consideration when gridding the visibilities in the (u,v) plane is what weighting to assign to the elements making up the grid. The two extremes of weighting are natural and uniform. For natural weighting each cell in the grid is weighted as inversely proportional to the noise variance of the samples in the cell. Given that arrays typically have significantly more short baselines (sampling large angular scales) such a weighting will degrade the resolution of the image but optimise the sensitivity. Uniform weighting weights cells proportional to the local density of (u,v) points so that all cells have the same total weight. This will give more weight to longer baselines and therefore improve resolution, but down-weights more data so reduces sensitivity. Uniform weighting will reduce the amplitude of side-lobes as the (u,v) plane is more uniformly filled. There is also Briggs weighting, which allows the user to select intermediate weighting schemes between uniform and natural [163].

For uncrowded fields with a single source at the phase centre, simply fast Fourier transforming the data may be sufficient for measuring the flux through fitting the synthesised

beam to the centre of the image with the amplitude as a free parameter. However for sources not at the phase centre the apparent flux, and spectral index, needs to be corrected by the antenna response function (which is frequency dependant) to obtain the intrinsic flux. If an image contains multiple sources the sampling function may interfere with the central component of other sources, making their flux hard to determine. Removal of the sampling function from the dirty image requires deconvolving the sampling pattern from the sky brightness distribution, which is usually performed with some variant of the CLEAN algorithm [164, 165, 166]. The basic form of the algorithm is as follows:

1. Locate the maximal point in the dirty image.
2. Subtract from that point the dirty beam multiplied by the flux at said point, further multiplied by a clean gain factor (0.1 is the default CASA value). This produces a residual image.
3. Add the flux subtracted from the image to a clean model image (at the pixel where the subtraction occurred).
4. repeat steps (1-3) until either an iteration threshold is reached, or the maximal point in the dirty image is consistent with the image noise (e.g. within $3\,\sigma$). The subtraction in step (1) should be performed on the most recent residual image.
5. Convolve the clean model with the synthesised (or clean) beam, which is a fit to the central 2D-Gaussian of the dirty beam (i.e. the dirty beam without the side lobes - artefacts in the dirty image from the off axis response of the interferometer).
6. Add to this the final residual image (which should just be noise).

Upon completing the algorithm you will have a clean (deconvolved) image. Additional steps have been implemented over time to increase the algorithm's efficiency or accuracy, but the guiding principle remains the same. The CLEAN algorithm is not without flaw, and was met with scepticism upon its presentation. The results it produces are not unique, and different users of the algorithm will inevitably produce different clean images. This is especially the case given that clean regions (portions of the image outside of which the CLEAN algorithm is forbidden from operating) are used to 'box' and then deconvolve sources - the placement of which is a user choice. Inherent to the CLEAN algorithm is the assumption that the sources being deconvolved are point like, and the algorithm performs well in this regime. If sources in an image are extended then CLEAN will attempt to recreate the source as a collection of point-like components, which may not construct the source structure well,

although cleaning on multiple spatial scales can alleviate this [167]. An example of the imaging process is shown in Figure 3.4.

3.1.3.1 Signal to noise in radio images

There is a simple formulation for determining the sensitivity of an interferometer, which is a function of the length of the observation (t), the total collecting area (summed over all antennae ($\sim ND^2$, modified by some antenna efficiency η), the number of polarisations (n_p) and the temperature of the system (T_{sys}) and is shown in Equation (3.9).

$$S \propto \frac{T_{sys}}{D^2\eta(n_p N(N-1)\Delta\nu t)^{1/2}} \approx \frac{T_{sys}}{ND^2\eta(n_p\Delta\nu t)^{1/2}} \tag{3.9}$$

The definition of temperature in 'system temperature' is defined as the black body temperature of an object that would provide the power received by the receiver. The electronics elements themselves will contribute to the system temperature, as will emission from the ground. Shielding can be used to reduce this effect.

3.2 X-ray observations

While I have predominantly utilised radio observations for this thesis, I have contrasted these observations with those at other wavelengths, primarily X-rays, when necessary. The techniques used in X-ray observing are more diverse than the applies-to-all basics of interferometry and so I will not try to give an overview here. I will briefly mention facilities that I have utilised below, and will address the data reduction and instrument specifics in the relevant chapters should it be necessary.

3.3 Facilities utilised

3.3.1 Radio

3.3.1.1 The Arcminute Microkelvin Imager Large Array

The Arcminute Microkelvin Imager Large Array (AMI-LA) is a radio interferometer located at the Mullard Radio Astronomy Observatory (MRAO; Lords Bridge, Cambridge, UK) and operated by the University of Cambridge. The array consists of eight 12.8 m dishes, which were re-purposed from their original inclusion as part of the 5 km/Ryle Telescope [168]. The AMI-LA antennas operate on baselines between 18 m and 110 m and therefore the array,

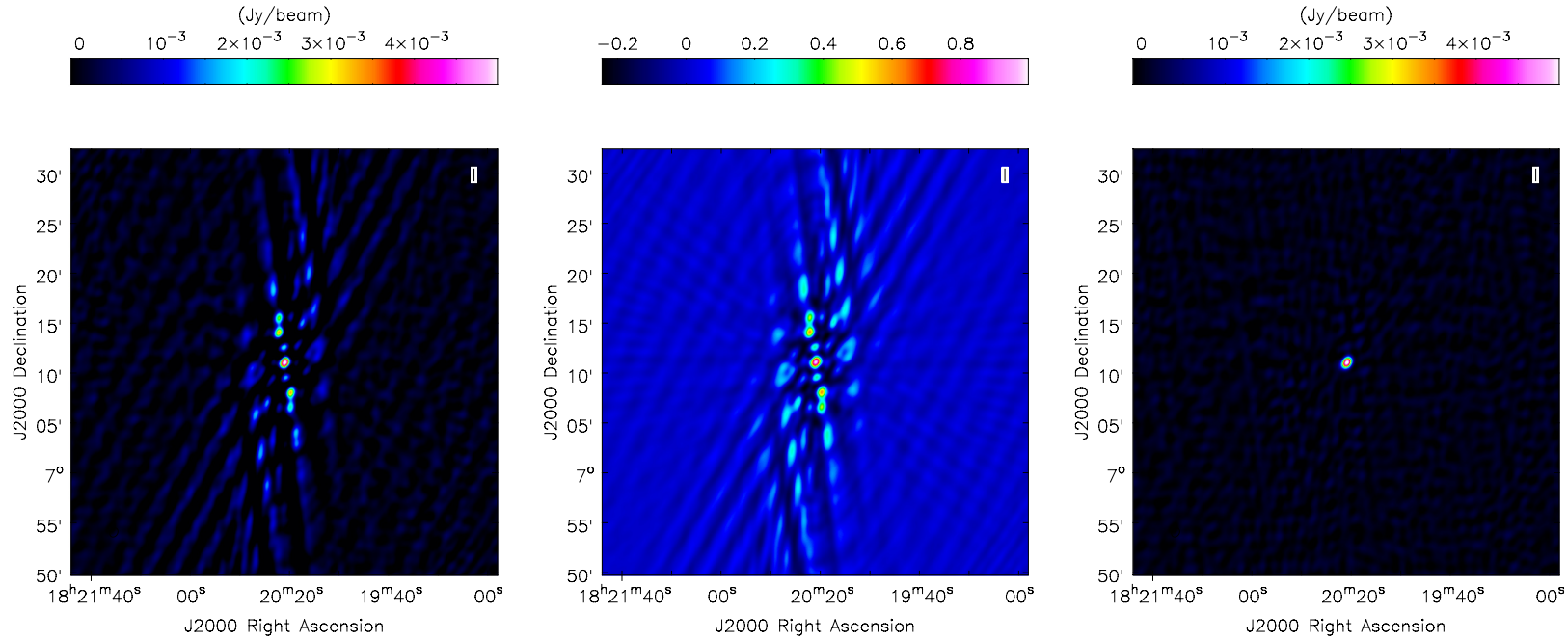

(a) A dirty image of the field of MAXI J1820+070. This is a direct Fourier transform of the calibrated visibilities, and shows the sky brightness distribution convolved with the sampling function of the array.

(b) The Fourier transform of the AMI-LA sampling function, which is iteratively subtracted from the dirty image during the implementation of the CLEAN algorithm.

(c) The cleaned, or deconvolved image, which is the model image convolved with the synthesised beam (a fit to the central component of the PSF). The side lobe structure has been removed and a point source recovered. Cleaning was performed within a user defined region, down to a threshold of ~ 350 μJy (4.5 times the image noise).

Figure 3.4: Demonstration of the output of the CLEAN algorithm with a 2 hour observation of the black hole X-ray binary MAXI J1820+070 using the AMI-LA telescope.

at its operational frequency of 15.5 GHz, has a characteristic angular resolution of $\sim 30''$. The original correlator was an analogue one, with eight channels covering the bandwidth between 13.9 GHz and 18.2 GHz [169]. In 2015 the AMI-LA was upgraded with a digital correlator covering a similar frequency range (13.1 GHz to 17.9 GHz), but now with 4096 frequency channels. This increase in spectral resolution significantly reduces the effects of radio frequency interference (which often only influences a narrow frequency range), minimising data loss [170]. The AMI-LA is sensitive to the $I + Q$ polarisation, and has a flux sensitivity of $3\,\mathrm{mJy\,s^{1/2}}$, e.g. $\sim 40\,\mu$Jy for 1 h on source. A primary flux calibrator (either 3C 286 or 3C 48) is observed every 12 or 24 h to set the flux scale of observations. An interleaved phase calibrator within 5°of the science target is observed for phase and further flux calibration. The AMI-LA raw data is reduced in one of two ways, either as 'quick look' data or with a full pipeline reduction. The 'quick look' data products are created by averaging the data, at the correlator, down to 8 frequency channels. These are then calibrated using a custom reduction pipeline (REDUCE_DC; e.g. [171]), with imaging then performed in CASA. Data are also recorded in full spectral resolution, which can then be reduced using standard reduction techniques. The advantage of the 'quick look' data is that reduction and imaging can be easily automated, and products made very quickly after an observation concludes. This can be important for early transient detections/characterisation. Advanced calibration techniques, beyond 1$^{\mathrm{st}}$ generation, are not required for data taken with the AMI-LA due to its small field of view, low angular resolution, and the relative emptiness of the 15.5 GHz sky. The AMI-LA robotically responds to alerts from the hard X-ray instrument on the *Swift* telescopes, and so can observe the early time radio emission from transient sources such as GRBs and XRBs [172].

3.3.1.2 MeerKAT

MeerKAT is a Square Kilometer Array (SKA) precursor radio interferometer located in the Karoo Desert in South Africa, and operated by the South African Radio Astronomy Observatory (SARAO). The array consists of 64 13.5 m dishes, 48 of which are located within a $\sim$ 1 km diameter core region with the rest distributed out to a $\sim$ 4 km radius. The maximum and minimum baselines are 29 m and 7698 m, respectively. At the central frequency of the telescope (1.284 GHz) this results in an angular resolution of $\sim 6''$ but, due to the diversity in baseline length, this depends strongly on the weighting scheme used for imaging [173]. MeerKAT operates between 0.856 GHz and 1.712 GHz and is sensitive to dual linear polarisation. MeerKAT observations presented in this thesis were taken as part of the image-plane transients large survey project ThunderKAT (**T**he **HUN**t for **D**ynamic and **E**xplosive **R**adio Transients with Meer**KAT**), specifically within the relativistic accretion

working group [174] which monitors active black hole X-ray binaries on a weekly basis with 15 min images per source. Typical sensitivities in such images are 20 μJy but this depends strongly on the specific field being observed. MeerKAT's large field of view ($\sim 1\,\mathrm{deg}^2$), low observing frequency, and compact core make it sensitive to extended structure that can prevent the thermal noise level from being reached. Some of these features (the large field of view and sensitivity to extended structure) prove challenging for standard 1$^{\mathrm{st}}$ generation calibration techniques as the far field assumption is violated. Direction dependent self-calibration is instead required for the highest quality images. However, given that targets observed as part of the ThunderKAT programme are either unresolved or only slightly extended, phase only reference calibration is usually adequate (a caveat to this would be if artefacts from a bright off-axis source corrupted the image at the phase centre). The MeerKAT data presented in this thesis was calibrated with a custom reduction pipeline utilising AOFLAGGER and CASA, with WSCLEAN used for imaging [175, 176, 177, 178].

3.3.1.3 The Karl G. Jansky Very Large Array

The Karl G. Jansky Very Large Array (VLA) is the most versatile radio interferometer currently in use [179, 180]. Operated by the National Radio Astronomy Observatory and located in New Mexico, the array consists of 27 25 m dishes with baseline ranged depending on the array configuration (the dishes can be moved along railway tracks improve the array's ability to perform certain science goals). The VLA has 4 configurations, its most compact (D-configuration) has baselines between 0.035 km and 1.03 km whereas the most extended configuration (A-configuration) has baselines between 0.068 km and 36.4 km. The telescope is also able to observe at frequencies between 74 MHz and 45 GHz, therefore having resolutions between 0.043″ and 850″. Due to the range of possible observing setups with the VLA, I will discuss specific data reduction processes in the relevant science chapters where VLA data is used. The sensitivity of the VLA depends on the observing configuration.

3.3.1.4 The Multi-Element Radio Linked Interferometer Network

The enhanced Multi-Element Radio Linked Interferometer Network (eMERLIN) is an interferometer consisting of seven inhomogeneous dishes with diameters between 25 m and 76 m. The array operates on baselines of up to 217 km and can observe at 1.5 GHz, 5 GHz, and 22 GHz allowing for angular resolutions between 0.02″ and 0.2″. eMERLIN data utilised in this thesis was reduced using a custom reduction pipeline (see `http://www.e-merlin.ac.uk/tools/eMCP-2.pdf`). In a 12 h observing run eMERLIN achieves sensitivities of $\sim 24\,\mathrm{mJy\,beam^{-1}}$ and $\sim 16\,\mathrm{mJy\,beam^{-1}}$ at 1.5 GHz and 5 GHz, respectively.

3.3.1.5 The Very Long Baseline Array

The very long baseline array (VLBA) consists of 10 25 m dishes spread throughout the United States of America. The baselines range from 236 km and 8611 km - some of the longest possible for ground based arrays. The array can observe at a range of frequencies between 326 MHz and 62 GHz allowing for angular resolutions of 0.17 mas and 22 mas. A single VLBA observation was used as part of this thesis at a frequency of 15.1 GHz providing angular resolution $\sim$ 1 mas. These data were reduced using standard VLBI reduction techniques and were taken as part of the observing campaign reported in [101].

3.3.2 X-ray

3.3.2.1 Neil Gehrels Swift Observatory

The Neil Gehrels Swift Observatory (*Swift* [181]) is a space-based X-ray, optical, and ultra-violet telescope with a primary science goal of discovery, early detection, and monitoring of gamma-ray bursts – a science goal facilitated by the fast slew rate of the telescope. *Swift* is also used extensively for monitoring other transient events that have an optical, UV, or X-ray component. The satellite is equipped with three instruments. The UV/Optical Telescope (UVOT) operates between 170 nm and 600 nm with an angular resolution of $\sim 0.5''$. The X-ray Telescope (XRT [182, 183]) is a focusing X-ray telescope operating between 0.2 and 10 keV and provides spectra and lightcurves within this range. The Burst Alert Telescope (BAT [184, 185]) operates between 15 and 150 keV and has a 1.4 steradian field of view. *Swift* will automatically slew and observe new sources of hard X-ray emission (mostly GRBs, but also XRBs) without human intervention, providing early time information from UV to hard X-ray wavelengths. *Swift* observations used within this thesis were, unless otherwise described, produced using the *Swift*-XRT data product generator [186, 187].

3.3.2.2 MAXI

The Monitor of All-sky X-ray Image (MAXI [188]) is a module on board the International Space Station designed to monitor the whole sky at soft X-ray wavelengths (between 0.5 and 30 keV depending on the exact instrument). While it is less sensitive than *Swift*, it provides consistent high cadence monitoring of bright sources, yielding light curves and spectral information on transient X-ray sources.

3.3.2.3 NICER

The Neutron star Interior Composition Explorer (NICER) instrument is also located on the International Space Station, and operated between 0.2 and 12 keV. NICER is primarily

designed (as the name suggests) to probe the interior properties of neutron stars, and will do so using spectroscopic and timing measurements of their soft X-ray emission. X-ray binary systems (including those containing black holes) are also active in the soft X-rays and NICER has already provided new insights into the accretion flows present in these systems [189, 190].

Chapter 4

The accretion – ejection connection in the black hole X-ray binary MAXI J1820+070

This chapter is based on work published in:

Bright *et al*. An extremely powerful long lived superluminal ejection from the black hole MAXI J1820+070. Nature Astronomy, March 2020.

Homan & Bright *et al*. A rapid change in X-ray variability and a jet ejection in the black hole transient MAXI J1820+070. MNRAS **891**, L29, 2020.

Bright *et al.* 2020 *in prep*.

4.1 Introduction

Stellar mass compact objects (white dwarfs, neutron stars, and black holes) can exist as part of binary systems with a main sequence, non degenerate, companion star. These systems are called cataclysmic variables (CVs), neutron star X-ray binaries (NSXRBs), and black hole X-ray binaries (BHXRBs), respectively. This chapter will focus on results from a binary system with a dynamically confirmed black hole and therefore from now on I will be implicitly referring to BHXRB systems when discussing compact objects accreting from a companion. Such binary configurations result in a complex gravitational potential, Φ, between and around the binary constituents, known as the Roche geometry, which is a function of the mass ratio of the binary companions and their orbital separation. An example of the Roche geometry is shown in Figure 4.1. A number of force free, or Lagrange, points

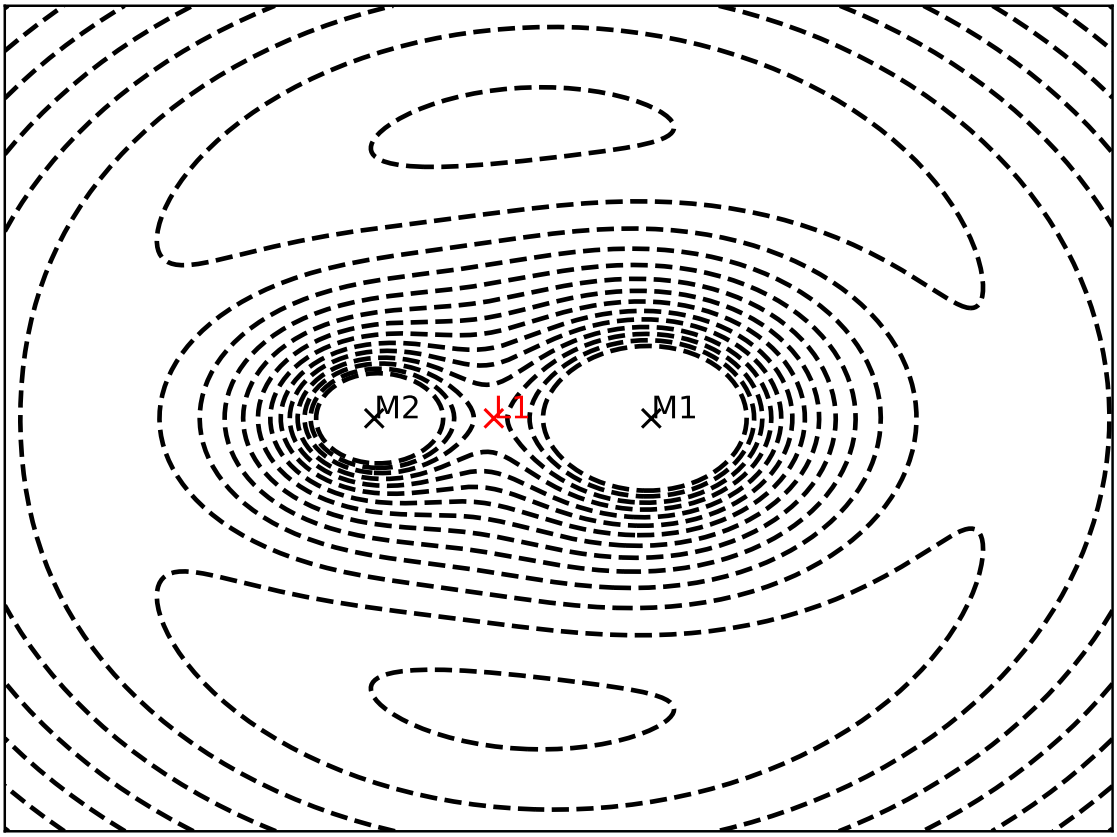

Figure 4.1: The Roche potential for a binary star system. M_2 is half the mass of M_1 and their positions are marked with labelled black crosses. Dashed lines mark curves of equipotential. Mass transfer occurs through the primary Lagrange point, L_1, marked with a labelled red cross. The absolute value of the potential, as well as the positions, are arbitrary. Contours have been removed close to the star positions, as they become more closely spaced.

exist in the Roche potential, where $\nabla\Phi = 0$. For binary star systems the most important of these Lagrange points is L_1, located between the binary partners. The location of L_1 is intrinsically linked to the Roche lobe of each star, which is a surface within which material is gravitationally bound to that star. L_1 is located at the point between the two stars where the two Roche lobes 'touch'. If the physical extent of one of the binary stars is comparable to, or larger than, its Roche radius then it will transfer mass through the L_1 point to its companion. Mass transfer can also occur if a star is driving matter away from it e.g. via a stellar wind [191]. In the case of the systems mentioned above, the compact object is constrained to a physical region well inside of its Roche lobe and as such only the main sequence companion will lose material. BHXRBs are therefore examples of semi-detached binaries (as apposed to contact binaries where both stars fill their Roche lobe), and the process of a star losing mass to a binary companion is known as 'mass transfer'.

The stream of material lost via mass transfer cannot simply fall into the black hole, as it must conserve its angular momentum, and so instead it will enter an elliptical orbit at a radius appropriate for its specific angular momentum. The stream of material is continuous, and as such it will self-interact after completing an orbit of the BH and eventually settle into a circular orbit. The material circling the black hole is not infinitesimally thin in the radial direction, and, from Kepler's laws, rings of material at different radii will orbit at different speeds (those closer to the BH will orbit faster, but contain less angular momentum). Such differential rotation will lead to the rise of friction processes which in turn heat the rings of material. This will lead to some of the material losing gravitational potential, and therefore angular momentum. However angular momentum is a conserved quantity, and so other parts of the orbiting material gains angular momentum, causing it to move to large radii. This radial spreading leads to the formation of a so-called 'accretion disk', which is a natural structure for material with angular momentum accreting onto an object. The exact mechanism allowing for the transfer of angular momentum through an accretion disk is not know, but a magnetic instability is thought to be the most likely [35, 36].

The continuum spectrum of an accretion disk is well described by a multi-component black body, with annuli closer to the black hole being hotter, having lost more gravitational potential energy. The disk is maintained as long as material is continually supplied by the stellar companion at a rate greater than it is lost from the inner edger of the accretion disk (whose radii is usually defined in units of the innermost stable circular orbit (ISCO) radius). Beyond the inner radius of the accretion disk matter quickly falls onto the black hole. A thorough treatment of binary systems and accretion disks is given in e.g. [37, 192]. This matter is not all lost beyond the black hole event horizon (a surface at which the escape velocity from the black hole is equal to the speed of light) and can instead be ejected at relativistic speeds by the black hole. In black hole X-ray binaries the exact form of outflow produced depends on the accretion state of the system (discussed further in the upcoming sections) but, for the majority of the time where outflows are present, they are in the form of a bipolar jet. These are collimated (and thought to be launched perpendicular to the plane of the disk, although they have been seen to precess [103]), constantly replenished, mildly relativistic, ($\Gamma \lesssim 2$) and have a flat radio spectrum (emitting synchrotron radiation, see Section 2.1.6). I will refer to such an outflow as a 'core jet'. The exact mechanism that is responsible for the acceleration and ejection of accreting material is unknown. The predominant theories to explain the connection rely on either tapping the spin energy of the black hole through a coupling with magnetic fields from the accretion disk, or outflows being centrifugally driven directly from the disk magnetic field itself [75, 80]. Despite

being located within our galaxy, the core jet of most BHXRBs subtends an angle smaller than the resolution of even the longest baseline VLBI instruments, and as such they remain unresolved in the majority of systems. This is in sharp contrast to the jets from nearby AGN, which can be probed in exquisite detail due to their massive angular extents.

Due to black holes being completely described by only three parameters (mass, angular momentum, and charge) it is thought that the process that produces jets in BHXRBs is the same as the one produces jets in AGN, leading to BHXRBs being alternatively named 'microquasars'. While the presence of jets, as well as their influence on their host galaxy, is obvious in multi-wavelength observations of nearby AGN, the presence of similar jets is less evident in BHXRBs. Only in two cases has the 'core jet' been spatially resolved with VLBI observations (which probe milli-arcsecond, or AU, scales at distances within our galaxy) [96, 95], and its presence is usually inferred from observing a compact radio source at the binary location with a flat ($\alpha \sim 0$) spectrum (demonstrated in Figure 2.5).

Due to the smaller mass (and therefore size) scales involved in BHXRB systems (as apposed to AGN), evolution in the accretion properties (and the associated outflows) occur on humanly accessible timescales. BHXRBs are therefore some of the best systems to probe this coupling, as well as to observe the impact that outflows have on their surrounding environments as they can be observed to propagate into, and interact with, the local ISM in near real time.

4.2 X-ray binary characteristics

4.2.1 Outbursts and accretion states

X-ray binaries spend the majority of their existence accreting at a low rate, remaining (for the majority of sources) undetected or undiscovered at both X-ray and radio frequencies. Occasionally, due to instabilities in the accretion disk (caused by the build up of accreting material reaching the critical density and temperature to fully ionise hydrogen, resulting in a sudden jump in the accretion rate), the rate of accretion, and thus the X-ray and radio luminosity, increases. At this point systems are said to be in outburst and are usually detected first by all-sky X-ray monitors such as *Swift*-BAT or MAXI. Through public transient reporting (e.g. The Astronomers Telegram) multiwavelength followup can be initiated. The magnitude of outbursts for most systems is unknown due to their quiescent fluxes being unconstrained but population studies have shown X-ray amplitudes between quiescence and outburst ranging between a factor of a few and 10^7 [193]. Radio amplitudes between

quiescence and outburst span $\sim$ 5 orders of magnitude [194]. During outbursts BHXRBs exhibit distinct accretion states, which couple to the form of outflow they produce - this makes them excellent candidates for studying accretion and jet production.

X-ray monitoring of BHXRBs during outburst (primarily within our Galaxy, although see e.g. [195]) has shown that systems evolve through distinct accretion states, and that these accretion states strongly influence the form of outflows these systems produce [196]. BHXRB systems begin outbursts in the so-called hard/low accretion state, accreting at a few per-cent of the Eddington Luminosity, $L_{\rm Edd}$. This is also the accretion state that BHXRBs are thought to be in when quiescent (although the accretion rate is significantly lower than when in outburst). The X-ray 'hardness' of an object is defined as the ratio of counts of two energy bands, with the exact bands chosen depending on the instrument being used. The hard state is characterised by the following properties:

- The X-ray spectrum has a strong power-law component, and peaks at $\sim$ 100 keV. The origin of this spectral component is not well understood, but is thought to be the result of a hot thermal population of electrons Compton up-scattering photons from the accretion disk. The geometry and origin of this 'corona' are not known. It has also been suggested that this spectral component could be a signature of the base of the core jet emitting soft X-rays via synchrotron emission and Compton up-scattering disk and synchrotron photons [197, 198].

- X-ray variability, revealed through timing analysis of X-ray light curves, shows strong ($\gtrsim$ 30%) broad band noise over many decades in frequency (between mHz and $\sim$ 100 Hz) in power density spectra.

- The hard state is always associated with a constantly replenished, flat spectrum, collimated, small scale, core jet. The luminosity of this jet is strongly correlated to the X-ray luminosity of the system [98].

After a period in the hard state, systems can (but do not always [199, 200, 201]) transition to the soft accretion state and the accretion rate increases [202, 100, 99]. The soft state is characterised by the following properties:

- The power-law component of the X-ray spectrum is now absent and instead it can be characterised entirely by a multi-component black body with the components corresponding to different anulii of the accretion disk (with $T_{\rm disk} \propto r^{-3/4}$). This is thought to be due to the inner radius of the accretion disk moving in to the ISCO and destroying or suppressing the corona.

- The X-ray variability is significantly suppressed, and is sometimes consistent with 0% [203].
- The core jet present in the hard state disappears (the flux drops), with a suppression factor (or quenching factor) of at least 10^3 [99, 100]. This indicates that the mechanism producing the core jet is either absent or significantly less efficient in the soft accretion state.

The transition between the hard and soft states is not instantaneous, and occurs on timescales of around 1 day to a few weeks [100, 204]. The accretion rate evolution throughout an outburst is best visualised through a hardness–intensity diagram such as the one demonstrated semi-schematically in Figure 4.2. During this time the X-ray spectrum evolves (first from hard to soft, then vice-versa on the reverse transition) and the core jet quenches (or restarts). Perhaps the most spectacular phase of the outburst cycle of a BHXRB begins during this quenching, where significant radio flaring can be seen superposed on the decaying core jet flux or at the start of the soft state. This flaring can be simple (a single or few isolated flaring events [100]) or incredibly complex (many confused flares [205]) and last from just hours [100], to weeks [205], or years in the case of GRS 1915+105. Over the weeks/months following such flaring activity, continued radio monitoring reveals that, while the core jet is no longer active, systems launch bi-polar transient ejections that appear no longer connected to the black hole and are observed to have an optically thin synchrotron spectrum from radio all the way up to X-ray frequencies (although X-ray detections are rare compared to radio ones) [97, 206, 207, 208, 204]. The ejections are observed to move between observing epochs (sometimes apparently superluminally [97, 99, 100]) and from modelling their proper motion a launch time can be inferred (as well as limits put on other source characteristics such as the distance and binary inclination [209]) and are usually found to be launched at a similar time to the onset of radio flaring. The properties of radio flaring and what physical information they encode will be discussed in some detail in this Chapter, and in more detail in Chapter 5.

4.2.2 The Radio X-ray Correlation

In order to probe the connection between accretion and core jet production in the hard accretion state it is useful to correlate the core jet radio flux with the X-ray emission from the accretion flow. This is known as the radio – X-ray correlation in the literature, and it extends more broadly into the fundamental plane of black hole activity when considering black holes of all masses, from Galactic to supermassive [105]. As discrete ejections are not

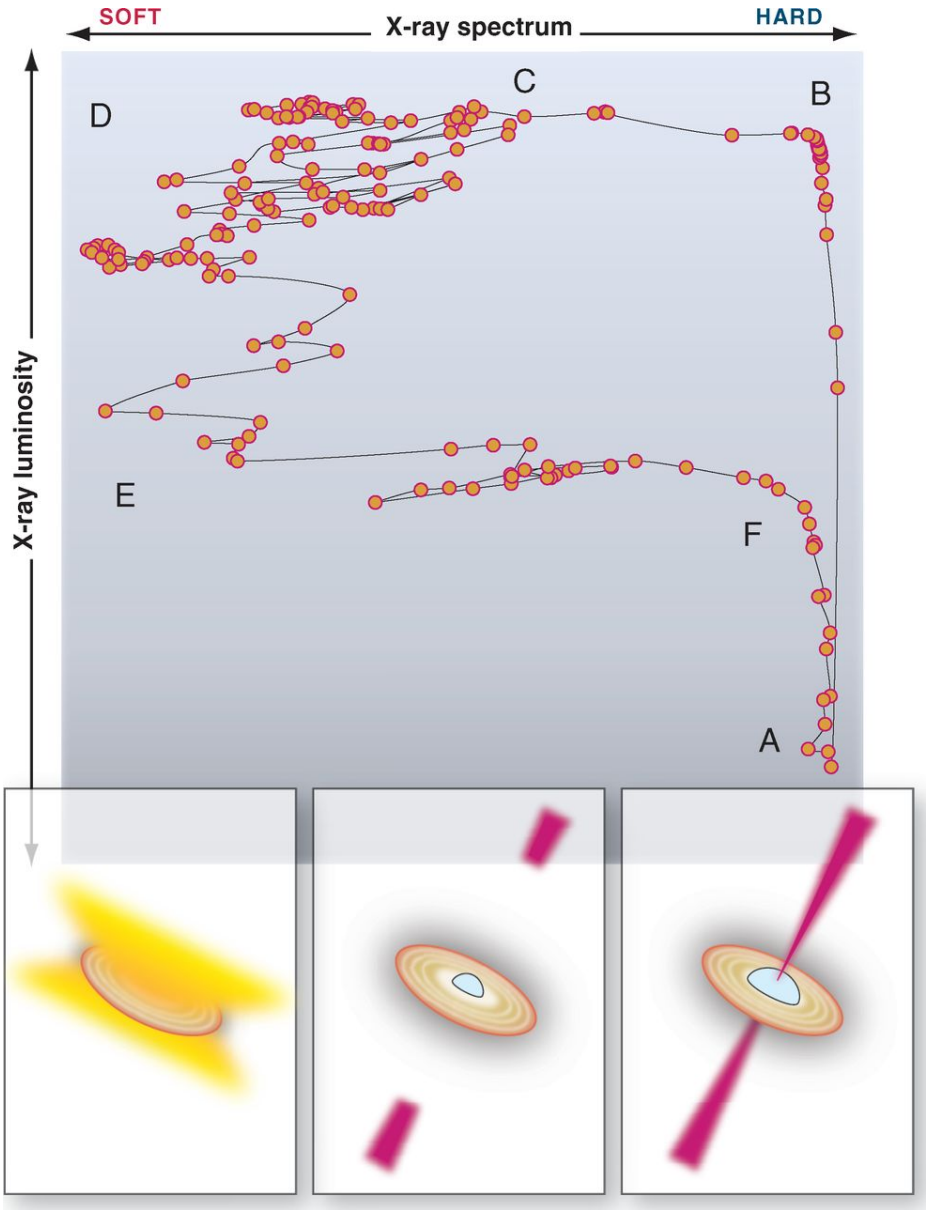

Figure 4.2: A semi-schematic hardness intensity diagram for the BHXRB GX 339−4, demonstrating the X-ray intensity evolution as a function of the X-ray hardness ratio over approximately 1 year of the source being in outburst. Such evolution is typical for all BHXRBs in outburst. Sources begin in the low hard state (A) and increase in luminosity at the beginning of the outburst to the high hard state (B). Some sources then undergo a hard to soft state transition at high accretion rates, the spectrum softens (D) and radio flares and ejections may occur (C). The X-ray luminosity fades in the soft state (during which the flux $F \propto T^{\sim 4}$ implying a constant size emitting region) and eventually a source will return to the hard state at a lower X-ray luminosity than it exited at (E-F) and then fade back to quiescence. The outflow properties of the system are a function of the accretion state, and are demonstrated schematically in the three panels at the bottom of the figure. From left to right the images show an accretion disk wind (there are cases of winds seen during the hard state [210]), discrete ejections (with an accretion disk at ISCO and a suppressed corona), and a core jet (with a dominant corona). Figure reproduced with permission from [211].

(apparently) physically connected to the black hole, and as such are not driven by ongoing accretion activity, they are not included in the correlation.

For a radiatively efficient accretion flow, where material is able radiate a significant fraction of its energy before being advected across the black hole event horizon (e.g. the Shakura & Sunyaev geometrically thin disk [37]), the X-ray luminosity is expected to scale with the mass accretion rate ($L_X \propto \dot{M}$), whereas for an inefficient flow material is quickly lost across the horizon (or ejected from the system as an outflow) and $L_X \propto \dot{M}^{2-3}$ [37, 212]. Additionally, it is common to assume that the total power of the jet from a system is some fraction of the accretion power, $P_{\rm jet} = bP_{\rm acc} \propto \dot{M}$, which is a natural assumption given that accretion is thought to result in jet production. It can also be shown [213], following the standard assumptions of synchrotron radiation as discussed in Chapter 5, that the jet luminosity should scale with the jets power as

$$L_{\rm jet} \propto P_{\rm jet}^{\epsilon} = P_{\rm jet}^{\frac{2p-(p+6)\alpha+13}{2(p+4)}} \tag{4.1}$$

with α the spectral index (which I define as $L_\nu \propto \nu^\alpha$). The index ϵ depends on the index of the power law distribution of electrons, as well as the spectral index of the core jet, which is ~ 0, and therefore ϵ has a characteristic value of ~ 1.4 (but see [214] for a more detailed analysis of the values that ϵ can adopt). Under these assumptions we have a relationship between the jet's radio luminosity and the disk luminosity (X-ray). For a radiatively efficient accretion flow this scaling goes as $L_{\rm jet} \propto L_X^{\sim 1.4}$ and for a radiatively inefficient flow the scaling is instead $L_{\rm jet} \propto L_X^{\sim 0.5-0.7}$.

Initially it was observed for the BHXRB source GX 339−4 that indeed the radio–X-ray correlation had an index consistent with the above formulation and a radiatively inefficient accretion flow [98], the same correlation was also seen for the BHXRB V404 Cygni [61]. This was consistent with the idea that all BHXRBs in the hard state were accreting with a radiatively inefficient flow, further supported by observations of X-ray emission from quiescent black hole systems showing significantly lower X-ray luminosity than neutron star systems (at similar orbital periods) [215] (see Chapter 1 for a discussion on advection dominated accretion). This hypothesis was challenged when observations of the candidate BHXRB H1743−322 showed that at high radio and X-ray luminosities the correlation was much steeper, and more similar to the one expected for a radiatively efficient flow. The original correlation was termed the standard track, while the new track was termed the outlier track. Subsequently the outlier track has proven to be the most populated of the tracks [216]. Puzzlingly, at intermediate radio and X-ray luminosities the outlier track rejoins the

standard one - although the correlation is difficult to track at low luminosities [217, 218]. The efficient/inefficient paradigm was further challenged when it appeared that neutron star X-ray binaries were globally consistent with the track associated with inefficient accretion, which should not be possible given the lack of an event horizon in such systems implying the inevitable release of energy once material interacts with the surface of the neutron star [219].

Attempts to identify the physical origin of the existence of the radio loud and radio quiet tracks have so far been unsuccessful. Differences have been explained in terms of different jet magnetic field configurations [220], the accretion flow radiative efficiency [214], or in the contribution from an additional inner accretion disc (in which case the outlier are X-ray bright rather than radio quiet) [221]. More recently, it was proposed that the morphology of the distribution is the result of an inclination effect, which, however, remains to be confirmed by more observations of black hole X-ray binaries in the hard state [216], although it is worth noting that MAXI J1820+070 goes against the proposed trend (see later Sections in this Chapter).

Additionally, clustering analysis of the radio – X-ray correlation for black hole X-ray binaries revealed that, for reasonable assumptions on the errors in L_R and L_X, a two-cluster description was not statistically preferred [194]. It is therefore not clear **a)** if two tracks are required to explain the observed correlation for all sources, or **b)** what the exact relation between L_R and L_X is, and **c)** what physically motivates the relation(s). However, what is clear is that sources make different tracks in the radio – X-ray plane, and that disentangling the relation is key to understanding how accretion and jet formation are connected. The radio – X-ray correlation is demonstrated in Figure 4.3 for a sample of black hole X-ray binaries.

4.2.3 Discrete ejections

Distinct from the compact core jet, BHXRBs launch discrete ejections of material as they transition between the hard and soft accretion states. The ejections appear no longer physically connected to the black hole position, as opposed to the constantly replenished core jet with its collimated and constantly replenished structure (inferred through direct observations or the signature flat radio spectrum associated with compact jets). These ejections appear to have higher bulk Lorentz factors ($\Gamma \gtrsim 2$) than the core jet and can be observed to move out to significantly larger distances than the (radio-bright) head of the core jet [97, 204, 207, 99, 100]. The spectrum of these ejections is consistent with optically thin synchrotron radiation, and can occasionally be seen all the way up to X-ray frequencies

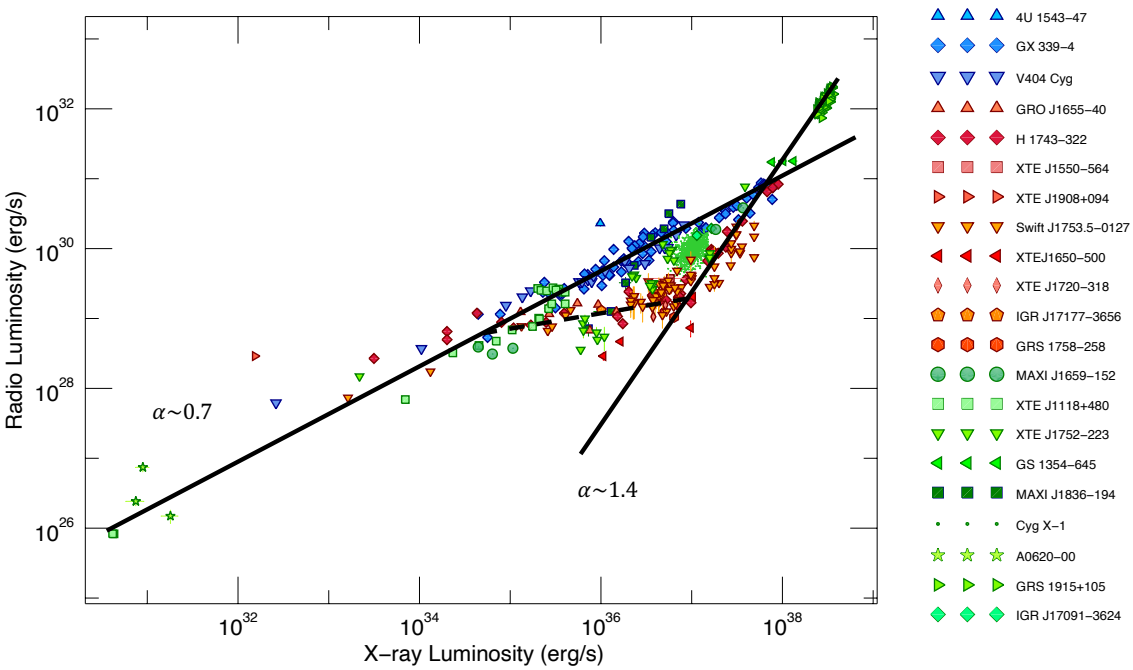

Figure 4.3: The monochromatic 5 GHz radio luminosity as a function of X-ray luminosity ($L_R \propto L_X^{\alpha}$) for 21 black hole X-ray binaries (the sources are labelled in the legend). I have marked on the so-called standard and outlier tracks, which are also known as the radio loud and quiet branches, with solid black lines. The dashed black line marks a transition where the two tracks appear to rejoin, a behaviour best demonstrated by the sources H J1743−322 and XTE J1752−223. Figure reproduced with permission from [216].

when the ejecta are resolvable by X-ray satellites such as Chandra [207, 222, 223, 224]. On occasions these ejections have been seen to re-brighten, presumably after interacting with over densities in the ISM, providing information on the local ISM density structure and the means to measure the internal energy possessed by the ejections. Understanding the energetics of ejections is a key component to constraining the total feedback budget from Galactic black holes, which may in turn provide information on the outflow processes from supermassive black holes, which are known to influence the growth of galaxies.

4.3 Radio observations of MAXI J1820+070

In the following sections I will describe an extensive observing campaign of the newly discovered outbursting BHXRB MAXI J1820+070, primarily at radio frequencies. I led this observing campaign, performing the entirety of the analysis. I also performed the reduction of a significant fraction of the observational data, including all of the AMI-LA and MeerKAT observations as well as some of the eMERLIN data. I will begin by introducing the discovery of the source and then detail our observations and analysis.

MAXI J1820+070 (ASASSN-18ey) was discovered by the All Sky Automated Search for SuperNovae (ASAS-SN [225, 226]) program on UT 2018-03-06.58 (MJD 58184.0799) after entering outburst and rising in V-band magnitude from > 16.7 to 14.88 over four days [227]. Six days later it was detected at X-ray frequencies by the Monitor of All-Sky X-ray Image (MAXI) Nova Alert System as a bright uncatalogued X-ray source which they designated MAXI J1820+070 [188, 228, 229]. MAXI J1820+070 was also detected by the *Swift* XRT (X-ray Telescope) and BAT (Burst Alert Telescope) instruments one day later and, after some confusion, the two sources were identified as being the same [230, 231, 232, 233]. Observational follow-up of MAXI J1820+070 was, due to its high optical, X-ray and radio flux, extensive, and covered the entire electromagnetic spectrum. Optical observations of the outburst prompted the classification of MAXI J1820+070 as a low mass black hole X-ray binary candidate, based on an empirical correlation between optical and X-ray flux for X-ray binary systems [234, 235, 236]. This classification was at odds with the initial one provided by the ASAS-SN team who suggested the source was a cataclysmic variable. This fact, coupled with X-ray observations of XRBs forming the back-bone of the observational followup, lead the source to be known as MAXI J1820+070 among the community. The black hole nature of the source was later dynamically confirmed, and the distance to the source (3 ± 0.3 pc; [101]) was well characterised through a variety of uncorrelated techniques, including an accurate radio parallax [237, 101, 19, 100]. In

addition to being a bright X-ray/optical source (observations which probe the accretion flow of such systems) MAXI J1820+070 was also bright at radio frequencies, indicating the source was producing outflows likely in the form of a collimated jet. I detail our radio observations of MAXI J1820+070 with a range of radio interferometers in the following Sections.

4.3.1 AMI-LA

As detailed in Section 3.3.1.1 the Arcminute Microkelvin Imager Large Array (AMI-LA) is designed to robotically trigger on, and observe, sources detected by the *Swift* BAT. The AMI-LA responded to *Swift* BAT trigger 813771 at UT 2018-03-12.0080948, and began observing the field of MAXI J1820+070 $\sim$ 1.5 hours later (MJD 58189.0709). The observation occurred at a time when the AMI-LA was down to only 5 antenna and therefore, coupled with the low source elevation and short observation length (2 hrs, preventing comprehensive (u, v) coverage) resulted in a poor image. Despite this, the source was convincingly detected at $\sim 6\sigma$ and a flux density of $\sim$ 3mJy. This represents one of the earliest radio detections of an outbursting BHXRB following its discovery at X-rays (although note that this is one week after the report of the outburst by the ASAS-SN team at optical frequencies). We have regularly monitored MAXI J1820+070 since its discovery, with an observing cadence between daily and weekly. Our monitoring of MAXI J1820+070 is still ongoing, two years after its discovery, and represents perhaps the best radio coverage of any single outburst from a BHXRB at radio frequencies ever obtained. The 15.5 GHz AMI-LA light curve is shown in Figure 4.4. Due to the relatively poor angular resolution of the AMI-LA (around 30″), MAXI J1820+070 is observed as an unresolved source in all epochs and Figure 4.4 demonstrates the flux evolution of this unresolved component. Additionally, I present data taken between MJD 58305.0 and MJD 58307.5 from the AMI-LA at a higher time resolution than shown in Figure 4.4. This is shown in Figure 4.5 and demonstrates a significant radio flaring event lasting $\lesssim$ 1 d.

4.3.2 eMERLIN

We first observed MAXI J1820+070 with eMERLIN around 9 days after its discovery by ASAS-SN, and an additional 13 times over the following 226 days. The details of our observations are given in Table 4.1. eMERLIN has a resolution of between 150 to 600 times that of the AMI-LA at 1.5 and 5 GHz, respectively. In the first 7 of these observations we observed a point source at a position consistent with that of MAXI J1820+070 (defined by VLBA observations of the field in the hard state showing a compact core [101]). Later

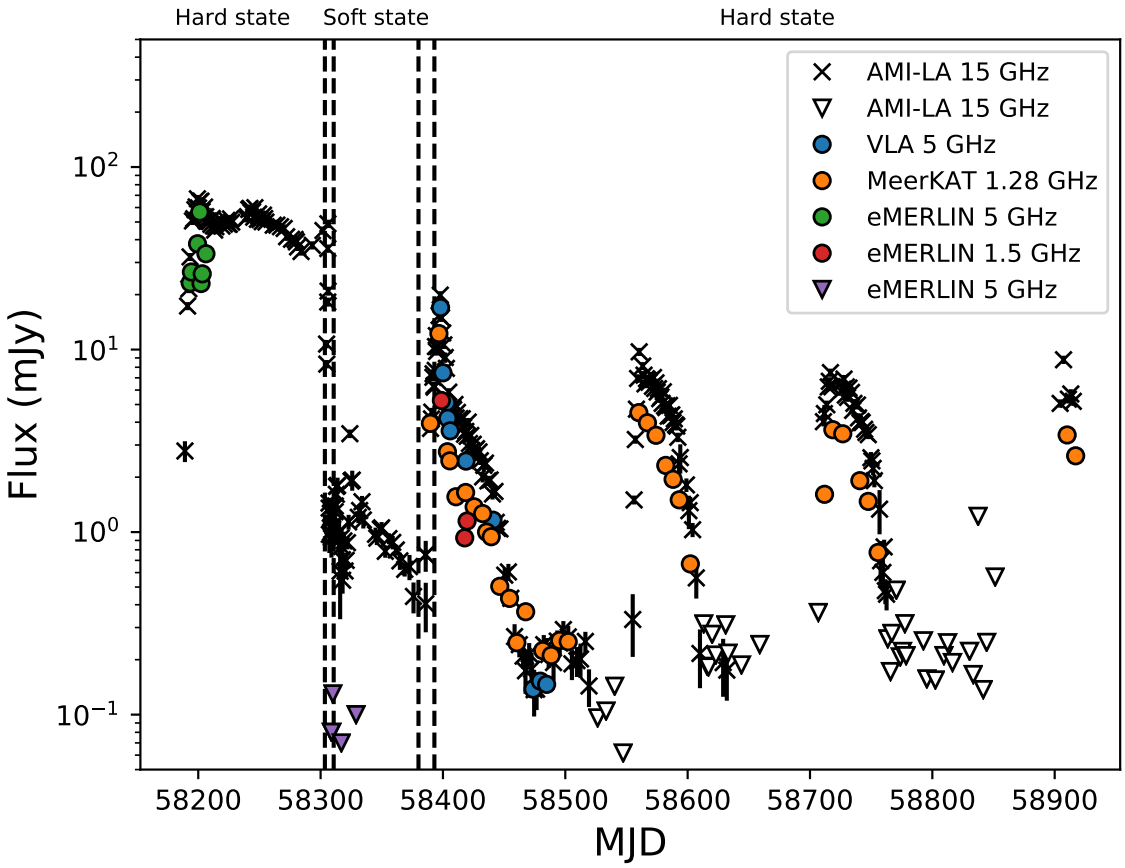

Figure 4.4: Radio monitoring of MAXI J1820+070 with the AMI-LA (black crosses for detections, unfilled triangles for upper limits), eMERLIN (green and red points for detections, purple triangles for upper limits), MeerKAT (orange points) and the VLA (blue points) radio telescopes. The accretion state of the source is labelled above the plot, based on the MAXI monitoring presented in [238]. The first and second pair of dashed vertical lines mark the start and end of the transition from the hard to soft accretion state, and then soft to hard accretion state, respectively.

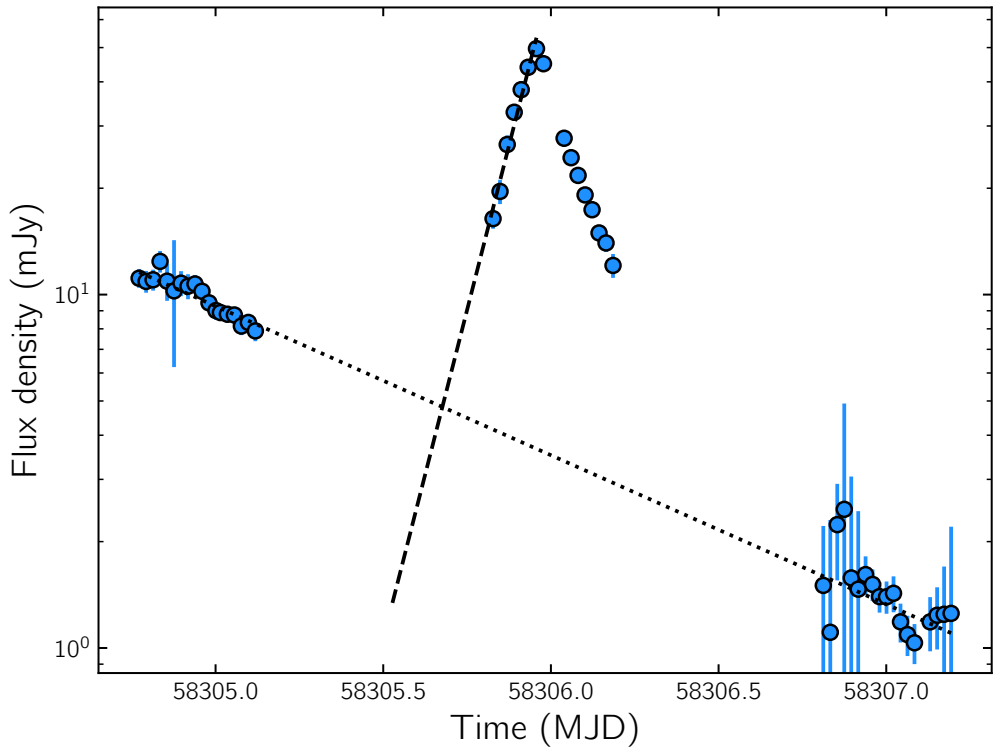

Figure 4.5: AMI-LA observations of a radio flare which occurred as MAXI J1820+070 transitioned from the hard to soft X-ray accretion state. The blue data points correspond to 30 min of (u,v) amplitudes averaged over all baselines and frequencies. The errors on individual points include a statistical error (calculated from the standard deviation of data within the 30 min bin) and a 5% calibration uncertainty, combined in quadrature. Dotted and dashed lines show exponential fits to the core quenching and the rise of the flare, respectively. We use these to estimate the rise time of the flare, which we take as the time between the intercept of these fits and the peak data point of the flare, as well as its start date. Error bars on data points indicate one sigma uncertainties. Note the log-linear axes.

Table 4.1: Summary of our eMERLIN observations of MAXI J1820+070.

Date	Start time[a] [UT]	Start date[a] [MJD]	Frequency [GHz]	Obs. length[b] [hrs.]	Antennas[c]	RMS noise[d] [μJy beam^{-1}]
16/03/2018	07:39:56.5	58193.31943	5.07	4.71	Mk2, Kn, De, Pi	319
17/03/2018	07:39:56.5	58194.31943	5.07	4.21	Mk2, Kn, De, Pi, Da, Cm	410
22/03/2018	07:09:56.5	58199.29859	5.07	4.83	Mk2, Kn, De, Pi, Da, Cm	766
24/03/2018	01:00:26.5	58201.04200	5.07	10.96	Mk2, Kn, De, Pi, Da, Cm	325
25/03/2018	02:53:02.5	58202.12019	5.07	9.08	Mk2, Kn, De, Pi, Da, Cm	1059
26/03/2018	01:07:56.5	58203.04720	5.07	10.27	MK2, Ln, De, Pi, Da, Cm	868
29/03/2018	01:07:56.5	58206.04720	5.07	10.83	Mk2, Kn, De, Pi, Da	217
09/07/2018	18:10:01.5	58308.75073	5.07	10.95	Mk2, Kn, De, Pi, Da, Cm	26
10/07/2018	20:03:01.5	58309.83546	5.07	8.95	Mk2, Kn, De, Pi, Cm	38
17/07/2018	17:01:00.5	58316.70906	5.07	11.95	Kn, De, Pi, Da, Cm	24
29/07/2018	20:05:01.5	58328.83685	5.07	7.95	Mk2, Kn, De, Cm	37
07/10/2018	12:01:02.0	58398.50073	1.51	10.95	Mk2, Kn, De, Da, Cm	69
26/10/2018	16:05:01.6	58417.67018	1.51	5.88	Mk2, Kn, De, Pi, Da, Cm	79
28/10/2018	13:31:02.0	58419.56323	1.51	7.95	Mk2, Kn, De, Pi, Da, Cm	42

[a] Start time and Start date columns refer to the beginning of the first scan on MAXI J1820.
[b] Observations length refers to the difference in time between the start of the first and end of the last scan on MAXI J1820. Roughly $\sim 9\%$ of this time was spent observing the interleaved phase calibrator.
[c] Mk2 = Mark II, Kn = Knockin, De = Defford, Pi = Pickmere, Da = Darnhall, Cm = Cambridge.
[d] RMS calculated from a region near the image phase centre. When the core was bright observations were dynamic range limited.

observations contain either **a)** no sources, **b)** no source at the position of MAXI J1820+070 and either a source or two sources in the south-easterly direction from the black hole position, or **c)** both a source at the position of MAXI J1820+070 and a source in the south-easterly direction from the black hole position. The radio flux evolution of the source at the position of MAXI J1820+070 (hereafter the core) is shown in Figure 4.4. The position of the source(s) in the south-easterly direction is(are) seen to move away from the black hole position between observing epochs. The flux evolution of this(these) component(s) is(are) shown in Figure 4.6. Note the limited extent of the x-axis in Figure 4.6 as compared to Figure 4.4.

4.3.3 MeerKAT

We began observing MAXI J1820+070 with MeerKAT around 200 days after it was discovered by ASAS-SN. Observations were conducted on a weekly cadence as part of the ThunderKAT large survey project, with two additional (longer) observations taken to be coordinated with Chandra observations of the source [224]. A total of 44 observations have been taken to date, and these are summarised in table Table 4.2. The angular resolution of MeerKAT is around 10 times better than the AMI-LA. From the initial observation of MAXI J1820+070 we observed a resolved source which appeared to consist of a component at the phase centre (the core) and an extension in the south-easterly direction. Over the course of our observations this south-easterly component appeared to move away from the black hole, and an additional extension became apparent in the north-westerly direction

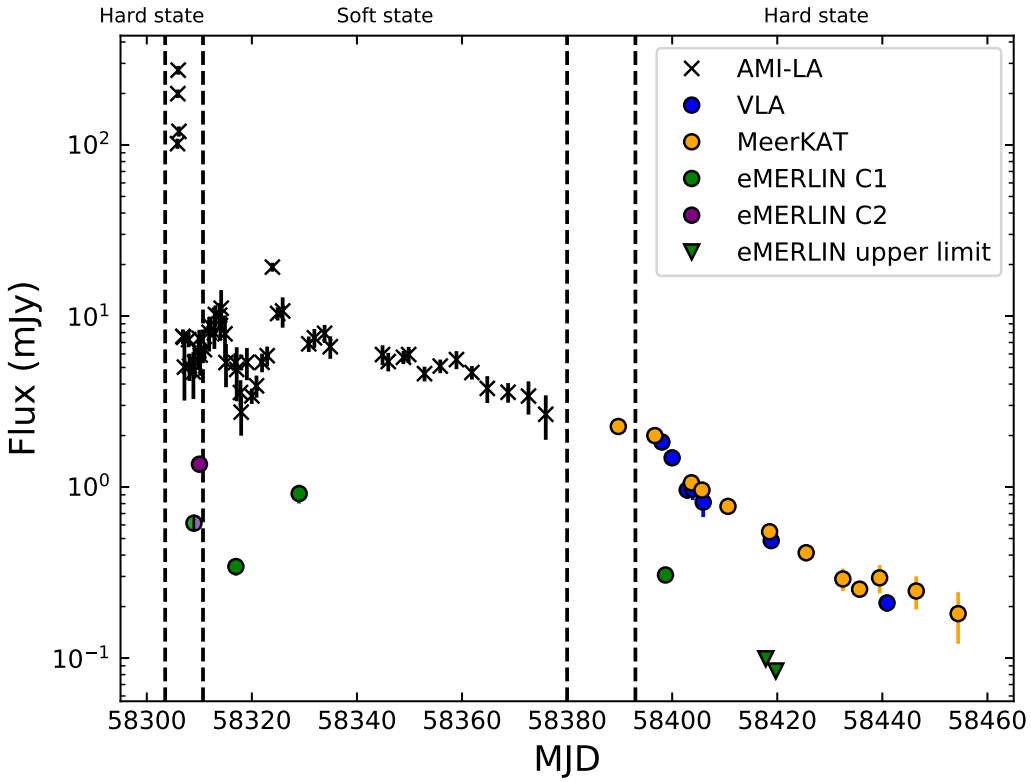

Figure 4.6: Flux monitoring of the south-easterly extension(s) (approaching ejection(s)) launched by MAXI J1820+070. Data taken at different frequencies have been scaled by a spectral index $\alpha = -0.7$ ($F_\nu = A\nu^\alpha$; appropriate for optically thin synchrotron emission from jet ejecta) to a common frequency of 1.28 GHz. We do not scale the upper limits. The MeerKAT, eMERLIN and VLA data are measurements of the approaching jet flux from images in which it is clearly spatially resolved from the core. We do not include AMI-LA data after MAXI J1820+070 returned to the hard state (around MJD 58390) as the flux density was dominated by the re-brightened core after this time. The accretion state of the source is labelled above the plot, based on the MAXI monitoring presented in [238]. The first and second pair of dashed vertical lines mark the start and end of the transition from the hard to soft accretion state, and then soft to hard accretion state, respectively. Error bars on data points indicate one sigma uncertainties. With our eMERLIN observations we see two sources in the south-easterly direction distinct from the core, which we call C1 (the component further from the core) and C2.

which was also observed to move away from the black hole. Beyond ~ MJD 58460 we only observed an unresolved component at the phase centre, the core. Examples of these different morphologies observed with MeerKAT are shown Figure 4.7. The flux evolution of the core component measured by MeerKAT is shown in Figure 4.4, the flux evolution of the south-easterly extended component is shown in Figure 4.6, and the flux evolution of the north-westerly extended component is shown in Figure 4.8.

4.3.4 VLA

We obtained a series of observations of the field of MAXI J1820+070 with the VLA at 6 GHz while it was in the D and C configurations, beginning 224 days after its discovery by ASAS-SN. The details of our observations are summarised in Table 4.3. While in the more compact D configuration the resolution of the VLA at 6 GHz is only around 3 times better than that of the AMI-LA, and MAXI J1820+070 appeared unresolved in all epochs in the image plane. In order to determine if there was evidence for extension in the VLA D configuration observations we attempted to fit the (u, v) data directly using UVMULTIFIT (once any additional spurious sources had been removed from the data). In the first 5 epochs we prefer a two point source component fit to the data, which produced noise-like residuals once propagated to the image plane. We validate this by fitting a single point source component in the UV plane and inspecting the residual image once this fit is propagated to confirm the presence of a source. This additional source is in the south-easterly direction which, given the presence of similar extensions with other interferometers gives us additional confidence in its legitimacy. In the final D configuration image we prefer a fit including an additional point source in the north-westerly direction (as well as the core and the south-westerly component), which we validate using the same methods. The first of our C band observations, which improved the resolution by a factor of 10 as compared to the D configuration, we clearly see the core and a component in the south-easterly and north-westerly direction. In our final three C band observations we see the core and the north-westerly extension only. Throughout our observing campaign we observed the two non-core components moving away from the core location. The flux evolution of the core component, the south-easterly component, and the north-westerly component are shown in Figures 4.4, 4.6 and 4.8, respectively.

4.3.5 VLBA

We obtained one observation of MAXI J1820+070 with the VLBA ~ 122 days after its discovery by ASAS-SN. This observation revealed no source at the position of MAXI

Table 4.2: Summary of our MeerKAT observations of MAXI J1820+070.

Date	Start time[a] [UT]	Start date[a] [MJD]	Frequency [GHz]	Obs. length[b] [hrs.]	RMS noise[c] [μJy beam^{-1}]
2018-09-28	17:46:44.535	58389.7408	1.28	0.24	42
2018-10-05	16:33:46.470	58396.6901	1.28	0.24	61
2018-10-12	15:46:28.907	58403.6573	1.28	0.24	35
2018-10-14	15:16:00.823	58405.6361	1.28	1.71	23
2018-10-19	14:44:20.033	58410.6141	1.28	0.24	48
2018-10-27	12:49:21.831	58418.5343	1.28	0.25	46
2018-11-03	11:54:40.663	58425.4963	1.28	0.24	45
2018-11-10	11:26:22.594	58432.4767	1.28	0.25	45
2018-11-13	15:46:16.428	58435.6571	1.28	0.84	27
2018-11-17	11:26:45.751	58439.4769	1.28	0.25	53
2018-11-24	10:39:31.087	58446.4441	1.28	0.25	47
2018-12-02	10:05:07.518	58454.4202	1.28	0.25	58
2018-12-08	09:38:58.040	58460.4021	1.28	0.25	49
2018-12-15	14:40:33.210	58467.6115	1.28	0.25	43
2018-12-29	13:21:48.762	58481.5568	1.28	0.25	47
2019-01-05	11:51:39.084	58488.4942	1.28	0.25	37
2019-01-12	11:11:41.348	58495.4665	1.28	0.25	49
2019-01-19	08:59:00.887	58502.3743	1.28	0.25	35
2019-01-26	08:59:27.180	58509.3746	1.28	0.25	55
2019-02-01	04:45:58.660	58515.1986	1.28	0.25	59
2019-02-09	06:08:22.669	58523.2558	1.28	0.25	31
2019-03-09	01:36:38.926	58551.0671	1.28	0.25	64
2019-03-18	03:15:05.101	58560.1355	1.28	0.25	43
2019-03-25	03:14:55.280	58567.1354	1.28	0.25	44
2019-04-01	02:54:33.589	58574.1212	1.28	0.25	41
2019-04-09	02:45:26.418	58582.1149	1.28	0.25	43
2019-04-15	02:46:10.724	58588.1154	1.28	0.25	40
2019-04-20	03:17:44.923	58593.1373	1.28	0.25	38
2019-04-29	04:58:37.303	58602.2074	1.28	0.25	38
2019-05-04	23:15:28.808	58607.9691	1.28	0.25	101
2019-05-11	22:56:46.905	58614.9561	1.28	0.24	54
2019-05-18	22:41:34.045	58621.9455	1.28	0.25	66
2019-05-25	01:37:05.971	58628.0674	1.28	0.25	41
2019-08-10	18:48:48.542	58705.7839	1.28	0.25	47
2019-08-16	21:14:16.608	58711.8849	1.28	0.25	55
2019-08-23	16:13:40.923	58718.6762	1.28	0.25	51
2019-08-31	18:14:11.999	58726.7599	1.28	0.25	42
2019-09-14	17:59:59.637	58740.75	1.28	0.25	45
2019-09-21	14:55:17.686	58747.6217	1.28	0.25	44
2019-09-29	15:31:05.833	58755.6466	1.28	0.25	64
2019-10-19	15:01:58.705	58775.6264	1.28	0.25	49
2020-02-21	06:48:08.003	58900.2834	1.28	0.25	45
2020-03-02	04:18:45.875	58910.1797	1.28	0.24	47
2020-03-09	02:54:50.041	58917.1214	1.28	0.25	51

[a] Start time and Start data columns refer to the beginning on of the first scan on MAXI J1820+070.

[b] Observations length refers to the difference in time between the start of the first and end of the last scan on MAXI J1820+070. For observations of length 0.24 or 0.25 hours this was a single scan and thus the entire time was spent on source. For longer observations $\sim$ 12% of this time was spent observing an interleaved phase calibrator.

[c] RMS calculated from a region near the image phase centre.

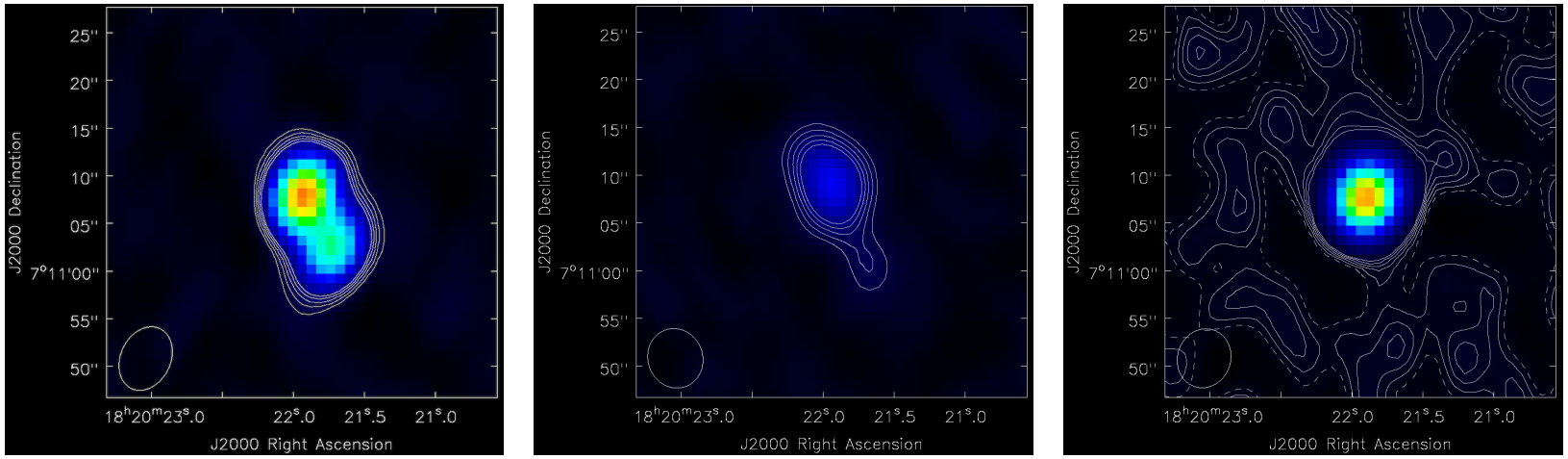

(a) Our first observation of the field of MAXI J1820+070 with MeerKAT on MJD 58389.7408, showing a core component and an extension towards the south-east.

(b) An observation of MAXI J1820+070 showing a core component and bipolar extensions to the south-east and north-west.

(c) An observation of MAXI J1820+070 showing only the core.

Figure 4.7: MeerKAT observations of the field of MAXI J1820+070. All three images show a 40 by 40 pixel cutout of the total field, centred on the phase centre (the position of MAXI J1820+070). Each pixel corresponds to 1″. The data are linearly scaled between 0.1 mJy and 1 mJy and contours occur at $n \times 0.05$ mJy for $n = -5, 5, 7, 9, 11, 13$. The synthesised beam is shown in the bottom left of each image.

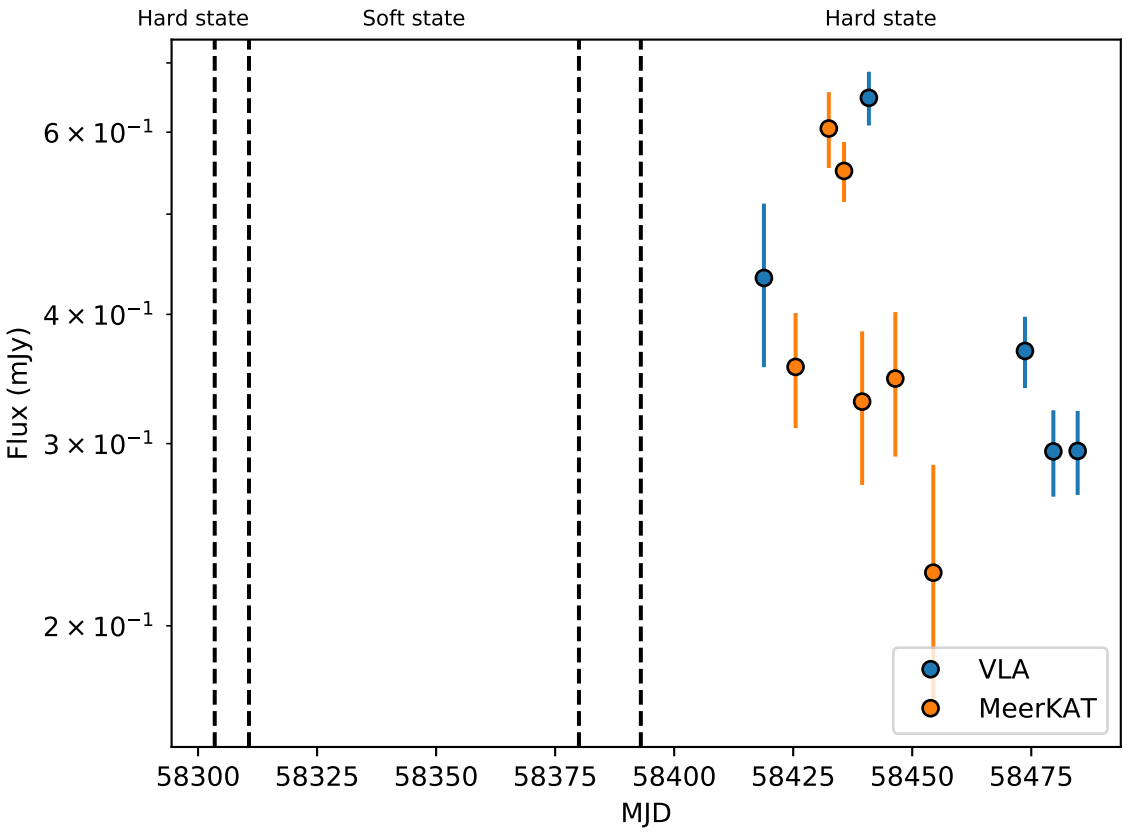

Figure 4.8: Flux monitoring of the north-westerly extension (receding ejection) launched by MAXI J1820+070. Data taken at different frequencies have been scaled by a spectral index $\alpha = -0.7$ ($F_\nu = A\nu^\alpha$; appropriate for optically thin synchrotron emission from jet ejecta) to a common frequency of 1.28 GHz. The data are measurements of the receding jet flux from images in which it is clearly spatially resolved from the core. We do not include AMI-LA as the core was bright for the entirety of the duration for which this component was visible. The accretion state of the source is labelled above the plot, based on the MAXI monitoring presented in [238]. The first and second pair of dashed vertical lines mark the start and end of the transition from the hard to soft accretion state, and then soft to hard accretion state, respectively. Error bars on data points indicate one sigma uncertainties.

Table 4.3: Summary of our VLA observations of MAXI J1820+070.

Date	Start time [UT]	Start date]MJD]	Frequency [GHz]	Obs. length [hrs.]	Array config.	RMS noise[a] [μJy beam^{-1}]
07/10/2018	00:55:22	59398.03845	5.87	0.19	D[b]	17
08/10/2018	00:05:38	58399.00391	6.00	0.06	D	19
11/10/2018	20:47:47	58402.86652	6.00	0.06	D	26
12/10/2018	22:06:17	58403.92103	6.00	0.02	D	39
14/10/2018	21:58:18	58405.91549	6.00	0.02	D	40
27/10/2018	20:24:57	58418.85066	6.00	0.05	D	23
18/11/2018	21:31:22	58440.89678	6.00	0.60	C[c]	7
21/12/2018	16:22:22	58473.68220	6.00	0.31	C	8
27/12/2018	20:24:57	58479.85966	6.00	0.31	C	9
01/01/2019	18:14:32	58484.76009	6.00	0.31	C	8

[a] RMS calculated from a region near the image phase centre.
[b] Maximum and minimum baseline length of 1.03 km and 0.035 km, respectively.
[c] Maximum and minimum baseline length of 3.4 km and 0.035 km, respectively.

J1820+070 (i.e. there was no core) but components in both the south-easterly and north-westerly directions. out VLBA image is shown in Figure 4.9 (note that it has been rotated by ~ 65 degrees to align the components horizontally. The resolution of the VLBA is $\sim 10^4$ times better than the AMI-LA.

4.4 The radio light curve morphology of MAXI J1820+070

The accretion state definitions based on MAXI observations of MAXI J1820+070 [238] agree well with the light curve morphology and spectral evolution as observed at radio frequencies as shown in Figure 4.4, where I have marked the evolving accretion state of the system. Between $\sim$ MJD 58200 and $\sim$ MJD 58300, MAXI J1820+070 had, after the initial rise, a relatively stable flux density which the AMI-LA in band spectral index and near simultaneous eMERLIN observations (MJD 58201.26 and MJD 58201.27, respectively) identified as being flat spectrum in nature ($\alpha \sim 0.15$) and thus consistent with the source being in the hard state (and therefore producing a compact core radio jet). This was followed by a change in accretion state [239, 238] at $\sim$ MJD 58300 where we observe the flux from the core jet drop by a factor of $\sim 10^3$ as seen by the AMI-LA. The source was then in the soft accretion state between $\sim$ MJD 58310.7 and $\sim$ MJD 58380.0 which we associate with a low level (~ 1 mJy) and slowly fading radio source as observed with the AMI-LA. Due to the relatively poor angular resolution of the AMI-LA the origin of this low level emission is not, when just considering the AMI-LA data, clear, as the source is too faint to obtain a reliable in-band spectral index. This inhibits us from distinguishing between a compact core jet (flat or slightly inverted spectrum) and transient ejecta(ions), which have an optically thin radio spectrum. It is not unprecedented for there to be radio emission in the soft accretion state, but it is usually transient (lasting nowhere near the ~ 100 days seen here, see e.g. [240, 241, 242, 243, 244]). I will discuss the origin of this emission, as well as the few other sources showing such prolonged emission, in a later section of this chapter, but it is natural to assume that the AMI-LA is observing emission from the bipolar extensions seen with the higher angular resolution radio interferometers.

Around MJD 58380.0 the flux from MAXI J1820+070, as observed by the AMI-LA, began increasing and rose by over an order of magnitude in the span of around 2 weeks. This shows the core jet turned back on while the source transitioned back to the hard accretion state (confirmed by the $\sim$ flat spectral index seen in Figure 4.4 between 1.28 and 15.5 GHz) [245, 246, 247]. MAXI J1820+070 then faded until $\sim$ MJD 58500 at which point it had re-entered quiescence (with a luminosity below $\sim 10^{31}$ erg s^{-1} at 15.5 GHz and $\sim 10^{30}$ erg s^{-1}

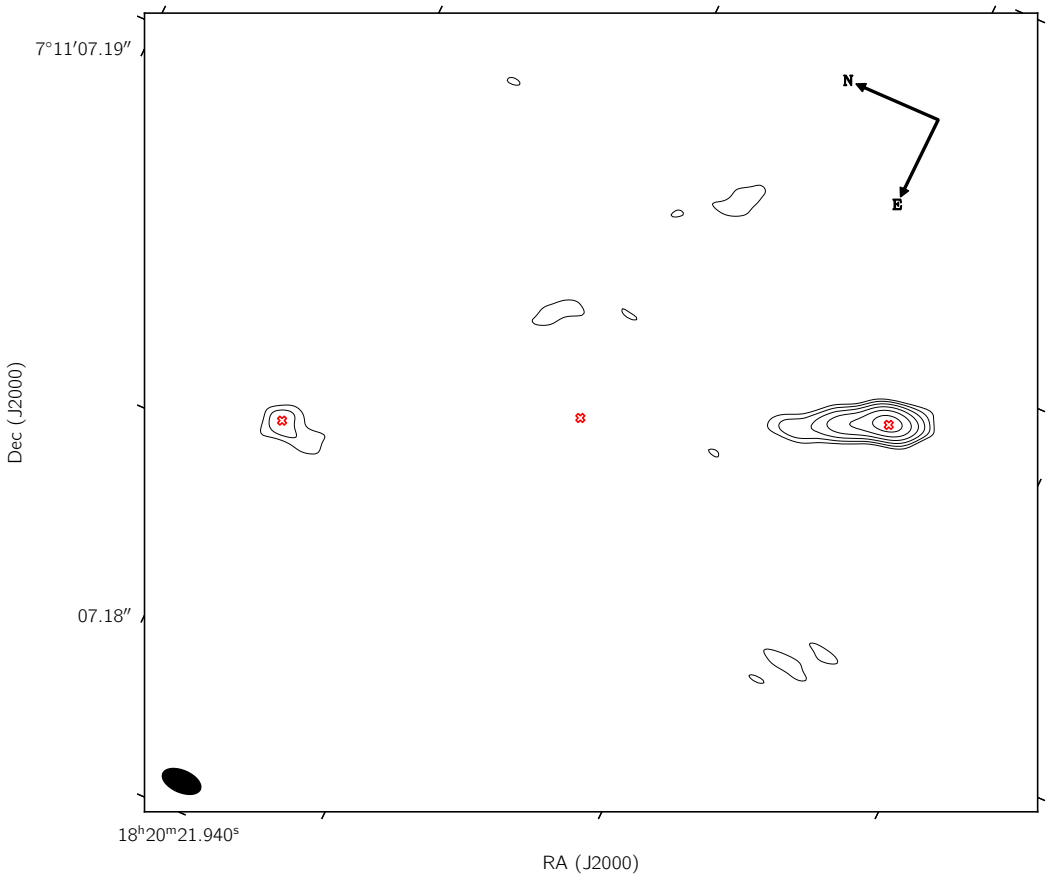

Figure 4.9: A VLBA observation of MAXI J1820+070. Contours mark 140 μJy$\times(\sqrt{2})^n$ for $n = 3,4,5,6,7,8,9$. We mark the position of the core (central red cross; inferred from previous hard state observations with the VLBA; James Miller-Jones, private communication) and the measured positions of the approaching (red cross to the right of the core) and receding (red cross to the left of the core) jet from the image. These are given in Table 4.4. The black ellipse in the bottom left corner shows the synthesised beam with a major and minor axis of 0.0009″ and 0.0005″, respectively.

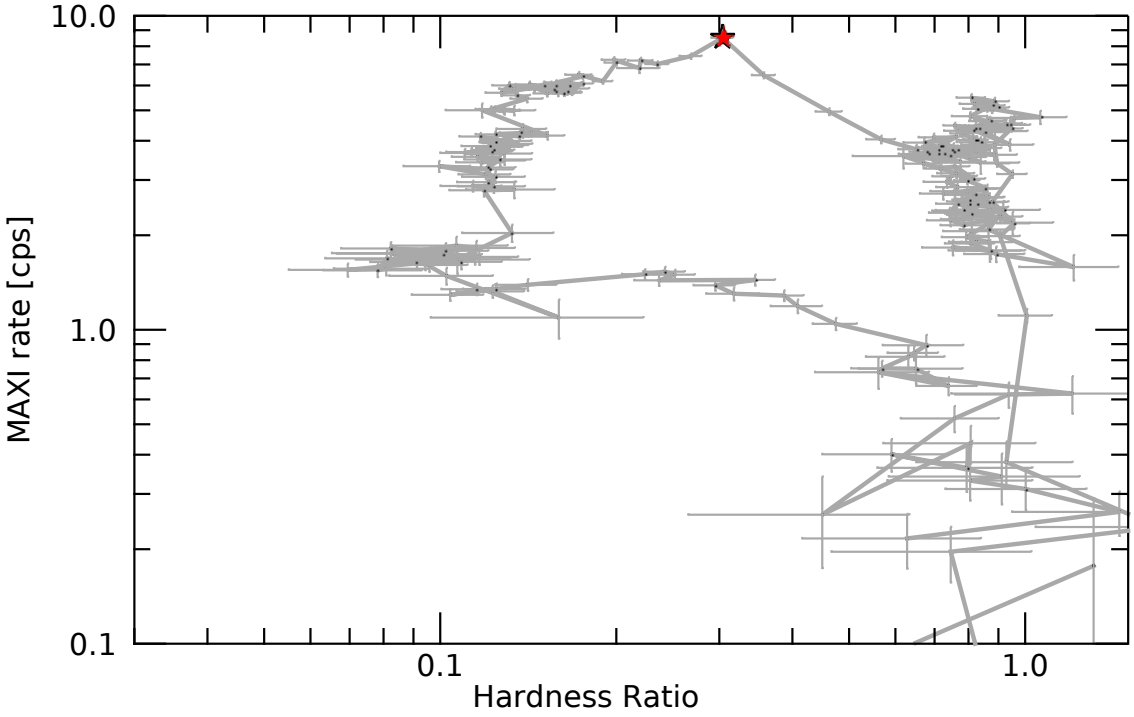

Figure 4.10: The hardness intensity diagram for MAXI J1820+070 created with data from MAXI from between MJD 58009.25 and MJD 58407.25. The hardness ratio is measured as the ratio of the counts in the 4-10 keV and 2-4 keV energy bands. MAXI J1820+070 evolved through the diagram starting from the bottom right and moving anti-clockwise. The red star marks the closest observation to the radio flare observed during the hard to soft state transition, which I show is associated with the launch of bipolar discrete ejections.

at 1.28 GHz) and completed an outburst cycle (a complete traversal of a Q-diagram as shown schematically in Figure 4.2, and for MAXI J1820+070 in Figure 4.10). Over the following two years MAXI J1820+070 underwent three re-brightening episodes both having similar peak amplitudes ($\sim$ 10 mJy at 15.5 GHz) and duration. These re-brightening episodes do not represent complete outbursts as the source remained in the hard accretion state (with a compact approximately flat spectrum core jet throughout), not transitioning to the soft state at any point.

There is a striking similarity between the shapes of the final hard state decay in the complete outburst and the first two re-brightening events (see Figure 4.12 for a comparison). As well as their similar amplitude and width, they undergo a change in decay slope after a similar time, and have statistically similar power law decay indices pre- and post-break. This behaviour is also mirrored in the final hard state decay of the complete outburst.

4.5 The radio – X-ray connection in MAXI J1820+070

4.5.1 Radio – X-ray correlation

In Figure 4.11 I present the radio–X-ray correlation for MAXI J1820+070, which includes radio data from the AMI-LA and X-ray data from *Swift*-XRT from the complete outburst cycle (i.e. between MJD 58192.2890 and MJD 58440.5170, not including the re-brightening events). MAXI J1820+070 is one of the few sources that lies on the standard track in the correlation, similar to the archetypal source GX 339−4, and we probe the correlation over 2 orders of magnitude in radio luminosity and 4 orders of magnitude in X-ray luminosity.

To quantify the relationship between X-ray and radio emission throughout the outburst, I fit the correlation using the ODR (orthogonal distance regression) module in SCIPY, which accounts for errors on both the independent and dependent variable. During the initial hard-state, MAXI J1820+070 moved along the radio-loud track following a power law of the form $L_R = AL_X^{\alpha}$, with $\alpha = 0.42 \pm 0.05$. The correlation showed the same slope throughout the long initial hard state, all the way up to X-ray and radio luminosities of $\sim 4 \times 10^{37}$ erg s^{-1} and $\sim 6 \times 10^{30}$ erg s^{-1}, respectively. During the intermediate state MAXI J1820+070 left the radio loud track, with its radio emission dropping rapidly. The source was then detected continually throughout the soft state (although we determine this does not represent a connection between accretion and core jet emission, as the AMI-LA was detecting the bipolar extensions and not the core). We then track the core-jet turning back on as MAXI J1820+070 returns to the radio loud correlation, following a track with $L_R = AL_X^{-1.3\pm0.4}$, and joining at a similar location to our first quasi-simultaneous radio/X-ray detection. Similar behaviour has been seen in GX 339−4 [217]. The radio–X-ray correlation during the end-of-outburst hard state shows $\alpha = 0.35 \pm 0.05$, consistent with (but slightly shallower than) that on the initial hard state. A joint fit of the initial and final hard state radio–X-ray correlation returns a slope of $\alpha = 0.58 \pm 0.03$, which is consistent with the value of 0.6 seen for other BHXRB systems on the standard (radio loud) track [217].

4.5.2 Re-brightening events

In addition to completing an outburst cycle (a complete traversal of the hardness intensity diagram), MAXI J1820+070 has since undergone three re-brightening events. These are shown in Figure 4.4 between MJD 58500 and MJD 59000 and the first two re-brightening events individually in Figure 4.12. We initiated *Swift* observations to complement our radio

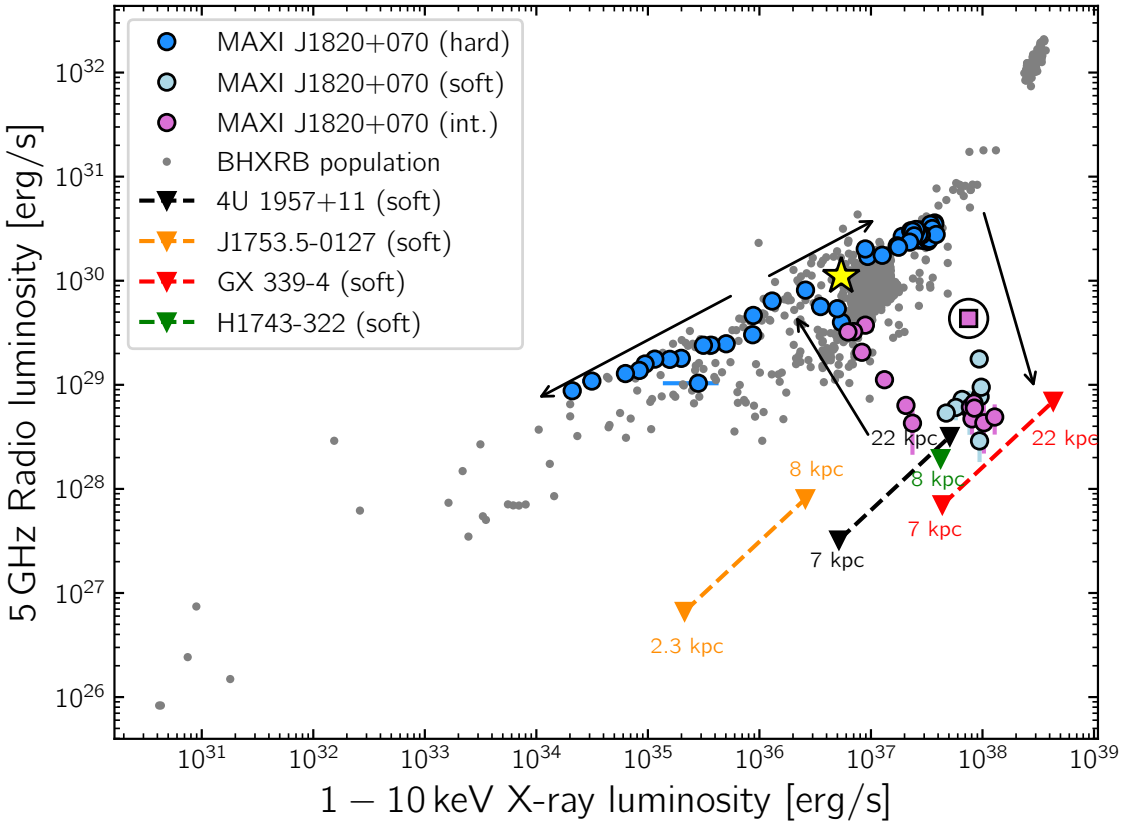

Figure 4.11: Radio luminosity as a function of X-ray luminosity for J1820+070, based on our monitoring at 15.5 GHz with the AMI-LA radio Telescope (scaled to 5 GHz assuming a flat spectrum) and X-ray observations from the *Swift* X-ray telescope. The data for J1820+070 in the hard state, soft state and intermediate state are shown by dark blue circles, light blue diamonds and purple squares, respectively. For the majority of data points the error bars are too small to be seen. The yellow star marks our first simultaneous radio/X-ray observation of J1820+070 (3.2 d after our first radio observation) and the black arrows show schematically the time evolution of the outburst. We only use X-ray observations within 8 h of our radio observations, with the exception of the purple square circumscribed with a circle. In this case the observations were taken $\sim$ 14 h apart. Error bars on data points indicate one sigma uncertainties. Data from the literature on other black hole systems are indicated by grey dots [216]. We mark upper limits for core soft state emission from the XRB systems 4U 1957+11, J1753.5−0127, GX 339−4 and H1743−322 [248, 214, 249, 250] for a range of possible distances. We do not include radio observations taken during the state transition flare. I use a distance of 2.96 kpc when calculating the luminosities [101].

observations throughout these rebrightenings, and the radio – X-ray correlation for two of the three rebrightenings is shown in Figure 4.13. I will refer to the three re-brightening events as R1, R2, and R3 from now on. Jointly fitting the data from R1 and R2 we find a correlation such that $L_R \propto L_X^{0.35\pm0.02}$. While fitting the entirety of the complete outburst cycle yielded a correlation index consistent with the canonical value of ~ 0.6, fitting the first and second hard state (of the complete outburst) individually, as well as jointly fitting R1 and R2 all provide correlation significantly shallower than ~ 0.6. The spectral index during the rebrightening events was mildly inverted, indicating that the source remained in the hard spectral state and the radio emission was likely from a core jet. Despite the changes in decay rate observed during the rebrightenings events (and at the end of the second hard state) we see no indication of a changing index on the radio - X-ray correlation.

4.6 Discrete ejections from MAXI J1820+070

Figure 4.5 shows a high time resolution light curve of MAXI J1820+070 at 15.5 GHz as it transitioned from the hard to the soft accretion state. Superposed on the decaying flux from the core jet (which is seen to switch off during this transition), there is a significant radio flaring event. Such flares are thought to indicate the launch of discrete ejections from the black hole, which move away from the core to greater distances and with larger Lorentz factors than the core jet. In most cases such flares are transient and sources are not detected for the majority of the time they spend in the soft accretion state. Our monitoring the with AMI-LA demonstrates that this was not the case for MAXI J1820+070, as it was detected at a low ($\sim$ 1 mJy, but slowly decaying) level for the entirety of the time it spend in the soft state. With the AMI-LA monitoring alone this may have been interpreted as the first detection of a compact core jet in the soft state. Our VLBA observation of the source less than a day after the flare occurred, however, reveals that the core has switched off (to a 3σ limit of 420 μJy beam^{-1}) and that there are two sources, along the same axis, either side of the black hole position. This strongly suggests that transient ejections were launched in association with the state transition radio flare. This interpretation is supported by our observations with eMERLIN, MeerKAT and the VLA, which all show either one or both of the ejections as extended components in addition to the core, in a subset of the images made with these observations, and both components are seen to move away from the black hole. We therefore attribute the soft state emission seen by the AMI-LA to these extended components, which the interferometer does not resolve, a scenario which is further supported by Figure 4.6 which shows that, when scaling to a common frequency, the AMI-LA data tracks remarkably well with the measurements of the south-easterly extended component's

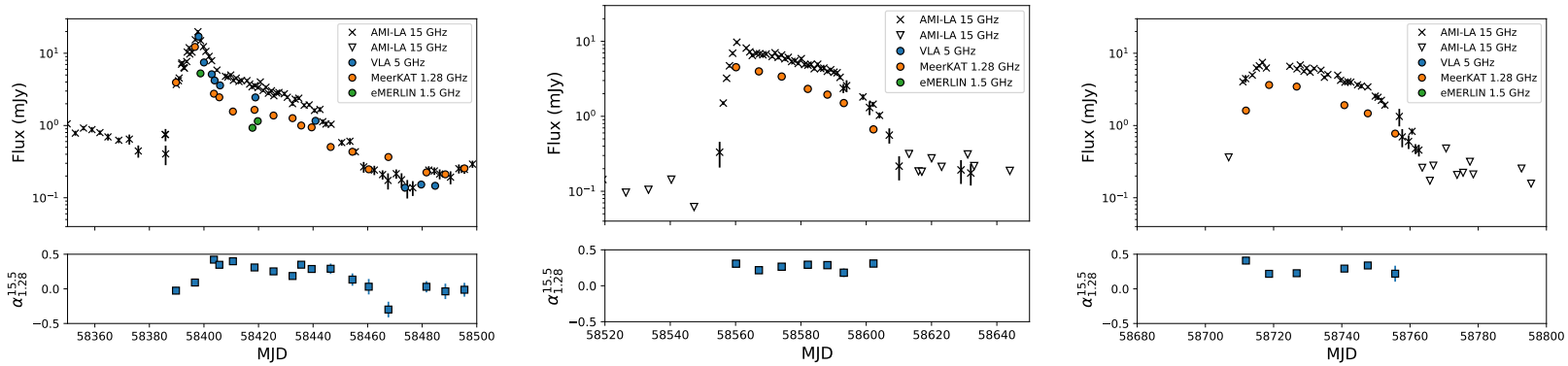

(a) Radio flux and 1.28 to 15.5 GHz spectral index evolution of the final hard state of the complete outburst cycle.

(b) Radio flux and 1.28 to 15.5 GHz spectral index evolution of the first rebrightening event, R1.

(c) Radio flux and 1.28 to 15.5 GHz spectral index evolution of the second rebrightening event, R2.

Figure 4.12: Comparison of the radio re-brightening events from MAXI J1820+070, including the return to the hard state and subsequent decay at the end of the complete outburst. The bottom panel in each case indicates the spectral index where only observations within with the two arrays that occurred within two days of one another were used.

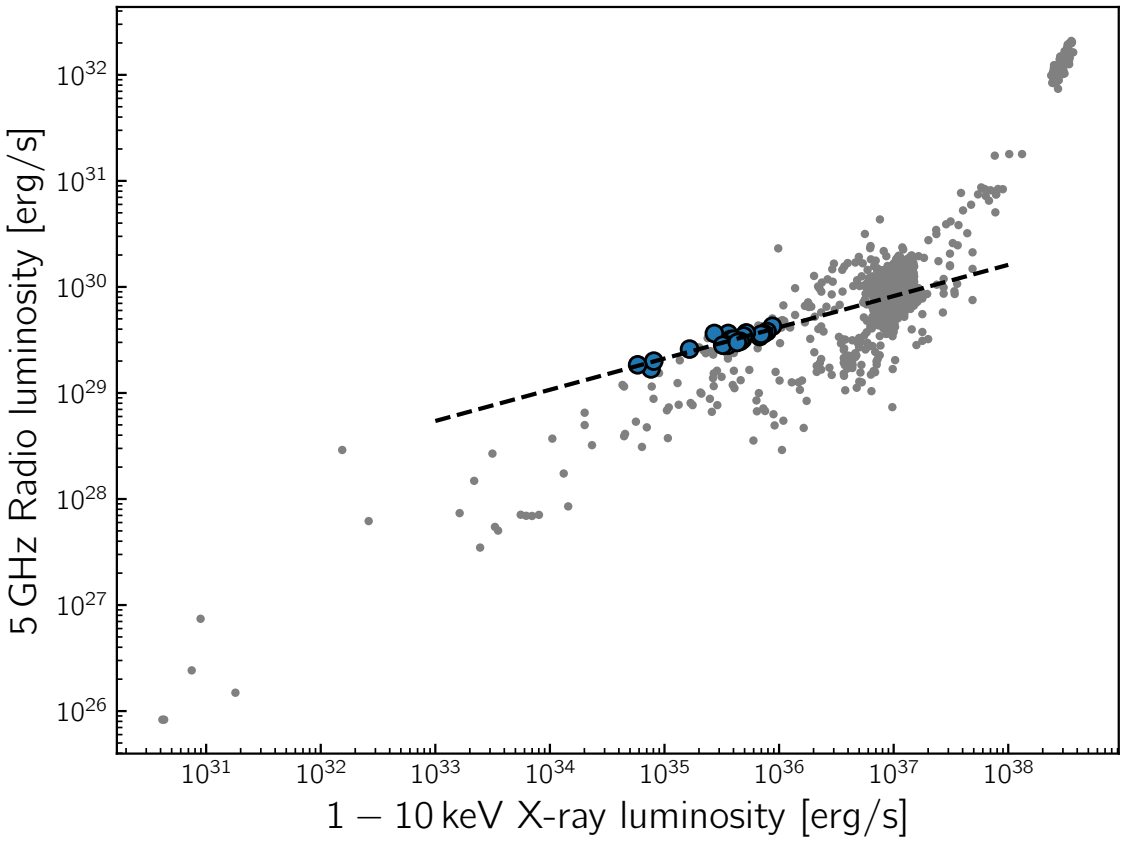

Figure 4.13: Radio luminosity as a function of X-ray luminosity for MAXI J1820+070, based on our monitoring at 15.5 GHz with the AMI-LA radio Telescope (scaled to 5 GHz assuming a flat spectrum) and X-ray observations from the *Swift* X-ray telescope. The correlation includes data from R1 and R2 where observations occurred separated by less than 1.2 d. Error bars on data points indicate one sigma uncertainties, for the majority of data points the error bars are too small to be seen. Data from the literature on other black hole systems are indicated by grey dots [216]. I use a distance of 2.96 kpc when calculating the luminosities [101].

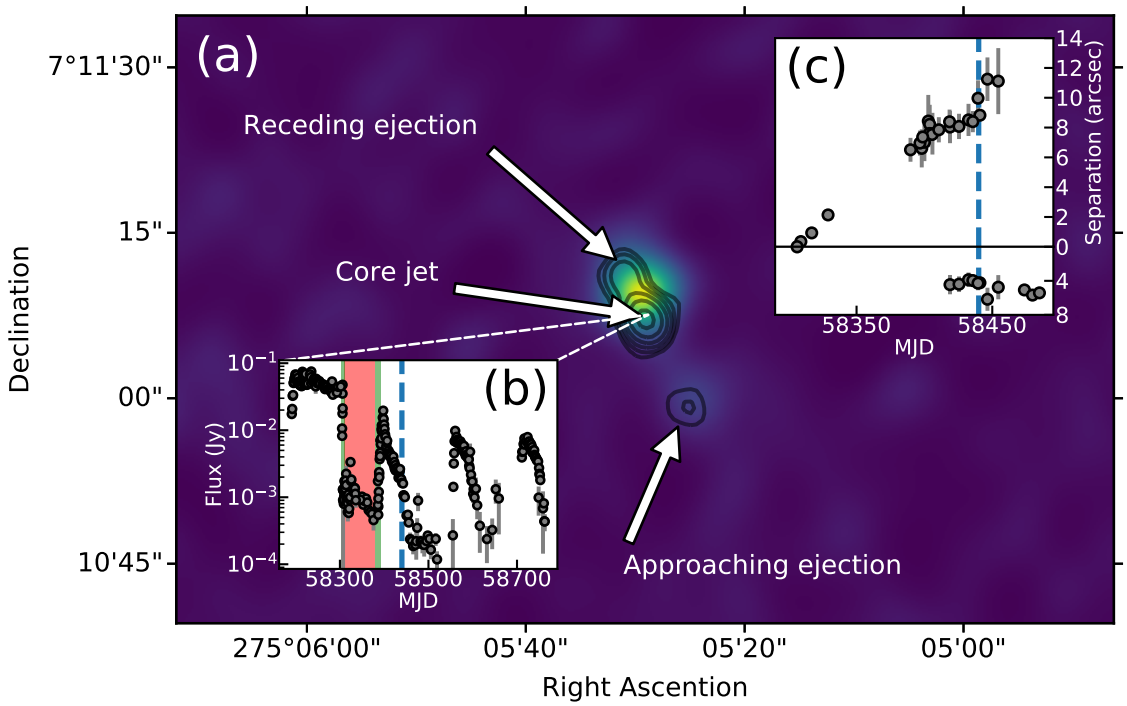

Figure 4.14: (a) A Pixel scale MeerKAT L band image of the field of BHXRB MAXI J1820+070, with a C band VLA image overlaid in contours (taken one day later). The image is scaled linearly between −0.2 and 0.9 mJy, and the contours are $7\,\mu\text{Jy} \times \sqrt{2}^n$ for $n = 2, 4, 6, 8$. The image shows three main components. The compact core (labelled), and approaching (bottom right) and receding (top left) ejections. (b) The 15.5 GHz radio flux density of the core, demonstrating periods in the *hard* (core jet dominating; not shaded), *soft* (core jet quenched, flux from fading ejections; shaded red) and *intermediate* (core jet switching on/off; shaded green) states, demonstrating the power of radio observations in tracking the connection between accretion and outflows. The vertical dashed blue line marks the epoch that the images in panel (a) were taken. (c) The angular separation of the approaching (top panel) and receding (bottom panel) ejections with time. These observations, demonstrating superluminal motion, allowed me to constrain geometric properties of the source. The vertical dashed blue line marks the epoch that the images in panel (a) were taken.

flux. Figure 4.14 demonstrates a compilation of our observations of MAXI J1820+070, detailing the radio morphology of the system, the flux evolution of the core, and the position evolution of the extended components.

Constraining the evolution of these bipolar ejections (both their positions and their flux) is useful for a number of reasons. Their proper motions provide constraints on the source geometry, including distance and jet angle, as well as the structure of the circumbinary material and the energy content of the discrete ejecta.

4.6.1 Source geometry

Figures 4.15 and 4.16 show a subset of our MeerKAT, VLA, and eMERLIN observations in such a way as to demonstrate the evolution of the positions of both of the bipolar extensions. With eMERLIN we never detect the north-westerly extension, but it is clearly seen with MeerKAT and the VLA (as well as with the VLBA). To calculate the proper motion we consider two models for the motion of the ejecta. In both models we assume the ejecta were launched at the same instant, and are travelling with the same physical velocity. It is clear from the images that the south-easterly component (or the right hand component in the rotated images) appears to move away from the black hole position more rapidly than its counter ejection. This is due to one of the ejections being launched towards our observing location, and the other away from it, resulting in relativistic Doppler abberation as well as a light travel time delay. Additionally, this will cause the approaching ejection's flux to appear to evolve more rapidly than its anti-parallel counterpart. We will therefore refer to the south-easterly and north-westerly components as the approaching and receding ejections, respectively, from now on. Our first model is that of constant proper motion, given in Equation (4.2).

$$s_{\rm app} = (t - t_{\rm launch})\mu_{\rm app} \tag{4.2a}$$

$$s_{\rm rec} = (t - t_{\rm launch})\mu_{\rm rec} \tag{4.2b}$$

Subscripts app and rec refer to quantities related to the approaching and receding ejections, respectively, s is the angular separation in arcseconds, and $t - t_{\rm launch}$ is the time since the ejection occurred and μ is the proper motion, which we discuss in units of milli-arcseconds per day. In this case the time of launch and the proper motions are free parameters in our model. We also test a description of the motion with a constant deceleration, as shown in Equation (4.3).

$$s_{\rm app} = (t - t_{\rm launch})\mu_{\rm app,0} + \frac{1}{2}(t - t_{\rm launch})^2\dot{\mu}_{\rm app} \tag{4.3a}$$

$$s_{\rm rec} = (t - t_{\rm launch})\mu_{\rm rec,0} + \frac{1}{2}(t - t_{\rm launch})^2\dot{\mu}_{\rm rec} \tag{4.3b}$$

Where here μ_0 indicates the initial velocity and $\dot{\mu}$ indicates the deceleration, which we discuss in units of milli-arcseconds per day per day and consider as an additional free parameter. In both models the launch time is a free parameter, but is prescribed as being the same for both the approaching and receding ejections. The linear and decelerated motion

fits are shown in Figure 4.17 as solid and dashed black lines, respectively, whereas the marginalised posterior distributions for the two models, which we fit using EMCEE [251], are shown in Figures 4.18 and 4.19. For the constant motion fits we find proper motions of 77 ± 1 mas d^{-1} and 33 ± 1 mas d^{-1} for the approaching and receding ejections, respectively, with a launch date of $t_{\rm launch}$ = MJD 58305.89 $\pm$ 0.02. For decelerated motion we find initial velocities for the approaching and receding discrete ejections to be $\mu_{\rm app,0} = 101 \pm 3$ mas d^{-1} and $\mu_{\rm rec,0} = 58 \pm 6$ mas d^{-1}, respectively. The acceleration was $\dot{\mu}_{\rm app} = -0.49 \pm 0.06$ mas d^{-2} and $\dot{\mu}_{\rm app} = -0.33 \pm 0.07$ mas d^{-2}. The predicted launch times for the linear and decelerating models are MJD 58305.89 $\pm$ 0.02 and MJD 58306.03 $\pm$ 0.02, respectively. To put this in context of the state transition we fit the flare profile and the decaying core flux with exponential functions (as shown in Figure 4.5). We define the start of the flare (t_0) to be the intercept between the decaying core jet flux and the rising flux from the flare. Due to the mechanism causing the launch of discrete ejections being unknown it is not clear if this is the best way to define the flare start. It could be that the head of the compact jet is accelerated away from the black hole during the quenching, in which case this may be a valid definition for the start of the flare. We will discuss the flare launch time in the context of the changing properties of the accretion flow in a later section. In relation to the state transition radio flare beginning we find the launch times to be $\Delta t = 0.21 \pm 0.02$ and $\Delta t = 0.35 \pm 0.02$, respectively.

A critical part of our analysis relies on measuring the positions of the core and ejections from MAXI J1820+070 with a range of telescopes. For our observations with eMERLIN, MeerKAT, and the VLA in C configuration, we fit the sources in the image plane using the CASA task IMFIT. For MeerKAT observations we attempt to fit three point source (fixed beam major and minor axes and position angle) components, allowing the position and amplitude to vary. For MeerKAT observations where a three component fit would not converge (early time observations when the receding jet had a small angular separation), we fit two components instead. We do not fix the core position in our MeerKAT analysis to the known position from our eMERLIN observations, so any systematic position errors will affect all components and cancel when calculating the separation. We used the same procedure for the VLA C configuration data. For eMERLIN observations the components are separated significantly and as such can be boxed and fit individually using IMFIT. When fitting the ejection components we do not fix the dimensions of the elliptical Gaussian used by IMFIT, as the ejection components are not point-like. We do fix the size of the component used to fit the (known to be compact) core. As core emission was not detected in all eMERLIN observations (due to core quenching in the soft

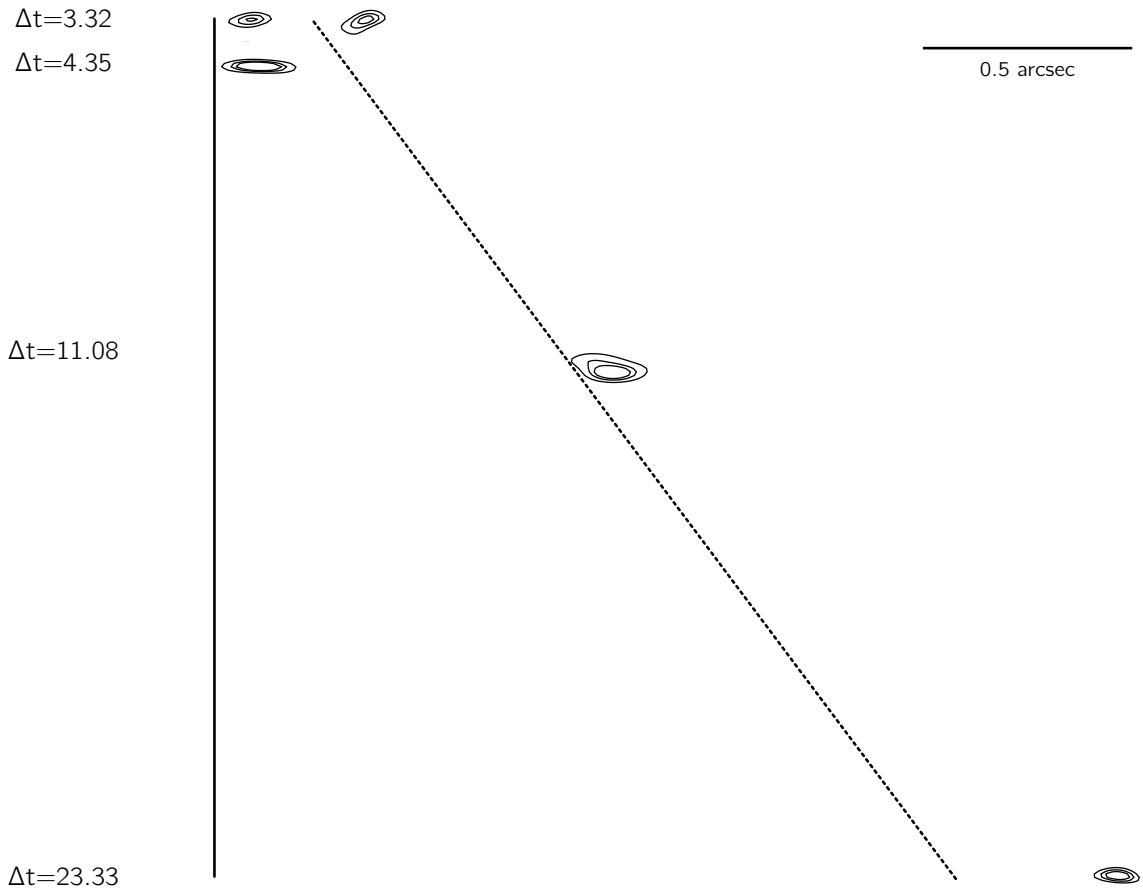

Figure 4.15: eMERLIN observations of J1820 show a jet component distinct from the black hole position. The beam sizes, chronologically, are 99.2 mas × 30.3 mas, 127.5 mas × 27.5 mas, 106.6 mas × 32.2 mas and 130.5 mas × 26.8 mas, respectively. All images have been rotated ∼ 65° anticlockwise. Contours mark (105, 150, 60, 125) μJy beam^{-1}× log(n) for $n = 4, 5, 6$, where the pre-factor corresponds to the images chronologically. The black vertical solid line marks the position of the core, determined from a hard state observation made with eMERLIN (not shown). The black dashed line shows the best fit ballistic trajectory of the (approaching) ejection, with the fit constrained by all observations presented in Table 4.4. Δt is the time, in days, since the start of a radio flare that occurred during the hard to soft state transition (Δt = 0 at MJD 58305.68), and is shown to the left of each observation. All observations have the same angular scale, and a scale bar is shown in the top right of the figure. Details on the data reduction procedure are presented in the Methods section, and flux densities are presented in Table 4.5.

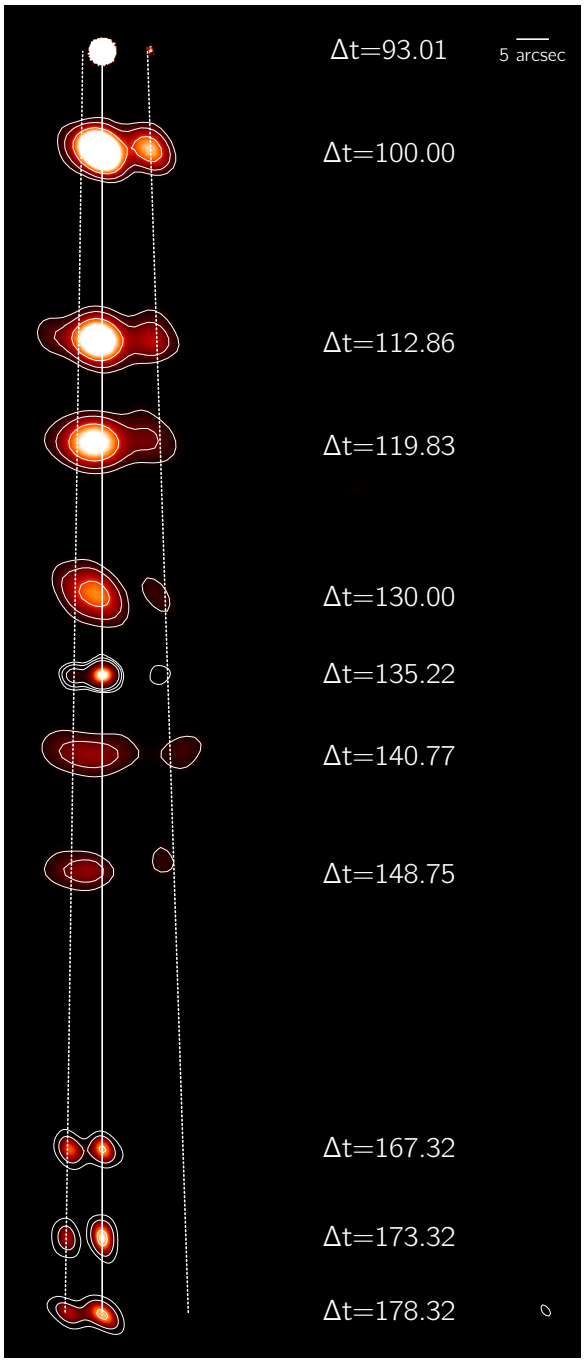

Figure 4.16: A subset of images of J1820 from eMERLIN (Δt = 93.01) MeerKAT (Δt = 100.00, 112.86, 119.83, 130.00 and 140.77, 148.75) and the VLA (Δt = 135.22, 167.32, 173.32 and 178.32) where we resolve at least one ejecta from the core. All images have been rotated $\sim 65^\circ$ anticlockwise. Δt is the time, in days, since the start of the radio flare that occurred during the hard to soft state transition (Δt = 0 at MJD 58305.68), and is shown to the right of each observation. All observations are shown with the same angular scale, and a scale bar is shown in the top right of the figure. For the MeerKAT observations, contours show $40\,\mu\mathrm{Jy\,beam^{-1}} \times (\sqrt{2})^n$ for $n = 4, 6, 8$ and the colour-scale is linear between $0.1\,\mathrm{mJy\,beam^{-1}}$ and $1\,\mathrm{mJy\,beam^{-1}}$. For the VLA observations, contours show $8\,\mu\mathrm{Jy\,beam^{-1}} \times (\sqrt{2})^n$ for $n = 4, 6, 8$, and the colour-scale is linear between $0.05\,\mathrm{mJy\,beam^{-1}}$ and $0.15\,\mathrm{mJy\,beam^{-1}}$ for all but the first observation, which shares the same scale as the MeerKAT data. The colour-scale for the eMERLIN observation is linear between $0.2\,\mathrm{mJy\,beam^{-1}}$ and $0.3\,\mathrm{mJy\,beam^{-1}}$. The white vertical solid line marks the position of the core, determined from hard state observations made with eMERLIN. The right and left dashed lines show the best fit ballistic trajectory of approaching and receding ejection components, respectively. These fits are constrained by the observations presented in Table 4.4. Details on the data reduction procedure are presented in the Methods section.

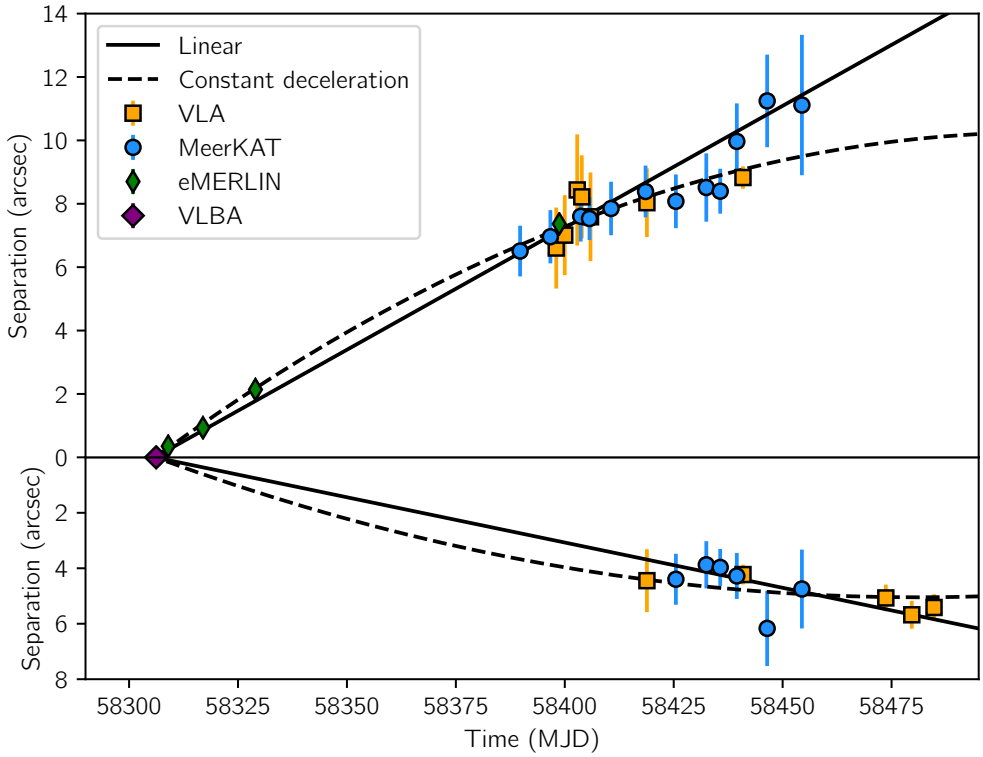

Figure 4.17: The angular separation of the approaching (top panel) and receding (bottom panel) ejections from J1820 with time. We jointly fit both the approaching and receding jet motion with two models. Firstly we assume that both components propagate with ballistic motion and were launched simultaneously. For this case we find $\mu_{\rm app} = 77 \pm 1$ mas d^{-1}, $\mu_{\rm rec} = 33 \pm 1$ mas d^{-1} and $t_{\rm launch} = 58305.89 \pm 0.02$ (Δt = 0.21 ± 0.02) (quantities correspond to the approaching jet velocity, the receding jet velocity and the launch time, respectively). The best fit for this model are shown by the solid black lines in the top and bottom panel. Assuming now as above, but allowing for the proper motion of each component to undergo constant deceleration, we find $\mu_{\rm app,0} = 101 \pm 3$ mas d^{-1}, $\mu_{\rm rec,0} = 58 \pm 6$ mas d^{-1}, $t_{\rm launch} = 58306.03 \pm 0.02$ (Δt = 0.35 ± 0.02), $\dot{\mu}_{\rm app} = -0.49 \pm 0.06$ mas d^{-2} and $\dot{\mu}_{\rm rec} = -0.33 \pm 0.07$ mas d^{-2} (quantities correspond to the initial approaching jet velocity, the initial receding jet velocity, the launch time, the deceleration of the approaching jet and the deceleration of the receding jet, respectively). Error bars on data points indicate one sigma uncertainties.

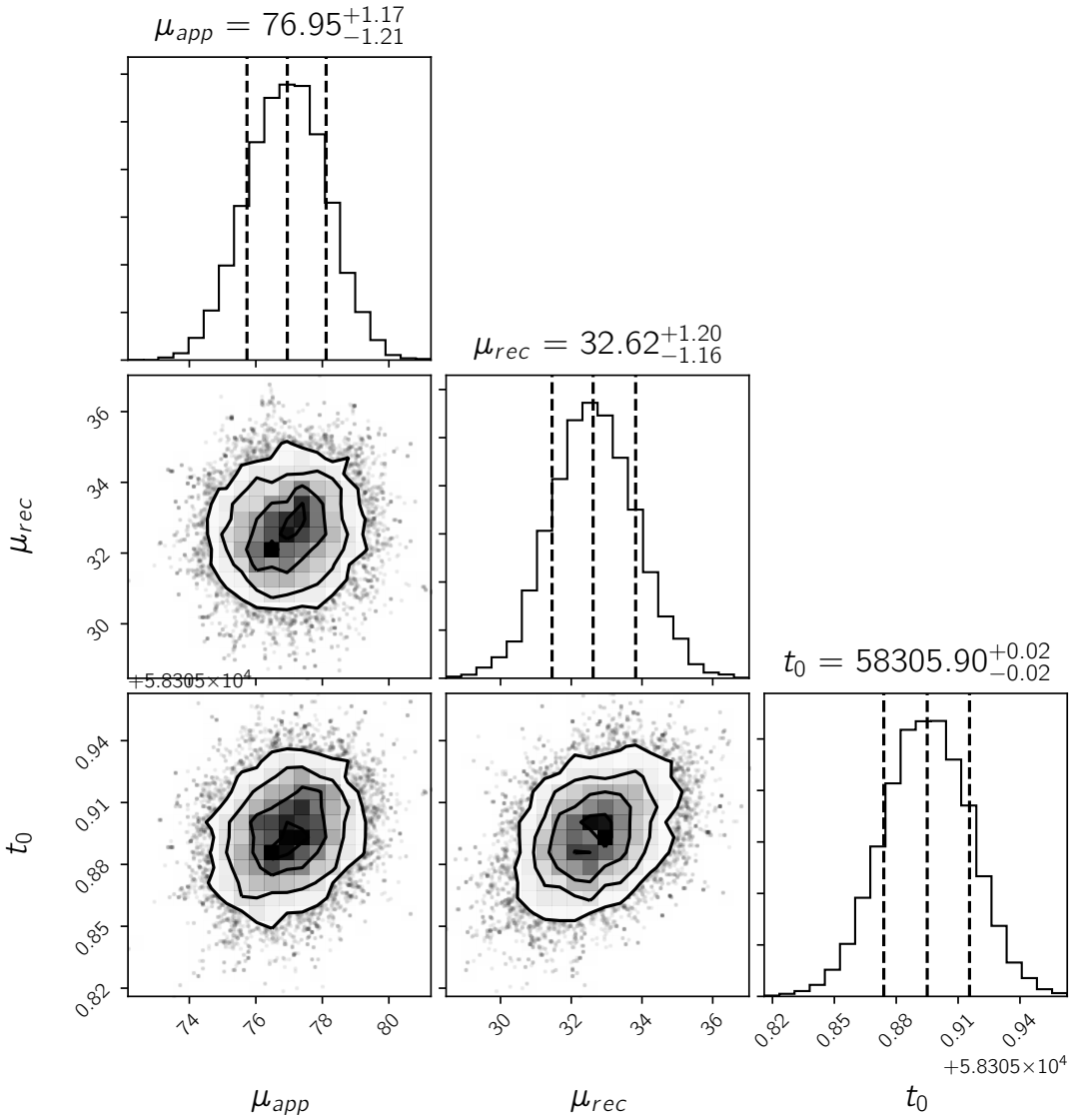

Figure 4.18: Posterior distributions for a constant velocity model to the positions of the approaching and receding data. The data were fit under the assumption that they were launched at the same moment. Histograms show the marginalised distribution of the parameters, whereas the contour plots show the correlation between parameters. The best fit values are labelled above the histogram of each parameter.

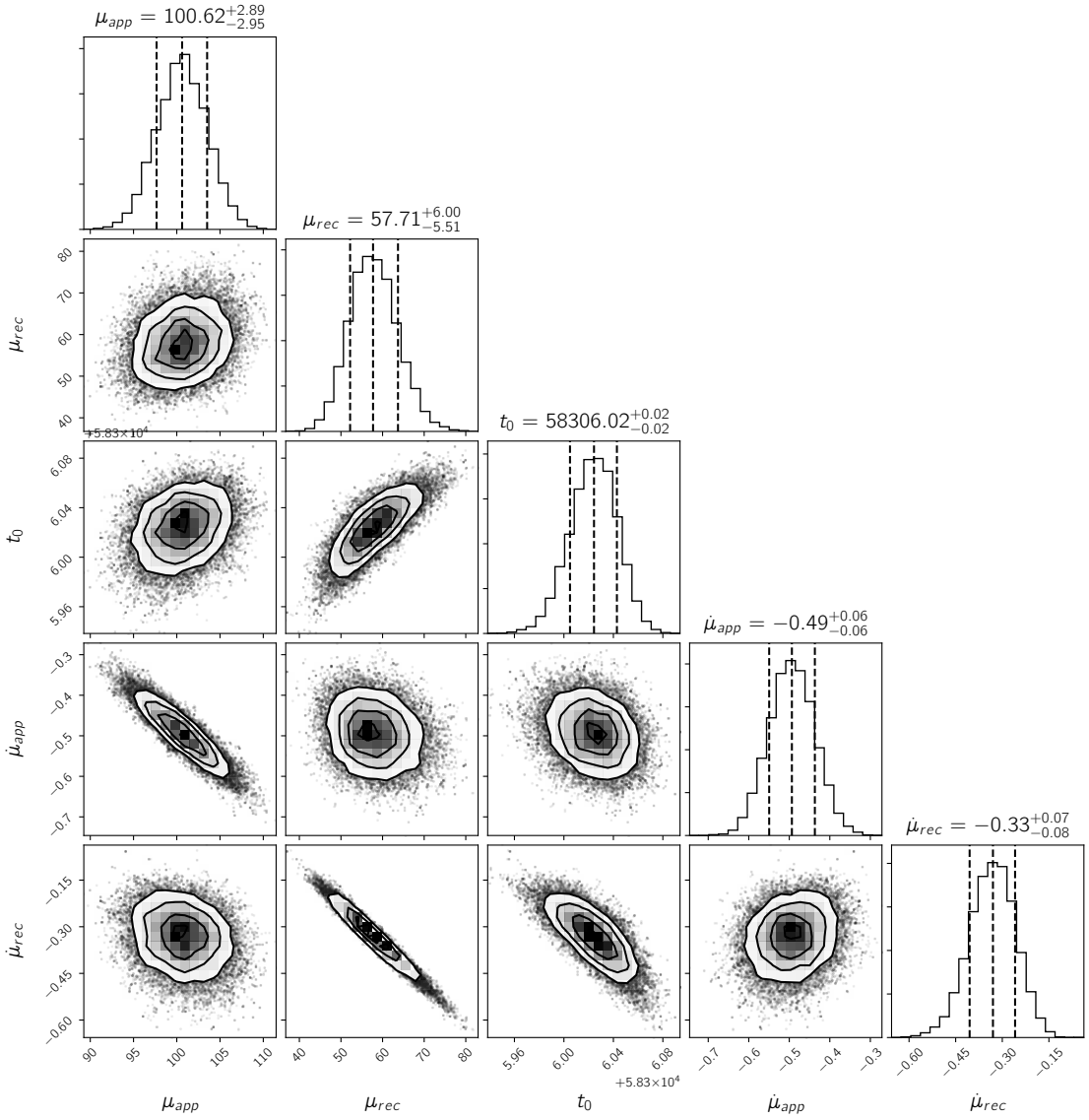

Figure 4.19: Posterior distributions for a constant velocity model to the positions of the approaching and receding data. The data were fit under the assumption that they were launched at the same moment. Histograms show the marginalised distribution of the parameters, whereas the contour plots show the correlation between parameters. The best fit values are labelled above the histogram of each parameter.

state) we use the position measured from a bright observation on MJD 58201 to calculate the separation. We did not use the position errors reported by IMFIT for analysis, as we found these tended (especially for bright components) to be many times smaller than the synthesised beam. While the centroid of an elliptical Gaussian is known to an accuracy determined by the ratio of the synthesised beam dimensions to the signal to noise ratio of the Gaussian, this is only true to a certain accuracy level before absolute astrometric uncertainties begin to dominate. For example, it is recommended by NRAO for the VLA (https://science.nrao.edu/facilities/vla/docs/manuals/oss/performance/positional-accuracy) that, unless special calibration steps are taken, positions are not reported to an accuracy of more than about 10% of the synthesised beam width. For all of our observations we report position errors as A/σ, where A is the amplitude of the fit component and σ is the width of the synthesised beam at an angle connecting the fitted component with its corresponding ejection/core component, but never to an accuracy greater than 10% of this width (we confirm using check sources in the MeerKAT field that the position errors calculated as such are sensible). There are two exceptions to this. When, in our eMERLIN observations, only the core was detected we simply report the IMFIT RA and Dec. errors, combined in quadrature. For eMERLIN observations when only an ejection component was detected we use the observation taken on MJD 58201 for the purpose of finding the angle at which to calculate σ. For VLA observations taken when the array was in the more compact D configuration the resolution was not good enough to fit sources in the image plane (images created through Fourier inversion depend on e.g. the weighting scheme and the convolution technique used). For these observation we performed fitting in the UV plane (fitting the calibrated data directly) using the CASA task UVMULTIFIT [252], after building a sky model and subtracting background sources using the CASA task UVSUB. This has the advantage of making it easier to model simple structures (in this case two point sources) without corruption from the imaging process. When fitting UV plane components we fix the spectral index of the ejecta to be –0.7, but allow the core spectral index to vary as a free parameter. Components were all specified to be point sources. The results of the positions and flux densities measured from this analysis are presented in Table 4.4 and Table 4.5, respectively. The position errors from our VLBA observation are described in a separate Methods sub-section. We do not correct the eMERLIN observations for the proper motion of the core as the change in separation caused by this motion ($\lesssim 3$ mas) is $\lesssim 1\%$ of the separation for all epochs, and is significantly less than the eMERLIN separation errors which are ≥ 15 mas. The proper motion fits are demonstrated graphically in Figures 4.15 and 4.16.

We opt to exclude measurements made from two of our eMERLIN epochs. These are marked in Table 4.4, and correspond to the smallest angular separation component in the first and second observations demonstrated in Figure 4.15. Between these two observations this component moves with a proper motion of $\sim 30\,\mathrm{mas\,d^{-1}}$, and was therefore launched around the same time as the faster approaching ejecta. It is evident, however, that this component is not well described alongside the rest of our measurements for either a linear or decelerating fit. Due to our lack of observations at multiple angular resolutions at this epoch, we cannot be sure if the two components detected in our first eMERLIN observation are part of a larger structure, the details of which we resolve out, or if they are distinct ejections. It is possible (though unlikely) that we missed a flare (and potentially associated ejection) with our AMI-LA monitoring, or that a single flare actually corresponded to a complex ejection morphology [205]. In this case the early time eMERLIN observations could be probing this morphology, and the later time data reveals the motion of the aggregated structure. We note that we could use the smaller angular separation component in our initial eMERLIN observation (MJD 58308; $\Delta t = 3.32\,\mathrm{d}$), instead of the larger angular separation component. While this provides a better fit to the first three eMERLIN observations (not underestimating the position of the component observed on MJD 58329; $\Delta t = 23.33\,\mathrm{d}$) it requires a significant deceleration to fit the entire data set. The inclusion of deceleration is not in itself an issue, however including this component when fitting both a linear and decelerating fit provides a launch date significantly *after* the radio flare observed by AMI. Additionally, the observation on MJD 58310 ($\Delta t = 4.35\,\mathrm{d}$) shows a component that is consistent with the smaller angular separation component on MJD 58308 as discussed above. Finally, our VLBA observation made earlier than our eMERLIN observation on MJD 58306 reveal a component is already present, well before the inferred launch date when including this component in the fitting.

It is important to attempt to account for systematic uncertainties that arise when measuring the positions of components observed at very different angular scales. There is no guarantee that the centroid of the emitting region is the same on these different angular scales when a significant amount of the flux density is resolved out, as is the case for the approaching ejection component here (the receding component was only measured quasi-simultaneously by telescopes with similar angular resolutions). Using the ratio of beam size to signal to noise for the positional error will cause the eMERLIN data to be artificially over constraining given the previous argument, so instead we derive errors based on physics considerations. Considering the ejection as a spherical region expanding at a speed of $\sim 0.05\,c$, launched at the start of the flare observed with the AMI-LA during the

hard to soft state transition, we estimate the emitting region would have an angular size of 0.015″, 0.051″, 0.11″, and 0.42″ on MJD 58308.98, 58316.96, 58329.00 and 58398.73, respectively, and use these values as our separation error. For the final observation we cap the error at 0.2″ as it is now comparable with the position error derived from our lower resolution images.

We have demonstrated the results of fitting the angular separation with both a linear proper motion model, and one with constant deceleration. Determining the statistically appropriate model for data with vastly different error bars is challenging. Even when reevaluating the errors on our eMERLIN measurements, the errors on the position for these observations (especially the ones only a few weeks after the launch of the approaching ejection) are significantly smaller than those made with the VLA and MeerKAT. This is also true for the VLBA observation. Adding a free parameter to our proper motion model (e.g. a deceleration) will essentially serve only to fit the early-time eMERLIN/VLBA observations, with other data barely constraining the model. There is also the issue that the centroids of the emitting regions do not necessarily align on the very different angular scales, and as such any inferred deceleration is not necessarily the physical deceleration of the ejections. It is also worth noting that different proper motions have been reported for the jets in XRB GRS 1915+105 from observations taken with different angular resolution, and do not necessarily imply that deceleration is occurring [204, 253]. We consider both models in the text, but note that the parallax distance [101] for MAXI J1820+070 is strong evidence against the deceleration model being required to fit this data set, as it requires a maximum distance below the now measured parallax distance [101]. The late-time X-ray observations presented in [224] suggest that the deceleration model is more feasible but, given the aforementioned issues with fitting data on extremely different angular resolutions, we are cautious not to over-interpret the data.

The proper motions of the ejecta from MAXI J1820+070 are among the highest ever measured from an astronomical object outside of the Solar System. Our linear proper motion model corresponds to apparent transverse velocities of at least 1.34 c and 0.55 c (for the approaching and receding components, respectively) at a distance of 3.8 kpc. MAXI J1820+070, therefore, becomes one of a small number of black hole binaries to have produced jets with apparent superluminal motion [97, 254, 243, 99]. The launch date for both models is consistent with MJD 58306, coinciding with the radio flare observed with the AMI-LA during the intermediate state, as the source moved from the hard to the soft state. The proper motion of each ejection can be independently related to its

velocity, ejection angle to the observer's line of sight, and the distance to the source from the observer. From a combination of the approaching and receding proper motions (from the linear fit) we can calculate the product $\beta \cos\theta = 0.40 \pm 0.02$ (where β is the ejection's velocity in units of c, and θ is the jet inclination angle to the line of sight), a quantity that is independent of distance and assumes symmetric ejections with the same speeds [97]. From this we constrain a maximum angle to the line of sight of $66^\circ \pm 1^\circ$ (for $\beta = 1$). We can also calculate a maximum distance to the source of 3.5 ± 0.2 kpc. This corresponds to the distance beyond which a more extreme angle to the line of sight than our calculated maximum angle would be required to explain the observed proper motions (or equivalently it is the distance at which $\beta = 1$). For the constant deceleration model we find a maximum angle to the line of sight of $74^\circ \pm 2^\circ$ and a maximum distance of 2.3 ± 0.6 kpc, respectively. However, a measured radio parallax distance to MAXI J1820+070 of 3 ± 0.3 kpc means the deceleration model is marginally disfavoured [101]. The uncertainty in distance, combined with a significantly relativistic jet, means that we can only place a lower limit on its bulk Lorentz factor of $\Gamma > 1.34$ (the apparent velocity, corresponding to $v \gtrsim 0.7\,c$) [209]. The maximum inclination of the radio jet is similar to that derived range from a grazing eclipse observed at X-rays of 66° to 81°, and suggests that it is at the lower limit of this range [210]. Assuming the measured maximum angle presented here is correct implies a black hole mass of $\sim 8.5 M_\odot$ [20].

Table 4.4: Positions of the core, approaching ejection, and receding ejection from the 2018 outburst of J1820. Positions of the approaching jet, receding jet, and core components for observations with eMERLIN, MeerKAT, the VLA and the VLBA. Dates report the observation mid-point.

	Core			Approaching ejection			Receding ejection			
Date	RA	Dec	Error	RA	Dec	Error	RA	Dec	Error	Facility
[MJD]	[hh:mm:ss.s]	[dd:mm:ss.s]	[″]	[hh:mm:ss.s]	[dd:mm:ss.s]	[″]	[hh:mm:ss.s]	[dd:mm:ss.s]	[″]	
58193.42	18:20:21.9384	+07:11:7.182	0.004	-	-	-	-	-	-	eMERLIN
58194.40	18:20:21.9386	+07:11:7.172	0.003	-	-	-	-	-	-	eMERLIN
58199.41	18:20:21.9391	+07:11:7.182	0.008	-	-	-	-	-	-	eMERLIN
58201.27	18:20:21.93867	+07:11:7.169	0.001	-	-	-	-	-	-	eMERLIN
58202.31	18:20:21.9385	+07:11:7.166	0.006	-	-	-	-	-	-	eMERLIN
58203.26	18:20:21.9384	+07:11:7.168	0.004	-	-	-	-	-	-	eMERLIN
58206.27	18:20:21.93858	+07:11:7.168	0.001	-	-	-	-	-	-	eMERLIN
58306.22[b]	-	-	-	18:20:21.9382	+07:11:07.157	0.003	18:20:21.93887	+07:11:07.1785	0.0007	VLBA
58308.98[c,d]	-	-	-	18:20:21.9368	+07:11:07.111	0.006	-	-	-	eMERLIN
58308.98[c]	-	-	-	18:20:21.9285	+07:11:06.853	0.005	-	-	-	eMERLIN
58310.02[c,d]	-	-	-	18:20:21.9361	+07:11:07.083	0.006	-	-	-	eMERLIN
58316.96[c]	-	-	-	18:20:21.9145	+07:11:06.308	0.005	-	-	-	eMERLIN
58329.00[c]	-	-	-	18:20:21.8780	+07:11:05.230	0.006	-	-	-	eMERLIN
58389.75	18:20:21.93	+07:11:08.1	0.6	18:20:21.73	+07:11:02.4	0.6	-	-	-	MeerKAT
58396.70	18:20:21.91	+07:11:07.6	0.6	18:20:21.71	+07:11:01.3	0.6	-	-	-	MeerKAT
58398.04	18:20:21.93	+07:11:07.1	0.9	18:20:21.70	+07:11:01.5	0.9	-	-	-	VLA
58398.73[e]	18:20:21.939	07:11:07.17	0.02	18:20:21.715	+07:11:00.60	0.03	-	-	-	eMERLIN
58399.99	18:20:21.94	+07:11:07.3	0.9	18:20:21.75	+07:11:00.9	0.9	-	-	-	VLA
58402.85	18:20:22.00	+07:11:07	1	18:20:21.73	+07:11:00	1	-	-	-	VLA
58403.66	18:20:21.92	+07:11:07.9	0.6	18:20:21.68	+07:11:01.2	0.6	-	-	-	MeerKAT
58403.91	18:20:21.93	+07:11:07.3	0.9	18:20:21.70	+07:10:59.8	0.9	-	-	-	VLA
58405.67	18:20:21.91	+07:11:07.9	0.5	18:20:21.68	+07:11:01.2	0.5	-	-	-	MeerKAT
58405.90	18:20:21.93	+07:11:07	1	18:20:21.66	+07:11:01	1	-	-	-	VLA
58410.62	18:20:21.94	+07:11:08.0	0.6	18:20:21.67	+07:11:01.3	0.6	-	-	-	MeerKAT
58417.79	18:20:21.938	+07:11:7.17	0.02	-	-	-	-	-	-	eMERLIN
58419.73	18:20:21.939	+07:11:7.17	0.02	-	-	-	-	-	-	eMERLIN
58418.54	18:20:21.91	+07:11:08.3	0.6	18:20:21.67	+07:11:00.8	0.6	-	-	-	MeerKAT
58418.85	18:20:21.96	+07:11:06.8	0.8	18:20:21.72	+07:10:59.6	0.8	18:20:22.10	+07:11:10.7	0.8	VLA
58425.50	18:20:21.91	+07:11:08.1	0.6	18:20:21.65	+07:11:01.1	0.6	18:20:22.02	+07:11:12.3	0.7	MeerKAT
58432.48	18:20:21.91	+07:11:07.8	0.6	18:20:21.66	+07:11:00.1	0.7	18:20:22.00	+07:11:11.4	0.6	MeerKAT
58435.67	18:20:21.90	+07:11:07.4	0.5	18:20:21.67	+07:10:59.8	0.7	18:20:22.01	+07:11:11.1	0.5	MeerKAT
58439.48	18:20:21.95	+07:11:09.0	0.6	18:20:21.63	+07:11:00	1	18:20:22.09	+07:11:12.7	0.6	MeerKAT
58440.90	18:20:21.94	+07:11:07.2	0.2	18:20:21.69	+07:10:59.2	0.2	18:20:22.06	+07:11:11.0	0.3	VLA
58446.45	18:20:21.89	+07:11:06.5	0.8	18:20:21.55	+07:10:57	1	18:20:22.03	+07:11:12	1	MeerKAT
58454.43	18:20:21.95	+07:11:09	1	18:20:21.53	+07:11:00	2	18:20:22.06	+07:11:13.4	1	MeerKAT
58473.68	18:20:21.94	+07:11:07.0	0.3	-	-	-	18:20:22.08	+07:11:11.6	0.3	VLA
58479.64	18:20:21.93	+07:11:07.1	0.4	-	-	-	18:20:22.10	+07:11:12.3	0.4	VLA
58484.75	18:20:21.96	+07:11:07.0	0.3	-	-	-	18:20:22.09	+07:11:12.0	0.3	VLA

[a] When only the core is detected the reported error is the statistical one reported by the CASA task IMFIT (RA and Dec error combined in quadrature). Otherwise it represents the uncertainty in the position along the angle connecting the components to the core (and the core to the components), further described in the Methods section.

[b] The position error reported for the VLBA observation is that along the jet axis, as described in the text. We use a core position measurement from the hard state, with a proper motion correction[237], when calculating the separation of the ejection components.

[c] This observation occurred when the source was not in the hard X-ray state, and as such the core was not detected.

[d] These observations were not included in our proper motion fits.

[e] While we detect the core in this observation, for the purpose of calculating the separation (Table 4.4) we use the bright core observation made on MJD 58201, see Table 4.5.

Table 4.5: Flux evolution of the core, approaching ejection, and receding ejection from the 2018 outburst J1820. Flux density of the approaching jet, receding jet, and core components for observations with eMERLIN, MeerKAT and the VLA. To calculate the flux density we use an unconstrained elliptical Gaussian and report the peak flux density. The error is the statistical one only, and was combined with a 5% calibration error for calculations. Upper limits are 3σ, although at early times when we cannot resolve the receding ejection component these may not reflect the true upper limit of the emitting region. We do not report upper limits before the launch date of the ejections. Dates report the observation mid-point.

	Core		App. ejection		Rec. ejection			
Date	Flux density	Error	Flux density	Error	Flux density	Error	Frequency	Facility
[MJD]	[mJy]	[mJy]	[mJy]	[mJy]	[mJy]	[mJy]	[GHz]	
58193.42	23.2	0.4	-	-	-	-	5.07	eMERLIN
58194.40	26.6	0.4	-	-	-	-	5.07	eMERLIN
58199.41	38	1	-	-	-	-	5.07	eMERLIN
58201.27	56.7	0.8	-	-	-	-	5.07	eMERLIN
58202.31	23	1	-	-	-	-	5.07	eMERLIN
58203.26	26	1	-	-	-	-	5.07	eMERLIN
58206.27	33.5	0.4	-	-	-	-	5.07	eMERLIN
58308.98	< 0.08	-	0.24	0.02	< 0.08	-	5.07	eMERLIN
58308.98	< 0.08	-	0.25	0.02	< 0.08	-	5.07	eMERLIN
58310.02	< 0.13	-	0.52	0.04	< 0.13	-	5.07	eMERLIN
58316.96	< 0.07	-	0.13	0.02	< 0.07	-	5.07	eMERLIN
58329.00	< 0.10	-	0.35	0.04	< 0.10	-	5.07	eMERLIN
58389.75	3.47	0.05	2.26	0.05	< 0.13	-	1.28	MeerKAT
58396.70	11.8	0.1	2.0	0.1	< 0.19	-	1.28	MeerKAT
58398.04	16.99	0.03	0.63	0.03	< 0.05	-	5.87	VLA
58398.73	5.26	0.08	0.31	0.02	< 0.41	-	1.51	eMERLIN
58399.99	7.46	0.05	0.50	0.04	< 0.06	-	6	VLA
58402.85	5.12	0.03	0.33	0.03	< 0.08	-	6	VLA
58403.66	2.62	0.04	1.06	0.04	< 0.11	-	1.28	MeerKAT
58403.91	4.20	0.04	0.33	0.04	< 0.13	-	6	VLA
58405.67	2.41	0.03	0.96	0.03	< 0.07	-	1.28	MeerKAT
58405.90	3.59	0.05	0.28	0.05	< 0.12	-	6	VLA
58410.62	1.52	0.06	0.77	0.06	< 0.016	-	1.28	MeerKAT
58417.79	0.93	0.04	< 1.05	-	< 1.05	-	1.51	eMERLIN
58419.73	1.15	0.03	< 0.21	-	< 0.21	-	1.51	eMERLIN
58418.54	1.61	0.05	0.55	0.05	< 0.14	-	1.28	MeerKAT
58418.85	2.49	0.03	0.17	0.01	0.15	0.03	6	VLA
58425.50	1.15	0.04	0.41	0.04	0.36	0.04	1.28	MeerKAT
58432.48	0.82	0.04	0.29	0.04	0.61	0.04	1.28	MeerKAT
58435.67	0.75	0.02	0.25	0.02	0.55	0.02	1.28	MeerKAT
58439.48	0.79	0.05	0.29	0.05	0.33	0.05	1.28	MeerKAT
58440.90	1.162	0.007	0.071	0.007	0.22	0.007	6	VLA
58446.45	0.36	0.05	0.25	0.05	0.35	0.05	1.28	MeerKAT
58454.43	0.34	0.06	0.18	0.06	0.22	0.06	1.28	MeerKAT
58473.68	0.138	0.008	< 0.02	-	0.13	0.008	6	VLA
58479.64	0.153	0.008	< 0.03	-	0.10	0.008	6	VLA
58484.75	0.147	0.008	< 0.02	-	0.10	0.008	6	VLA

4.6.2 Approaching ejection flux decay rates

While BHXRBs are in the soft accretion state the compact core jet is significantly quenched and any radio emission from it drops by many orders of magnitude (always below observing sensitivity limits) or switches off completely. Radio emission observed during the soft state is almost certainly associated with ejections launched during the hard to soft state transition. This radio emission is transient, and is seen to fade as the ejections expand and cool. The e-folding decay timescale (which we will hereafter refer to as simply the decay timescale) of the emission from the ejections is seen to vary significantly between sources,

but can broadly be categorised as either short (decay timescales from a few to $\sim$ 10 d) or long (decay timescales from a few tens to hundreds of days). Short decay timescales are thought to be the result of ejecta expanding and cooling, with minimal ongoing energy injection resulting from interactions from the ISM. When longer decay rates are seen, it is thought that ongoing ISM interaction provides a source of particle acceleration, partially offsetting cooling, and results in the slowed flux decline. Example of fast decays include GRS 1915+105 during its 1994 and 1997 outbursts, showing decay timescales of $\sim$ 7 d and $\sim$ 2 d, respectively [97, 204]. XTE J1748−288 showed a radio flux density decay timescale of $\sim$ 7 d at the start of the soft state during its 1998 outburst [242]. Slow decays have been seen in XTE J1550−564, which showed a flux density decay timescale of $\sim$ 85 d (at 1.4 GHz) following a plateau period [223]. This decay rate appeared to be wavelength dependent, with X-ray observations revealing an exponential decay rate of $\sim$ 340 d from the same ejection component. An ejection from H1743−322 decayed with a timescale of $\lesssim$ 28 d.

To demonstrate the different decay rates for MAXI J1820+070 we present a modified version of Figure 4.6 (Figure 4.20), in which we fit for the decay timescale for different segments of the light curve. The first segment, between MJD 58314 and MJD 58320, shows an exponential decay timescale of 6 ± 1 d. We refer to this as a 'fast decay'. The second segment, dates after MJD 58320, we fit with a broken exponential which shows decay rates of 51 ± 6 d and 21.0 ± 0.9 d with a break occurring at MJD 58386 ± 4. We refer to these as a 'slow decay'. Both of these decay phases are also seen in our eMERLIN data, although due to the coarse sampling we do not include them in Figure 4.20. It appears, therefore, that the approaching ejection from MAXI J1820+070 showed an initial phase of fast adiabatic losses with no/little re-acceleration of particles, followed by a slower decay phase in which the adiabatic losses were offset by some in-situ particle acceleration. We note that for both XTE J1550−564 and H1743−322 the decay rate of the ejecta were frequency dependent, with higher frequencies decaying slower [223, 208]. This is similar to what we see for MAXI J1820+070, with the slower decay rate corresponding to the higher frequency (AMI-LA) data. This is likely caused by the fact that higher resolution observations resolve out continually more flux as the region expands resulting in a steeper decay. The short delay between the ejection launch and this slow decay phase (in contrast to XTE J1550-564) may indicate that MAXI J1820+070 is not contained within an ISM cavity (and the decay is due to ongoing ISM interaction from the outset), or, if present, such a cavity may have a significantly smaller radius causing an earlier transition to the slow decay phase. The cause of the rise in flux between the two light curve segments (and between the end of the flare and the start of the first segment) is uncertain, but could be indicative of multiple ISM density

enhancements (a similar rise was seen between the end of the radio flare and the start of the fast cooling period).

The measured time of the break in the second light curve segment is remarkably close to the date where MAXI J1820+070 returned to the hard X-ray state (MJD 58393), and the core jet turned back on. For the two events to be connected there would have to be transport of information between the core and the approaching jet (separated by $\sim 7''$ at this epoch) on a ~ 7 d timescale. This would require an extremely high inferred proper motion of ~ 1 arcsec day^{-1} ($22\,c$ at 3.8 kpc). This is obviously significantly superluminal, and we would require the approaching ejection component to have a small angle (maximum $\theta \sim 5^{\circ}$) to the line of sight for the actual velocity to be at or less than c. This angle is not compatible with the one that we measure from our fitted proper motions. It is more likely that the difference in decays is either due to the fact that the AMI-LA is probing much larger angular scales, or that contamination from the receding jet (which is contained within the AMI-LA synthesised beam) is altering the decay rate. While we have no direct measurement of the flux density from the receding jet during the AMI-LA observations presented in Figures 4.6 and 4.20, we note that the receding jet is not detected in any of our eMERLIN observations and is below $\sim 600\,\mu$Jy in our MeerKAT observations and so is likely to be a significantly less dominant component.

4.6.3 A new method for estimating ejecta energetics in BHXRBs

On MJDs 58396 and 58398 we observed the field of MAXI J1820+070 with MeerKAT and eMERLIN, respectively, at similar frequencies (1.28 GHz and 1.51 GHz, respectively). In terms of the decay timescale of the approaching ejection (Figure 4.20) these observations are close enough together that I will consider them (and refer to them) as quasi-simultaneous. Additionally, the frequencies differ by a small enough amount that, for a typical spectral index for ejections from BHXRBs (optically thin: $\alpha \sim -0.7$) the flux difference caused by the different observing frequencies will be small (of the order 10%). Due to the nature of aperture synthesis, these arrays are only sensitive to flux from a range of angular scales, with eMERLIN blind to emission from the larger angular scales probed by MeerKAT. If the two facilities observed a point source of the same flux (at the very similar frequencies), then the emitting region is contained below the angular scales accessed by eMERLIN. However, if they recover different flux densities, then there is emission on angular scales between those to which eMERLIN and MeerKAT are sensitive. In both observations the approaching ejection component is detected as an unresolved source. The flux density of the ejection measured by MeerKAT is ~ 2 mJy (see table Table 4.5 for a more detailed breakdown of our

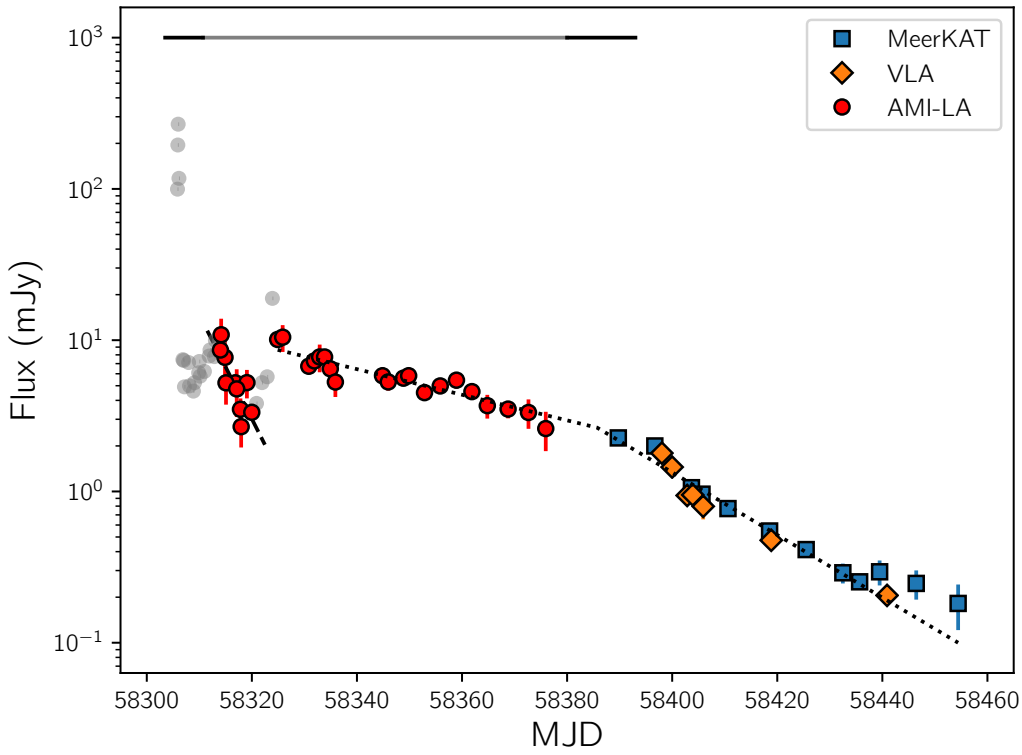

Figure 4.20: As with Figure 4.6, with the eMERLIN and VLBA data removed. We fit sections of the light curve with exponential decay functions of the form $F_\nu = Ae^{-\Delta t/\tau}$. Data shaded grey are not included in the fitting. The first light curve segment (fast decaying AMI-LA data; MJD 58314 to 58320), is well described ($\chi^2_\nu = 1.21$) by a decay with a characteristic time scale of 6 ± 1d (dashed line). We opt to fit the apparently slower decay (MJD 58324 onward) with a broken exponential function (dotted line). The best fit decay rates are 51 ± 6 d and 21.0 ± 0.9 d, with the break occurring at MJD 58386 ± 4 ($\chi^2_\nu = 1.59$). Error bars on data points indicate one sigma uncertainties.

observations), whereas with eMERLIN we measure a flux density of ~ 0.3 mJy. Due to its longer baselines, eMERLIN is resolving out $\sim 85\%$ of the flux observed by MeerKAT. As the source was unresolved in the images for both observations we know that this resolved out flux (~ 1.7 mJy) is emitted between the angular sizes of the synthesised beams of the telescopes for these two observations and, if a distance to the source is know, these can be converted to a physical size and therefore volume. The synthesised beams of MeerKAT and eMERLIN at these epochs had sizes of $7.9'' \times 5.4''$ and $0.31'' \times 0.2''$, respectively. We are able to constrain the distance to MAXI J1820+070 through measuring the proper motion of its bipolar ejections. This constraint, however, is only an upper limit which would leave large uncertainty in the physical size of the ejections. Thankfully the distance to MAXI J1820+070 has been better constrained by the GAIA mission, which measured a distance of $3.8^{+2.9}_{-1.2}$ kpc [237]. More recently the distance was constrained further through a VLBA campaign measuring the radio parallax of the compact core jet to be 2.96 ± 0.33 kpc [101]. Note that the radio parallax distance, our limit from the ejecta dynamics, and the Gaia distance all agree well with one another. A comparison of the distance measurements, and their impact on system parameters is shown in Figure 4.21. Using the radio parallax distance, and the minimum angular size probed by both observations ($5.4''$ and $0.2''$ for MeerKAT and eMERLIN, respectively), we can attribute the resolved out flux to being emitted from a region with a physical scale of between 5.9×10^2 AU and 1.6×10^4 AU. Assuming a spherical geometry this corresponds to a volume $V = (4/3)\pi(r_{\rm out}^3 - r_{\rm in}^3) \approx 5.8 \times 10^{46}$ m^3. It is a well known phenomenon for synchrotron radiation that the observed radiative power from most sources integrated over any humanly accessible time scale is a large underestimate of the total internal synchrotron energy. In other words the synchrotron cooling timescale is, for most sources, very long ($t_{\rm synch} \approx 10^9 B^{-2}\gamma^{-1}$ years where B is measured in Gauss). It is therefore incorrect to assume knowledge of the internal energy of a synchrotron sources based only on the observed flux from it. Instead, the synchrotron minimum energy is $E_{\rm min} \approx 3.0 \times 10^{11} \eta^{4/7} V^{3/7} \nu^{2/7} L_\nu^{4/7}$ erg, where V is the volume of the emitting region (which may be partially filled), ν is some observing frequency, L_ν is the observed luminosity at this observing frequency, and η is the ratio of energy in all particles to that in electrons, and the simplifying assumption has been made that the spectral index is -0.75 [136]. This equation was an important component in the realisation that extra-galactic radio sources, while having relatively modest luminosities, had, due to their vast size, extremely high internal energies [68, 255, 256]. From our range of possible sizes we can therefore calculate the minimum synchrotron energy associated with the approaching ejection, finding it to be in the range 2.1×10^{41} erg $< E_{\rm f} < 1.5 \times 10^{43}$ erg. This is the first time that such a calculation has been possible for a BHXRB system. In other cases where where ejecta had

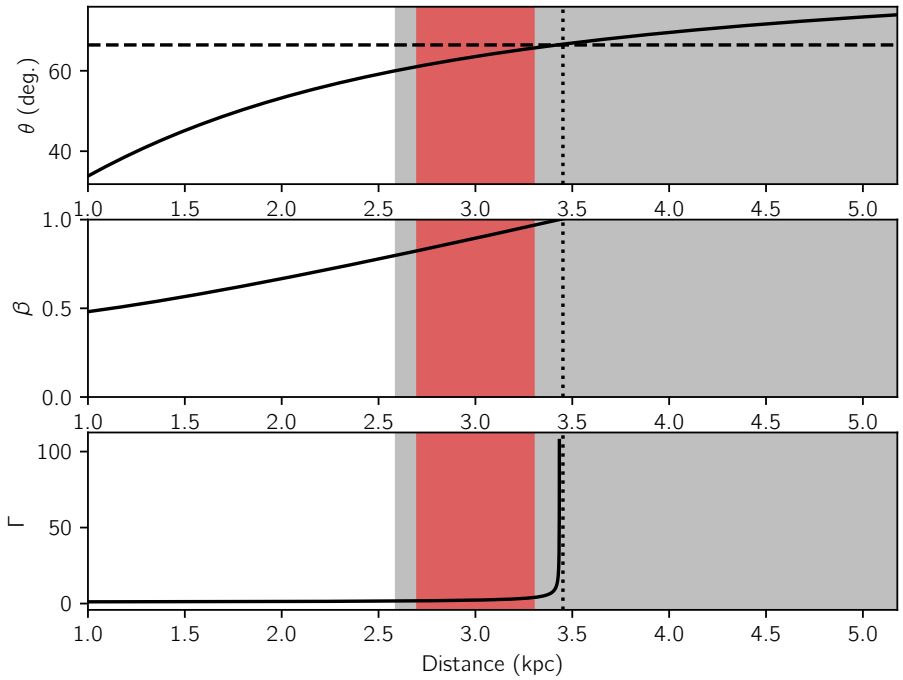

Figure 4.21: The inferred inclination angle (top panel), jet speed (middle panel), and Lorentz factor (bottom panel) as a function of the distance to MAXI J1820+070. The vertical dotted line marks the maximum source distance measured from the jet proper motions. The grey shaded region is the one sigma confidence region for the distance as measured by Gaia [237]. The red shaded region shows the one sigma confidence region for the distance as measured by radio parallax [101].

been resolved (either at X-ray or radio frequencies) they were only marginally so (and with a single instrument) making it difficult to attribute a flux to a bounded range of emitting volumes as we have done here [257, 99, 224].

Due to the solid association between ejecta launch and hard to soft state transition radio flaring it has been common to attempt to estimate the energy content of ejecta from the flares. There are two methods for making such a calculation. The first makes the assumption (which in chapter Chapter 5 I show is not necessarily always valid) that radio flare are the result of the initial expansion and optical depth evolution (from thick to thin) of an emitting region. In this case the peak of the flare corresponds approximately to the point where the optical depth to synchrotron radiation is unity [258]. In this case we estimate the energy content of the flare to be $E \approx 2 \times 10^{37}$ erg (see Chapter 5 for more detail). Another estimate can be made by just considering the rise time of the flare and its peak flux density. Under the assumption that an expanding emitting region is responsible for the radio flare, and that it is expanding at $0.05\,c$ for ~ 6.7 hours and reaches a peak flux density of ~ 46 mJy (see Figure 4.5 for details), we estimate the energy associated with the flare to be $E \approx 2 \times 10^{39}$ erg.

This expansion speed is based on strong emerging evidence that if expanding ejections are responsible for state transition radio flares, they do not expand at mildly or highly relativistic speeds (such as the 3D free expansion velocity $c/\sqrt{3}$) [259, 205, 99]. Both estimates are at least two orders of magnitude less than the ones we calculate based on the resolved out radio emission.

Persistent, slowly evolving radio emission from moving relativistic ejections has been observed in three XRB systems (XTE J1550−564, H1743−322 and MAXI J1535−571) previously. In XTE J1550−564, dynamic ejections were observed on small (< 300 mas) angular scales following a radio flare [260]. These ejections then went 'dark' (although observations were sparse), and were detected again over two years later due to a re-brightening episode thought to be the result of an interaction with the wall of an ISM density cavity [206, 222, 223]. A similar explanation has been invoked to explain the large scale jets in H1743−322 [208]. In MAXI J1535−571 the approaching ejection was tracked for ~ 300 d, after being detected for the first time ~ 90 d after its inferred launch date [99]. The ejection was not resolved at an angular separation from the core of less than $4''$, but was tracked out to over $15''$. This allowed the launch time to be constrained to a ~ 5 d window, consistent with occurring just before a radio flaring event (although the start time of the flare is not well constrained). The flux density from the ejection decayed steadily, with re-brightening events possibly indicating internal shocks in the ejecta or interaction with ISM density enhancements.

Our radio observations of J1820 track the entire evolution of the approaching ejecta, where we temporally resolve the transition from a short timescale decay phase (more typical of the timescales associated with transient soft state emission), a subsequent re-brightening, and then a long timescale decay phase (Figure 4.20). The most likely explanation for the slowly decaying flux density is that there is constant *in situ* particle acceleration as the jet decelerates via interactions with the nearby interstellar medium (ISM) [261]. In this scenario, by the time of our energetic analysis based on the resolved emission, all of the supplied energy, E_f, responsible for the observed radio emission would have come from this deceleration. The kinetic energy of the ejecta at a given moment is $KE = (\Gamma - 1)E$, where E is the internal energy of the ejecta and Γ is the bulk Lorentz factor. We denote the initial and final (at the time of our measurement of E_f) internal energies and Lorentz factors by the subscripts (i,f). From the condition that deceleration has provided the observed energy, we have that $(KE)_i - (KE)_f \gtrsim E_f$ or, equivalently, $(KE)_i = (\Gamma_i - 1)E_i \gtrsim (\Gamma_f - 1)E_f + E_f = \Gamma_f E_f$.

Given our estimates for E_i and E_f, we see that $\Gamma_i \gtrsim (\Gamma_i - 1)/\Gamma_f \gtrsim 70$. Such a large initial Lorentz factor is extremely unlikely for most jet geometries since the ejecta would be extremely Doppler de-boosted and intrinsically more luminous by orders of magnitude (in the manner of an off-axis gamma-ray burst). Therefore we must conclude that our initial estimate of the initial internal energy, E_i, is at least two orders of magnitude too low (there is no clear way that E_f can have been overestimated), and that the majority of kinetic energy released is not well traced by early-time radio flaring.

Regardless of the powering mechanism, we may take $E_f \sim 10^{42}$ erg as a strong lower limit to the total energy supplied to the jet, and assume that the jet was launched over a phase of $\lesssim 6.7$ hr, the rise time of the optically thin flare during the state transition. From this we derive a required energy supply rate to the launched ejection of $4 \times 10^{37}\,\mathrm{erg\,s^{-1}}$, around 50% of the contemporaneous X-ray luminosity. Consistent values of the minimum internal energy were subsequently derived using the radio through X-ray spectrum of the approaching ejection to constrain the radiative luminosity.

4.6.4 Connection to X-ray timing

Many attempts have been made to associate the launch of transient ejections with distinct properties of the accretion flow, with a view of better understanding how ejections are produced. One such method is to observe the timing properties of the X-ray emission from XRBs. In addition to the RMS variability of the X-ray emission from sources evolving as their accretion state evolves, there are also distinct quasi-periodic oscillations (QPOs) revealed when undertaking Fourier analysis of such time series X-ray data. These manifest as broadened (as they are not purely periodic) Lorentzian profiles in the frequency-power domain. There is a complex phenomenology used when classifying QPOs, but in BHXRBs they (low frequency QPOs) are generally classified as being type A, B or C [262]. The type A QPO is broad and weak, whereas the types B and C are narrow and strong. QPO characteristics (the combination of A/B/C visible, and their central frequencies) are variable throughout BHXRB outbursts, and couple to the accretion state of the system. Type C QPOs are observed as sources enter the hard state at the beginning of an outburst, and then throughout the entire outburst cycle (although predominantly in the hard and intermediate states). The type-C QPO frequency increases as the source transitions to the intermediate state. The type-B QPO is only seen during the intermediate state, and has been associated with the launch of transient ejections from BHXRBs. Type-A QPOs are rare and weak features. The physical origin of QPOs is disputed, but it is commonly believed that they are

related to the motion of the accretion flow as it orbits the black hole in a warped space-time (although alternative models propose wave modes in the accretion flow as possible drivers of QPOs [263]). A popular model to explain the physical origin of QPOs is the relativistic precession model (e.g. [264, 265]), which attributes the type-C QPO as being due to relativistic precession of the disk (nodal precession) and two higher frequency QPOs from periastron precession and orbital motion. The nature of the type-B and type-C QPOs is less clear, however the type-B QPO's association with state transitions and their stronger appearance for face-on sources has led authors to suggest their association with jet launching [266, 267].

MAXI J1820+070 was observed extensively by the NICER instrument (see Chapter 3) throughout its 2018 outburst, and most interestingly over its hard to soft state transition. The high sensitivity and timing precision of NICER means that tracking the evolution of QPOs from the object was possible. Figure 4.22 shows the dynamic power density spectrum of the source as it made this transition, along with the radio and X-ray light curves over this period. Figure 4.23 shows two examples of the power density spectrum of MAXI J1820+070, one demonstrating a type-C QPO (and its harmonic) and the other a type-B QPO. The type-C QPO can be identified by its high amplitude and small width, as well as the associated broadband noise. The type-B QPO appears just as the type-C QPO disappears, occurring at a lower frequency, lacking a harmonic, and having a smaller amplitude. The type-C QPO (and its harmonic) can be seen in Figure 4.22 to move to higher frequencies as the source began transitioning to the soft state and the core jet was quenching, which is interpreted in the context of the relativistic precession model as the QPO emitting region (perhaps the ISCO) moving closer to the black hole. This is consistent with the X-ray spectral evolution between the hard and soft states showing the suppression of the hard X-ray component. The type-B QPO appears to occur during the hard X-ray flare in the 7-12 keV energy band as shown in **(f)** in Figure 4.22, while the start of the type-B QPO was associated with an increase in the count rate in all X-ray bands. In [190] we make a comparison with the radio timing properties and the properties of the radio flare seen during the state transition. The most striking feature of this comparison is the association between the start of the radio flare and the presence of the type-B QPO. We found that the start of the radio flare was delayed with respect to the onset of the type-B QPO by ~ 2 hrs. The AMI-LA in-band spectral index for the radio flare showed that it was optically thin for the entirety of its evolution (during the rise and decay). This is indicative of continued particle acceleration in the emitting region (as opposed to radio flares that rise while being optically thick and then transition to the optically thin regime [258]) and could represent a time delay between the launch of the

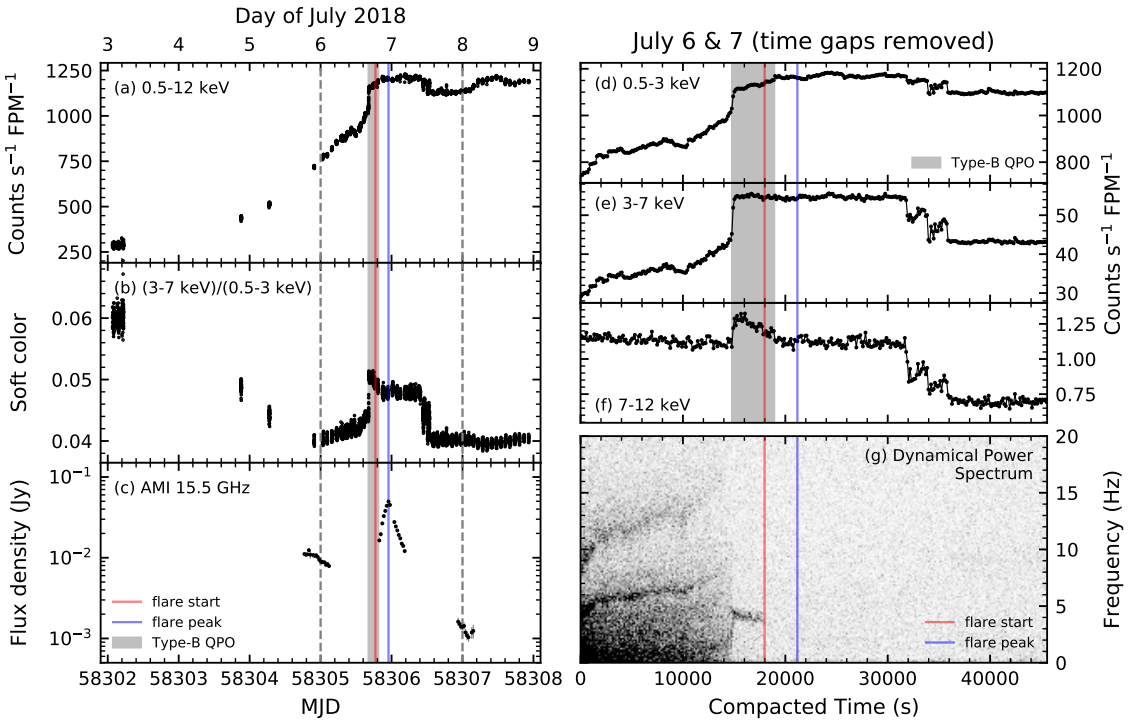

Figure 4.22: The X-ray properties of MAXI J1820+070 during its hard to soft accretion state transition. Panels **(a)** and **(c)** show the X-ray counts (per focal plane model) and the soft colour, respectively, with the energy range used labelled on the plot. **(c)** shows the state transition radio flare seen by the AMI-LA for the same time period (as in Figure 4.5). The grey shaded region marks the time range where the type-B QPO was observed, the blue vertical line shows the peak of the radio flare and the red its start time. In panels **(d)**–**(g)** only data taken on July 6 and 7 (MJDs 58305 and 58306) are shown (this period is marked with dashed vertical lines in panels **(a)**–**(c)**, with gaps in the observation removed which is referred to as compacted time (t_c). Panels **(d)**–**(f)** have a time resolution of 128 s. The dynamical power spectrum in panel **(g)** has a frequency resolution of 0.125 Hz.

ejection and its initial interaction with ISM material or from internal shock caused by interactions between different outflow components with distinct velocities [268]. This occurred before our first resolved detection of the ejection with the VLBA at which time the radio flare had ended. It is worth noting that our inferred launch time from the dynamical study of the ejecta is *after* the radio flare occurred. It is possible therefore that the flare itself signals the launch of the ejecta (rather than the flare appearing as a result of the ejecta interacting with the external medium). It is also possible, given the caveats in comparing data from different angular resolutions, that our inferred launch time has a larger error than the statistical one implies. The launch time is constrained based on two early observations with the VLBA and eMERLIN, and a calculation of the proper motion based on data from a single instrument would help to clarify this point. Further analysis of early time VLBI data (of where there are more than presented in this work) are ongoing and will be reported in a future paper.

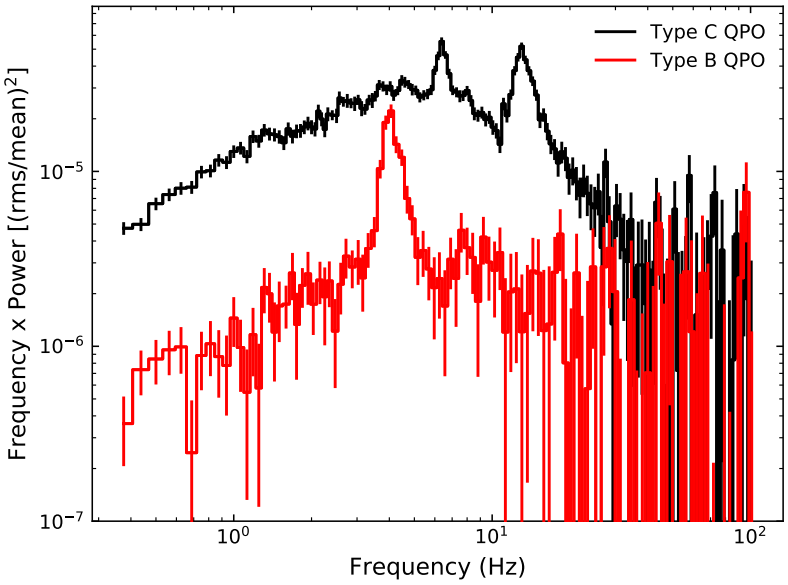

Figure 4.23: Two 0.3-12 keV power density spectra of MAXI J1820+070. The black power spectrum is the average taken from the time interval t_c = 2000 – 2700 s in panel **(g)** of Figure 4.22 and shows a type-C QPOs. The red power spectrum is the average taken from the time interval t_c = 16000 – 17600 s and shows a type-B QPO. Both time-averaged power spectra were rms normalised (Belloni & Hasinger 1990) and the Poisson-noise level was subtracted.

This is not the first time that a connection between state transition radio flaring and the presence of a type-B QPO has been made, but it represents a step forward in the robustness of the association. Discrete ejections were observed from the source H1743−322 as well as a radio flare during the state transition. The radio flares overlapped a type-B QPO also seen during the state transition and a dynamical study of the ejecta implied a launch time a few days before the flare (but was only known to an accuracy of ∼ 1 d). Additionally while a radio flare was clearly present during the state transition it was inferred from only a single data point making the association with the QPO more tentative. A similar evolution was seen more recently in the system MAXI J1535−571 but suffered from similar data issues when attempting to make the association between flaring, ejecta launching, and the type-B QPO [99]. The association between radio and X-ray timing properties is discussed in more detail for BHXRBs in [269], but the radio and X-ray coverage of the objects studied at that time was significantly more limited than for more recent events. While the data presented here (and in [100, 190]) represent the most solid association between jet launching, radio flaring, and X-ray timing variability, the exact origin of these three features is uncertain, and while their association perhaps suggests a common origin (the launching of ejections) this is still tentative. While continuing to study state transition with high time resolution radio and X-ray observations is certainly valuable, it is worth noting that the dynamical timescale

at the inner edge of the accretion disk is ~ 0.1 ms (for a black hole of mass $3M_{\odot}$), and so ejection and flaring times would have to be known to extremely high precision to cement the association.

4.7 Contamination of the radio – X-ray correlation

Our simultaneous radio and X-ray monitoring ended on MJD 58439 at which point we measure, with the VLA, the receding jet flux density to be around 20% of the core flux density at 6 GHz. Assuming the core has a flat spectrum [270] and the ejection is optically thin with a spectral index of –0.7, we estimate that the ejection could be contributing around 10% of the flux density measured by the AMI-LA by this date. Fifteen days previous, a detection of the core and receding ejection with MeerKAT at 1.28 GHz measured the receding component flux density to be around 30% of the core flux density. Under the same assumptions this would imply around a 5% contribution to the AMI-LA flux density at this epoch. Removing (quasi-)simultaneous observations after MJD 58424 alters the slope during the second hard state to $L_R = AL_X^{0.34\pm0.06}$, and the jointly fit slope becomes $L_R = AL_X^{0.55\pm0.02}$. We conclude that the slopes are not being significantly altered by the presence of ejecta components contaminating the AMI-LA measurements of the core. The radio X-ray correlation for the re-brightening events will not be affected by the ejections, as they will have faded very significantly by the time MAXI J1820+070 switched back on.

Chapter 5

Radio flaring from black hole X-ray binaries

This chapter is based on work published in:

Bright *et al. in prep.*

Rob Fender & Joe Bright. Synchrotron self-absorption and the minimum energy of optically thick radio flares from stellar mass black holes. MNRAS **489**, 4836-4846.

Rob Fender, Joe Bright *et al.* Late-outburst radio flaring in SS Cyg and evidence for a powerful kinetic output channel in cataclysmic variables. MNRAS **490**, L76-L80.

5.1 Introduction

As discussed, and demonstrated, in Chapter 4, black hole X-ray binaries undergo radio flaring as they transition between the hard and soft accretion states (but not when making the reverse transition). There is strong evidence connecting radio flaring with the launch of discrete ejecta, which can be resolved from the core jet and seen to evolve over time. The physical process causing the launching of the ejections is unknown, as is the one causing the state transition radio flaring, although many models exist in the literature to explain them [258, 271, 196, 272]. The temporal and spectral evolution of these radio flares provides clues to the properties of the emitting region. However the unpredictability of state transitions, coupled with the short timescales of these flares, has mostly prevented them from being sampled at multiple widely separated frequencies. There are some notable exceptions to this, firstly the BHXRB V404 Cygni, which underwent an extended period of radio flaring in 2015. This allowed the flares to be sampled at multiple radio and sub-mm frequencies

at high time resolution due to the extreme brightness of the source [205]. Secondly, flares from the BHXRB GRS 1915+105 have been observed extensively at very disparate frequencies (radio through infrared). These flares have very similar widths and amplitudes at these different frequencies, unlike the flares from V404 Cygni which are seen to be lower amplitude at lower frequencies, as well as having a wider profile [273, 274]. Another issue with determining the process causing radio flaring is that they do not necessarily occur as isolated events, and many flares can occur in quick succession causing them to overlap and become difficult to disentangle when modelling (a problem exacerbated by more frequently occurring flares or for worse high frequency observational coverage).

A general consensus has built up around the XRB community that, as the flares from BHXRBs have been connected with discrete ejections, the flares are caused by the initial evolution of the plasma blob(s) (also known as plasmoids) as they are launched by the accreting compact object. In this paradigm, which I will call the optically thick flaring case, or thick flare case, there is a very specific temporal and spectral evolution that a flare should follow.

5.2 Optically thick radio flares

Optically thick flares are simply the result of an expanding region emitting synchrotron radiation undergoing optical depth evolution as they expand. I will discuss these in the context of the van der Laan model (hereafter vdL66 [258], or the vdL model) and using results from Pacholcyzk's *Nonthermal Processes in Galactic and Extragalactic Sources* and Longair's *High Energy Astrophysics*, my preferred texts on radio synchrotron emission [275]. Consider an expanding spherical region (with an angular extent θ and expansion velocity $v_{\rm exp}$) containing a population of electrons accelerated into a power law distribution ($N(E) = k(t)E^{-p}$, with $E_{\rm min}(t) < E < E_{\rm max}(t)$ and $N(E)$ is a number density) which is threaded by a magnetic field, resulting in the production of synchrotron radiation. From Chapter 2 we take the results that the emission spectrum for synchrotron radiation is $J(\nu) \propto kB^{(p+1)/2}\nu^{-(p-1)/2}$ and the absorption coefficient is $\chi(\nu) \propto kB^{(p+2)/2}\nu^{-(p+4)/2}$. Solving the radiative transfer equation, the flux density from such an emitting region can be written as

$$S(\nu) = \frac{\Omega J(\nu)}{4\pi\chi(\nu)}[1 - \exp(-l\chi(\nu))]. \tag{5.1}$$

Here $\Omega = \pi\theta^2$ is the solid angle of the spherical emitting region, and l is the depth of the region. There are two important limits of the optical depth ($\tau = \chi(\nu)l$) to consider here, where $\tau << 1$ and $\tau >> 1$, which are the optically thin and thick limits, respectively. In the

optically thick limit, which will be satisfied below some frequency for our emitting region, we have:

$$S(\nu) \propto B^{-1/2}\theta^2\nu^{5/2} \tag{5.2}$$

and we recover the familiar self-absorbed spectrum from Chapter 2. In the optically thin limit we have:

$$S(\nu) \propto kB^{(p+1)/2}\theta^2\nu^{-(p+1)/2}l \propto kB^{(p+1)/2}\theta^3\nu^{-(p+1)/2} \tag{5.3}$$

where I have used the fact that $l = \theta d$ where d is the distance to the emitting region and is constant. This is the familiar optically thin spectrum, again from Chapter 2. We now consider the fact that the magnetic fields, angular sizes, and electron energies are all evolving with time (due to the expanding emitting region), and so the spectrum is not static (and so neither is the flux at any particular frequency). We therefore want to put constraints on how these quantities evolve with time. For the angular size of the region this is simply $\theta = \theta_0(r/r_0)$, where a quantity with subscript 0 is specified at some instant, as we have linear expansion (r is the radius of the region). For the magnetic field we invoke ideal MHD (and therefore the frozen flux condition) which implies the relationship $B = B_0(r/r_0)^{-2}$. If the expansion is adiabatic then the individual electrons cool and their energy evolves as $E = E_0(r/r_0)^{-1}$. While there is no explicit dependence on E in Equations (5.2) and (5.3) this relationship will help us to determine the evolution of k with time. We can use the fact that we are assuming no particles enter or exit the emitting region to say

$$r^3(t)k(t)\int_{E_{\rm min}}^{E_{\rm max}} E^{-p}dE = \text{const} = r^3(t)k(t)\frac{E_{\rm max}^{1-p} - E_{\rm min}^{1-p}}{1-p}. \tag{5.4}$$

Now invoking our adiabatic expansion condition we write:

$$r^3(t)k(t) \propto \frac{1}{E_{\rm max,0}^{1-p}(r/r_0)^{p-1} - E_{\rm min,0}^{1-p}(r/r_0)^{p-1}} = E_{\rm max,0}^{p-1}(r/r_0)^{1-p}[1-(E_{\rm min,0}/E_{\rm max,0})^{1-p}]^{-1}. \tag{5.5}$$

Dropping all the constants and just seeing how k evolves with radius (or time) we find that $k = k_0(r/r_0)^{-(p+2)}$. This condition is implied in vdL66 but not directly derived. From this we can revisit the optically thick and thin flux limits and write them entirely in terms of radius (which itself is linear with time). In the optically thick limit we have $S(\nu, r) = S_0(\nu)(r/r_0)^3$ and in the optically thin limit $S(\nu, r) = S_0(\nu)(r/r_0)^{-2p}$. So in the optically thick limit (at a frequency well below the turnover frequency) the flux will rise with time as a powerlaw with index 3, whereas well above the turnover frequency the flux

declines with powerlaw $-2p$. To fully characterise the spectral evolution we finally need to characterise the movement of the peak, which can be derived in two ways. The first is to simply find the maximum of the source function (Equation (5.1)). Such an approach leaves the following condition:

$$\exp\left(ClkB^{(p+2)/2}\nu_m^{-(p+4)/2}\right) - ClkB^{(p+2)/2}\left(\frac{p+4}{5}\right)\nu_m^{-(p+4)/2} - 1 = 0 \tag{5.6}$$

where $C = \frac{\sqrt{3}e^3}{2\pi c m_e}\left(\frac{3e}{2\pi m_e^3 c^5}\right)^{p/2} b(p)$, $b(p)$ is a weak function of p (and is defined in equation (2.11)), and ν_m is the frequency at which the maximum in the spectrum occurs. Inverting this equation to solve for ν_m involves invoking the product log function, $W(x)$, which is the solution to equations of the form $y\exp(y) = x$. The solution takes the form

$$\nu_m = \left[\frac{1}{ClB^{(p+2)/2}k}\left(-W\left(-\frac{5}{p+4}\exp\left(\frac{-5}{p+4}\right)\right) - \frac{5}{p+4}\right)\right]^{-2/(p+4)} \tag{5.7}$$

which appears intractable, but if we consider that $W(x)$ is real for $x > -1/e$ we see that the product log function in Equation (5.7) is just a constant for any reasonable value of p (in fact for $p > -4$). In the region $-\frac{1}{e} < x < 0$ the product log function has two real values, one of which will be the uninteresting solution $W\left(-\frac{5}{p+4}\exp\left(\frac{-5}{p+4}\right)\right) = -\frac{5}{p+4}$ giving $\nu_m = 0$. The other branch will give a real negative value. Taking the non-trivial solution we can therefore say the following

$$\nu_m \propto l^{2/(p+4)}B^{(p+2)/(p+4)}k^{2/(p+4)} \propto r^{-(4p+6)/(p+4)} \tag{5.8}$$

where we have used the previous dependencies of l, B and k on r. Using Equation (5.1) allows us to calculate evolution of the flux at the break frequency as

$$S(\nu_m) \propto \theta^2 B^{-1/2}\nu_m^{5/2}\left[1 - \exp\left(-lB^{(p+2)/2}\nu_m^{-(p+4)/2}k\right)\right] \propto r^{-(7p+3)/(p+4)} \tag{5.9}$$

again using the same dependencies of l, B and k on r. From Equations (5.8) and (5.9) we see that the break moves to lower frequencies with time and the maximum flux at the break drops. Physically this makes sense, as when the emitting region expands it becomes optically thin to lower frequencies but has cooled during the expansion. These same relations are derived in vdL66 and fully characterise the spectral evolution of such an emitting region (and the flux evolution at any given frequency). In vdL66 the synchrotron self-absorption condition (the brightness temperature of the synchrotron emitting electrons

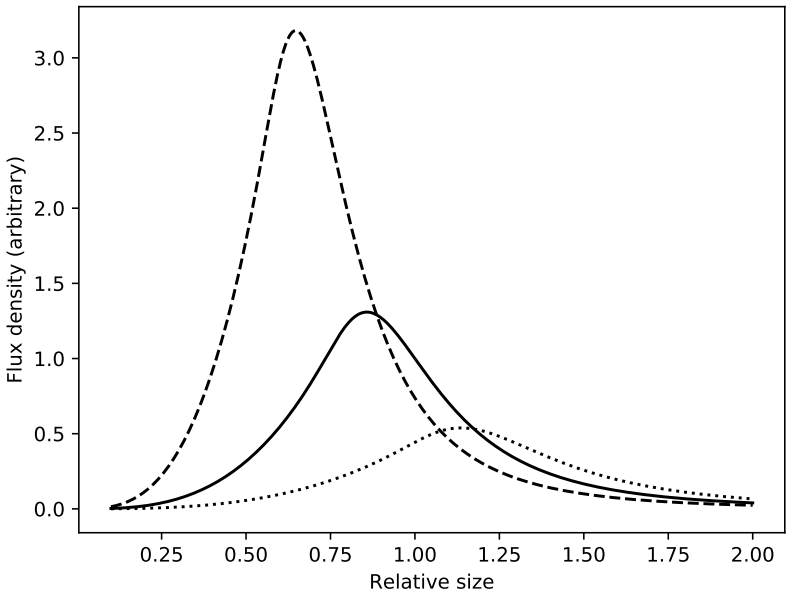

Figure 5.1: The flux density evolution of a synchrotron emitting expanding cloud of electrons according to vdL66 shown at three different frequencies. The solid line is the reference frequency ($\nu/\nu_{m_0} = 1$), the dashed line is double the reference frequency, and the dotted line is half the reference frequency. Higher frequencies peak earlier and at a higher flux when compared to lower frequencies. Note how, as I have used the same reference frequency as in Figure 5.2, that the solid line is not normalised to one.

sets an upper limit for the brightness temperature of the region) and the flux evolution in the optically thin limit are used to infer the evolution of the break flux and frequency . Taking the conditions $\nu_m = \nu_{m_0}(r/r_0)^{-(4p+6)/(p+4)}$ and $S_m = S_{m_0}(r/r_0)^{-(7p+3)/(p+4)}$ (where again subscript 0 quantities are those defined at a specific time) and using the source function we can finally say, by choosing the instant at which our subscript 0 values are defined to be at the time when the spectrum peaks at the reference frequency (it is worth noting that this does not mean that the light curve measured at the reference frequency will peak at $(r/r_0) = 1$ which can be seen directly in Figure 5.1), that

$$S(\nu, r) = S_{m_0}\left(\frac{r}{r_0}\right)^3\left(\frac{\nu}{\nu_{m_0}}\right)^{5/2}\frac{1-\exp\left(-\tau_m(\frac{r}{r_0})^{-(2p+3)}(\frac{\nu}{\nu_{m_0}})^{-(p+4)/2}\right)}{1-\exp(-\tau_m)}. \tag{5.10}$$

Here quantities with subscript m_0 are defined to be related to the maximum in the spectrum at the instant we have chosen (occurring at $(r/r_0) = 1$). τ_m is the optical depth at the peak of the spectrum and is actually the solution to equation Equation (5.6) for $\tau_m = ClkB^{(p+2)/2}\nu_m^{-(p+4)/2}$ and must be found numerically. The temporal and spectral evolution for vdL66 type events are shown schematically in Figures 5.1 and 5.2, respectively.

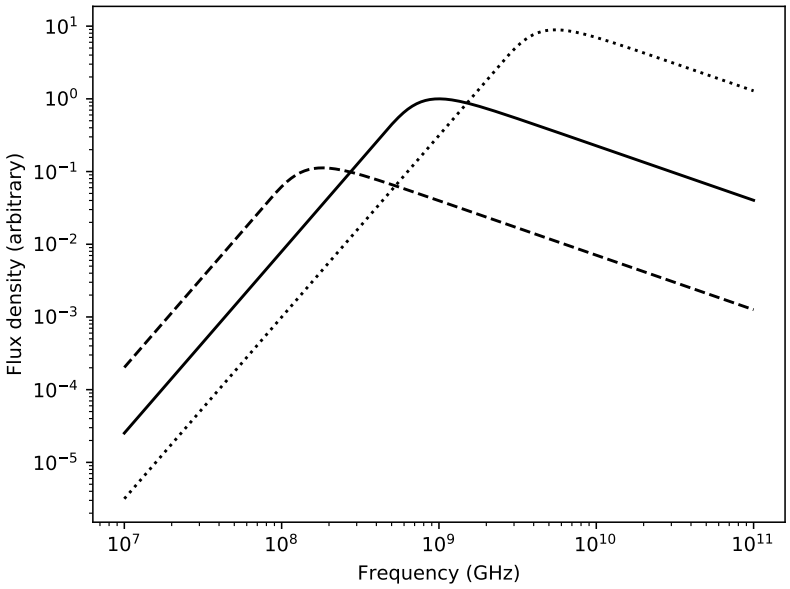

Figure 5.2: The spectral evolution of a synchrotron emitting expanding cloud of electrons according to vdL66 shown at three different relative sizes. The black line is the spectrum at the reference size ($r/r_0 = 1$), the dotted line is at half of the reference size, and the dashed line is at double the reference size.

Some authors formulate the vdL66 model in a slightly different way, by instead of differentiating the source function with respect to frequency and finding how the maximum evolves with emitting region size, differentiating with respect to source size and seeing how the peak in the light curve evolves with frequency. This leads to an equation similar to Equation (5.6):

$$\exp\left[C\theta_0 k_0 B_0^{(p+2)/2}\nu^{-(p+4)/2}\left(\frac{r}{r_0}\right)_m^{-(2p+3)}\right]-\frac{C(2p+3)}{3}\theta_0 k_0 B_0^{(p+2)/2}\nu^{-(p+4)/2}\left(\frac{r}{r_0}\right)_m^{-(2p+3)}-1=0 \tag{5.11}$$

where C is the same as defined in Equation (5.6). Just as before $\tau'_m = C\theta_0 k_0 B_0^{(p+2)/2}$ $\nu^{-(p+4)/2}(r/r_0)_m^{-(2p+3)}$ is an optical depth, however where τ_m was the optical depth at the frequency where the spectrum is at a maximum, τ'_m is the optical depth where the light curve is peaking (which will have the same value for light curve peaks at any frequency). We therefore define the reference time as the time that the light curve at some reference frequency peaks (as opposed to the time at which the spectrum at some reference frequency peaks in the previous case). As mentioned previously these two conditions do not coincide. The reason for this is that the optical depth when the spectrum peaks at some frequency is not the same as the optical depth at the peak of the light curve measured at that frequency ($\tau_m \neq \tau'_m$). This does not change the properties of the model at all, but using one definition or the other can be useful depending on which data are available to fit, which will be taken

advantage of later in this chapter (defining the model with respect to a peak in the light curve is equivalent to defining it with respect to the peak in the spectrum but with a different frequency).

The model of vdL66 is regularly invoked to explain flaring from BHXRBs and Galactic transients (as well as extra-galactic ones, e.g. [276, 277]). It is therefore interesting to examine exactly how well this model can be applied, what inferences can be made using it, and what extensions, if any, are required to explain observational data.

5.2.1 Examples of optically thick radio flares

Given the prevalence of the vdL model there are a surprising lack of BHXRBs (or galactic compact object transients in general) that demonstrate clear and obvious vdL flares, with the signature spectral evolution. Particularly obvious is that, while flares are observed to be, in some cases, optically thick, they are rarely as spectrally steep as predicted (with slopes of 2 or 2.5). One excellent example of a clear vdL type flare, however, was observed from the dwarf nova (accreting binary systems that contain a white dwarf rather than a black hole) SS Cyg [278]. This system was observed during outburst with the AMI-LA and, due to the 5 GHz bandwidth, light curves can be created at three distinct frequencies with good signal to noise in each sub-band. These light curves, as well as the fits and best fit parameters from the vdL model, are shown in Figure 5.3. In this model the fitted parameters are a low level background spectral component (parameterised as $F_{\rm offset} = F_{\rm offset,ref}\nu^a$ where $F_{\rm offset,ref}$ and a are fitted parameters), the flare start time, the flare peak time, the peak flux at the reference frequency, and the optical depth depth at the peak ($t_{\rm start}$, t_0, F_0, and τ_0, respectively). This model does a reasonable job of fitting the data presented in Figure 5.3 with the only caveat being the relatively close frequency bands being used. What information does such a model provide? The fitted value of τ_0 (which is a fitted parameter in the model to save the computationally expensive inversion from p) implies p through Equation (5.11) which is essentially just a description of the optically thin region of the flare. The start and peak times of the flare are in and of themselves are not overly interesting, but provide some information on the size of the expanding region, and the expansion speed required to reach the size at peak. We can write $\beta_{\rm exp} = R_0/(t_p - t_s)$ under the assumption of uniform expansion from a negligible starting volume and therefore we can constrain the speed if we have an expression for the size at peak. Considering Equation (5.1) we can write

$$R_0 = \left[\frac{d^2 F_0 \chi_0}{J_0(1-\exp(-\tau_0))}\right]^{1/2} \tag{5.12}$$

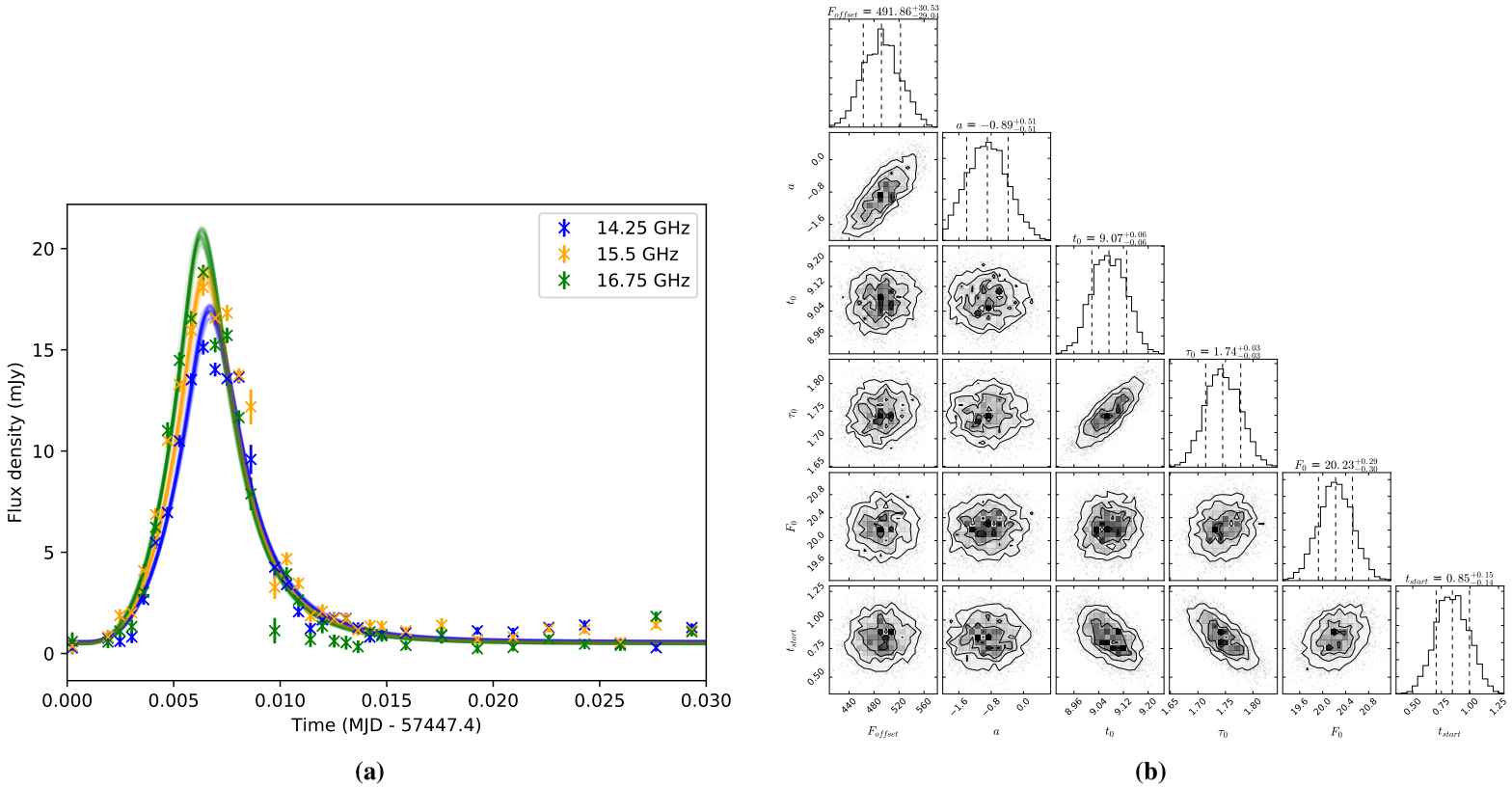

(a) **(b)**

Figure 5.3: (**a**) AMI-LA observations of a flare during an outburst from SS Cyg in three sub-bands, the frequencies are labelled in the legend. Shaded regions of the corresponding colours demonstrate fitting using the vdL model simultaneously to all three bands. (**b**) The posterior distribution for the fits shown in the first panel. Parameters are described in the text and 16.75 GHz was used as the reference frequency. Time in the corner plot are given in minutes since MJD 57447.4. Data originally from [278], where the calibration procedure is outlined.

where we have inferred F_0 and τ_0 from our fits and d is the distance to the source of interest which can be measured independently in a number of ways (see Chapters 1 and 4 for examples). Unfortunately the fits do not provide a constraint on the size of the region, and only provide a constraint on the ratio $\beta_{\rm exp}/R_0$. As we know that, at the peak, self-absorption is causing the turnover we can write

$$R_0 = \left[\frac{d^2 F_0 A(p) B_{\rm ssa,0}^{1/2} \nu_0^{-5/2}}{1-\exp(-\tau_0)}\right]^{1/2} \tag{5.13}$$

where $A(p)$ is a 'constant' that depends on p only (which we determine from τ_0), $B_{\rm ssa,0}$ is the magnetic field assuming synchrotron self-absorption, and ν_0 is the observing frequency at which the peak is seen. To make progress with inferring the physical properties of these flares we need further constraints to the problem. An obvious condition to consider is equipartition, which is regularly assumed to be satisfied for synchrotron emitting plasma. In the case of equipartition, the energy density in the magnetic field is similar to the energy density of the radiating electrons ($E_B = (4/3)E_e$). Minimising the total energy under the assumption of equipartition (for a fixed source size) gives the condition

$$B_{\rm eq,0} = (18\pi c_{12} d^2 F_0 \nu_0)^{2/7} R_0^{-6/7} \tag{5.14}$$

where c_{12} is a 'constant' which depends only on p (see [275, 259] for details). Given, however, that we know the flare peak is due to a transition between the optically thick and thin regimes, we know that at the time of peak the magnetic field is given by the synchrotron self-absorption condition and we have a prescription for how the magnetic field evolves with the size of the source. I have therefore given terms subscript 0 to indicate that I am considering the equipartition magnetic field at the instant when the expanding knot is at a size such that the optical depth to synchrotron radiation is approximately (although not exactly) unity (I have shown previously in this chapter that the optical depth at the peak is not exactly one, but is a weak function of p). This constraint allows for the equipartition magnetic field at this time to be calculated as well as the corresponding size as:

$$B_{\rm min,0} = \left(\frac{144\pi c_{12}}{11}\right)^{4/17} A(p)^{-6/17} d^{-4/17} F_0^{-2/17} \nu_0^{19/17} \left(1-\exp\left(-\tau_0\right)\right)^{6/17} \tag{5.15}$$

and

$$R_{\rm min,0} = \left(\frac{144\pi c_{12}}{11}\right)^{1/17} A(p)^{7/17} d^{16/17} F_0^{8/17} \nu_0^{-33/34} \left(1-\exp\left(-\tau_0\right)\right)^{-7/17} \tag{5.16}$$

The minimum energy occurs close to the condition where the synchrotron self-absorption magnetic field is equal to the equipartition condition. Equipartition, for the case of synchrotron self-absorption with an unknown variable source size, is satisfied when $E_B = (6/11)E_e$. As we now have a constraint on R_0 determined entirely from our fitting (plus the distance) we have also constrained the expansion speed to be

$$\beta_{\rm exp} = \frac{\left(\frac{144\pi c_{12}}{11}\right)^{1/17} A(p)^{7/17} d^{16/17} F_0^{8/17} \nu_0^{-33/34} \left(1 - \exp\left(-\tau_0\right)\right)^{-7/17}}{t_{\rm peak} - t_{\rm ej}}. \tag{5.17}$$

The scaling of the energy contained in the (synchrotron self-absorbed) magnetic field and the energy contained in the electrons are both strong functions of the size and therefore expansion rate. We have (from e.g. Equation (5.2)) that $B_{ssa} \propto r^4$ and therefore $E_B = VB^2/8\pi \propto r^{11} \propto \beta_{\rm exp}^{11}$, and $E_e \propto B^{-3/2} \propto r^{-6} \propto \beta_{\rm exp}^{-6}$. Given the two-sided steepness of the minimum energy curve, the total energy budget quickly becomes unrealistic (examples shown below) for sources slightly out of equipartition (however the total energy budget is still somewhat uncertain as the protons will carry some energy but not emit or absorb synchrotron radiation efficiently, and there is also some kinetic energy, but our calculation is a strong lower limit). The size is better constrained as it is not affected by the 'hidden' energy in the protons (as they do not contribute significant synchrotron radiation or absorption, and thus the sharp minimum energy condition limits the source size to a small range) and the expansion speed is limited by how well we known the launch time.

In [259, 279] we discuss additional constraints that can be placed on the physics of the regions responsible for radio flaring in addition to the magnetic field and size/expansion speed. We obviously constrain the minimum energy, which occurs when the size/expansion rate are those given in Equations (5.16) and (5.17), respectively. The minimum energy under the assumption of synchrotron self-absorption (as well as the assumption of a flat spectrum, i.e. $L = 4\pi d^2 F_\nu \nu$, where L is the source luminosity) is

$$E_{min} = \frac{17}{36}\left(\frac{144\pi c_{12}}{11}\right)^{11/17} A(p)^{9/17} F_\nu^{20/17} D^{40/17} \nu^{-23/34} \left(1 - \exp\left(-\tau_0\right)\right)^{-9/17} \tag{5.18}$$

and we can also estimate the brightness temperature based on our constraints to be

$$T_B = \left(\frac{144\pi c_{12}}{11}\right)^{-2/17} \frac{c^2}{2\pi k_B} A(p)^{-14/17} F_\nu^{1/17} D^{2/17} \nu^{-1/17} \left(1 - \exp\left(-\tau_0\right)\right)^{14/17}. \tag{5.19}$$

The flat spectrum luminosity approximation is not necessary if observations at two frequencies have been made. In this case the luminosity can be calculated based on the measured spectral index. Resolving the constants in Equations (5.15) and (5.17) to (5.19) and recasting observable quantities in commonly used units we finally have the equipartion/SSE estimates

$$\beta_{\rm exp} = 1.7 \times 10^{2} D_{\rm kpc}^{16/17} F_{\nu,\rm mJy}^{8/17} \nu_{\rm GHz}^{-33/34} t_{\rm rise}^{-1} \left(1 - \exp\left(-\tau_0\right)\right)^{-7/17} \tag{5.20a}$$

$$E_{\rm min} = 5.8 \times 10^{35} D_{\rm kpc}^{40/17} F_{\nu,\rm mJy}^{20/17} \nu_{\rm GHz}^{-23/34} \left(1 - \exp\left(-\tau_0\right)\right)^{-9/17} \text{ erg} \tag{5.20b}$$

$$B_{\rm min} = 1.0 \times 10^{-1} D_{\rm kpc}^{-4/17} F_{\nu,\rm mJy}^{6/17} \nu_{\rm GHz}^{19/17} \left(1 - \exp\left(-\tau_0\right)\right)^{-9/17} \text{ G} \tag{5.20c}$$

$$T_{\rm min} = 4.6 \times 10^{10} D_{\rm kpc}^{2/17} F_{\nu,\rm mJy}^{1/17} \nu_{\rm GHz}^{14/17} \left(1 - \exp\left(-\tau_0\right)\right)^{-9/17} \text{ K} \tag{5.20d}$$

which can be determined from simple observables (these can be written in terms of luminosity as well as flux density for the a non-flat spectrum, which I will employ for all calculations below, as was done in [259, 279]). These values deviate slightly from those in [259] as I have not made the assumption of unity optical depth at the peak of the light curve, and also due to factors of order unity discrepancies between the coefficients of the synchrotron emission and absorption coefficients between Longair and Pacholczyk. Note that the expansion velocity is the only parameter that depends on the rise time of a flaring event, and that the brightness temperature is only very weakly dependent on observable parameters and so will not be far altered from 4.6×10^{10}.

There is an additional consideration for the expansion rate in that it is degenerate with the filling factor (f) of the expanding region, as both influence the volume. It is useful to define an effective expansion rate, $\beta_{\rm eff} = f^{1/3}\beta_{\rm exp}$, which encapsulates both of these factors and is the expansion velocity of a totally filled region with the same volume as the partially filled one. For the case where the region is totally filled the effective expansion velocity is the same as the actual one, and for a partially filled region expanding at the speed of light it is $f^{1/3}$. This also allows an effective volume to be defined as $V_{\rm eff} = fV$. The expansion speed defined in Equation (5.20a) is therefore, including a filling factor, an effective expansion speed. It is important to mention why the consideration of a partially filled region does not alter the other parameters. As we are considering a time in the evolution of the emitting region where the optical depth is approximately unity, it is at a point where we can just about 'see' into its centre, and so are sensitive to the entire emitting volume. We are not sensitive, however, to how filled the region is (as long as our source is unresolved), and would derive the same conditions from a volume that is totally filled and therefore covers a small angular

extent, or an identical volume that is sparsely filled but covers a larger angular extent. The fact that the angular extent is degenerate with the filling factor is why it is necessary to define an effective expansion speed. The actual expansion speed is larger than the effective expansion speed by a factor $f^{1/3}$ and so our derived lower limit is still a good one, but not quite as good as the strong energy dependence on effective expansion speed would suggest (this will not alter our conclusions significantly unless the region has an extremely low filling factor, e.g. if the effective expansion β is 0.1, then the real expansion velocity is $c/\sqrt{3}$ for a region that is $\sim 0.5\%$ filled). A similar minimum effective radius can be defined simply as $R_m = \beta_m c \Delta t$ where Δt is the event rise time. The minimum actual radius is always greater than the minimum effective radius in the same way as for the filling factor. So the minimum actual size/velocity are not quite as well constrained as the steep energy dependencies imply.

Returning now to the flare from SS-Cyg shown in Figure 5.3 we can infer the effective expansion beta to be $\sim 8 \times 10^{-3}$, the minimum energy to be $\sim 2 \times 10^{33}$ erg (minimum power $\sim 6 \times 10^{30}$ erg s^{-1} using the event rise time as the timescale for energy input), and the corresponding magnetic field to be ~ 10 G. I have not propagated uncertainties from the MCMC fitting as the minimum energy assumptions made in the derivation of these parameters likely dominate any statistical errors significantly. It is also interesting to examine the effect of the effective expansion speed on the equipartition and synchrotron self-absorption magnetic fields graphically, as this allows the constraint on the minimum energy and expansion speed to be visualised as in Figure 5.4. The top panel shows that the brightness temperature places a strong lower limit on the effective expansion speed. The second panel shows the equipartition and synchrotron self-absorption magnetic fields as a function of effective expansion speed. As we know the flare peak was due to synchrotron self-absorption we can minimise the total energy for a variable source size with the self-absorption magnetic field, as shown in panel three. This minimum occurs close to the effective expansion speed where $B_{\rm ssa} = B_{\rm eq}$ (for a constant source size). The effective expansion speed is well constrained due to the steepness of the dependence of the energy in the magnetic field and in the electrons on the size.

Consider finally the lowest panel in Figure 5.4, where we show the minimum power (using the minimum energy and estimated rise time) under the assumption of synchrotron self-absorption and compare this to the expected X-ray and optical power from SS Cyg. This minimum energy (and therefore power) is very much a lower limit, as the jet could contain energy in non-radiating protons, we don't consider the kinetic energy from the bulk jet motion (although this is likely small), and the synchrotron luminosity is only calculated

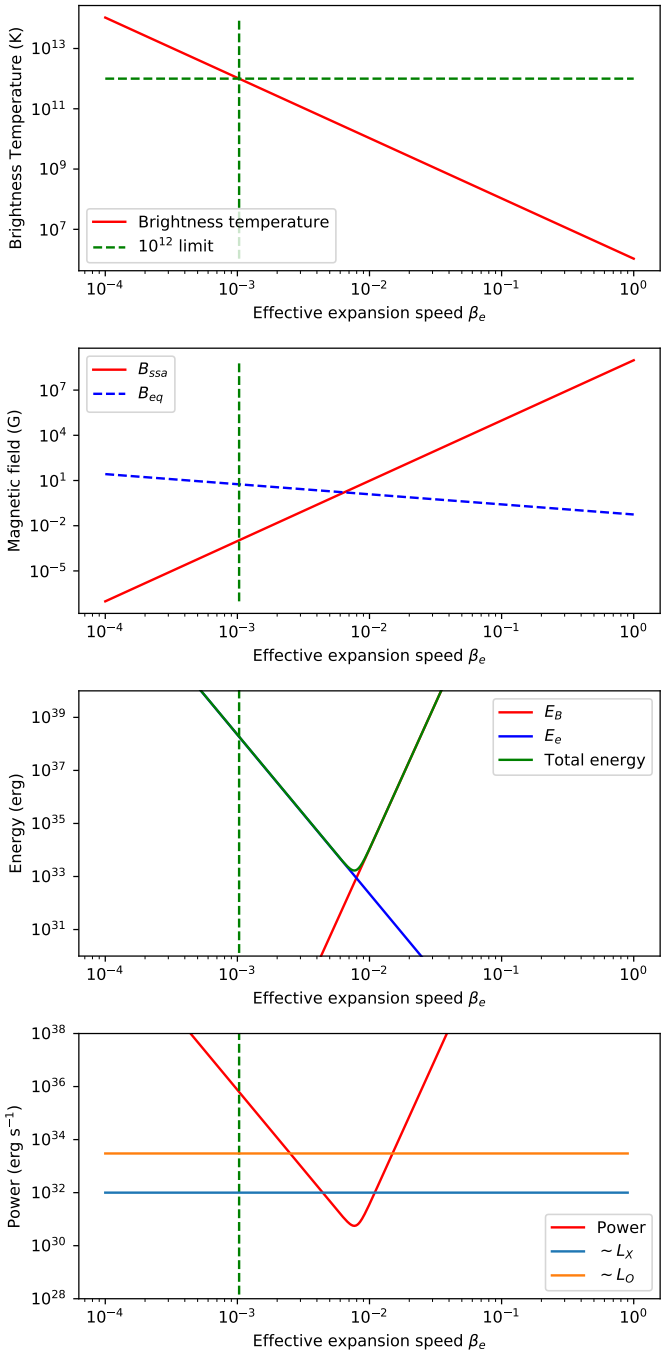

Figure 5.4: Parameters as a function effective expansion speed for the optically thick flare from SS-Cyg shown in Figure 5.3. In descending order the panels show the dependence of the brightness temperature, the magnetic fields (both from self-absorption and equipartition), the energy (in the magnetic field, the electrons, and in total), and the power derived from the flare rise time. In the final panel the approximate X-ray and optical powers at the time of the outburst are demonstrated.

from our observing band. Additionally, at earlier times the emitting region would have contained more energy as expansion losses imply that particles lose energy as $E \propto r^{-1}$. X-ray observations were not conducted simultaneously with our radio observations, so to infer the X-ray power we consider observations from previous outbursts which place the X-ray luminosity between $\sim 10^{31}$ and $\sim 4\times10^{32}$ erg s^{-1} [280, 278, 281]. The total radiative output (traced by optical emission) likely peaks at $\sim 10^{33}$ ergs^{-1} [280]. Based on our estimates we can say that the synchrotron emitting region responsible for the flare was being powered at a level greater than $\sim 10\%$ of the X-ray power and $\gtrsim 1\%$ of the total radiative power. It is worth noting that this is far larger than the power estimate simply considering the observed radio luminosity alone ($L_R \sim 4\pi d^2 \nu F_\nu \sim 10^{27}$ erg s^{-1}). Although these calculations are essentially independent of the assumed geometry (minor alterations to the calculation of Ω will occur for non-spherical sources), it is likely that the source of the radio emission from SS Cyg is a jet, given the outburst similarities with BHXRBs which certainly produce jets.

It is interesting to compare these results for a CV system with similar flaring activity from a BHXRB, for which I choose a flare from V404-Cygni from its 2015 outburst, for a number of reasons. Firstly, observations with the AMI-LA and eMERLIN (Fender *et al*,. in prep) show a flare with clear optical depth evolution (moving from thick to thin) at two well separated frequencies (5 and 15.5 GHz). Secondly, flaring from the same outburst was observed extensively from radio through sub-mm frequencies allowing for extensions to the vdL model to be applied to the data, and the expansion velocity of the expanding region to be derived independently [205]. Finally, V404 has a well constrained distance via radio parallax [282]. The flare and constraints on parameters derived from the profile are shown in Figure 5.5. For this flare we find that $\beta_{\rm eff} \sim 0.1$ at an energy of 8×10^{38} erg and with a magnetic field of 0.7 G. While the expansion speed of the ejection from V404 is comparable to the one we derived for SS Cyg, the minimum energy of the emitting region is larger by five orders of magnitude. It is also interesting to note that our results for both SS-Cyg and V404 Cygni rule out expansion close to the speed of light unless the filling factor is extremely low, as the energy dependence would, for larger expansion speeds, quickly exceed the Eddington limit by many orders of magnitude (due to the scaling of the minimum energy of the magnetic field going as β^{11}, see panels three and four of Figures 5.4 and 5.5, respectively). The value of the filling factor is, however, uncertain and an independent check on our inferred expansion speeds would be useful. For V404 Cygni this opportunity was provided during its 2015 outburst, where [205] carried out an exquisite set of radio and sub-mm observations with excellent sampling over a ~ 5 hr period of radio flaring. These observations revealed a number of temporally sharp radio flares as

measured at mm-wavelengths which were temporally smeared out and delayed at longer wavelengths. This is indicative of optical depth evolution as discussed previously in this Chapter. The number of flares (eight in total), and the eight distinct frequencies they were observed at, allowed the authors to fit multiple vdL like flares while extending the model to be more constraining. As mentioned previously, in the baseline formulation of the vdL model the expansion velocity is degenerate with the size of the emitting region at the peak at a given frequency, a degeneracy we avoided by considering the minimum energy condition in conjunction with that of synchrotron self-absorption. Another way to disambiguate these two quantities is through a consideration of the bulk motion of the emitting region, the opening angle of the region as it expands, which is assumed to be constant, and the fact that systems are typically observed to produce bipolar ejections travelling both away from and towards Earth. An observer will then see an optical depth evolution flare from both the approaching ejection and the receding ejection, with the timescales and amplitudes modified by relativistic and light travel time affects. These modifications allowed, with extensive MCMC maximum likelihood calculations, for the bulk Lorentz factor to be calculated, as well as the opening angle and inclination (which is well constrained in V404 Cygni), which together with fitting the rise time of the flare gave the size at peak. It is encouraging to note that the expansion velocities (which are true expansion velocities, rather than effective ones) inferred by this method are consistent with the significantly sub-relativistic value we obtain for V404 Cygni (from our work $\beta_{\rm eff} \sim 0.1$, and the values from [205] are in the range 0.01 to 0.1 from the 8 flares they fit). The free expansion velocity of a relativistic spherical region is $c/\sqrt{3}$ and so both methods for measuring the expansion speed indicate a significantly confined jet during the 2015 outburst of V404 Cygni.

In most cases data quality is not sufficient to fit this extended version of the vdL model, as it requires multiple frequencies as well as a sub-mm component to disambiguate flaring events. Simply fitting the standard vdL model from [258] is the best that can be done for most observed flares, and then inferring additional information from the minimum energy constraint. Even if the entire flare is not well sampled, and the vdL model cannot be applied directly to the data, if a peak is observed and there is evidence for optical depth evolution from thick to thin then similar calculations to those outlined above can still be made. This is the case as the expansion speed is the only quantity I have discussed that is dependent on the rise time of the event. Fitting the data directly is a more accurate method of determining the peak flux and the rise time in the cases where it is probed. Additionally, even if a light curve consists of multiple superimposed flares, if optically thick to thin spectral evolution and a light curve peak is observed then the above method can be applied as, at the time

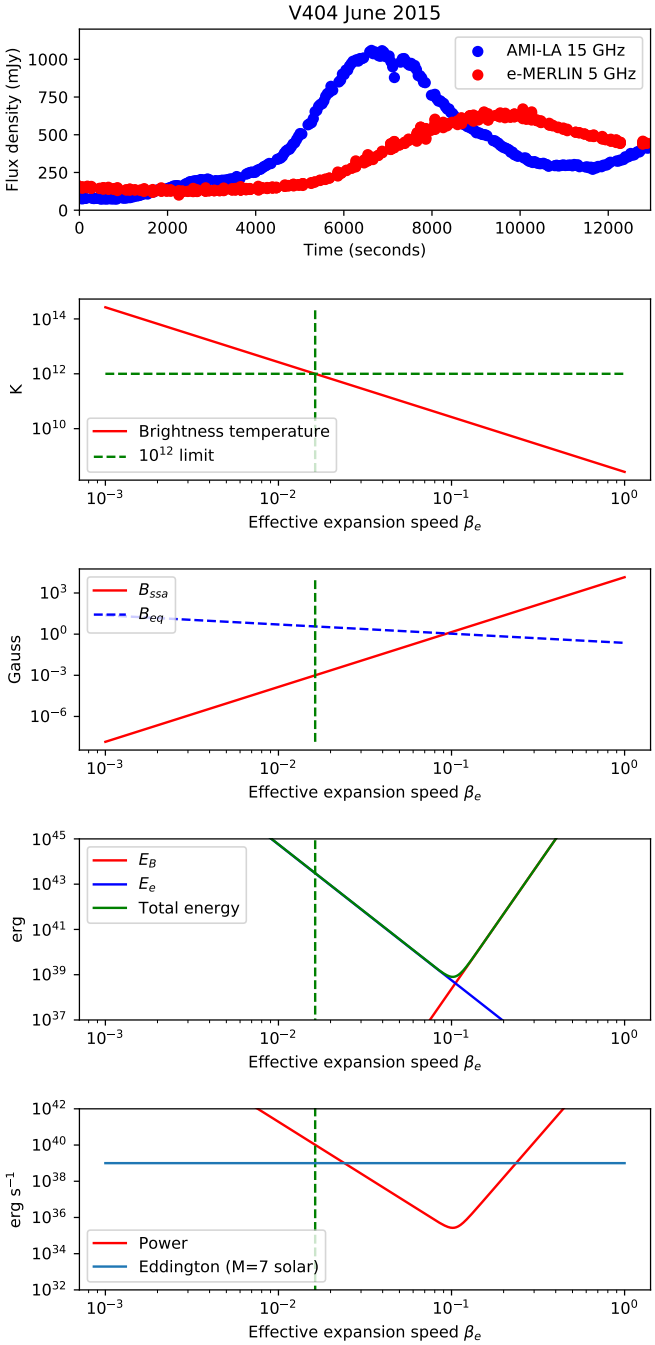

Figure 5.5: Parameters as a function effective expansion speed for the optically thick flare from V404-Cyg from its 2015 outburst. In descending order the panels show the dependence of the brightness temperature, the magnetic fields (both from self-absorption and equipartition), the energy (in the magnetic field, the electrons, and in total), and the power derived from the flare rise time. In the final panel the approximate X-ray and optical powers at the time of the outburst are demonstrated.

of turnover, the optical depth of the dominant emitting region is approximately unity. The results in this case should be taken with more caution however, as closely spaced flaring events could cause an overestimation of the peak flux.

Another apparently excellent example of an apparent vdL type flare has been seen from the X-ray binary Circinus-X1 (see figures 3 and 4 in [283]) demonstrating the classic evolution from optically thick to thin. Without fitting the data directly this may appear to represent the evolution associated with a vdL flaring event, however the calculation of a few key diagnostics and a comparison with the data show otherwise. Due to the simplicity of the spectrum and spectral evolution from the vdL model, the ratio of peak fluxes at different frequencies/times, as well as the time difference between them, are well defined. We have the conditions that:

$$S_m(\nu_2) = S_m(\nu_1)\left(\frac{\nu_1}{\nu_2}\right)^{-(7p+3)/(4p+6)} \tag{5.21a}$$

$$t_2 = t_1\left(\frac{\nu_1}{\nu_2}\right)^{(p+4)/(4p+6)} \tag{5.21b}$$

which apply to the peaks of either the light curve or spectrum.

Considering flare two from [283], which peaks at ~ 1.2 Jy at 8.5 GHz, we would expect its peak flux at 1.9 GHz to be in the range ~ 0.007 to ~ 0.02 Jy for p between 2 and 3. Considering that the peak at the higher frequency arose ~ 0.5 d after the start of the flare, the peak at 1.9 GHz should occur between ~ 0.9 and ~ 1 days after the flare start for p between 2 and 3. The time delay is consistent with their observations, however the peak of the flare at 1.9 GHz is ~ 0.8 Jy, which is much higher than predicted by the vdL model. Given the discrepancy in peak flux it is clear that, despite the evolution appearing vdL-like, the evolution of Circinus X-1 cannot be explained from a single vdL event (confirmed by attempts to fit the data with such a model not finding convergence). It is possible that the vdL model is still applicable but that the radio emission results from a number of flaring events which are unresolved (due to temporal smearing) in the GHz range observations. A similar deviation from the vdL model is also evident in the flare from V404 Cygni shown in Figure 5.5, where, for the vdL model, the ratio of the peaks at the upper and lower frequencies should be ~ 4 to ~ 5, which is clearly not the case, with the lower frequency appearing to have a much higher flux than expected (or, conversely, the higher frequency peaking at a flux value that is too low). I will denote these types of flares as 'anomalously

thick', indicating that they follow the generally expected thick to thin evolution but not in a way consistent with the vdL model.

5.2.2 Anomalously thick flares

At this point it is useful to define a new quantity which I will call the peak to peak spectral index, $\alpha_p = \log(F_1(t_1)/F_2(t_2))/\log(\nu_1/\nu_2)$. This differs from the standard spectral index in that it is the power law index associated with the flux at peaks occurring at t_1 and t_2, where we do not require $t_1 = t_2$. Defining this will allow for quantitative comparison between flares and the vdL model, as well as allowing us to see if certain modifications to the model alter α_p in such a way as to better reproduce observational data. Equation (5.21a) gives the peak to peak spectral index for the vdL model to be $(7p + 3)/(4p + 6)$ which is only weakly dependent on p and, for characteristic values of p, is expected to be in the range 1.2 to 1.3. Rather than only considering individual flares, I have accumulated observations of a total of 64 radio flares from 6 sources (including the two flares shown graphically previously in this chapter) and calculated the peak to peak spectral index from the observations, which are shown in Figure 5.6. This shows that, for this (still relatively small) sample of flares, that almost none of the measured peak to peak indices are close to that predicted by the vdL model, even in the case where qualitatively they appear to agree with it (having a positive α_p). In almost all cases the lower frequency is peaking at a higher flux density than expected, and in some cases is peaking higher than the higher frequency. These flares are optically thin throughout and discussed in the next section. The only exception to this is the flare from SS-Cyg (Figure 5.3). The peak to peak index in this case was derived from light curves created at two frequencies within the observing bandwidth of one receiver, and so is perhaps less reliable than the rest of the sample which are derived from either distinct instruments or distinct receivers on the same instrument. Considering these caveats, the peak to peak index is not too dissimilar from the vdL value. Generally, any model that is designed to fit radio flares from compact objects must be able to 'flatten' the the peak to peak spectral index closer to 0 from the vdL model's value.

There are a few notable ways that the peak to peak spectral index could be flattened. Consider a number of temporally distinct vdL-like flares observed at higher frequencies, and how these would appear at lower frequencies. The vdL evolution of flares prescribes that they will peak at lower total fluxes and will have their peaks delayed. The distinct high frequency flares appear as a single smoothed flare at lower frequencies with a combined flux $\lesssim$ than the sum of the expected flux from evolving each flare distinctly. This buildup of flux will be evident at any frequency low enough such that the flares have blended together

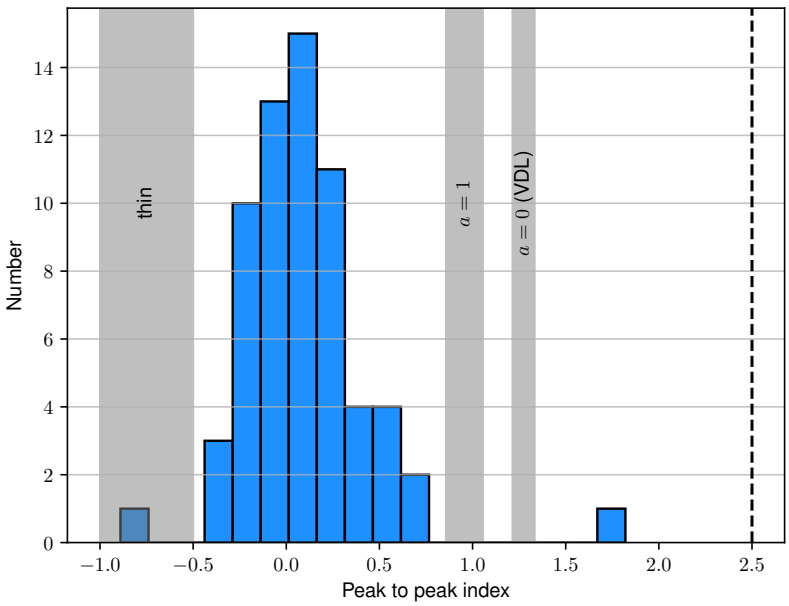

Figure 5.6: The peak to peak spectral index for 64 radio flares from the sources Cygnus X-3 (27 flares, data from the GBI), LS I +61 303 (16 flares, data from the GBI), GRS 1915+105 (12 flares, data from the GBI), Sco X-1 (4 flares, data from the GBI), SS-Cyg (1 flare, data from the AMI-LA), V404-Cygni (4 flares, data from the AMI-LA). Regions of interest are highlighted in grey. From left to right these are: a typical optically thin spectral index ($F_\nu \propto \alpha^{-(p-1)/2}$) (labelled 'thin'), the peak to peak index for constant particle injection (labelled $a = 1$), and the expected peak to peak index for the vdL model (labelled $a = 0$). All are calculated for p in the range 2 to 3. The dotted vertical line is the expected index during for an optically thick region which is not dependent on p (i.e. standard synchrotron self-absorption for $\nu_a > \nu > \nu_m$ in GRB models).

and so will increase the flux at both of the peaks and therefore flatten the peak to peak spectral index. However this effect is not as drastic as you might first expect, as at lower frequencies the peaks of the flares will be more spread out and thus the maximum of the blended light curve will be enhanced less than at higher frequencies where the flares are more tightly packed. Overlapping flares can also explain why the spectral index during the rise of flares does not reach the expected 2.5, as the decline phase of previous flares will add optically thin flux to the rising phase of later flares and reduces the (actual) spectral index. Another way that the peak to peak spectral index can be flattened is if the bulk velocity of the emitting region is being reduced with time for configurations with Doppler factors less than one (i.e. 'de boosted').

In addition to multiple flares and relativistic affects, another possibility for the discrepancy seen in the peak to peak index (for flares like those from [283], Figure 5.5, and flares with peak to peak index below zero) is that the condition of impulsive particle acceleration (as assumed in the vdL model) is not valid. It is appropriate to consider how the continual addition of high energy electrons to the emitting region will change its emission properties. The condition of a constant number of electrons in the emitting volume is explicit in Equations (5.4) and (5.5) and was used to derive the condition that $k = k_0(r/r_0)^{-(p+2)}$ where $N(E) = kE^{-p}$. A more complete consideration of the kinetic equation for adiabatically cooling electrons leads to the condition

$$N(E,t) \propto r^{1-p}E^{-p}\int_0^t Q(t')dt' \tag{5.22}$$

where Q is an injection function [284, 285, 286, 287]. In the vdL model there is no particle injection and so $Q(t') = \delta(t')$, implying that $n(E,t) \propto r^{-(2+p)}E^{-p}$ (and so we recover the condition $k = k_0(r/r_0)^{-(p+2)}$) and that the total number of particles is constant ($\int_{E_{max}}^{E_{min}} N(E,t)dE \propto r^{1-p}E^{1-p} \propto r^0$ as the expansion is adiabatic). The exact form of the injection function is likely complex and source dependent, but to make progress it is worth considering how simple functional forms alter the observed radio evolution. The simplest to consider is a polynomial injection function where the total number of electrons increases as a power law with index a with time (with the potential to decline to zero at some point). This is equivalent to an injection function $Q \propto t^{a-1}$. We should therefore reconsider Equations (5.7) to (5.9) but instead of using the condition $k = k_0(r/r_0)^{-(p+2)}$ we use $k = k_0(r/r_0)^{-(p+2-a)}$. Doing so shows that while the flux rise rate in the optically thick regime is unchanged, the decay rate is slowed down to having a power law index $-2p + a$ from $-2p$ in the case of a standard vdL flare. For $a \gtrsim 4$ the optically thin part of the light curve never peaks and continues to rise with time until the injection of particles becomes

less dramatic or stops. Before performing any calculations lets first consider what changes when additional particles are being added to the emitting region as it emits. Consider observing at some high frequency, where we would see rising flux followed by an optically thick to thin transition. At some lower frequency there will also be a rising flux density to start, and the peak will be delayed due to the optical depth dependence on frequency. This delay will be longer than for the vdL model as the additional particles that are present for the peak at our lower frequency will prolong the optically thick phase of the evolution. Once the optically thin phase is reached there are more synchrotron emitting electrons and thus the flux is higher as the energy losses have been offset. This will flatten the peak to peak index as required.

In line with our method of derivation for the vdL flares we can opt to either define this modified version of the model in terms of the maximum of the spectrum at some reference time or the light curve at some reference frequency. Given that we are considering time series data I opt to do the latter. Considering where the source function peaks as a function of source size we get the conditions **(1)** $S_m = S_{m0}(\nu/\nu_0)^{(7p+3-5a)/(4p+6-2a)}$ and **(2)** $(r/r_0)_m = (r/r_0)_{m0}(\nu/\nu_0)^{(p+4)/(4p+6-2a)}$ (i.e. updated versions of Equation (5.21)) which describe how the peak flux of the light curve evolves with frequency, and how the time of peak evolves with frequency, respectively. These equations show the light curve peaks first at higher frequencies, and with a greater flux (for most cases), as expected. There is a region of parameter space for which the peak at lower frequencies is *larger* than the one at higher frequencies. This occurs when $(7p + 3 - 5a)/(4p + 6 - 2a) < 0$, or $(7p + 3)/5 < a < 2p$. Where I have used the condition that if $a > 2p$ then the light curve never peaks at any frequency. For $p = 2.2$ the allowed range of a is rather narrow ($3.4 < a < 4$) and would imply an extremely shallow flux decay index of $-0.6 < -2p + a < 0$. Expression **(1)** leads to a general definition for the peak to peak spectral index under the condition of polynomial particle injection, $\alpha_p = (7p + 3 - 5a)/(4p + 6 - 2a)$, while expression **(2)** describes how particle injection will change the delays between peaks. It is clear that for $a > 0$ the peak to peak index will be closer to zero, and the delays between peaks extended, compared to the vdL model. For the case $a < 2p$ the light curve never peaks at any frequency as the injection of new particles overcomes the adiabatic expansion (unless the injection rate drops or goes to zero). With the addition of particle acceleration the temporal and spectral flux evolution from the emitting region can be written as

$$S(\nu, r) = S_{m_0}\Big(\frac{r}{r_0}\Big)^3\Big(\frac{\nu}{\nu_{m_0}}\Big)^{5/2}\frac{1 - \exp\big(-\tau_m(\frac{r}{r_0})^{-(2p+3-a)}(\frac{\nu}{\nu_{m_0}})^{-(p+4)/2}\big)}{1 - \exp(-\tau_m)} \tag{5.23}$$

where all terms have been defined previously, but τ_m is now generally given as $\exp(\tau_m) - \tau_m((2p+3-a)/3) - 1 = 0$. With this modification the peaks in light curves at successively lower frequencies still decreases but will do so more gradually when compared to the vdL model. The times of the peaks are more spread out than in the vdL model. It is actually the case that, regardless of the form of the injection function, as long as it is continuous, a modified version of the vdL model can be written as

$$S(\nu, r) = S_{m_0} \left(\frac{r}{r_0}\right)^3 \left(\frac{\nu}{\nu_{m_0}}\right)^{5/2} \frac{1 - \exp\left(-\tau_m \left(\frac{r}{r_0}\right)^{-(2p+3)} \left(\frac{\nu}{\nu_{m_0}}\right)^{-(p+4)/2} f\left(\frac{r}{r_0}\right)\right)}{1 - \exp(-\tau_m)} \tag{5.24}$$

where $f(r/r_0)$ describes the injection process of particles (so in the case of linear expansion $f(r/r_0) = r/r_0$). How the functional form of f affects the condition for the optical depth at the peak needs to be considered on a case by case basis for maximising with respect to time (the optical depth at the peak of the spectrum is not changed through the injection of particles). Whatever the form of the injection function it does not have the ability to modify the cubic rise in the optically thick limit, only to alter the form and time of the turnover as well as the shape in the optically thin region. Figure 5.7 shows the flare from Figure 5.5 now fit with both the vdL and a polynomial particle injection model. While it is clear that particle injection is more properly describing the ratio in peaks for this flare from V404 Cygni, the time of peaks is still not correct (the increased spacing is an unavoidable by-product of continued particle injection). It is possible that a different form of particle injection function could correct for this spacing issue. Two natural extensions are i) particle injection that is peaked, and ii) polynomial particle injection that stops at a certain time. Such configurations could provide the additional electrons required to produce the high second peak, but if the injection stops before the second peak occurs then the delay will not be as large as for constant injection [285, 287].

5.3 Optically thin radio flares

Some flares evidently do not follow the expected vdL evolution even in the case of particle injection, and instead remain optically thin throughout their evolution. These flares simply cannot be explained as being due to optical depth evolution, even when considering the possibility of multiple overlapping flares. Inferences on the conditions of the physical regions causing these events are more difficult as, unlike for thick flares, we do not have both

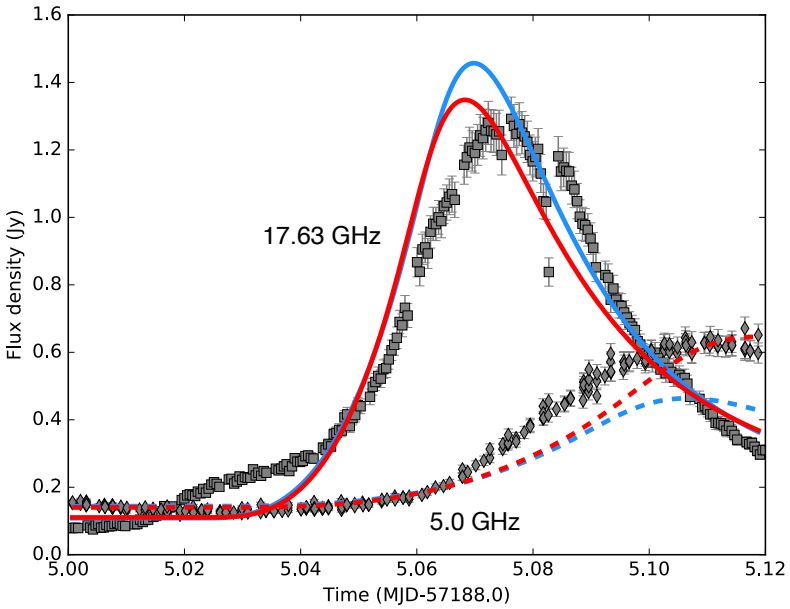

Figure 5.7: A anomalously optically thick radio flare from the BHXRB V404 Cygni observed at 5.0 (grey diamonds) and 17.63 GHz (grey squares), respectively. I show two model fits to the data, the blue curves show the best fitting vdL model whereas the red curves show a model with polynomial particle injection ($a \sim 3$ from the fitting). The solid curves fit the higher frequency data whereas the dashed curves fit the low frequency data.

the equipartition and optical depth constraints at the flare peak. We are therefore forced to make more crude estimates on physical parameters. Firstly, we can make the assumption that the physical size of the region is limited to $t_{\rm rise}c/\sqrt{3}$ (even though we've seen in the previous section that this is, at least in some cases, a significant overestimate) and calculate the minimum energy magnetic field (Equation (5.14) and the corresponding minimum energy). Two flares from the XRB Cygnus X-3 are shown in Figure 5.8 (that were also part of the sample presented in the previous section) at 2.25 and 8.3 GHz, along with the evolution of the associated two-point spectral index. The first (lower amplitude) flare does show some evidence for thick to thin optical depth evolution, however the second (higher amplitude) event appears optically thin throughout. The peak of the flare is best defined at the lower frequency, and we estimate a rise time of ~ 20 d and therefore a maximum size of $\sim 3\times10^{14}$ m. The equipartition magnetic field is then (taking a distance of 7.2 kpc [288, 289], and the flux at peak as 18 Jy) 22 G and the corresponding minimum energy is 7×10^{43} erg. Performing a similar calculation for the optically thick flares from V404 Cygni discussed in the previous section does not give drastically different results for the minimum energy as compared to the assumption of self-absorption, but the SSA condition removes the assumption of the size (and therefore magnetic field) and so better constrains the physical parameters of the system. So from this weaker method we can place lower limits on the

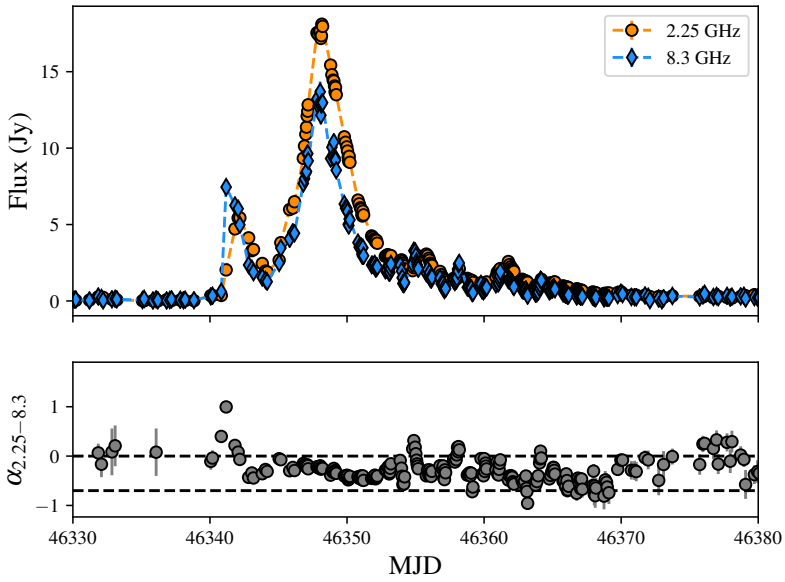

Figure 5.8: Two radio flares from Cygnus X-3 observed with the Green Bank Interferometer (GBI). The top panel shows the flux evolution at 2.25 and 8.3 GHz, whereas the bottom panel shows the spectral index between those frequencies where the error on the index was below 0.5.

magnetic field and minimum energy, although the assumption of free expansion means they are weak lower limits.

As for the anomalously thick flares previously considered, particle injection plays an important role in the evolution of thin flares. While the rise time of a thick flare is probing the time required for the emitting region to reach approximately unity optical depth, the same is not true for the thin flares. The reason that optically thick flares rise is that the expanding region takes up a larger angular size on the sky while being self-absorbed, in the case of optically thin flares the rise is likely caused by continued particle acceleration of an optically thin region countering the expansion cooling, and the turnover is now the point where the continued energy injection ceases. Another indication that this is the case is the apparently achromatic break seen in Figure 5.8 (see also [242, 243, 240], as well as the GBI archive, for more examples). While thick flares peak at later times at lower frequencies (taking longer to become optically thin) all frequencies experience particle injection (and its termination) simultaneously, and the different peak flux value is just indicative of the synchrotron spectrum. Consider a synchrotron emitting region observed at a frequency such that it is optically thin. If the region expands the observed flux density declines as $-2p$ due to the electrons in the region cooling adiabatically. However, in the case of polynomial particle injection the decline goes as $-2p + a$ which, as mentioned previously, gives a rising optically thin emitting region for $a > 2p$ (note that while this is easiest to formulate for

polynomial injection, any injection function that is applying electrons significantly quickly could mimic this effect). At some point an optically thin flare begins to decline and resumes the expected rate of flux decay due to the particle injection stopping. This tells us about two interesting time scales in the regions responsible for radio flaring. Firstly the rise time of the flare is the timescale that particle injection, secondly the duration of the flare turnover tells us about the rate that the injection function switches off. At some sufficiently low frequency a thin flare might appear thick, and would then follow the evolution discussed previously for the so-called anomalously thick flares.

5.4 Conclusions

Black hole X-ray binaries, other galactic compact object transients, nearby SMBHs (e.g. Sgr A* [276, 277]), distant AGN, some SNe, GRBs, and more, demonstrate synchrotron flaring showing evidence of optical depth evolution in the emitting region. Since the 1960s simple models of expanding regions have been invoked to explain these observed events, to varying degrees of success. I have presented evidence here that, in the case of > 50 flares from XRBs, that the simple model of vdL66 cannot explain the observed temporal evolution, mostly due to an inability to predict the ratio of flare peaks at different frequencies. In some cases - the optically thin flares - optical depth evolution is completely unable to describe the light curve morphology. I have shown that, in the case of many optically thick flares, the peak to peak spectral index as presented in vdL66 needs to be 'flattened', and have given initial evidence that particle acceleration is able to play this role for these anomalously thick flares. For the optically thin flares particle acceleration is almost certainly the physical mechanism driving the flare morphology, where we probe the timescale of particle acceleration (and its switch off). The analysis presented here will be extended to include more models of particle injection, and individual sources will be examined in more detail in a future work (Bright et al. *in prep.*).

Adiabatic expansion in core radio jets is expected to lead to catastrophic energy losses, and thus an unreasonably high input power and accretion rate [290]. It is thought that constant re-collimation is the mechanism hindering such expansion [291]. The model of vdL66 explicitly invokes adiabatic expansion to explain radio flaring, and predicts the general optically thick to thin evolution seen from many flares from BHXRBs (although it does not accurately reproduce the flux radio at different frequencies, a problem potentially solved by ongoing particle injection). In this chapter I have also invoked particle acceleration to explain the so-called optically thin radio flares, which show a flat or slightly inverted

spectrum similar to collimated core jets. It could be, therefore, that the optically thin radio flares originate from a more traditional flat spectrum jet, rather than from ejections. I will not discuss this in any more detail, but note that sources (for example Cygnus X-3; [292]) show flaring episodes consisting of both thin and thick flares. I therefore find it unlikely that a different 'form' of jet is responsible for the thin flares, as this would require rapid evolution of the jet geometry.

Chapter 6

A multi-frequency radio study of the long GRB 171010A

This chapter is based on work published in Bright, J. S. *et al.* A detailed radio study of the energetic, nearby and puzzling GRB 171010A. MNRAS **486**, 2721-2729 (2019).

6.1 Introduction

Long gamma-ray bursts (GRBs) and their associated afterglow are some of the most energetic transient events in the Universe. They are believed to be the result of the core collapse of massive stars (see e.g. [293] for a review of GRB progenitor systems) due in part to their association with supernovae [294, 295], although supernovae are not always found with long GRBs [296, 297, 130]. The emission from GRBs is typically separated into two temporal phases: 'prompt' emission in γ-rays, and 'afterglow' emission which is broadband (ranging from radio to high energy X-ray frequencies) and can be detected months or even years after the GRB is first detected (e.g. [298, 299]). The prompt emission is thought to be produced in processes internal to the out-flowing material, with magnetic reconnection and internal shocks both invoked as the physical process responsible [300, 301, 302]. The afterglow is the result of the ejected material interacting with the circumburst environment, which results in broadband synchrotron emission from shock accelerated electrons [303, 304, 141]. This outflow is believed to be an initially collimated and highly relativistic jet [305, 306]. The presence of such a high velocity jet is invoked as the solution to the so called 'compactness problem', which arises when considering the optical depth to pair production in regions of size $c\Delta t$ where Δt is the typical variability timescale of the prompt emission from a GRB. Combining the typical fluence from a GRB with the compact region implied by the variability timescale (~ 1000 km) provides an extremely high optical depth to the production of electron positron pairs. This condition appears at odds with the

clearly non-thermal (not self-absorbed) γ-ray spectra observed from GRBs. This problem is avoided if the outflow is significantly relativistic (note that this does not necessarily imply the outflow is anisotropic). Not only is the rest frame energy of the photons reduced by a factor γ compared to the observer's frame (meaning there are a smaller fraction of photons able to produce pairs), the radius implied by the variability timescale is reduced by a factor γ^2. These effects combined are enough to reduce the optical depth to pair production to $\tau_{pp} \lesssim 1$ for $\gamma \approx 100$ [307, 308]. Relativistic beaming (in the event that the outflow is not only relativistic but also collimated into an angle θ) plays a role in the inferred event rate (enhancing the rate by a factor of $4\pi/\theta^2$ with respect to the observed one) as well as the intrinsic energy of GRBs, reducing the total energy by a factor of $\theta^2/4\pi$ with respect to the inferred isotropic equivalent and bringing the inferred total energy down by roughly two orders of magnitude [309] (and therefore reducing the very high conversion efficiency of stellar mass to observed radiation).

6.1.1 The Fireball Model

Both the prompt and afterglow emission from GRBs are typically interpreted in the context of the fireball model [310, 311, 312], detailing the evolution of the jet and its eventual interaction with the circumburst material. I will focus mainly on the afterglow interaction as its evolution will be the subject of this chapter, but I will briefly describe the early evolution of the fireball which results in the prompt emission and sets the initial conditions for the interaction of the fireball with the ISM. The evolution of a fireball will depend on its make-up, with the simplest case being one that is purely dominated by radiation. Such a fireball will initially be (as discussed in the compactness problem) optically thick to pair production but will, after expansion, eventually become optically thin to pair production and radiation 'escapes'. Such a fireball would not produce the spectrum associated with the prompt emission from the GRB [307]. In a more realistic case baryonic matter will likely be entrained with the radiation, and some of the input energy will go in to accelerating this component. For a baryonic fireball the interaction between electrons and photons can delay the onset of radiation escape, but eventually the fireball will become matter dominated (where the majority of the energy is the kinetic energy of the baryons). Different shells of material in the fireball will have different Lorentz factors and these will therefore collide with one another, converting the kinetic energy of the baryonic matter into radiation and producing the observed γ-rays [28, 300]. While the fireball model considers a spherically symmetric relativistically expanding sphere, in reality the outflow will be collimated (jetted). However, due to the high bulk Lorentz, factor elements of the fireball decouple from other elements if separated

by small angular scales, due to beaming and each element acting independently the situation can, despite the non-spherical nature, be well approximated by a spherical shell model.

While the internal shocks account for the early time γ-ray emission they do not explain the long lived and broadband afterglow emission observed from GRBs. This process is mediated by shocks generated as the shells of the fireball drive into the ISM, which acts to convert the kinetic energy of the baryons to radiation through shock acceleration and can emit over weeks to years (in the observers reference frame). The afterglow from GRBs is the relativistic analogue to supernova, but GRBs lose significantly less mass, while accelerating the mass they do lose to much higher velocities (compared to the non-relativistic supernova shells). As the interaction occurs, two shocks form – a forward shock (FS) and reverse shock (RS) – and accelerate electrons into a power law energy distribution ($N(\gamma_{\rm e}) \propto \gamma_{\rm e}^{-p}$, with p typically in the range 2 to 3). These electrons emit via the synchrotron process as they spiral in the shock-enhanced magnetic field. The broadband spectrum from each shock is expected to be described by a series of power laws, with breaks occurring at the synchrotron self-absorption, minimum electron, and cooling frequencies ($\nu_{\rm a}$, $\nu_{\rm m}$ and $\nu_{\rm c}$, respectively; [141]). The exact values of the power law indices describing the spectrum depends on the ordering of these frequencies [312], with $\nu_{\rm m} < \nu_{\rm c}$ defined as the slow cooling and $\nu_{\rm c} < \nu_{\rm m}$ the fast cooling case (see Chapter 2 for details).

The FS propagates into the circumburst material and is decelerated from its initially relativistic velocity. The temporal and spectral evolution of the emission from the FS depends on the density profile of the circumburst material, which is typically assumed to vary as $\rho(r) \propto r^{-k}$, with $k = 0$ for a constant density (ISM-like; [141, 313]) environment and $k = 2$ for a wind-like environment, such as might be produced around a Wolf-Rayet star (e.g. [314, 315]). For a constant density ISM and the fast cooling case the evolution can either be adiabatic (slow energy loss via radiation compared to the shock evolution) or radiative (electrons quickly radiate their energy and are limited by the energy generation of the shock [316]). This depends on the value of ϵ_e (the fraction of energy that is imparted to the electrons, with a larger value implying more efficient acceleration of particles) and ϵ_B (the fraction of energy that is imparted to the magnetic field, with a larger value implying a smaller synchrotron cooling time) which will influence how the break frequencies evolve with time. The energy density in electrons and the magnetic field are difficult to derive observationally, however there have been cases where authors have inferred values for each parameter not significantly less than unity, and not dissimilar from one another (implying at least approximately that equipartition is satisfied [304]). Even with ϵ_e and ϵ_B being close

to unity, the cooling time must be less than the dynamical one in order for a shock to be radiative.

For a constant ISM density profile in the adiabatic (radiative) case the cooling break evolves as $\nu_c \propto t^{-1/2}$ ($\nu_c \propto t^{-2/7}$) whereas the minimum energy break evolves as $\nu_m \propto t^{-3/2}$ ($\nu_m \propto t^{-12/7}$) [141]. Therefore a populations of electrons that is initially fast cooling will always end up in the slow cooling regime eventually. The self-absorption break moves as $\nu_a \propto t^{-1/2}$ ($\nu_a \propto t^{-4/5}$). Once the electron population is in the slow cooling regime the shock can only evolve adiabatically (note that a shock can be evolving adiabatically even if the electrons are fast cooling if the dynamic timescale of the shock is shorter than the cooling timescale). Slow cooling electrons always produce an adiabatically evolving shock and ν_m and ν_c evolve as in the fast cooling adiabatic case. In the slow cooling case the self-absorption break does not evolve with time for a constant ISM density and so, again, the minimum energy break will always end up below the self-absorption break.

In the case of a wind like ISM density profile the evolution is different. For adiabatic (radiative) shock evolution in the fast cooling case the cooling break evolves as $\nu_c \propto t^{1/2}$ ($\nu_c \propto t^{1/3}$) whereas the minimum energy break evolves as $\nu_m \propto t^{-3/2}$ ($\nu_m \propto t^{-5/3}$) and the self-absorption break moves as $\nu_a \propto t^{-8/5}$ ($\nu_a \propto t^{-22/15}$) [313, 317]. For adiabatic shock evolution in the slow cooling case the cooling break evolves as $\nu_c \propto t^{1/2}$, whereas the minimum energy break evolves as $\nu_m \propto t^{-3/2}$ and the self-absorption break moves as $\nu_a \propto t^{-3/5}$ [313]. So we have the same general (although with different exact power laws) evolution from fast to slow as for the constant ISM case.

The flux in the different spectral segments in the fast and slow cooling case (see Chapter 2) also evolve with time in a way that again depends on the nature of the ISM density profile as well as the adiabatic/radiative nature of the evolution. As there are four segments to a synchrotron spectrum each with flux evolution that varies depending on the order of the break frequencies, the ISM density profile, and the nature of the evolution (adiabatic/radiative) it is simpler to present the possible evolution channels graphically as in Figures 6.1 and 6.2, which show the evolution of the fast and slow cooling spectrum for a ISM and wind like density profile. I do not include the radiative case for the flux evolution, mainly as I will show below that the shock evolution from GRB 171010A is consistent with being adiabatic (based on analysis of the X-ray light curve) and also as it has been found to be the case that afterglow shocks interpreted in terms of the fireball model are consistent with being adiabatic for populations studies of GRBs [318], although differences between

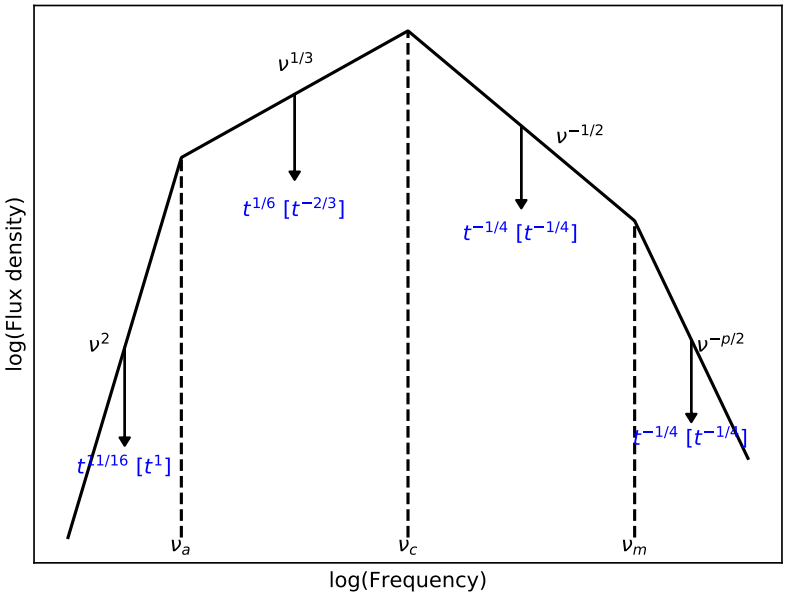

Figure 6.1: The temporal evolution of the segments of a fast cooling ($\nu_c < \nu_m$) synchrotron spectrum, shown in blue. The arrows are schematic and do not necessarily indicate the direction of flux evolution. A positive index indicates a flux increase with time. The first quantity indicates the evolution for a flat ISM density profile ($\rho \propto r^0$) whereas the quantity in square brackets indicates the evolution for a wind like density profile ($\rho \propto r^{-2}$).

the two cases can be relatively subtle and difficult to confirm without high quality data.

The RS propagates *back* into the ejected material and its final velocity depends on the properties of the shock and the ISM (and its existence is dependent on the condition that the outflow is baryonic [319]). The reverse shock exists in one of two regimes, either Newtonian or relativistic. The reverse shock is initially Newtonian due to the high density contrast between the outflowing material and the ISM but will increase in velocity as the density contrast falls. The development of the reverse shock depends on the radius at which the shock becomes relativistic. In the Newtonian (or thin-shell) case the ejecta have a narrow distribution of Lorentz factors and as such the RS does not have a chance to become relativistic before it interacts with the inner edge of the outflowing shell. A Newtonian shock does not extract a significant fraction of the energy from the shell, where this instead is done by the FS. In the relativistic, or thick-shell, case the dispersion of Lorentz factors is large enough such that the RS reaches relativistic velocities before interacting with the inner radius of the shell. A relativistic RS can extract a significant fraction of the kinetic energy of the shell to thermal energy in a single shell crossing time, whereas a Newtonian shell requires many crossings to achieve this [319], and the properties of the reverse shock are altered after its first crossing [320]. Both Newtonian and Relativistics RSs are pos-

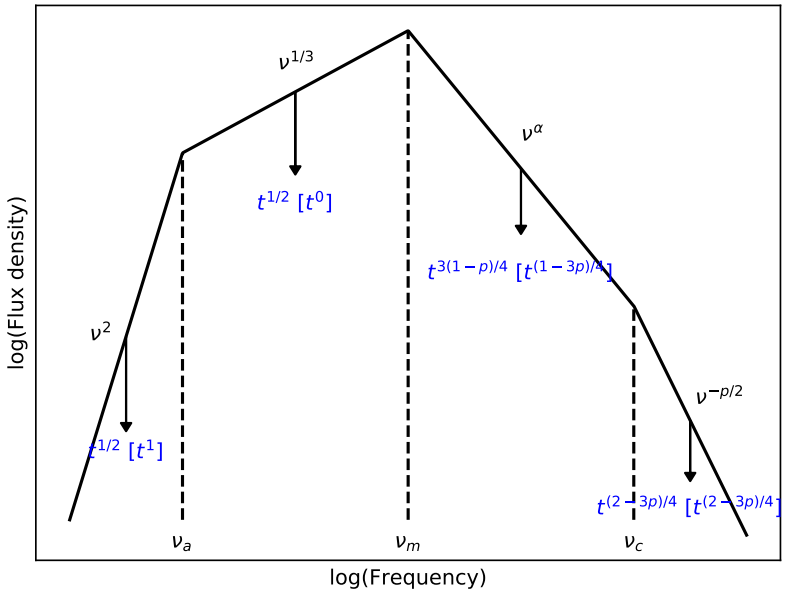

Figure 6.2: The temporal evolution of the segments of a slow cooling ($\nu_m < \nu_c$) synchrotron spectrum, shown in blue. The arrows are schematic (indicating motion is in the vertical direction) and do not necessarily indicate the direction of flux evolution. A positive index indicates a flux increase with time. The first quantity indicates the evolution for a flat ISM density profile ($\rho \propto r^0$) whereas the quantity in square brackets indicates the evolution for a wind like density profile ($\rho \propto r^{-2}$).

sible for reasonable GRB shock properties [321], and both have been invoked to explain observational data [322, 323]. The RS is short lived, and dominates at early times (if at all [319]). Flashes of optical emission [324, 325] are an expected – and observed – feature of a reverse shock, as well as a radio flare which peaks on time scales of the order of days [326, 327, 328, 329]. The FS contributes to the afterglow emission at all times, whereas the RS only contributes significant radiation (especially at high frequencies) at early times. If the RS is relativistic, like with the FS, its evolution will be determined by the circum-burst density profile [320, 330] whereas in the Newtonian case the radial Lorentz factor distribution of the burst material (with $\Gamma(r) \propto r^{-g}$ the often assumed form; e.g. [331]) is the most important parameter governing the evolution [320, 314, 332]. When analysing the broadband spectra of GRBs it is therefore important to consider the contribution from both of the shock components which will contribute distinct synchrotron spectra (with distinct break frequencies) [329, 333, 334, 335, 336].

Now we have an understanding of how a GRB afterglow should evolve both spectrally and temporally we are in the position to make inferences on the properties of GRBs based on broadband follow-up observations. In some cases studying the afterglow emission can be used to calculate the total energy released by the burst through calorimetry [298].

6.2 GRB 171010A

Throughout the rest of this chapter I will present an extensive multi-frequency radio observing campaign on the nearby and energetic GRB 171010A, carried out with the Karl G. Jansky Very Large Array (VLA) and the Arcminute Microkelvin Imager Large Array (AMI-LA; [169, 337]), see Chapter 3 for details on these facilities. We obtained a high cadence (22 observations made approximately every 1-4 d) light curve at 15.5 GHz from the AMI-LA and multiple – broadband – VLA spectra of the source. These observations, combined with publicly available data at other wavelengths, allowed for the spectral and temporal evolution of the source from early to late times to be monitored and our observations compared with the theoretical understanding of GRB afterglows presented in the previous section. This provides insight into the afterglow blast wave itself, as well as the environment surrounding this energetic and nearby GRB.

GRB 171010A was detected at T_0 = MJD 58036.79 by the Fermi Large Area Telescope (LAT) after an automated slew was triggered by the Fermi Gamma-ray Burst Monitor (GBM [338, 339, 340, 341]). GRB 171010A was also observed by *AstroSat*, with the results reported in [342]. The GBM location was found to be consistent with the LAT position, measured as RA (J2000) = 66.°74, Dec (J2000) = −10.°53 with a circular 90 per cent confidence region of radius 0.2°, later refined to RA (J2000) = 66.°58, Dec (J2000) = −10.°46 with a circular 90 per cent confidence region of radius 1.4 arcsec from observations [343, 344] obtained with the Neil Gehrels *Swift* Observatory X-ray Telescope (XRT; [181]). Analysis of spectral emission lines in optical follow-up observations showed that the position of the afterglow was consistent with a galaxy at redshift $z = 0.33$, which was identified as the probable host [345, 346]. Considering a cosmological model with $H_0 = 72\,\mathrm{km\,s^{-1}Mpc^{-1}}$, $\Omega_\mathrm{M} = 0.27$ and $\Omega_\Lambda = 0.73$ provides a luminosity distance to GRB 171010A of 1698 Mpc for $z = 0.33$ [347, 348]. The γ-ray fluence of GRB 171010A, as measured by the Fermi-GBM was $(6.42 \pm 0.02) \times 10^{-4}\,\mathrm{erg\,cm^{-2}}$ in the 10−1000 keV energy band, where the fluence is the flux in the energy band being considered integrated over the duration of the GRB [341]. While the fluence of GRB 171010A was high (in fact this is the third highest fluence in the 10−1000 keV energy band as measured by the Fermi GBM out of almost 3000 events), its intrinsic energy release is of course entirely depending on the distance. It has been suggested that while GRBs cover a wide range of luminosity space there are two distinct populations [349]. These consist of common, under-luminous events only observable in the nearby Universe, and more energetic events which form the population observed between $z \sim 2$ and 3. Members of the latter populations have isotropic γ-ray energies several

orders of magnitude greater than those typically found at $z \lesssim 0.5$ ($10^{52}-10^{54}$ erg verses $10^{48}-10^{52}$ erg; see e.g. figure 1 in [323]), and are rarely observed in the local Universe due to both geometric and star formation rate considerations. Combining the distance with the fluence measured by the Fermi-GBM gives an isotropic equivalent gamma ray energy of $E_\gamma \sim 2.2\times10^{53}$ erg in the cosmological rest frame of the source. GRB 171010A is therefore one of the most energetic long GRBs observed below a redshift of 0.5 (with an isotropic γ-ray energy release similar to GRBs 030329, 090818 and 130427A), and is therefore a member of the higher energy population usually found at larger redshifts which very rarely occur locally. These nearby yet luminous GRBs, such as GRB 171010A (along with the well studied GRBs 030329 and 130427A), provide an excellent opportunity to probe the intricacies of afterglow emission.

6.3 Observations

6.3.1 Radio

6.3.1.1 Arcminute Microkelvin Imager Large Array

As part of a GRB afterglow follow-up campaign we began observing GRB 171010A using the AMI-LA at T_0 + 1.27 d [350]. While the AMI-LA responds robotically to events that trigger the *Swift*-BAT telescope, GRB 171010A did not trigger the BAT and therefore I triggered observations of the source manually. An initial 4 hour observation was conducted at a central frequency of 15.5 GHz with a 5 GHz bandwidth spread over 4096 channels. Data were reduced using the Common Astronomical Software Applications (casa) package with a custom reduction pipeline, which flagged the data for radio frequency interference and instrumental effects, and calibrated the flux, bandpass and phases. We used 3C286 as the flux/bandpass calibrator, and J0438−0848 as the phase calibrator. Due to the low declination of GRB 171010A, the synthesised beam is elongated when compared to more northerly observations, with characteristic dimensions of ~ 100 by ~ 35 arcsec. We detected a bright (3 mJy, with an image RMS of ~ 45 μJy) unresolved source at phase centre (RA (J2000): 04h 26m $19\overset{s}{.}3 \pm 0\overset{s}{.}7$, Dec (J2000): $-10^\circ\,27'\,45.1'' \pm 10''$) in the initial image which overlaps with the *Swift* 90 per cent confidence region and is ~ 7 arcmin away from the nearest source in the NVSS catalogue [351]. We therefore identified the source as the radio afterglow of GRB 171010A. To calculate the source flux density we used the casa task imfit, adding a 5 per cent calibration error (in line with the RMS variability of the phase calibrator flux) in quadrature with the statistical one.

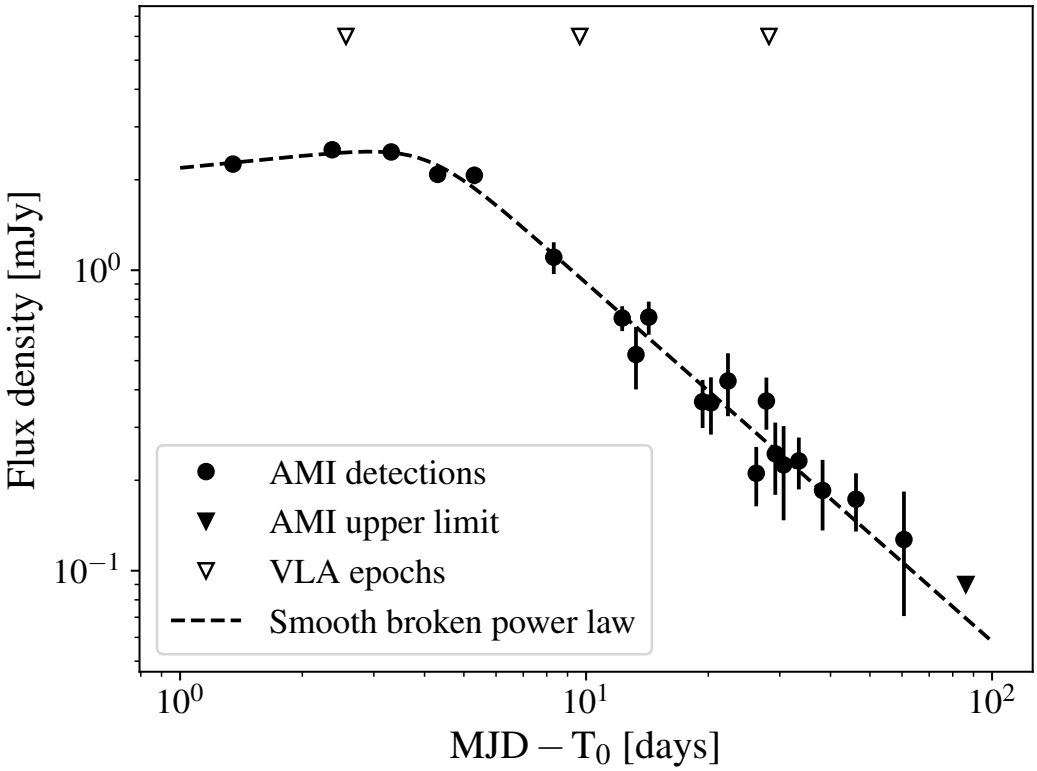

Figure 6.3: 15.5 GHz radio observations of GRB 171010A made with the AMI-LA. Filled circles and the filled triangle represent AMI-LA detections and upper limits at a 3σ significance, respectively. The error bars demonstrate 1σ uncertainties. Unfilled triangles at the top of the plot indicate the epochs at which VLA measurements were made. The dashed line is a smoothed broken power law fit to the data (excluding upper limits). The break time is found to be $T_0 + 4.1 \pm 0.4$ d. The temporal power law index before and after the break is $\alpha = 0.1 \pm 0.1$ and $\alpha = -1.19 \pm 0.06$, respectively. The reduced chi-square of the fit is $\chi^2_\nu = 0.79$ for 16 degrees of freedom.

Upon detecting the radio afterglow of GRB 171010A we initiated a radio follow-up campaign which consisted of multiple epochs of AMI-LA observations, as well as multiple observations with the VLA, with our first observation reported via the gamma-ray coordinates network [352]. All other AMI-LA observations were carried out in the same instrumental configuration as the initial observation, and the reduction procedure was identical. A summary of the AMI-LA observing campaign is presented in Table 6.1 and the light curve is shown in Figure 6.3.

6.3.1.2 Karl G. Jansky Very Large Array

We obtained three observations of GRB 171010A with the VLA (publicly available on the VLA archive through project code S81171) in B configuration at 2.57, 9.66 and 28.59 d after

Table 6.1: Summary of AMI-LA Observations of GRB 171010A. Errors are statistical and calibration (5%) combined in quadrature. ΔT is the number of days between T_0 = MJD 58036.78 and the observation midpoint. The upper limit at ΔT = 86.03 d is three times the RMS noise in the image. All observations were taken at a central frequency of 15.5 GHz.

Date [ΔT]	Obs. Length [hours]	Flux Density [mJy]	Error [mJy]
1.35	4	2.26	0.13
2.37	3.5	2.52	0.14
3.31	4	2.48	0.14
4.31	4	2.08	0.13
5.31	4	2.07	0.14
8.33[a]	3	1.11	0.13
12.27	4	0.69	0.07
13.27[a]	4	0.52	0.12
14.27	4	0.70	0.09
19.37	3	0.37	0.07
20.30	4	0.36	0.08
22.36	3	0.43	0.10
26.25	4	0.21	0.05
27.80[b]	8	0.37	0.07
29.24	4	0.25	0.07
30.66[b]	8	0.23	0.08
33.42[b]	8	0.23	0.05
38.24	4	0.19	0.05
46.21	4	0.17	0.04
60.66[a,b]	11	0.13	0.06
86.15	4	<0.09	–

[a] The source in these observations was not well fit by the clean beam due to residual noise. Thus the peak flux density was used.

[b] These observations combined data from multiple days in order to lower the noise level. In this case the time is the centroid of all observations used.

the initial Fermi LAT detection (the times of these observations are shown in the context of our AMI-LA observations in Figure 6.3). During the first epoch (1 hr total observation length) we recorded data between $\sim$ 4 and $\sim$ 12 GHz spread across 64 spectral windows, each consisting of 64 channels of width 2 MHz. During epochs two and three (1.50 hr each) we recorded data between 4 and 12 GHz and 18 and 26 GHz, across a total of 128 spectral windows, each consisting of 64 channels of width 2 MHz per channel. Data were binned according to Table 6.2 for imaging. Data were calibrated in CASA using the NRAO VLA scripted calibration pipeline with 3C138 and J0423−0120 as the absolute flux and phase calibrator, respectively. Imaging was also performed in CASA using natural weighting, with a clean gain of 0.1. In order to calculate spectral information across the VLA observing band we opt to split our data into $1-2$ GHz frequency chunks. To calculate the flux from the source (which is well detected as an unresolved source in almost all epochs) we use the CASA task IMFIT. The only exception to this procedure was for the 18 to 26 GHz frequency range in the third epoch. At almost a month post detection, the source had become faint enough at these high frequencies such as to be no longer significantly detected in each 1 or 2 GHz range. To increase our sensitivity we therefore image using a 4 GHz bandwidth between 18 and 22 GHz for this epoch. Data above 22 GHz were not used due to artefacts corrupting the image in this frequency band. A summary of our VLA observations are given in Table 6.2, and the data are plotted in Figure 6.4. Note that while all frequencies within each epoch were not observed strictly simultaneously, they were observed $<$ 1hr apart and as such we consider them simultaneous for the purpose of spectral fitting.

6.3.2 X-ray

The afterglow of GRB 171010A was first observed in the 0.3−10 keV energy band by the *Swift* XRT at $T_0 + 6.72$ hours, and then regularly over the following 16 days. GRB 171010A was observed for a total of $\sim$ 104 ks over 24 observing segments, with the majority of observations performed in photon counting (PC) mode (this observing mode has a lower time resolution than windowed timing mode, but is more useful when observing fainter sources where timing information is not desired). We retrieved the light curve and spectrum for GRB 171010A from the on-line burst analyser [186, 187, 353]. We use a photon index of 1.95 (from the best fit of the time averaged spectrum) when converting the observed flux to a flux density at an energy of 1 keV ($\nu = 2.4 \times 10^8$ GHz), following the method described in [354]. The *Swift*-XRT light curve is shown in Figure 6.5.

Table 6.2: Summary of VLA Observations of GRB 171010A. Errors are statistical and calibration (3% for C and X band, 5% for K band) combined in quadrature. ΔT is the number of days between T_0 = MJD 58036.78 and the observation midpoint.

Date [ΔT]	Frequency [GHz]	Bandwidth [GHz]	Flux Density [μJy/beam]	Error [μJy/beam]
2.57	4.5	1	369	21
2.57	5.5	1	510	21
2.57	6.5	1	719	26
2.57	7.5	1	936	33
2.56	8.5	1	1204	40
2.56	9.5	1	1580	54
2.56	10.5	1	1858	64
2.56	11.5	1	2009	71
9.66	4.5	1	929	42
9.66	5.5	1	978	33
9.66	6.5	1	1025	35
9.66	7.5	1	1090	35
9.67	8.5	1	1147	37
9.67	9.5	1	1161	38
9.67	10.5	1	1140	38
9.67	11.5	1	1187	41
9.64	19.1	2	1034	60
9.64	21.1	2	930	55
9.64	23.0	2	822	51
9.64	25.1	2	829	55
28.59	4.5	1	367	20
28.59	5.5	1	393	18
28.59	6.5	1	405	17
28.59	7.5	1	386	17
28.60	8.5	1	341	16
28.60	9.5	1	345	17
28.60	10.5	1	306	15
28.60	11.5	1	303	20
28.57[a]	20.0	4	141	29

[a] This was a marginal detection, and so we assign it a conservative 20% error.

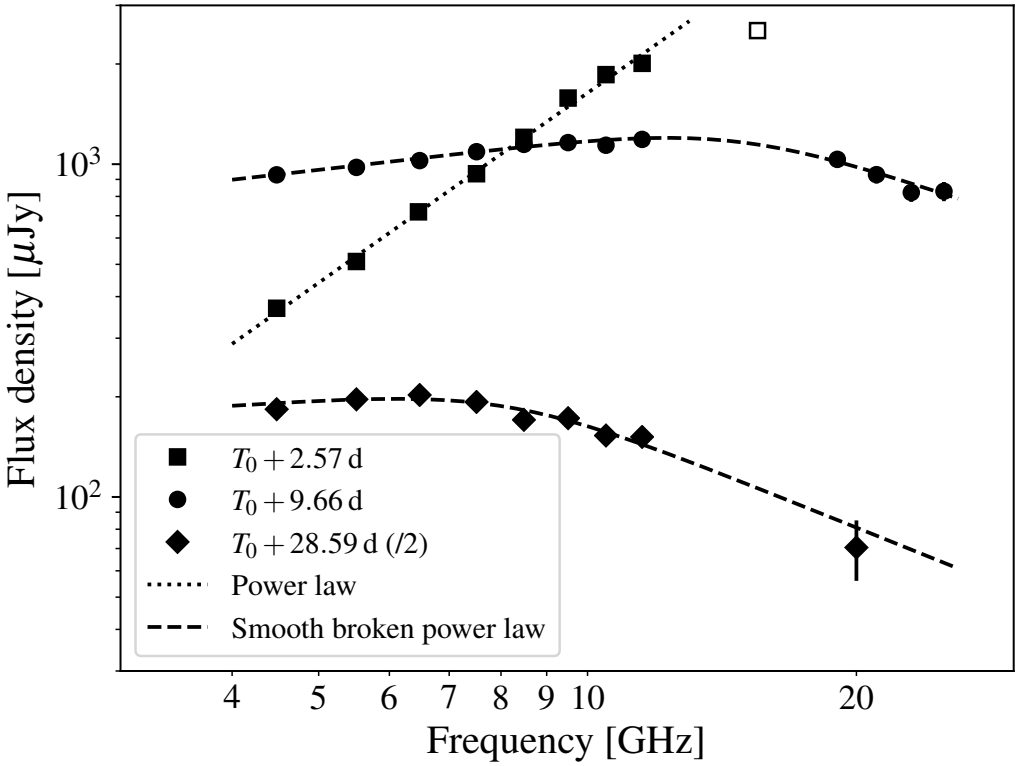

Figure 6.4: The radio spectrum of GRB 171010A between 4.5 and 25 GHz at three epochs. Squares, circles and diamonds are data from VLA observations made on $T_0 + 2.57$ d, $T_0 + 9.66$ d and $T_0 + 28.59$ d, respectively. The flux density measured from the third epoch has been divided by 2 for clarity. The error bars demonstrate 1σ uncertainties. The unfilled square point is data from an AMI-LA observation which was taken 0.25 d before the first VLA epoch. The dotted line shows a power law fit to the first epoch whereas dashed lines show smooth broken power law fits to the second and third epochs. The details of the fits are given in section Section 6.4.1 and are summarised in Table 6.3. Data are given in Table 6.2

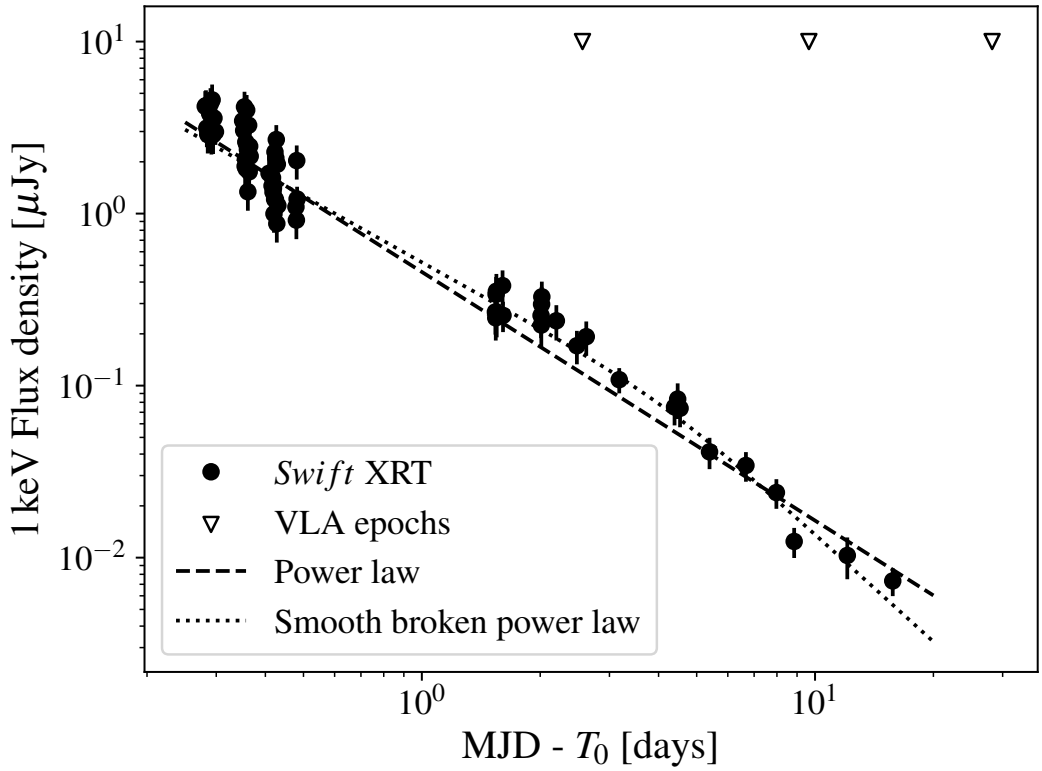

Figure 6.5: *Swift*-XRT PC mode light curve for GRB 171010A. Solid points show the flux density at 1 keV. The dashed line shows a power law fit to the data with a temporal index of $\alpha = -1.45 \pm 0.03$. The reduced chi-square of the fit is $\chi^2_\nu = 1.88$ with 68 degrees of freedom. The dotted line shows a smoothed broken power law fit to the data. The break occurs at 4 ± 2 d and the pre and post break slopes are -1.18 ± 0.05 and -2.1 ± 0.3, respectively. The reduced chi-square of the fit is $\chi^2_\nu = 1.68$ with 66 degrees of freedom. Unfilled triangles show the epochs at which VLA measurements were made.

6.4 Results

Here we detail the results obtained from the X-ray and radio observations of GRB 171010A. We adopt the following convention when referring to the temporal and spectral flux dependence: $F(t, \nu) \propto t^{\alpha}\nu^{\beta}$. We refer to α as the temporal index and β as the spectral index. We use separate subscripts for the radio and X-ray data to distinguish the indices, with subscripts R and X referring to the radio and X-ray properties, respectively. When referring to the power law index of the time evolution of a break frequency we use a ($\nu_{\rm break} \propto t^{a}$), and the index of the flux evolution at a break frequency will be referred to as b ($F_{\nu_{\rm break}} \propto t^{b}$).

6.4.1 Radio spectra

The spectra of GRB 171010A between 5 and 25 GHz at three different epochs are shown in Figure 6.4. Fitting an unbroken power law to the first epoch (for which there is no apparent spectral break present in our data), we find a spectral index of $\beta_{\rm R} = 1.90 \pm 0.05$. Any break occurring at this time does so above approximately 10 GHz. We fit the second and third epochs (due to their obvious breaks) with smoothed broken power laws. We use a smoothing parameter of $s = 5$ and the functional form

$$F(\nu) = A\nu_b^{b_1}\left[\left(\frac{\nu}{\nu_b}\right)^{-b_1 s} + \left(\frac{\nu}{\nu_b}\right)^{-b_2 s}\right]^{-1/s} \tag{6.1}$$

as presented in [355], where $F(\nu << \nu_b) \propto \nu^{b1}$ and $F(\nu >> \nu_b) \propto \nu^{b2}$, ν_m is the break frequency, and s defines how sharply the transition between the two regimes occurs. Our chosen value of s defines a relatively sharp transition between power law segments (an increased s implies a sharper transition), which we use for all smoothly broken power laws we fit in this work. The choice of s is slightly arbitrary. When attempting to fit for s as a free parameter in our MCMC fitting, the convergence was not satisfactory and s was essentially unconstrained by the process. This problem is exacerbated due to the fact that there are not good constraints on physically motivated values for the sharpness of the spectral evolution and approximations are complex functions of the exact break being crossed, the value of p, and the density profile of the ISM forcing the use of an uninformative prior for the parameter [313]. Additionally, our spectra are relatively coarse and, especially in VLA epoch 2, do not sample the break well. We therefore opt to set a sharp break in order to better measure the spectral slopes either side and the break position. For the second epoch we find that the spectrum breaks at 15^{+2}_{-2} GHz, transitioning from $\beta_{\rm R} = 0.31^{+0.08}_{-0.06}$ to $\beta_{\rm R} = -0.9^{+0.3}_{-0.3}$. For the third epoch we find a break at 8^{+1}_{-1} GHz transitioning from $\beta_{\rm R} = 0.2^{+0.3}_{-0.2}$ to $\beta_{\rm R} = -1.1^{+0.2}_{-0.2}$. For epoch 1, errors and maximum likelihood values are derived from fitting using the python

Table 6.3: Summary of best fit parameters when fitting the VLA radio spectra of GRB 171010A. Details of the techniques used to calculate the best fit values and their errors are presented in Section 6.4.1.

VLA Epoch (ΔT) Days	Pre break slope –	Post break slope –	Break frequency GHz	χ^2_ν –
2.57	1.90 ± 0.05	–	$\gtrsim 10$ GHz	1.43
9.66	$0.31^{+0.08}_{-0.06}$	$-0.9^{+0.3}_{-0.3}$	15^{+2}_{-2}	0.34
28.59	$0.2^{+0.3}_{-0.2}$	$-1.1^{+0.2}_{-0.2}$	8^{+1}_{-1}	0.84

module CURVE_FIT (part of the SCIPY module [356]). For epochs two and three we use a Markov Chain Monte Carlo sampler (EMCEE [251]) to fit the data. In this case the quoted best fit parameter value is the 50^{th} percentile of the trace (or the marginalised posterior distribution) for a given parameter (after burn-in where samples are discarded while the walkers converge) while the lower and upper errors are the 16^{th} and 84^{th} percentile of the trace (after burn-in), respectively. The marginalised posterior distributions from this analysis are presented in Figures 6.6 and 6.7. The marginalised posterior distributions are shown to consist of a single node (a single peak in the marginalised parameters spaces) for all parameter combinations. There is, however, some obvious parameter degeneracy for both epochs. In Figure 6.8 we demonstrate the effect of fitting both spectra simultaneously, this time with a sharply broken power law. To reduce the number of parameters and avoid degeneracy we fix the pre break slope in both epochs to $1/3$ as predicted by [141]. This leaves us with 5 variable parameters to optimise. The post-break slope (determined by p as $\beta = -(p-1)/2$), the break frequency for the second epoch, the index of the power law evolution of the break, the maximum flux (the flux at the break) for the second epoch and finally the evolution of the maximum flux which depends on the density profile index as $F_{\text{max}} \propto t^{-k/2(4-k)}$. We opt to make the break frequency evolution a free parameter as we could not find a converging fit when prescribing this to move as $-3/2$ (as it should if it is the minimum energy break) or to depend on k as $-(4-3k)/2(4-k)$ if it were the cooling break. The marginalised posterior distribution for this fit is shown in Figure 6.8. While the results of this analysis do agree well with those derived from individually fitting the spectra, I rely more on the individual spectral fits. This is as we do not know *a priori* if the break in each of the spectra is the same one, or which part of the broadband spectra we are sampling (assumptions which are made during the fitting the joint spectral fit, where we are assuming that the break frequency is the minimum energy break and the there is a single synchrotron spectrum with $\nu_a < \nu_m < \nu_c$).

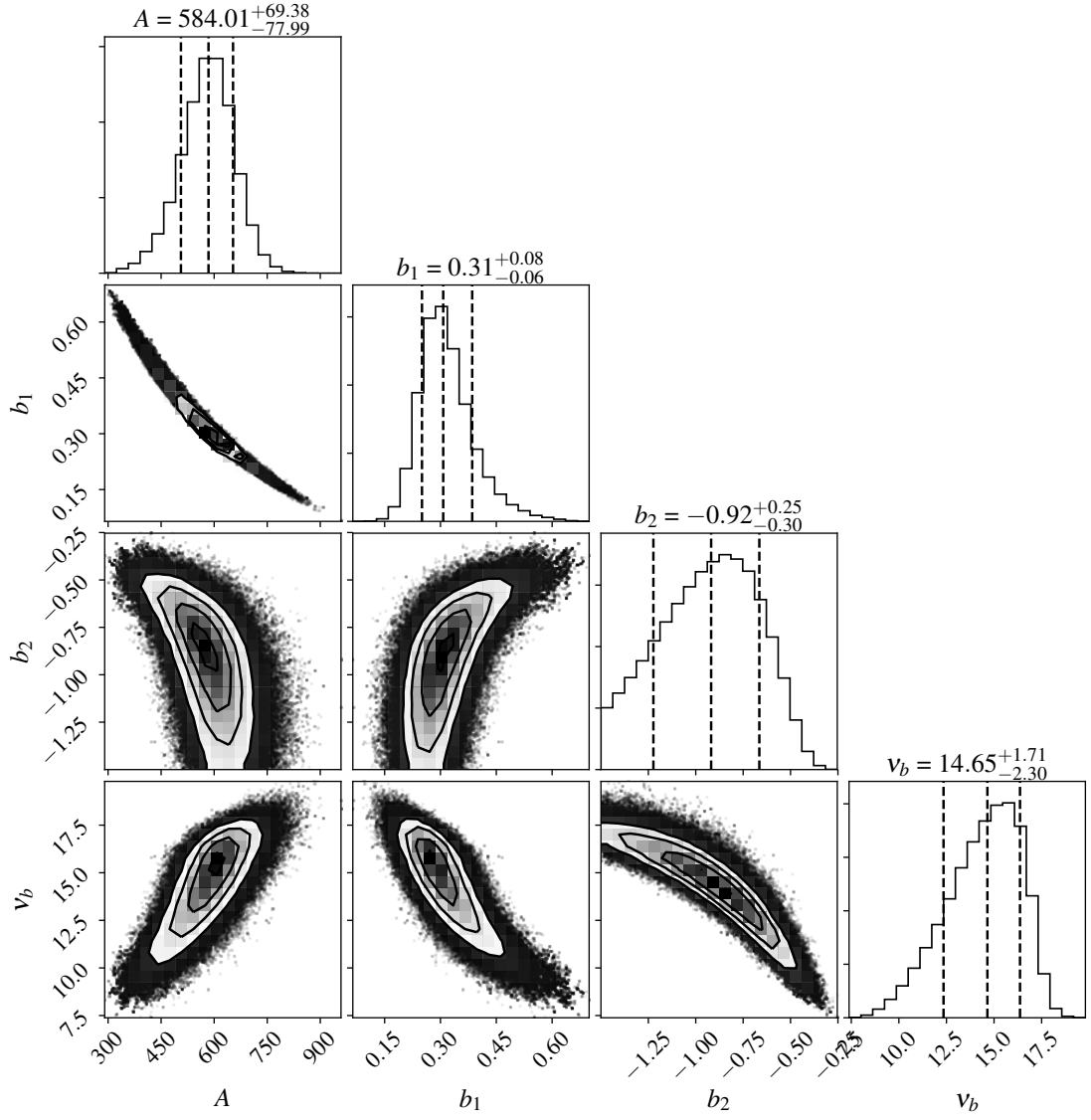

Figure 6.6: Marginalised posterior distribution for the smooth broken power law fit of the VLA epoch 2 spectrum. A, b_1, b_2, ν_b are the maximum flux, pre break slope, post break slope and break frequency respectively. The dotted lines indicate the 16$^{\text{th}}$, 50$^{\text{th}}$ and 84$^{\text{th}}$ percentiles on the parameters which are used to estimate the error. Uniform priors were used on all parameters, and we limit the post break spectral index such that $b_2 > -1.5$. This corresponds to the steepest theoretically predicted slope (fast cooling) for $p = 3$.

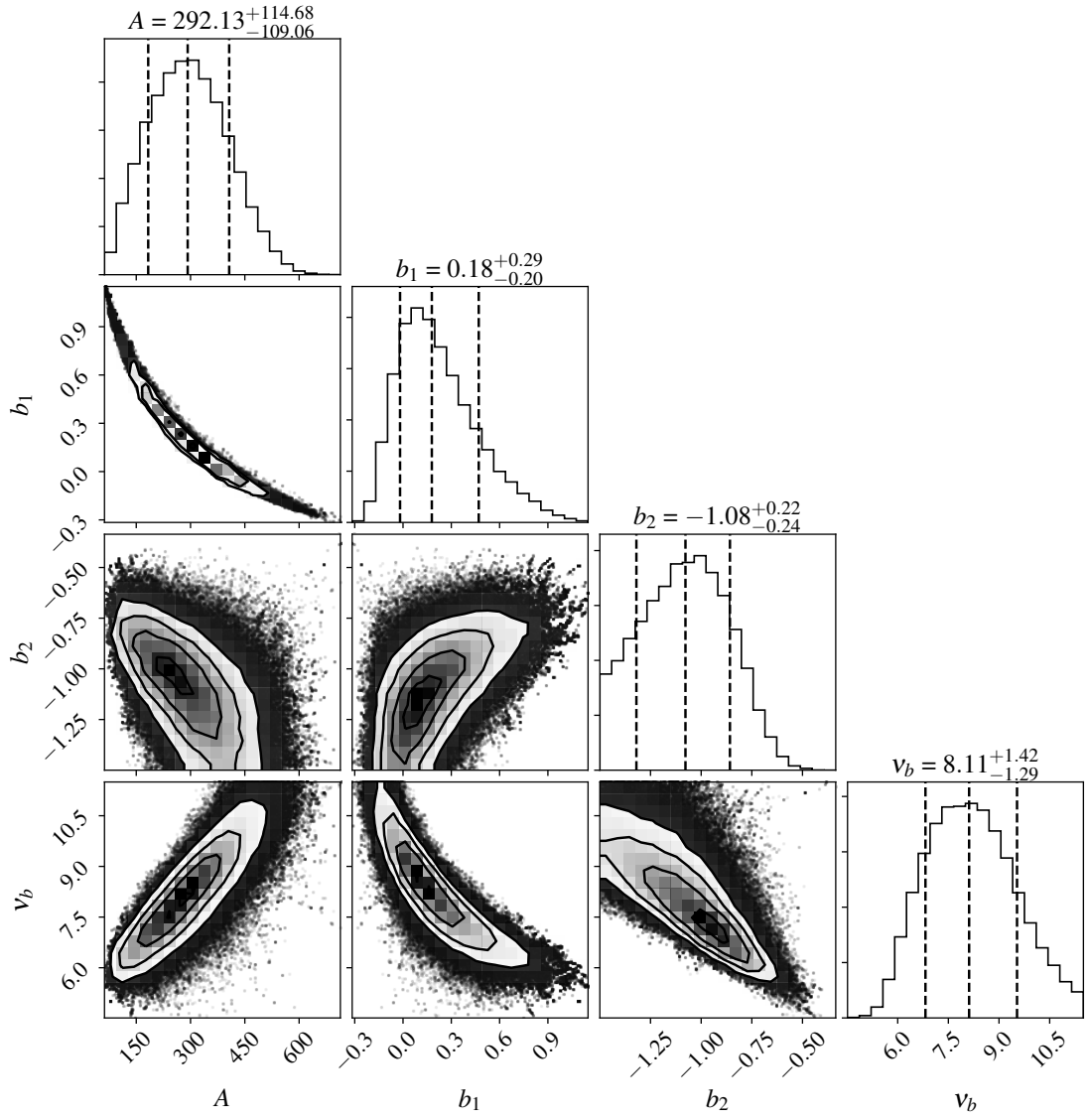

Figure 6.7: Marginalised posterior distribution for the smooth broken power law fit of the VLA epoch 3 spectrum. A, b_1, b_1 and ν_b are the maximum flux, pre break slope, post break slope and break frequency respectively. The dotted lines indicate the 16$^{\text{th}}$, 50$^{\text{th}}$ and 84$^{\text{th}}$ percentiles on the parameters which are used to estimate the error. Uniform priors were used on all parameters, and we limit the post break spectral index such that $b_2 > -1.5$. This corresponds to the steepest theoretically predicted slope (fast cooling) for $p = 3$.

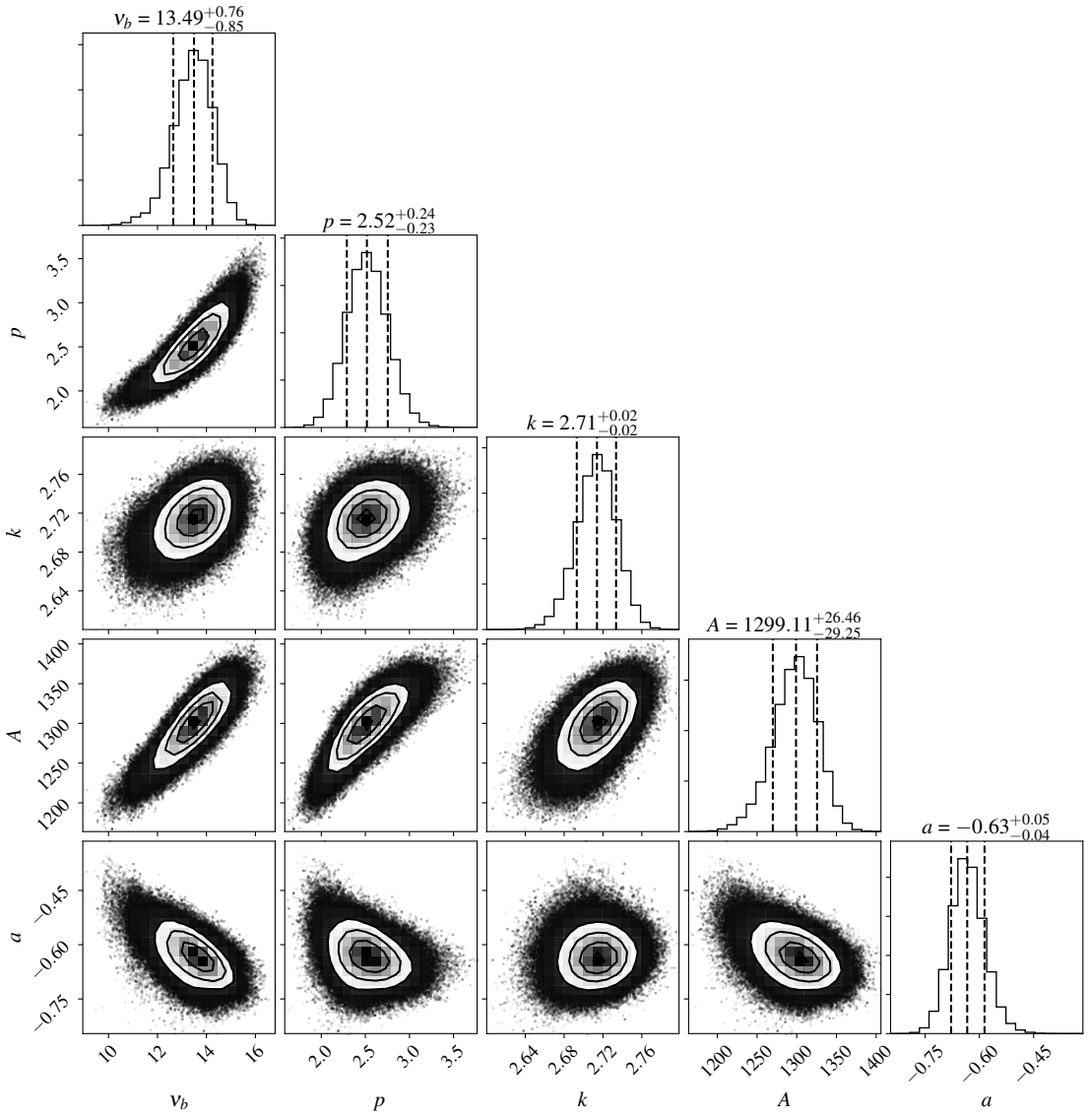

Figure 6.8: Marginalised posterior distribution for the joint sharply broken power law fit of the VLA epoch 2 and 3 spectra. ν_b, p, k, A and a are the epoch 2 break frequency, electron energy index, density profile index, maximum flux and the power law index of the break frequency movement, respectively. The dotted lines indicate the 16^{th}, 50^{th} and 84^{th} percentiles on the parameters which are used to estimate the error.

Table 6.4: Summary of movement of characteristic frequencies of GRB 171010A.

	ν_a	ν_m	ν_c
a	$\lesssim -0.7$	-0.6 ± 0.2	unknown

6.4.2 Radio light curve

The AMI-LA 15.5 GHz light curve (shown in Figure 6.3) demonstrates almost no flux evolution between 1.27 d (the first AMI-LA observation) and 4.1 ± 0.4 d post burst (the fitted time of the temporal break, 3.1 ± 0.3 d in the GRB rest frame). The break time is computed using a smoothed broken power law fit, as clearly the first three data points do not follow the decaying trend at later times. The pre-break index is $\alpha_R = 0.1 \pm 0.1$ and the post-break index is $\alpha_R = -1.19 \pm 0.06$. At around 80 d the flux density from GRB 171010A has reached the sensitivity limit of the AMI-LA and we are only able to place upper limits at $\sim 90\,\mu$Jy on the 15.5 GHz.

6.4.3 X-ray light curve and spectrum

The X-ray light curve for GRB 171010A (Figure 6.5) shows the flux density declining from ~ 6 to $\sim 0.01\,\mu$Jy over the 20 day observing period. Fitting a single power law decay to the data gives a temporal index of $\alpha_x = -1.45 \pm 0.03$. We also demonstrate a smoothed broken power law fit, with a break occurring at 4 ± 2 d, and a pre and post break slope of -1.18 ± 0.05 and -2.1 ± 0.3, respectively. The time averaged (between $T_0 + 0.28$ d and $T_0 + 0.48$ d) X-ray spectrum is well described ($\chi^2_\nu = 0.87$) by an absorbed power law with a photon index of $\Gamma = 2.0^{+0.2}_{-0.1}$ and a total column density of $N_H = 3.4^{+0.7}_{-0.6} \times 10^{21}\,\mathrm{cm}^{-2}$ [344] which is in excess of the galactic value of $N_H \sim 7 \times 10^{20}\,\mathrm{cm}^{-2}$ along that line of sight, indicating absorption intrinsic to the source or its host galaxy. The measured photon index, Γ, gives a spectral index of $\beta_X = \Gamma - 1 = 1.0^{+0.2}_{-0.1}$.

6.5 Discussion

We will begin with attempting to explain our radio and X-ray observations in the context of the fireball model with a single FS component. This is a good first order step, as typically GRBs showing reverse shock radio emission are already declining on ~ 1 d timescales (e.g. [327, 328, 329]) whereas in our case the decline occurs a few days later. We then discuss issues with this simple model, and potential solutions.

6.5.1 A Forward shock model

6.5.1.1 Radio

All three VLA spectra are well described by simple single or broken power laws. The slope in the first epoch, $\beta_R = 1.90 \pm 0.05$, is consistent with synchrotron self-absorption and $10\,\mathrm{GHz} \lesssim \nu_a < \nu_m$. In that case, the theoretical spectral index is $\beta = 2$, while for a self-absorbed spectrum with $10\,\mathrm{GHz} \lesssim \nu_m < \nu_a$ we would expect a steeper spectrum with an index of $\beta = 2.5$. There is the hint of a turnover at the highest VLA frequency at the first epoch (11.5 GHz), which is further supported by the closest in time AMI-LA observation taken 0.25 d earlier. However, given that the observation was not simultaneous and the spectrum is evolving most quickly at early times, we set the limit $\nu_a \gtrsim 10\,\mathrm{GHz}$. In the second and third epochs the self-absorption break has moved below the VLA observing band, and the spectra are each well described by a broken power law with consistent indices below and above an evolving break frequency. A spectral slope of $\beta = 1/3$ is expected between ν_a and $\nu_m (< \nu_c)$, while the spectral slope between ν_m and ν_c is expected to be $\beta = -(p-1)/2$ (regardless of the density profile of the surrounding medium). Comparing these theoretical slopes with the observed ones suggests that the spectral break in both epochs is due to the peak (or minimum energy) frequency. The observed slopes below the break are consistent with $\beta = 1/3$, and using the best-constrained spectral slope above the break (for epoch 3) we obtain $p = 2.6^{+0.4}_{-0.4}$. The steepness of the post-break slope also confirms the order of the breaks to be $\nu_a < \nu_m < \nu_c$, as a shallower slope with $\beta = -0.5$ would be expected between the peak and cooling breaks if they were reversed. This is unsurprising since the cooling break is expected to reside at higher frequencies, and the minimum energy break moves to lower frequencies faster than the cooling break, regardless of the surrounding density profile.

The fireball model makes predictions for the temporal evolution of the spectral breaks, the flux at these breaks, and the flux in the different segments of the broadband spectrum. The evolution is tied to the density profile of the region surrounding the GRB. We see a very different spectrum between epochs one and two, with no sign of self-absorption in epoch two. The self-absorption break has therefore moved through and below our observing band, and we can constrain the self-absorption frequency to be $\nu_a \lesssim 4.5\,\mathrm{GHz}$ at the second epoch. We can therefore put a limit on the evolution of the self-absorption break frequency, assuming that it is a power law, to have an index of $a \lesssim -0.7$ ($\nu_a \propto t^a$). The limit placed on the temporal evolution of ν_a is most consistent with a steep density profile (wind-like) with $k \gtrsim 2.2$ (see e.g. table 5 in [335]) assuming the spectrum is in the slow cooling regime. While the self-absorption frequency has moved through the band, a second and

distinct spectral break is present in the second epoch at 15^{+2}_{-2} GHz and in the third epoch at 8^{+1}_{-1} GHz. Identification of this break in the context of the forward shock model proves to be more puzzling, even though the spectral slopes below and above the break indicate that this is $\nu_{\rm m}$. From the spectral fitting we derive a value for the time evolution of this break which, again assuming a power law, has an index $a = -0.6 \pm 0.2$ (this is constrained significantly better, albeit consistently, by jointly fitting the spectra). The movement of the break frequencies are summarised in Table 6.4. The prediction is that $\nu_{\rm m}$ should, for all density profiles, move towards lower frequencies with a temporal power law index of -1.5 (or even faster in the case of a radiative shock). While we do see this break moving in the expected direction, it is moving significantly slower. The flux evolution at the break, which evolves with $b \sim -1$, is consistent with the minimum energy break for $k \sim 2.7$ (or a post jet break minimum energy peak occurring once the beaming angle is approximately the opening angle of the jet [357, 335]). The presence of a jet break at ~ 4 d (as hinted at by fitting the X-ray light curve) would, however, cause $\nu_{\rm m}$ to move to lower frequencies even faster and so we disfavour it.

Considering the temporal flux evolution presents additional complications for a simple forward shock model. From the AMI-LA (15.5 GHz) light curve, we see a clear break at around 4 d, which falls between the first and second VLA epochs. It is clear that the spectral break we see in the second and third epochs is not responsible for the temporal break we see with the AMI-LA, as if we extrapolate back in time at its derived rate it would be found at around 25 GHz at 4.1 d (the observed VLA break has only just reached 15 GHz at 10 d post burst so it is unlikely it caused the AMI-LA turnover). Therefore the self-absorption break is the most likely cause of the break in the AMI-LA band. When considering the AMI-LA light curve before its temporal break (which we infer is due to the self-absorption break, and thus in the range $\nu < \nu_{\rm a} < \nu_{\rm m} < \nu_{\rm c}$) we see an almost constant flux. This is hard to explain for any density profile considering just a forward shock (see table 5 in [335]). After the turnover in the AMI light curve (caused by the passage of the self-absorption break through the AMI-LA band) the decay is well described by a single power law, despite the fact that what we infer as the minimum energy break must also move through the AMI-LA band before ~ 10 d. Again referring to table 5 in [335], it is possible for the flux evolution to be the same on either side of the minimum energy break. In the region $\nu_{\rm a} < \nu < \nu_{\rm m} < \nu_{\rm c}$ (observed with the AMI-LA at $T_0 + 4.1$ to $\sim T_0 + 10$ d) the decay slope can be explained with a steep density profile with $k \sim 3.1$ which is broadly consistent with estimates for the density profile we have derived previously. However, the minimum energy break must move through the AMI-LA band, but we see no change in the temporal slope. To remain

consistent with this requires an extremely hard electron energy index (which contradicts the measured VLA spectral index) of $p \sim 0.6$.

6.5.1.2 X-ray

Given that the forward shock model predicts a simple spectral shape across a huge (radio through to X-ray) range of frequencies, we can use the *Swift* data to further constrain the parameters for GRB 171010A. We can attempt to identify the section on the spectrum that the 1 keV emission is from, and thus where it lies with respect to the characteristic frequencies. The X-ray spectrum is well described by a power law with index $\beta_X = -1.0^{+0.2}_{-0.1}$, which is similar to the spectral slope above the break as measured by the VLA. Indeed, jointly fitting the (post-break) radio data from VLA epoch 2 and the closest in time X-ray measurement implies a radio through X-ray spectral slope of -1.12 ± 0.01 (however these data were taken over a day apart from one another). It is unclear, from just measuring the spectral slope, from which section of the spectrum the 1 keV emission is from. Looking at the light curve, which decays with $\alpha_{\rm X} = 1.45 \pm 0.03$ (considering only the power law fit) we immediately confirm that the X-ray emission is above the minimum energy break, as we only see the flux density decline. The GRB closure relations (e.g. table 1 in [358]; a set of consistency relations relating α and β in different regions of the synchrotron spectrum) favour $\nu_{\rm c} < \nu_{\rm X}$, but given the error on the X-ray spectral slope it is far from definitive (the jointly fit slope is consistent with both components originating from the same spectral region). For the broken power law fit, the decline post break is too steep to be explained by the cooling frequency moving through the *Swift* observing band. The break is, however, consistent in time with the break at 15.5 GHz. Such an achromatic break, if real, could indicate that a jet break occurred at around this time, although it is difficult to confirm the legitimacy of this feature.

To summarise, we find that the most likely explanation of the data in the context of the forward shock model is as follows. At early times (< 5 d) we have that $15.5\,{\rm GHz} < \nu_{\rm a} < \nu_{\rm m} < \nu_{\rm c} < \nu_{\rm X}$. Then at ~ 5 d the self-absorption break moves through the AMI-LA band and $\nu_{\rm a} \lesssim 15.5\,{\rm GHz} < \nu_{\rm m} < \nu_{\rm c} < \nu_{\rm X}$ with our VLA measurements sampling the minimum electron energy break at the second and third epochs. The spectral segment responsible for the X-ray emission is not well constrained. We find the data to be most consistent with a steep density profile, with $k \sim 3$, although there are significant deviations from a simple forward shock model.

6.5.2 Inconsistencies: Explaining the unusual behaviour

While we have attempted to contextualise our observations in terms of the forward shock model, there are obvious inconsistencies with the picture we have provided. For example, we would expect to see two breaks in the AMI-LA light curve when $\nu_{\rm a}$ and then $\nu_{\rm m}$ move through the band. Also, the movement of the $\nu_{\rm m}$ is significantly slower than that predicted by a simple forward shock model. As we have inferred the movement of the self-absorption break below all of our observing bands, there are only two possible orderings of the minimum energy (ν_m) and cooling (ν_c) frequencies. Previously we inferred the most likely configuration of the spectrum, and the location of the observed radio band in said configuration, but it is also worth considering if this could be the cooling break moving through the radio band. For both the fast and slow cooling cases this is easy to rule out. For fast cooling, there is no good value of k for which the cooling break moves to lower frequencies and the flux drops off as quickly as we observe between epochs 2 and 3. In fact, avoiding an increasing density profile with radius, ν_c is not expected to move to lower frequencies any slower than with an index of -0.5 which occurs for $k = 0$ and would imply the flux at the cooling break should not evolve at all, which we do not see. For the slow cooling case the spectrum should have a negative index before and after the break, whereas we clearly see a rise before the break and so rule this out. Below we detail some possible explanations for the puzzling behaviour of GRB 171010A.

6.5.2.1 A reverse shock component

Perhaps most perplexing is the apparent movement of the break frequency between VLA epochs two and three. We established above that this is most likely the minimum energy frequency $\nu_{\rm m}$. We measure $\nu_{\rm m}$ moving with a power law index $a = -0.6 \pm 0.2$, as opposed to the theoretical expectation of $a = -1.5$. In the context of a simple forward shock this discrepancy is very hard to explain. We briefly consider the effect of including emission from a reverse shock in our model for GRB 171010A. To properly constrain forward plus reverse shock models, it is vital to have observational data across the electromagnetic spectrum from early times, particularly at optical, sub-mm and radio frequencies where the reverse shock will dominate. Unfortunately GRB 171010A was not observed extensively at all of these frequencies (from an early time) and so constraining the properties of a reverse shock is quite difficult. We can, however, make some qualitative statements on the effect of a reverse shock based on more completely observed GRBs. GRB 130427A is an obvious source to compare with. It is at a very similar redshift to GRB 171010A and also had an isotropic energy release more typical of GRBs at larger redshifts, just like

GRB 171010A. The AMI-LA carried out long term monitoring on GRB 130427A, and a comparison to GRB 171010A is shown in Figure 6.9. In order to perform this comparison a k-correction must be applied to segments of the data, accounting for the redshifts of the sources and the different spectral indices and decay rates through the evolution. When corrected the specific luminosity is $L_{\nu,k} = L_{\nu}(1+z)^{\alpha-\beta-1}$ where α and β are the temporal and spectral indices are previously defined [359]. A reverse shock component was invoked to explain both the AMI-LA light curve as well as the broadband spectrum of GRB 130427A [334, 335, 329, 323]. Both GRBs show a slowly rising/flat early time 15.5 GHz light curve, which turns over and decays after a few days. GRB 130427A, however, turns over close to 1 d after the initial detection, faster than for GRB 171010A. This timescale is a clear sign, along with the additional change in slope at around 4 days, of a reverse shock dominating the radio emission at early times and becoming sub-dominant later on. The reverse shock has a velocity that is suppressed compared to that of the forward shock by a factor $\xi^{3/2}\Gamma$, where ξ is a dimensionless quantity depending on the Sedov length of the system and the width of the shell (and is less than one for a relativistic shock and greater than one for a Newtonian one) and Γ is the bulk velocity of the outflow [321]. For reasonable values of ξ and Γ this suppression is significant and, as the minimum energy of shell-accelerated electrons depends linearly on the shock velocity, the reverse shock accelerates electrons to less high energies. The reverse shock therefore does not contribute emission at frequencies much above radio (or optical at early times). No such secondary break is seen for GRB 171010A. Perley 2014 [323] attributed the early peak in GRB 130427A's radio light curve as being due to the self-absorption frequency of the reverse shock (although it was later shown by [335] that $\nu_{\rm m}$ and $\nu_{\rm a}$ for a thin-shell reverse shock model were at similar frequencies at the time of this peak). Our analysis of GRB 171010A determines that it is likely a self-absorption break that causes the early peak in GRB 171010A. If this break had come from a reverse shock we would perhaps expect to see a secondary break in the light curve as was seen with GRB 130427A. If, however, the reverse shock dominates until a few days, we would predict that the secondary break may also occur later and so this secondary turnover may have happened after GRB 171010A was no longer detected by the AMI-LA. However, we could just be seeing the transition from reverse shock to forward shock domination and have missed the RS peak, which would be the natural assumption if not for the unusual spectral behaviour. Alexander 2017b [336] also invoked a reverse shock to explain the early time radio emission from GRB 160625B, whereas [360] invoked two reverse shock components (one caused by a shell collision) to explain the broadband emission properties of GRB 140304A. Our relatively limited spectral coverage, as well as small number of spectral epochs, makes confirming the presence of a reverse shock difficult. However the

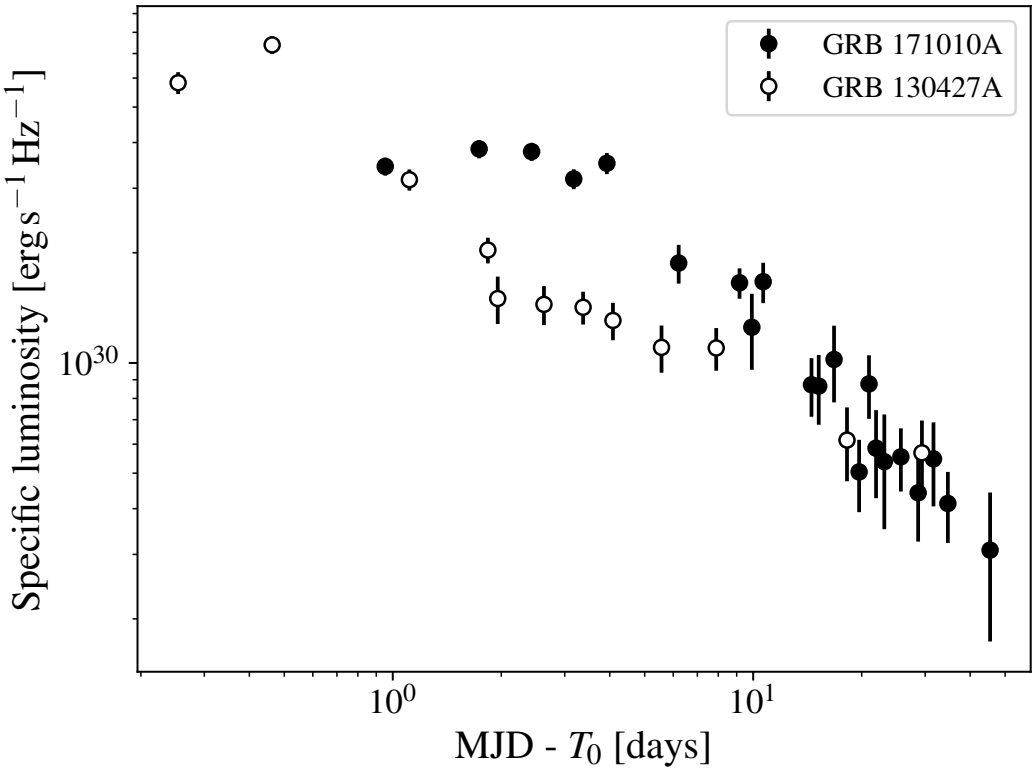

Figure 6.9: Specific luminosity of GRB 130427A (unfilled circles) and GRB 171010A (filled circles) at 15.7 GHz and 15.5 GHz, respectively, made with the AMI-LA. We have k-corrected each section of both light curves according to [359]. For GRB 171010A the spectral and temporal indices used for the correction were taken from this work. For GRB 130427A they were taken from [323] and [329].

relatively early radio peak, identified as being due to a self-absorption break, along with the unusual spectral evolution are compelling puzzles. This is especially true as the observed movement of $\nu_{\rm m}$ in GRB 171010A of $a = -0.6 \pm 0.2$ is not consistent with the predicted movement for a reverse shock alone (for any density profile), and thus we would require two spectral components to explain the movement of this break. This again is challenging for the simple spectral shapes we observe. It is, however, potentially unsurprising that a basic reverse shock model does not completely describe the data. The simple density structure usually invoked for the ejected material (inside which the reverse shock occurs) likely does not accurately reflect physical conditions in the jet. More complex density structures in the out-flowing material could lead to significantly more complex overall evolution, most notably early time X-ray flares (e.g. [361]).

6.5.2.2 Evolution of microphysical parameters

It has been suggested that time evolution of microphysical parameters such as the fraction of energy in electrons and magnetic field (ϵ_e and ϵ_B) could account for the deviation of $\nu_{\rm m}$ from the predicted value [144, 335]. Such evolution is not accounted for in the standard fireball model. For $p > 2$ and adiabatic evolution it can be shown that $\nu_{\rm c} \propto \epsilon_B^{-3/2} t^{-1/2}$ and $\nu_{\rm m} \propto \epsilon_B^{1/2} \epsilon_e^2 t^{-3/2}$ [312, 362, 314]. As we have no constraint on the evolution of the movement on $\nu_{\rm c}$ we can state generally that if both ϵ_e and ϵ_B are functions of time as $\epsilon_e \propto t^{\xi}$ and $\epsilon_B \propto t^{\psi}$ then $2\xi + \psi/2 \approx 1.8$ to match our observations. The required evolution is therefore not modest, even if it is distributed approximately evenly between the electrons and the magnetic field. Even more problematic is that one expects, based on theoretical considerations and simulations, ϵ_e and ϵ_B to decline over time, not increase. We therefore strongly disfavour microphysical parameter evolution as the primary driver of the unusual spectral/temporal evolution.

6.5.2.3 Scintillation effects

It is also worth considering the possible effect of scintillation on our radio observations of GRB 171010A. Scintillation is the apparent modification of the flux and originating position of electromagnetic radiation diffracted as it moves through the ISM (and interacts with free electrons), and is more pronounced for radiation from compact sources, such as GRBs. For example, observations of GRBs 160625B and 161219B show scintillation inducing large amplitude variability in flux and radio spectral index on timescales as short as minutes, as well as unusual spectral shapes, across the radio band [336, 363, 364]. To check for short time-scale scintillation effects in our radio data we imaged each VLA epoch in 5 m time chunks in each of the frequency bands used to create the spectra shown in Figure 6.4. We see no evidence of significant short term variability in any of the bands. Scintillation can also occur on longer timescales, but given our simple spectra (well described by a single or broken power law) with similar slopes across epochs 2 and 3, we disfavour scintillation causing the unusual spectral break evolution.

Other more complex pictures have also been invoked to explain unusual GRB behaviours. These include multiple jet components [365, 335] as well as variable energy injection into the fireball through either external density variations in the surrounding material [366, 367] or refreshed shocks from variable Lorentz factors in the out-flowing material [368, 369]. While these additional complications are worth considering, they require broadband observations (particularly early-time optical data), which are not presented in this work. When a more

complete set of observations for GRB 171010A is available these models will be worth further analysis. In particular a more complete set of VLA observations of the source were taken in addition to the ones initiated by us, but they remain private on the VLA archive over two years after the burst occurred.

6.6 Conclusions

This work highlights the benefits of early and regular monitoring of long GRBs at multiple radio frequencies, as well as in other wavebands. Having high cadence light curves and multiple broadband spectral energy distributions is essential to characterise the spectral and temporal behaviour of this source class. In some ways GRB 171010A can be well described by a simple forward shock model, propagating into a medium with a steep density profile. However, the evolution of the spectra and a number of features of the light curves are hard to explain. Most striking is the extremely slow movement of the minimum energy frequency, which should evolve to lower frequencies faster than observed. We have considered several possibilities for this discrepancy, including time evolution of microphysical parameters, extreme scintillation and the addition of a reverse shock but cannot conclusively attribute any of these to the observed unusual evolution.

Chapter 7

A radio study of the tidal disruption event ASASSN-14li

This chapter is based on work published in Bright *et al.*, Long-term radio and X-ray evolution of the tidal disruption event ASASSN-14li. MNRAS, **475**, 4011-4019.

7.1 Introduction

A tidal disruption event (TDE) occurs when a stellar object passes within the tidal radius of a supermassive black hole (SMBH) on a highly eccentric orbit (which is potentially misaligned with the black hole's spin) and is torn apart when strong tidal forces overcome the star's self gravity. At some separation between the star and the SMBH the differential gravitational force from the black hole (tidal force) is sufficient to overcome the gravitational binding force of the star. This critical radius can be derived through a simple approximation. Consider an instant in the star's orbit where it is at a radial distance R from the SMBH, with the star having radius $R_\star$. Due to the spherical symmetry of the system we can 'collapse' the stellar mass down to two points at distances $R - R_\star/2^{5/3}$ and $R + R_\star/2^{5/3}$ from the black hole, respectively. The gravitational force between the two masses (each with $M = M_\star/2$) is simply equal to $2^{-2/3}GM_\star^2/R_\star^2$, whereas the differential force due to the gravitational influence of the SMBH is $\Delta F = GM_\star M_{BH}[(R-R_\star/2^{5/3})^{-2} - (R+R_\star/2^{5/3})^{-2}]$ which is (using the binomial approximation, and noting that $R_\star \ll R$) approximately $GM_\star M_{BH}R_\star/R^3$. Equating these gives the tidal radius:

$$R_\mathrm{t} = R_\star\left(\frac{M_\mathrm{BH}}{M_\star}\right)^{1/3} = 0.5\ \mathrm{AU}\left(\frac{M_\mathrm{BH}}{10^6 M_\odot}\right)^{1/3}\left(\frac{R_\star}{R_\odot}\right)\left(\frac{M_\star}{M_\odot}\right)^{-1/3}. \quad (7.1)$$

Approximately half of the mass of the disrupted object forms a complex accretion flow onto the SMBH (initially orbiting the black hole on a highly elliptical orbit, requiring circularisation through self-interaction of the precessing steams of disrupted material dissipating energy via shocks [370]), while the other half becomes unbound and is ejected from the system (see e.g. [124, 371, 372]). Considering the condition that

$$R_{\rm t}/R_{\rm sch} \approx 23\left(\frac{R_\star}{R_\odot}\right)\left(\frac{M_{\rm BH}}{10^6 M_\odot}\right)^{-2/3}\left(\frac{M_\star}{M_\odot}\right)^{-1/3} > 1 \tag{7.2}$$

for the stellar disruption to occur outside of the Schwarzschild radius, we see that the tidal radius approaches the Schwarzschild radius for larger black hole masses and more dense stellar objects (although the assumption of a uniform density object is of course naive, and will influence the radius of total disruption and lead to the possibility of partial disruption [373]). As an example a star with the same density as the Sun could participate in a TDE for $M_{\rm BH} \lesssim 10^8\, M_\odot$. Note that the black hole spin alters the position of the event horizon (smaller event horizon for larger SMBH angular momentum) allowing for larger black holes to cause TDEs [374]. The impact parameter of the stellar orbit (the perpendicular distance between the stellar trajectory and the black hole) will also play an important role in determining if the disruption will be partial or total, and will influence how the accretion flow evolves.

The study of TDEs provides a unique method for determining properties of galaxies, as well as inactive SMBHs, while being physically interesting transient events in their own right. Stars will only enter within the tidal radius of a SMBH if they are placed on 'loss cone' orbits. Stars that initially posses loss cone orbits will quickly be disrupted and accrete onto the SMBH and so a mechanism is required to replenish the supply of disruptable stars. This could occur through gravitational interactions between the stellar population evolving the orbital dynamics of individual stars, or from global asymmetries in the stellar population itself (see e.g. [375] for a review). Studying the rates of TDEs therefore provides information on the stellar populations of the types of galaxy they preferentially occur in [376, 377, 378]. TDEs also provide another line of evidence for the existence of SMBHs, and provide an opportunity to probe the population of SMBHs in galaxies that are not otherwise electromagnetically active [379, 380]. Furthermore, TDEs could provide evidence for the existence of intermediate mass black holes [381]. TDEs also represent a new class of object from which to study the formation of accretion disks (with initially super-Eddington accretion rates [382, 383]) in real time, as well as the formation of jets associated with this accretion that interact with material close to the SMBH providing information on the inner

regions of galaxies [384, 385].

Tidal disruption events are observed to apparently consist of two classes of source, named 'thermal' and 'jetted', although the sample size of well studied events remains small. As their names suggest, the (non-radio) emission from the thermal population of TDEs can be well described by one or more black body emitting regions. For jetted events the broadband emission (particularly the radio, X-rays and γ-rays) is consistent with arising from non-thermal synchrotron emission from a jet close to our line of sight (while a thermal component is, in some cases, still observable and likely associated with an accretion disk [125]). I will now briefly discuss the different emission properties of the classes of TDE.

7.1.1 Optical, UV, and X-ray emission from thermal TDEs

The accretion of the bound material onto the SMBH results in a transient event, with the electromagnetic emission sometimes also called a tidal disruption flare (TDF). They are identified as TDE candidates based on a their location being consistent with the nucleus of a galaxy (with particular galaxy types favoured [377]), their spectral and temporal properties, and luminosity. Thermal TDEs can be identified through their strong blue continuum, showing significant brightening in optical, UV – and sometimes X-ray – compared to archival observations of the host galaxy. Spectral signatures of TDEs include broad hydrogen (Balmer series) emission lines as well as emission in He I, and He II (with a variety of line widths; examples given in [377]), although the abundance of specific elements varies significantly between events, and will depend on the properties of the star being disrupted [386, 377]. Absorption lines have been observed from a few TDEs [387, 388], and understanding the processes for line formation remains challenging. The TDF, and the subsequent months to years of flux evolution, is usually visible at optical [384, 386, 377, 389, 390, 387, 391] and/or UV [392, 393, 394] and/or X-ray [395, 396, 397, 398, 399, 400, 401] frequencies and discovered by wide field transient surveys, sometimes in galaxies with a previously inactive SMBH [402]. The SED from optical/UV TDEs peaks at around $10^4\,\mathrm{K} \approx 1\,\mathrm{eV}$ wheres the X-ray events have an SED peaking at $10^5\,\mathrm{K} \approx 10\,\mathrm{eV}$, i.e. at soft X-rays. This distinction is merely describing where the blackbody SED of the 'thermal' TDEs peak, and is not to be confused with the 'thermal'/'jetted' paradigm discussed previously, as jetted TDEs are discovered through their γ-ray emission and show non-thermal spectra (e.g. X-ray emission consistent with being from a jet or from a forward shock [403]). Early models of TDEs predicted that the observed luminosity should follow the fallback rate of material after the disruption (due to the timescale of accretion being shorter than the orbital timescale of the self-interacting streams), with $L \propto t^{-5/3}$ [124]. However it can be shown that the fallback

rate will depend on stellar structure [404]). While a good number of TDEs do appear to follow this relation, there are both observational and theoretical suggestions that this may not be a universal relationship [405, 406]. The $-5/3$ relationship has been observed for a number of systems, although the black body radius implied by fitting the SEDs suggests emission from regions significantly larger than the outer radius of an accretion disk, and therefore possibly from a different emitting region [384, 407]. This is further supported by narrow optical line widths inconsistent with the orbital motion of an accretion disk with radius comparable to the tidal radius (e.g. [370] and references therein). Suggestions for the discrepancy include an optically thick reprocessing region at larger radii that thermalises X-ray and extreme UV emission from the disk and emits it at a lower temperature whereas X-ray emission, if seen, is from the disk itself [408, 372, 409, 410]. It has been suggested that the origin of this reprocessing region could be the unbound stellar material [126] or outflows driven off of the accretion disk [409]. The timescale for accretion disk formation is itself an open question, and will depend on the self-interaction of steams of stellar material, which are also suggested as another possible source for the large radii optical/UV emission [370, 411]. Given the range of configurations possible in a TDE (e.g. impact parameter, stellar structure, orbit eccentricity, SMBH mass, etc.) and how these can alter the proposed arguments for the origins of thermal TDE emission it is perhaps not surprising that there is a diversity in the emission properties of the thermal TDE population.

The accretion flow formed in a TDE is unlike classical AGN accretion disks, consisting of orders of magnitude less mass but producing, on average, significantly higher accretion rates, which can be (initially) super-Eddington. The material that remains bound to the SMBH is expected to form an accretion disk, with the circularisation timescale depending on relativistic precession effects, which dictate the chance of stream self-interaction [412, 413, 414] and are in part dictated by the spin of the SMBH. It has also been shown [412] that the radiative cooling efficiency can affect the circularisation timescale, as well as the thickness of the disk. The observational signatures of such an accretion flow will depend on the circularisation, radiative cooling and viscous timescales which are described and discussed by [415, 413]. Alternatively, it has been suggested that the dominant component of the optical/UV emission could be the result of the bound debris stream self-interacting (and shocking) as it circles the black hole, with the disk predominantly contributing X-ray emission [370, 416].

7.1.2 Radio emission from thermal TDEs

A small number (currently only 5, see Figure 7.5) of thermal TDEs have also been observed to produce significant radio emission. The physical region responsible for this emission is still contested, as is the cause of the apparent lack of radio loud candidates (although it is possibly just a selection effect due to the relatively low radio luminosity of thermal TDEs [417]). As discussed in detail in Chapter 2, radio synchrotron emission is produced as shocks accelerate electrons to high energies and they radiate as they spiral around magnetic field lines. There are a number of processes in TDEs that could produce such conditions. Firstly, while I have so far focused on the material that is bound during the tidal disruption, a significant amount of material (approximately half of the stellar mass) is ejected (no longer gravitationally bound) from the system with significant (but sub-relativistic) velocity [124]. The unbound stellar remnant has the potential to drive shocks into nuclear material near the galactic centre (compared to which it will have a large velocity and density). Radio emission from the resulting interaction has been invoked by some authors to explain the emission from the thermal TDE ASASSN-14li [411]. It has also been suggested that the high velocity material shocking the nuclear ISM could originate from the accretion disk, being driven off radiatively due to the high accretion rate as suggested for the TDEs ASASSN-14li and XMMSL1 J0740−85 [128, 417]. Finally, as TDEs are accreting objects it is natural to consider the possibility that they produce a jet, which again was proposed to explain the radio emission for the TDE ASASSN-14li (having the best coverage at radio frequencies of the thermal population) [384, 127]. Recent evidence has made this latter consideration more compelling, with the TDEs J12580+0134 and Arp 299 both showing evidence for the presence of a (directly resolved) jet, despite having lower radio luminosities (Figure 7.5) and, in the case of J12580+0134, showing the presence of an accretion disk (although in hard X-rays which are interpreted as a corona rather than the standard black body emission [418]). Arp 299 was too absorbed to infer the presence of a disk. Similarly, radio morphology studies of ASASSN-14li with the EVN have revealed tentative evidence for a jetted outflow [419].

7.1.3 Jetted TDEs

There are some TDEs for which the production of jets is not disputed. This subsection of the population, the 'jetted TDEs' is a tiny fraction of the total pool of TDE candidates, with currently only three sources, Swift J1644+57, Swift J2058+05, and Swift J1112.2 (this does not include J12580+0134 and Arp 299 as these sources lacked multiwavelength data and appeared to be significantly less energetic, possibly suggesting an off axis jet [420]).

Swift J2058+05, and Swift J1112.2 have significantly worse data sets associated with them than the bright and long-lived (bright for over 10 yr at radio frequencies) Swift J1644+57. However, all three sources share similar properties with one another that make them distinct from the thermal class of TDEs. The primary difference is the inferred presence of a highly collimated and at least mildly relativistic on-axis jet. The presence of this jet is inferred in a number of ways, firstly the accretion rate for these systems would, without significant beaming, be super-Eddington on timescales of months to years. Secondly, the radio luminosity of these sources, and the fact that the brightness temperature of a radio emitting region cannot exceed $\sim 10^{12}$ K without suffering catastrophic cooling via Compton processes, combine to place a lower limit on the expansion rate of the region of $\sim 0.9c$. Interestingly, for the source Swift J2058+05 the optical/UV SED was consistent with black body radiation indicating that both an accretion disk and a jet were observed from the source simultaneously. Despite the richer data set on Swift J1644+57, heavy dust obscuration prevented a similar analysis being performed. The radio spectra from the jetted TDEs varies from optically thick to flat and therefore could, in some cases, have different conditions than the flat spectrum jet discussed in Chapter 2. The small number of sources making up this class of TDEs has left authors to suggest that the jets are highly collimated, or that only a small fraction of TDEs are able to produce relativistic jets (for an as yet unknown reason), or a combination of these two factors. Swift J1112.2 was not detected at radio frequencies and thus its classification as a relativistic TDE is based on its optical through γ-ray emission which showed similar properties to the other sources of its class. High resolution VLBI observations have constrained the properties of the jet produced by Swift J1644+57, but the outflow has not been resolved directly [421]. There is an additional jetted TDE candidate in the galaxy Arp 299, where a superluminal jet was observed to expand on the timescale of years [422]. Due to heavy obscuration by dust, the source was not detected at optical or UV frequencies but the source was IR bright likely due to dust reprocessing of this radiation. The canonical jetted events have so far only been detected at larger redshifts (e.g. $z \gtrsim 0.35$) when compared to the thermal population ($z \lesssim 0.1$), which is another indication of their rarity (a larger sampling volume if required to detect them regularly) and of course their higher intrinsic luminosity. Another distinguishing characteristic of the relativistic TDEs is that they are producers of γ-rays, unlike the thermal population. Such high frequency radiation could not be produced in stream self-interactions or an accretion disk but a relativistic jet is a natural source of γ-rays (cf. blazars [423]). TDE jets have also been proposed as sources of high energy neutrinos, with one possible candidate identified to date [424].

Throughout the remainder of this chapter I will present the results of long-term radio and X-ray monitoring of the TDE ASASSN-14li, as well as a short update on the outburst of the long-lived jetted TDE Swift J1644+57 at radio frequencies.

7.2 ASASSN-14li

ASASSN-14li was discovered by the All Sky Automated Search for Supernova (ASAS-SN) on UT 2014–11–22.63 (MJD 56983.63) as a 16.5 magnitude source in the V-band [425]. The position of the source was found to be consistent with the centre of the post-starburst galaxy PGC 043234, with a measured projected separation of 0.04″. This galaxy is at redshift $z = 0.0206$ with a luminosity distance of 90.3 Mpc (for cosmological parameters $H_0 = 73\,\mathrm{kms}^{-1}\,\mathrm{Mpc}^{-1}$, $\Omega_{\mathrm{matter}} = 0.27$, and $\Omega_\Lambda = 0.73$). It was established through archival X-ray observations of PGC 043234 from the ROSAT All-Sky Survey [426] that the galaxy does not contain an efficiently accreting AGN, with the count rate implying a luminosity orders of magnitude below standard active nuclei [409]. A small number (currently 8) of confirmed TDEs, including ASASSN-14li, have also been detected at radio wavelengths and the population appears to form a bi-modal distribution, consisting of more common non-relativistic 'thermal' events and rarer events with relativistic jets. Three events (Swift J1644+57; [427, 428, 429], Swift J2058+05; [125], Swift J1112.2; [430]) have isotropic ~ 5 GHz luminosities of between 10^{40} and $10^{42}\,\mathrm{erg\,s}^{-1}$ whereas the rest (IGR J12580+0134; [431], XMMSL1 J0740-85; [417], ASASSN-14li; [127, 128, 432]; Arp229 [422]; AT2019dsg [424]) have luminosities in the range 10^{35} to $10^{39}\,\mathrm{erg\,s}^{-1}$ at similar frequencies. The higher power events are believed to result from observing down the axis of a relativistic jet, resulting in the energy of photons being significantly boosted. Even accounting for boosting, these relativistic events have a higher total energy output than their thermal counterparts. The origin of the radio emission from the thermal events is currently uncertain, with transient jets [127], non-relativistic winds [128], off-axis jets [420], and shocks driven by unbound material [411] all feasible scenarios. ASASSN-14li is by far the best studied of the 'thermal' TDE category, having been observed extensively at Optical, UV, X-ray (where ASASSN-14li is unusually loud for an optically selected TDE) and radio wavelengths. The high cadence X-ray and radio observations in particular allow for the X-ray/radio coupling to be probed.

7.2.1 Observations

7.2.1.1 Swift-XRT

Swift [181] observations of ASASSN-14li were first initiated on MJD56991.5 and a total of 130 observing segments have been conducted to date (128 of which had photon counting (PC) mode data), with exposure times ranging between 90 and 4000 s. The 6 segments between MDJ57819.6 and MJD57833.5 were triggered due to a target of opportunity request submitted by the authors, whereas all other observations were archival or have occurred since this work was published. The position of the source was measured as J2000 RA/Dec = 12h 48m 15.05s/+17° 46′ 31.5″ with a circular 90% confidence region of radius 3.5" [433, 187]. The source was observed multiple times per week for the first ∼ 200 days post flare, and more sporadically afterwards. Observations utilised the X- ray telescope (XRT) instrument in PC mode as well as the ultraviolet and optical telescope (UVOT), with the exact filter depending on the observation (we requested observations with the UVOT filter of the day to reduce scheduling constraints). We are primarily interested in the X-ray data, and the Swift XRT product generator online reduction pipeline [186, 187] was used to extract count rates in the 0.3–10 keV energy band from the observations. In order to probe the X-ray – radio luminosity correlation we converted our count rates into fluxes. To do this, we first binned the X-ray light curve of ASASSN-14li into 6 broad time bins and extracted a spectrum from each bin. We defined the bins in a way that allowed us to both obtain acceptable S/N spectra, and to evenly sample the decay phase of ASASSN-14li. These spectra were then fit with an absorbed black-body model, from which the flux could be calculated. The resulting best-fits show a black-body temperature variation consistent with those reported by [409]. The relationship between flux and counts across the 6 bins was described by a linear fit, which was then used to convert the full light curve from count rate to flux. The Swift X-ray light curve is shown in the bottom panel of Figure 7.1.

7.2.1.2 Arcminute Microkelvin Imager Large Array

Radio observations of ASASSN-14li were initiated with the Arcminute Microkelvin Imager Large Array [169, 170], hereafter AMI-LA, on MJD 57014.1, about 22 days after the first Swift observations of the source. ASASSN-14li was monitored on an approximately weekly basis (apart from a significant gap between ∼ 180 and ∼ 400 days post flare due to technical work being performed on the AMI-LA) with typical exposures lasting between 2 and 4 hours, yielding an RMS flux in a typical image of ∼ 35 and 25 μJy, respectively. Observations pre MJD − 56983.6 = 200 were taken with an analogue correlator at an effective central frequency of 15.7 GHz, and are published in [127]. Observations after the

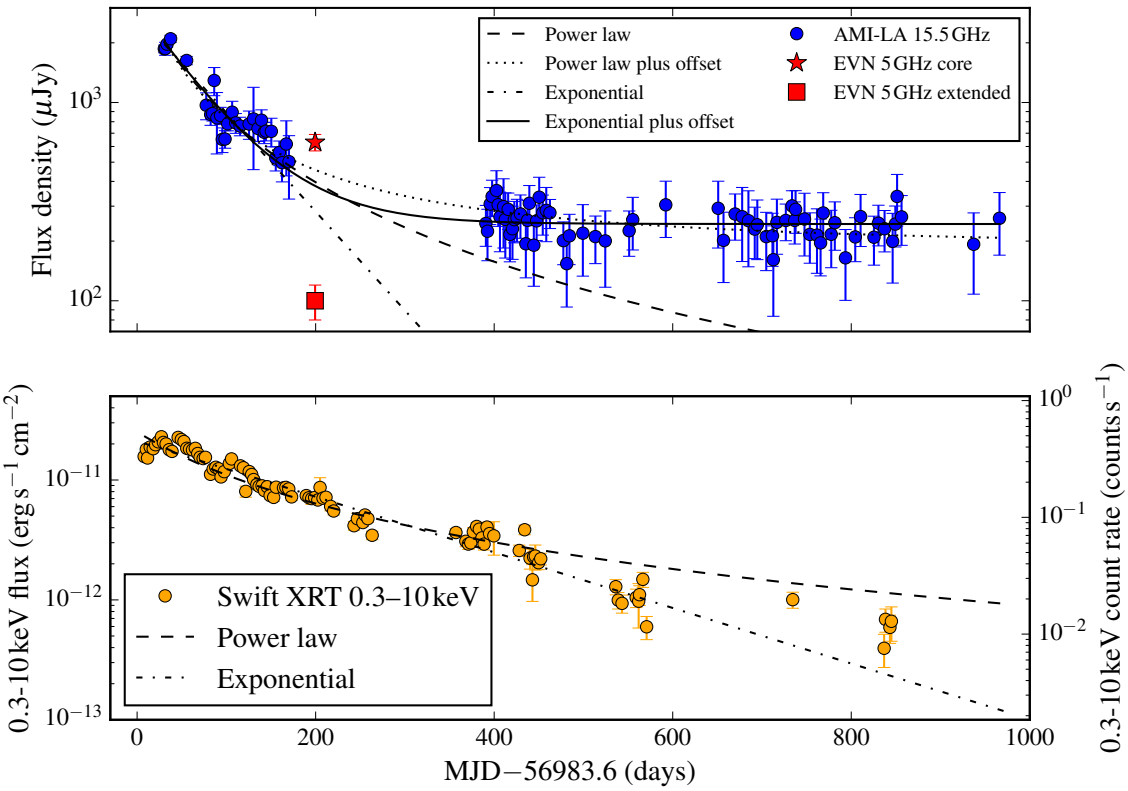

Figure 7.1: Radio and X-ray emission over the first 1000 days post-detection of TDE ASASSN-14li. Upper panel: Blue circles indicate observed radio flux measured by the AMI-LA at 15.5 GHz (15.7 GHz for epochs up to MJD − 56983.6 = 200). Lower panel: Swift XRT observations in the 0.3–10 keV energy band, measured in both counts per second and flux. In both panels error bars indicate 1σ uncertainties on measurements, dashed lines show a power law decay with the exponent fixed to $-5/3$, dash-dot lines show an exponential decay. Exponential and power law decays plus a constant offset are fit to the radio data only and are shown by solid and dotted lines respectively. The red star and square indicate measurements of core and extended components (respectively) of ASASSN-14li at 5 GHz with the EVN [419]. Fit parameters are summarised in Table 7.1. Note the logarithmic scale on the y-axis.

Table 7.1: Summary of light-curve fit parameters for the exponential, exponential plus offset and power law fits shown in figure Figure 7.1. The (entire) radio light curve is best fit by an exponential plus constant offset which is used to estimate the plateau flux. The reduced chi-squared statistic, $\chi^2_{\rm red}$, indicates that the X-ray light curve is significantly better fit by an exponential rather than a $-5/3$ power law. The large $\chi^2_{\rm red}$ values result from deviations from simple decay models.

Radio					
Fit type	t_0 (MJD $-$ $t_{\rm d}$)	Decay timescale (days)	Power law index	Offset (μJy)	$\chi^2_{\rm red}$
Exponential[a]	–	87 ± 6	–	–	3.24
Exponential and offset[b]	–	66 ± 3	–	244 ± 8	0.99
Power law[a,c]	-71 ± 8	–	$-5/3$	–	2.48
Power law and offset[b,c]	-47 ± 5	–	$-5/3$	180 ± 10	0.94
X-ray					
Fit type	t_0 (MJD $-$ $t_{\rm d}$)	Decay timescale (days)	Power law index	–	$\chi^2_{\rm red}$
Exponential	–	187 ± 6	–	–	8.54
Power law[c]	-155 ± 9	–	$-5/3$	–	13.99
Power law[d]	-132.35	–	-1.60 ± 0.05	–	14.95

[a] Only radio measurements in decay phase used for fit.
[b] All radio measurements used for fit.
[c] Power law index fixed to $-5/3$.
[d] Start date fixed.

gap utilised the new digital correlator, which has 4096 channels across a 5 GHz bandwidth between 13 and 18 GHz and were first published in [432]. J1255+1817 was used as the interleaved phase calibrator and was observed for ~ 2 mins for every ~ 10 mins on source while 3C286 and 3C48 were used for absolute flux calibration. The AMI-LA data were binned into 8 channels, each of width 0.625 GHz, and were calibrated and flagged for radio frequency interference (RFI) using the automated AMI reduction software pipeline reduce [434]. The data were then imported into CASA [176] where additional RFI flagging was performed using the flagdata task in rflag mode, which removed interference localised in time and frequency at the 3σ level. The data were then cleaned using the clean task, with a stopping threshold of 3 times the background RMS of the image and a gain of 0.1. To calculate flux measurements from ASASSN-14li we used the python based PySE source extraction software, which was developed as part of the LOFAR Transient Pipeline [435]. A detection threshold of 3.5σ was used for source identification, and a 3-sigma threshold was used for fitting the source in the image plane for each observation. A 2D Gaussian, with the same dimensions as the clean beam, was used to fit the unresolved source at phase centre (corresponding to ASASSN-14li). Typical dimensions of the clean beam major and minor axis FWHM are ~ 60 and ~ 30" respectively. The AMI-LA light curve is shown in the top panel of Figure 7.1. Stacking the plateau phase radio observations in each of eight equally-spaced frequency bands, we are able to estimate a spectral index of -0.9 ± 0.5.

7.2.2 Results

Radio and X-ray light curves of ASASSN-14li for ~ 1000 days post discovery are shown in Figure 7.1, along with power law and exponential fits to both data sets. The fit parameters are summarised in Table 7.1. We find that the X-ray light curve is better characterised by an exponential decay, rather than the canonical [371] $-5/3$ exponent power law decay, demonstrated by the significantly improved reduced chi-squared statistic (Table 7.1). The large reduced chi-squared values, however, indicate that while we may be describing the long-term trends in the light curve, there is significant deviation from this simple decay model on shorter timescales (discussed in [416, 436]). For ease of discussion we will refer to epochs up to MJD $-$ 56983.6 = 200 as the decay phase (although it is only the radio light curve that ceases to decay after this date), and later observations as the plateau phase. When fitting the radio light curve, we opt to consider two cases. First, we fit the decay phase during the first ~ 200 days and find that the $-5/3$ power law explains the data marginally better than an exponential. The whole set of radio observations (decay and plateau) is well characterised by an exponential decay plus a constant offset (a $-5/3$ power law plus offset provided a worse fit). Whilst it would be natural to attempt to fit the decays with a varying

index and start date, we are unable to resolve the inherent degeneracy in these two parameters given that we do not observe the peak of the light curve. Using the most recent date of non-detection of ASASSN-14li at optical wavelengths presented in [437] as an estimate of the start time allows for a crude estimate of the power law index to be calculated. The index, when adopting this start date, is similar to $-5/3$ but the reduced chi-squared is still significantly worse than for an exponential decay.

In order to correlate the X-ray and Radio observations of ASASSN-14li, which were not simultaneous, we binned each light curve into bins of width 4 days and compared the radio and X-ray flux where both had been measured in the same bin. This width was found to optimise the number of data points available for comparison. If multiple measurements at the same wavelength were contained within a specific bin then a numerical average of the data was used to represent the flux in that bin. In the case of either light curve having no data within a bin, no comparison was made. In order to ensure we were only comparing radio and X-ray emission resulting from the TDE, and not just from the host, we exclude data taken during the plateau phase from our correlation analysis. Before this date both the X-ray and radio emission were still declining and thus dominated by the TDE. We find that the radio flux density and X-ray flux (and thus the luminosities) are strongly correlated during the decay phase. The form of the relationship is $L_R \propto L_X^{1.9\pm0.2}$ and the Spearman rank correlation coefficient is 0.86. To obtain these results we subtract the plateau radio measurement of $244 \pm 8\,\mu$Jy from the decay phase radio observations. L_R is the isotropic, monochromatic, luminosity at 15.7 GHz and L_X is the X-ray luminosity in the the 0.3–10 keV energy band. The correlation can be seen in Figure 7.2.

7.2.3 Explaining the radio plateau

It is clear from Figure 7.1 that the radio light curve plateaus from an initial fading phase into a phase of constant flux of around 250 μJy which it maintains for around 600 days. During the radio plateau period, the X-ray count rate continues to decline, showing no sign of mirroring the behaviour at 15.5GHz. We discuss a number of possible contributors to the radio flux density plateau observed by the AMI-LA.

7.2.3.1 Host galaxy radio emission

We assume here that the plateau emission is unconnected to the TDE, which presumably continues to decline, and discuss briefly below its possible origin. The host galaxy of ASASSN-14li, PGC 043234, has archival measurements in the FIRST (November 1999)

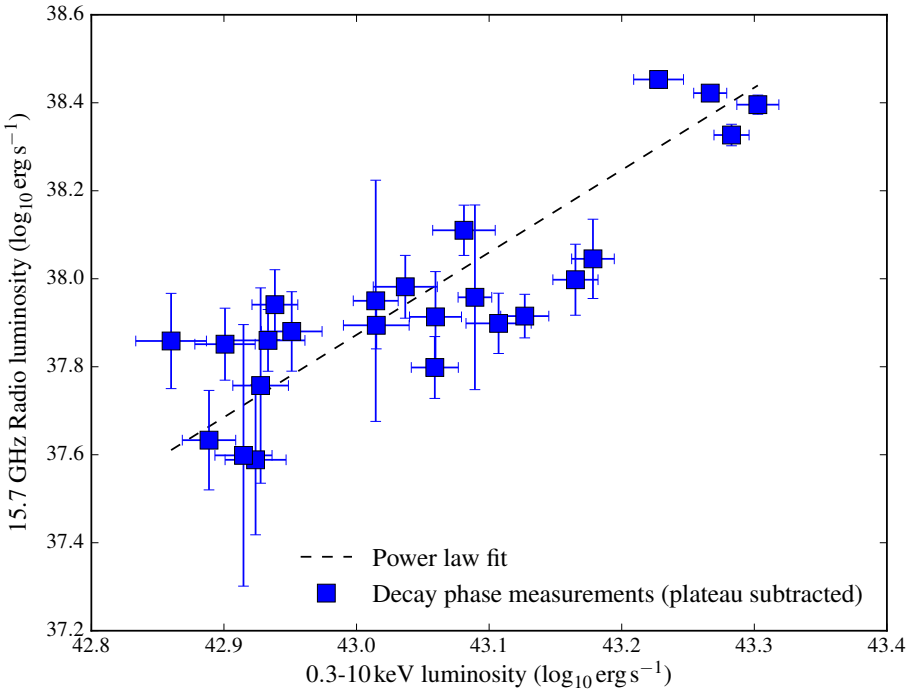

Figure 7.2: Radio–X-ray correlation for ASASSN-14li, produced by binning the respective light curves during the decay phase and subtracting the plateau flux of 244 μJy. The black dotted line is a fit to the data, with a best fit power law index of $\alpha = 1.9 \pm 0.2$ ($L_R \propto L_X^{\alpha}$).

and NVSS (December 1993) surveys, both at 1.4 GHz [438, 351]. The measured flux densities are 2.96 ± 0.15 and 3.2 ± 0.4 mJy, respectively. Due to the resolution of the AMI-LA we are unable to resolve individual sources in the host galaxy and so all radio emitting elements from the galaxy will be observed to be combined into a single unresolved source.

Firstly, supernova remnants in the host galaxy could be responsible for background emission. The small scale radio morphology of PGC 043234 has not been probed with long baseline observations (outside of the central few parsecs; [419]) so we must turn to analogous galaxies which have been studied more extensively. Arp220 is a nearby (77 Mpc) ultra-luminous infrared galaxy, which has been well studied at 18, 13, 6, 3.6 [439, 440] and most usefully 2 cm (15 GHz) with VLBI observations ([441]). These observations revealed a population of compact (sub-parsec) sources which are believed to be a mixture of supernovae (SNe) and supernova remnants (SNR). The 15 GHz radio flux from these individual sources ranges from 91 to 693 μJy which would correspond to 66 and 504 μJy at the distance of ASASSN-14li. Although this galaxy is a more extreme environment than the host of ASASSN-14li, it illustrates that even a single radio loud SNe or SNR, or a population of fainter objects, could be responsible for the observed radio plateau of ASASSN-14li.

An alternative, and more likely, possibility is emission from relic radio lobes from past AGN activity (discussed briefly also in [127]). Such lobes would be expected to remain constant in flux over long timescales and to have an optically thin spectrum. Considering the lack of star formation indicators (discussed in [442, 128, 127]) in PGC 043234, the clear presence of a supermassive black hole (hence the TDE) and the EVN observations revealing the majority of the flux to be combined within a few parsecs of the central object, we conclude that past AGN activity is the more likely scenario for the quiescent component.

Optically thin relic AGN lobes with a spectral index of approximately -0.9 (consistent with both our in-band measurements and those reported towards the end of the decay phase by [128]) and a 15 GHz flux density of 244 μJy would correspond to a 1.4 GHz flux density of ~ 2.1 mJy, broadly consistent with the quiescent component assumed in [128]. It has been proposed [127] that the onset of the TDE suppressed optically thick emission from a steady AGN jet in PGC 043234. Our discovery of a plateau is not inconsistent with this idea, if the system contained both AGN lobes and a compact jet pre-TDE (the sum of which gave the archival 1.4 GHz measurements of ~ 3 mJy). It is also possible [128] that the observed decline in 1.4 GHz emission in the 16 years since the FIRST measurement is simply due to long-term AGN variability of a compact component.

7.2.3.2 Radio emission still from ASASSN-14li

We also consider the possibility that the radio emission we are observing is now steady emission from the TDE. It is, however, hard to reconcile the combined observed X-ray and radio behaviour with any of the TDE models currently being considered. If the radio emission results from some form of outflow (radiatively driven wind, unbound material, discrete jet launch) we can see no reason why the radio emission would stop declining, despite it not being coupled to the likely source of X-ray emission (the accretion disk). In the case of core jet activity we would expect the X-ray and radio emission to remain coupled. In all scenarios, barring an unexpected increase in accretion rate, the decaying nature of the X-ray light curve is expected. Given the numerous possibilities for constant (on the timescale of the decay of ASASSN- 14li) sources of radio emission in PGC 043234 and the fact that we can see no physical motivation for the radio emission in any of the currently considered models (core-jet emission, relativistic jet, radiatively driven wind, shocking disrupted material) to plateau, we strongly disfavour this scenario, instead attributing the quiescent radio flux density to background emission from PGC 043234.

7.2.4 Radio - X-ray correlation

It is clear that prior to the radio plateau the radio and X-ray emission are fading together (Figure 7.1). When correlating the decay phase data we subtract the plateau emission and find a strong positive correlation between the X-ray and radio flux (Figure 7.2). The correlation can be described by a power law, with a power law index of $\alpha = 1.9 \pm 0.2$ ($L_R \propto L_X^{\alpha}$). This correlation can be interpreted in two ways. The more conventional explanation is that the core X- ray emission arises in the accretion flow while the radio emission is from decoupled ejecta, and both are fading independently. Two variants of this scenario are outlined in [411, 128]. Even under the assumption that one of these models is correct, it is not clear if or how our new radio and X-ray data could discriminate between them. Alternatively, the core X-ray and radio emission may be correlated because they are coupled via an accretion flow feeding a core jet. Such an interpretation has not (until recently) been generally invoked for thermal TDEs, although for this source it is also raised to explain shorter-timescale radio and X-ray correlations [416], and there has been increasing evidence for more jets from TDEs which should couple to the accretion flow creating them. The observed correlation, $L_R \propto L_X^{1.9\pm0.2}$, is similar to that observed for stellar mass black holes in 'radio quiet' black hole X-ray binaries [214]. While in such systems the radio spectrum is usually flatter than is observed in ASASSN-14li ([128, 432]), it is not inconsistent with the range observed [443]. Typically core jet emission in stellar mass black hole binaries is seen to coincide with a hard X-ray spectrum, peaking at $\sim 100\,\mathrm{keV}$. The majority of X-ray photons from ASASSN-14li are below $\sim 1\,\mathrm{keV}$, however not enough is known about the nature of the accretion flows in TDEs for this to exclude core jet emission. We also note that there are examples of galactic X-ray binaries (e.g. GRS 1915+105; [196]) showing core radio emission with a soft X-ray spectrum, when averaged over a certain time period and at a high accretion rate.

Applying the approximate relationship between core radio luminosity and jet kinetic power presented in [444] to the peak radio luminosity of ASASSN-14li gives $L_{\mathrm{jet}} \sim 10^{43}\,\mathrm{erg\,s^{-1}}$. It is reassuring to note that [436] find that ASASSN-14li falls on the fundamental plane of black hole activity [445, 105], although with the caveat that the X-ray luminsoity was derived using the 0.3-10 keV energy band rather than the traditional 2-10 keV. Further VLBI observations similar to those reported in [419] may help to resolve uncertainties in the origin of the radio emission, although ASASSN-14li itself is likely now too faint to probe with VLBI observations.

7.2.5 Light curve fits

It is clear that the forced $t^{-5/3}$ power law fit does not well describe the X-ray data compared to the exponential decay, demonstrated by the significantly increased reduced chi-squared statistic and the overestimate of the late-time flux. It is, however, likely that the fit would be significantly improved if there was a better constraint on the start date (t_0) of the flare (see more estimates in [437]). In either case it is evident that a simple decay model for the X-ray emission from ASASSN-14li does not explain the significant short-term variability in the light curve, demonstrated by the large reduced chi-square value. During the first $\sim$ 150 days of X-ray observations, deviations from the simple decay models are dominated by an apparently quasi-periodic signal, described as resulting from stream self-interactions modulating the accretion rate [416].

The early time radio light curve is well characterised by both a $-5/3$ power law and an exponential (although marginally better by a power law), and the entire data set is well fit by an exponential plus constant offset. The exponential fits for the light curves provide characteristic decay times for the X-ray and radio emission which are $\sim$ 190 and $\sim$ 90 days, respectively. Fitting the radio light curve with a free index suffers from the same issues as the X-ray light curve, however see [405] for a more detailed analysis of TDE decays at X-ray wavelengths.

If core jet coupling is present in ASASSN-14li we might expect short-term variation in the X-ray light curve to be mirrored in the radio light curve, a possibility explored in [416]. The observation that the short-term radio variability appears to be less pronounced than in the X-ray light curve could be explained by the fact that the radio emitting region is both larger than, and removed from, the X-ray emitting region, which would result in short-term variability being washed out.

The assumed start date of X-ray emission (t_0 in Table 7.1) has a significant impact on the power law index derived to describe the decay. It is important to constrain this parameter as well as possible, as the decay index provides important information on e.g. the mass return and accretion rate and potentially the make-up of the disrupted body [413, 404, 414]. It may also be the case that these decays are not power laws at all. To investigate this effect, we fit a power law decay to the X-ray light curve with a varying t_0, beginning from the latest ASASSN non-detection ($t_0 = -132.35$; [437]; although note that this is an optical, not X-ray, non-detection) and ending at the ASASSN discovery date ($t_0 = 0$) which is shown in Figure 7.3. For the range of start dates considered the best fit power law index varies

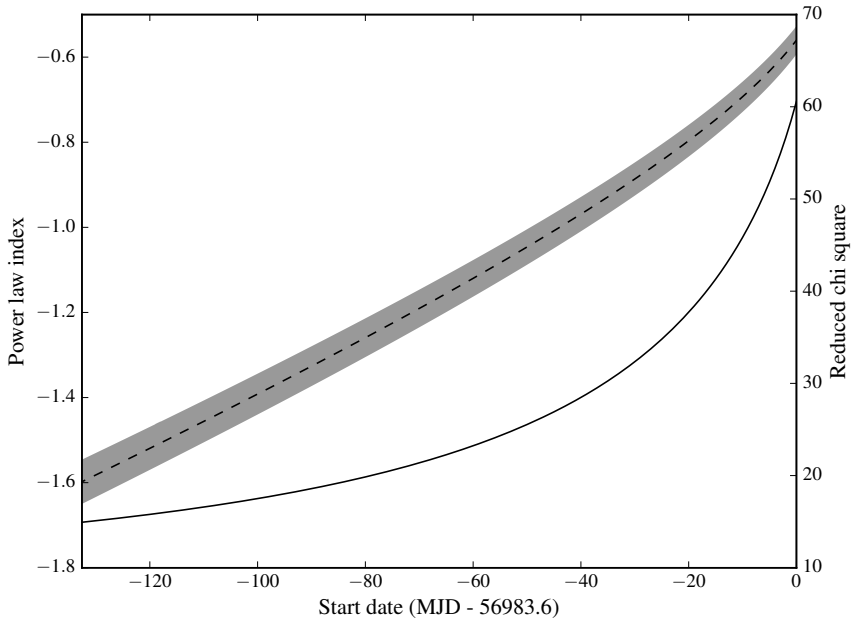

Figure 7.3: Best fitting power law index for the X-ray light curve (black dashed line and shaded one sigma confidence region), and the associated reduced chi-square (solid black line) as a function of fixed start date (t_0).

between ~ -1.6 and ~ -0.6 with the goodness of fit reducing dramatically with later start dates. Care must be taken, however, as earlier start dates will naturally provide a better fit and so without prompt observations, that sample the rise and peak of the light curve, the true start date and power law index cannot be well constrained. For example, [405] find a best fit power law index of -0.92 ± 0.12 (although they bin the X-ray light curve with much larger bins) whereas [127] report an index of -1.7.

7.2.6 Conclusions

I have presented radio observations of the tidal disruption event ASASSN-14li from the Arcminute Microkelvin Imager Large Array and explore their relation to new and archival Swift X-ray observations of the source. We find that the evolution at both wavelengths is well described by an exponential decay. We then show that the early time (~ 200 days) X-ray and radio emission are correlated, with a power law index of $\alpha = 1.9 \pm 0.2$, with $L_R \propto L_X^{\alpha}$. This correlation suggests the possibility that we are observing core disk-jet coupling from ASASSN-14li, which would contradict previous interpretations of the site of radio emission, but in the light of more recent observations is a compelling discovery. While the X-ray emission from the source decays in a similar way throughout the observing campaign, the

radio emission tails off into a plateau at $\sim 250\,\mu$Jy. We discuss the possibility that this radio plateau is constant emission from the TDE, but conclude that it is most likely that we are now observing background radio emission from ASASSN-14li's host galaxy, which we show could easily arise from supernova remnants or low level AGN activity (although we favour archival AGN activity). If the radio emission from ASASSN-14li has continued to follow the correlation derived from the first $\sim$ 200 days of observations, using the most recent X-ray measurements we would expect a radio flux from the TDE of $\sim 5\,\mu$Jy. We therefore expect that, barring a re-flaring event, radio observations of ASASSN-14li with the AMI-LA will remain at their current level.

7.3 Swift J1644+57

Swift J1644+57 is the most well studied of the three relativistic (jetted) TDEs. Of particular interest to this work is the extended multi-frequency radio monitoring presented in [429, 385, 446, 403], which lasted until ~ 2000 d after the initial γ-ray trigger. A subset of these data (the 15.5 GHz monitoring with the AMI-LA) are presented in Figure 7.4, and show a multi-peaked rise followed by a sharp drop-off in flux at ~ 300 d. In addition to the AMI-LA monitoring, the authors collected 23 broadband (radio through sub-mm) SEDs during the first ~ 2000 d of evolution. These observations probe the evolution of the jet-ISM interaction and the synchrotron emitting electrons caused by the resulting shock. In [385, 446] the authors apply a blastwave model based on the GRB formulations presented in [313] and the TDE jet modelling in [126]. These formulations produce spectra with similar properties to those discussed in Chapters 2 and 6 - i.e. synchrotron spectra with characteristic breaks (ν_m, ν_a) and slopes depending on the order of these breaks. The cooling break is not considered for the radio emission, but is discussed in [446] where X-ray observations are shown. The model differs from that of a standard GRB afterglow models in that it considers the affect of the rarefaction wave produced by the reverse shock once it reaches the base of the outflowing material. This wave will propagate back up the ejecta and modify the shocked material as it does so. Once it reaches the forward shock, the material behind the shock will have been modified and the evolution of the emission from the shock will be altered. This approach was motivated by an apparent achromatic break in the radio light curves, which cannot be the result of a break frequency passing through a band [126]. Additionally, it has been proposed that at around 500 d the jet switched off, resulting in a steep decline in X-ray flux [446] that was not mirrored in the radio flux, suggesting the radio emission is from the jet–ISM interaction region and not the jet itself. This prediction for the X-ray emission was confirmed in [403] where it was seen that the X-ray emission

plateaued at a new level post drop, consistent with now coming from the forward shock itself (similar to what is seen in GRBs). The later work of [403] adopted a different approach, considering the evolution of the radio afterglow of Swift J1644+57 simply in terms of the GRB afterglow models of e.g. [313] and not discussing any contribution from a rarefaction wave. This model is also presented in Figure 7.4 using all of the SEDs available to predict the flux from our most recent AMI-LA observations.

I will briefly describe the model of [126], and the impact of these new observations on its applicability. I will also discuss them in the context of the updated models presented in [403]. Based on the X-ray light curve of Swift J1644+57, the kinetic luminosity of the outflow is constant up to a time $t_j \approx 12\,\mathrm{d}$ (which they name the jet duration, although I will refer to it as the transition time) and, after this, scales with the fallback timescale of the tidally disrupted material (the canonical $\propto t^{-5/3}$) and results in a gradual increase in the jet kinetic power. This is not mirrored in the more complex radio light curve morphology. Based on the work of [429, 126] it is also apparent that, in the formulation of the blast wave models, the density of the circumnuclear material is wind like $\rho \propto t^{-2}$ (based on the slopes before and after the early break in the radio light curves). Based on the shock jump conditions and the derived density profile we can write the evolution of the self absorbed radio flux, the shock Lorentz factor, the shock radius, and the characteristic spectral breaks as a function of the shock luminosity, circumburst material density, the time, as well as the fraction of energy injected into the electrons and the magnetic field. The scaling with time is altered after the rarefaction wave alters the shock conditions and (from [385] but noting the difference in the normalisation in the fraction of energy in the magnetic field, which is correct in [126]) gives the following relations for the break frequencies and the self absorbed flux density

$$\nu_{sa} = 4.2\times10^{9}\epsilon_{e,-1}^{-1}\epsilon_{B,-2}^{0.1}L_{j,\mathrm{iso},48}^{-0.4}t_{j,6}^{-1}n_{18}^{1.2}\left(\frac{t}{t_j}\right)^{-0.6}\ \mathrm{Hz} \tag{7.3a}$$

$$\nu_{m} = 3.5\times10^{11}\epsilon_{e,-1}^{2}\epsilon_{B,-2}^{0.5}L_{j,\mathrm{iso},48}^{0.5}t_{j,6}^{-1}\left(\frac{t}{t_j}\right)^{-1.5}\ \mathrm{Hz} \tag{7.3b}$$

$$F_\nu(\nu=\nu_a) = 345\epsilon_{e,-1}L_{j,\mathrm{iso},48}^{0.5}t_{j,6}^{1.5}n_{18}^{-1.5}\theta_{j,-1}^{2}\nu_{a,10}^{2}\left(\frac{t}{t_j}\right)^{0.5}\ \mathrm{mJy} \tag{7.3c}$$

which are valid for $t \gtrsim t_j$. For $t \lesssim t_j$ the equation are the same but the indices for scaling with t changes to -1, -1, and 2 for Equations (7.3a) to (7.3c), respectively. Quantities are normalised according to $X = 10^n X_n$. If some reasonable assumptions are made for the quantities ϵ_e, ϵ_B, and θ_j, then the spectra at a given epoch are function of only L_{iso} and n_{18}.

While this is clearly model and assumption dependent it provides a framework for fitting the relatively sparsely sampled SEDs (with the addition of the smoothing parameters [313]) with fewer free parameters

The overall morphology of the light curve, discussed in terms of the breaks, has been explained in a number of ways as the source was observed to evolve. I refer to case **a)** and **b)** which reference the framework of [126, 429, 385, 446] (evolution influenced by a rarefaction wave) and [403] (standard GRB fireball), respectively. The flattening of the light curve at ~ 12 d is **a)** the result of the rarefaction wave reaching the forward shock or **b)** the self absorption break moving through the radio band. The subsequent rise to peak is caused by **a)** an increase of energy into the jet attributed to a structured outflow (the Lorentz factor being a function of radius) or **b)** the same as for **a)**. The peak at ~ 100 d is the result of **a)** the energy into the jet beginning to plateau **b)** the same as for **a)**. The steep falloff at ~ 300 d is caused by **a)** the plateauing energy injection into the jet or for **b)** the minimum energy break passing below the self absorption break (although it is not made clear why this would result in the apparent change in flux decay rate). The model presented in [403] simply fits the power-law breaks and the peak flux density to the SEDs, rather than parameterising the evolution in terms of $L_{\rm iso}$ and n_{18}. The complex radio morphology and variation of model parameters required to explain the observations indicates the challenge encountered when trying to consistently explain the jetted TDEs. Further observations of events similar to Swift J1644+57 are bound to be enlightening.

I was unable to reproduce the SED fits or the light curves presented in [385, 446] using the values given in their table 2, nor from the SED fit results presented in [403]. I therefore re-fit the entire set of SEDs using the model presented in [403] (the standard GRB afterglow model) and [385, 446] (rarefaction wave). My recreated light curves are presented in Figure 7.4 and extended to the epoch of our most recent set of radio observations. It is clear that a simple extension of the initial model underestimates the flux at this late-time (as opposed to the prediction by [446]), which could have occurred for a number of reasons. Firstly, a simple extrapolation puts particular constraints on the temporal evolution of L_{48} and n_{18} which were not prescribed to evolve in any particular way when individually fitting the SEDs. Secondly, as I found for ASASSN-14li, the emission we are seeing now could be produced from the host galaxy. The apparent drop seen during our observations provides some evidence that the original transient event is still declining, although the decline is inferred from only a handful of data points and could be probing galactic emission due to the long timescales between observing epochs. Archival observations of the host galaxy

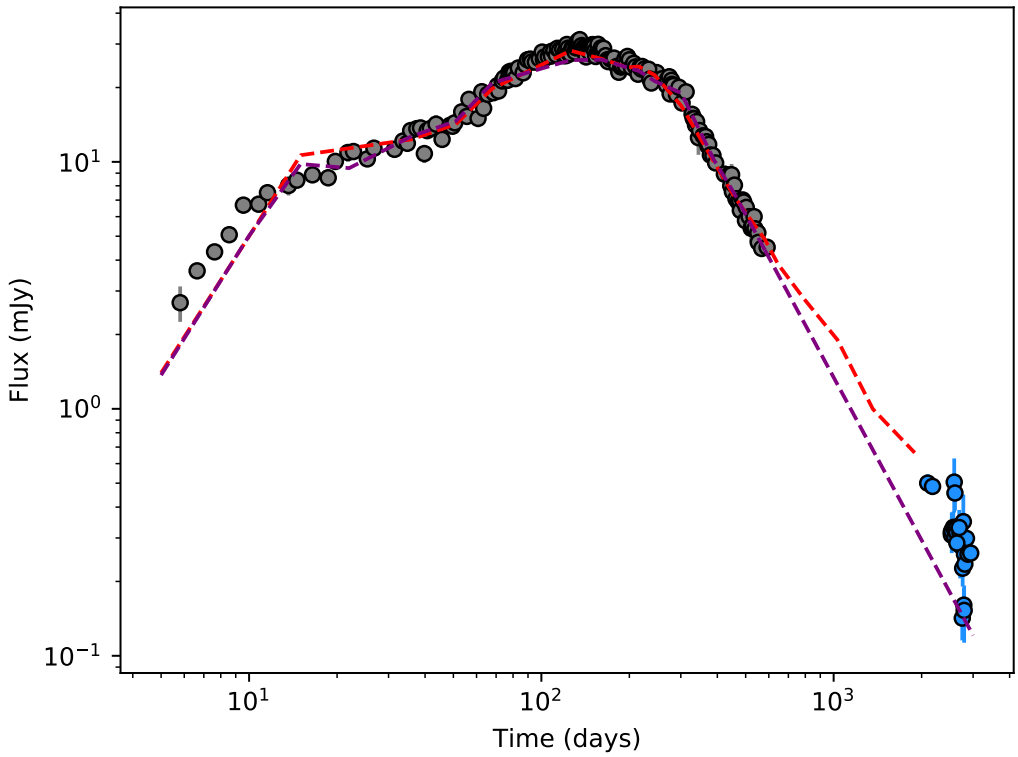

Figure 7.4: An updated light curve from the relativistic TDE Swift J1644+57. Grey data points are published in [385, 446] whereas the blue data points are unpublished new data. AMI-LA monitoring did not take place during the gap. The red dashed line shows a model to the light curve based on fitting radio SEDs in the formalism of the GRB afterglow model, based on the complete set of SEDs. The purple line describes a simple power law extension of the fits found in [385, 446] (rarefaction wave) where I have extended the final segment of the fit to the most recent epoch of AMI-LA observations, which apparently underestimates the 15.5 GHz flux.

suggest that before the TDE no AGN was present, based on the most constraining 1.4 GHz observation made by the FIRST survey of $\lesssim 0.45$ mJy ($\lesssim 2 \times 10^{30}$ erg s^{-1}) [447]. Considering the two extreme cases of optically thin galactic emission ($\alpha = -0.7$) and flat spectrum AGN activity, this FIRST limit provides a 15.5 GHz upper limit of $\sim 80\,\mu$Jy and $\sim 450\,\mu$Jy, respectively. The majority of our late-time AMI-LA observations are consistent with a flux density of ~ 200 to $\sim 300\,\mu$Jy which is easily described by an intermediate spectral index of ~ -0.3. Given the long timescales involved in this data set it is difficult to say with any confidence that the observed decline is not just long-term variability in (unresolved) galaxy emission (e.g. AGN activity). It is apparent however that the updated SEDs reveal a shallower decline than predicted by the initial models, likely due to a transition from relativistic to non-relativistic expansion, as discussed in [403]. Given the assumptions inherent in the model fitting it is perhaps not surprising that such discrepancies are seen, and indeed the later modelling appears to predict well the late-time AMI-LA fluxes shown in Figure 7.4 (although again this is not overly surprising given that the SEDs are being fit directly without a theoretically motivated prescription for how fundamental jet parameters should evolve).

Finally in this Chapter I present an updated plot of the radio luminosity of the current population of observed radio loud TDEs, which is shown in Figure 7.5. The population of radio loud TDEs has not grown significantly during the duration of my thesis and the apparent dichotomy in isotropic equivalent radio luminosity remains in place. However, continuing to populate plots such as Figure 7.5 will aid in further understanding the differences in the radio properties of the two classes of TDE. It is particularly interesting to note that the jetted TDEs do not necessarily only occupy the top half of this figure meaning this plot is not reliable as a diagnostic for the nature of a TDEs outflow (however it may still imply a difference between high power and Lorentz factor jetted events and lower power jetted events). It is also encouraging that constraining follow-up observations are being taken both at early and late-times. Additionally, I highlight the contribution of the AMI-LA telescope in providing high cadence and long-term monitoring of TDEs.

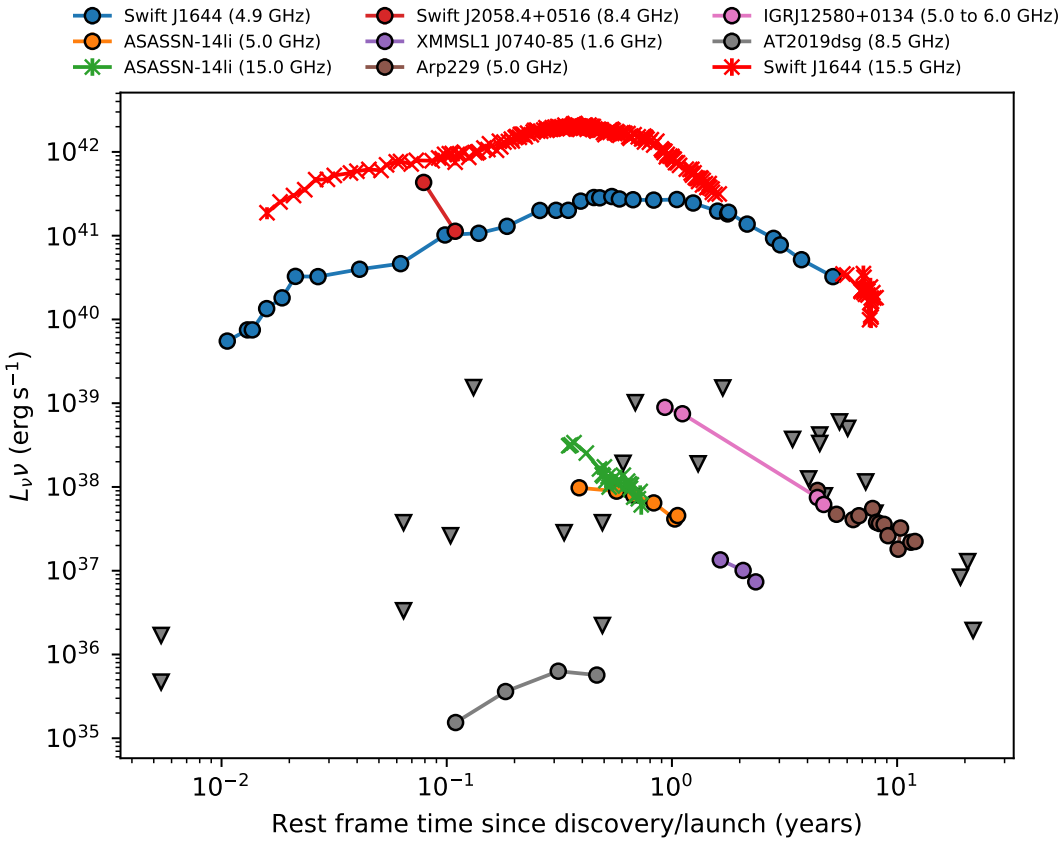

Figure 7.5: The evolution of the radio luminosity of the known radio loud TDEs as a function of rest frame time since their discovery, as well as upper limits for non-detection. The observing frequency for the detected sources is shown in the legend, and the upper limits are taken at a range of frequencies (between 3 and 22 GHz). I have k-corrected the detection luminosities assuming a flat spectrum, but these corrections will only be large for Swift J1644 and Swift J2058 which are at redshifts above ~ 0.3. Detections are taken from [378, 432, 446, 385, 403, 128, 417, 430, 125, 431, 422, 448, 449, 424] whereas upper limits are from [377, 390, 450, 451, 391, 452, 453]. Where available I have used published redshifts for the cosmological corrections with the cosmological model of [454], otherwise I used distances quoted in the literature. It is worth noting that, while it is clear there is a dichotomy in the radio luminosities of TDE jets (if indeed jets are the source of radio emission), without considering emission from the accretion flow plots such as this do not provide information on the efficiency of the accretion mechanism at work.

Table 7.2: AMI-LA radio observations of ASASSN-14li.

Date (MJD) (MJD)	Frequency (GHz)	Flux density (μJy)	Flux density error (μJy)
57014.078	15.7	1865	83
57015.170	15.7	1871	141
57017.096	15.7	1969	67
57021.111	15.7	2096	84
57039.088	15.7	1629	78
57061.053	15.7	969	150
57065.995	15.7	870	103
57068.089	15.7	879	72
57069.970	15.7	1291	209
57072.982	15.7	836	286
57077.055	15.7	860	86
57079.057	15.7	652	93
57082.105	15.7	654	66
57085.088	15.7	781	61
57090.081	15.7	894	121
57094.062	15.7	789	90
57098.952	15.7	761	82
57109.041	15.7	779	127
57113.984	15.7	826	367
57118.978	15.7	740	103
57122.941	15.7	814	104
57125.982	15.7	708	87
57127.975	15.7	717	76
57133.958	15.7	715	117
57138.941	15.7	525	73
57142.951	15.7	560	79
57145.921	15.7	497	99
57150.749	15.7	617	191
57153.735	15.7	503	177
57374.323	15.5	245	57
57376.128	15.5	224	65
57379.112	15.5	307	65
57381.291	15.5	336	70
57386.186	15.5	360	93
57388.098	15.5	305	68
57390.092	15.5	265	88
57392.087	15.5	132	89
57394.081	15.5	298	114
57396.066	15.5	257	93
57399.243	15.5	289	60
57401.211	15.5	216	59

Table 7.2: AMI-LA radio observations of ASASSN-14li.

Date (MJD)	Frequency (GHz)	Flux density (μJy)	Flux density error (μJy)
57404.097	15.5	231	69
57406.156	15.5	257	61
57409.182	15.5	262	63
57413.019	15.5	274	68
57419.077	15.5	194	63
57421.028	15.5	255	66
57422.981	15.5	310	71
57428.013	15.5	191	72
57431.133	15.5	253	51
57434.038	15.5	333	87
57438.027	15.5	278	63
57441.950	15.5	286	87
57446.040	15.5	278	46
57461.083	15.5	201	49
57464.874	15.5	154	61
57467.897	15.5	213	60
57482.937	15.5	219	86
57496.982	15.5	211	57
57500.989	15.5	169	72
57508.040	15.5	200	83
57534.795	15.5	226	58
57538.815	15.5	256	76
57575.815	15.5	305	96
57632.565	15.5	143	99
57634.542	15.5	293	108
57640.501	15.5	202	78
57649.483	15.5	187	89
57653.480	15.5	274	72
57661.399	15.5	265	108
57668.399	15.5	254	105
57675.482	15.5	230	67
57678.358	15.5	242	81
57688.384	15.5	211	69
57695.340	15.5	213	64
57696.316	15.5	161	78
57700.305	15.5	249	77
57710.302	15.5	254	53
57717.262	15.5	301	58
57720.272	15.5	254	61
57721.227	15.5	289	70
57731.224	15.5	258	90

Table 7.2: AMI-LA radio observations of ASASSN-14li.

Date (MJD)	Frequency (GHz)	Flux density (μJy)	Flux density error (μJy)
57737.204	15.5	216	61
57745.226	15.5	214	77
57749.236	15.5	196	62
57752.184	15.5	277	74
57761.183	15.5	216	70
57765.172	15.5	248	68
57769.141	15.5	199	95
57777.143	15.5	165	64
57783.100	15.5	195	130
57788.087	15.5	210	52
57794.050	15.5	266	78
57799.122	15.5	218	89
57809.033	15.5	209	58
57814.037	15.5	246	57
57820.918	15.5	231	54
57829.971	15.5	199	77
57832.963	15.5	244	57
57834.958	15.5	336	98
57839.945	15.5	265	74
57888.911	15.5	188	119
57920.723	15.5	193	85
57949.661	15.5	261	91

Table 7.3: *Swift* 0.3-10 keV observations of ASASSN-14li.

Date (MJD)	Count rate (counts s^{-1})	Count rate error (counts s^{-1})	Flux (10^{12} erg s^{-1} cm^{-2})	Flux error (10^{12} erg s^{-1} cm^{-2})
56998.259	0.410	0.016	18.8	0.7
57001.637	0.397	0.017	18.2	0.8
57004.197	0.429	0.024	19.7	1.0
57007.296	0.454	0.017	20.8	0.8
57010.835	0.524	0.018	24.0	0.8
57013.099	0.448	0.016	20.6	0.7
57016.092	0.435	0.019	20.0	0.9
57019.576	0.390	0.015	17.9	0.7
57022.745	0.377	0.016	17.3	0.7
57029.582	0.494	0.015	22.7	0.7
57033.144	0.474	0.023	21.7	1.0
57036.110	0.456	0.021	20.9	1.0
57039.234	0.401	0.016	18.4	0.7
57042.296	0.394	0.018	18.1	0.8
57045.624	0.388	0.015	17.8	0.7
57048.821	0.400	0.016	18.4	0.7
57051.534	0.363	0.017	16.7	0.8
57054.139	0.337	0.012	15.5	0.6
57057.560	0.329	0.013	15.1	0.6
57060.165	0.337	0.012	15.5	0.6
57065.849	0.243	0.014	11.2	0.6
57068.779	0.269	0.015	12.3	0.7
57071.737	0.278	0.012	12.8	0.6
57074.910	0.270	0.011	12.4	0.5
57077.633	0.231	0.013	10.6	0.6
57081.189	0.256	0.010	11.8	0.5
57086.917	0.299	0.013	13.7	0.6
57089.381	0.327	0.013	15.0	0.6
57099.421	0.286	0.016	13.1	0.7
57102.655	0.276	0.012	12.7	0.6
57105.311	0.175	0.019	8.0	0.9
57109.208	0.256	0.012	11.8	0.6
57111.933	0.242	0.012	11.1	0.6
57114.128	0.220	0.014	10.1	0.6
57117.720	0.199	0.011	9.1	0.5
57120.317	0.193	0.011	8.9	0.5
57123.578	0.195	0.010	9.0	0.5
57126.243	0.178	0.009	8.2	0.4
57129.400	0.191	0.012	8.8	0.6
57132.560	0.162	0.010	7.4	0.5
57136.560	0.156	0.012	7.2	0.6

Table 7.3: *Swift* 0.3-10 keV observations of ASASSN-14li.

Date (MJD)	Count rate (counts s^{-1})	Count rate error (counts s^{-1})	Flux (10^{12} erg s^{-1} cm^{-2})	Flux error (10^{12} erg s^{-1} cm^{-2})
57139.347	0.190	0.011	8.7	0.5
57147.597	0.187	0.010	8.6	0.5
57150.256	0.189	0.009	8.7	0.4
57153.486	0.183	0.009	8.4	0.4
57156.647	0.157	0.010	7.2	0.5
57173.106	0.161	0.010	7.4	0.5
57176.134	0.155	0.010	7.1	0.5
57179.194	0.152	0.016	7.0	0.7
57182.465	0.155	0.013	7.1	0.6
57186.055	0.148	0.010	6.8	0.5
57188.549	0.189	0.039	8.7	2.0
57191.845	0.154	0.009	7.1	0.4
57195.195	0.156	0.009	7.2	0.4
57200.382	0.131	0.011	6.0	0.5
57203.807	0.120	0.009	5.5	0.4
57226.617	0.090	0.007	4.1	0.3
57230.379	0.103	0.011	4.7	0.5
57236.470	0.096	0.007	4.4	0.3
57238.860	0.111	0.008	5.1	0.4
57242.120	0.104	0.007	4.8	0.3
57246.907	0.075	0.006	3.5	0.3
57340.745	0.079	0.006	3.6	0.3
57351.843	0.067	0.007	3.1	0.3
57354.698	0.063	0.006	2.9	0.3
57357.365	0.065	0.006	3.0	0.3
57360.258	0.080	0.007	3.7	0.3
57363.951	0.089	0.006	4.1	0.3
57366.940	0.084	0.006	3.9	0.3
57369.900	0.071	0.006	3.3	0.3
57372.255	0.063	0.007	2.9	0.3
57375.579	0.088	0.009	4.0	0.4
57378.411	0.078	0.007	3.6	0.3
57383.203	0.074	0.023	3.4	1.0
57411.684	0.056	0.006	2.6	0.3
57417.730	0.084	0.008	3.9	0.4
57423.806	0.048	0.009	2.2	0.4
57426.466	0.032	0.011	1.5	0.5
57427.758	0.050	0.006	2.3	0.3
57429.669	0.050	0.012	2.3	0.6
57433.319	0.044	0.006	2.0	0.3
57435.743	0.048	0.005	2.2	0.2

Table 7.3: *Swift* 0.3-10 keV observations of ASASSN-14li.

Date (MJD)	Count rate (counts s^{-1})	Count rate error (counts s^{-1})	Flux (10^{12} erg s^{-1} cm^{-2})	Flux error (10^{12} erg s^{-1} cm^{-2})
57519.819	0.028	0.004	1.3	0.2
57522.607	0.021	0.003	1.0	0.1
57526.827	0.020	0.004	0.9	0.2
57542.686	0.022	0.004	1.0	0.2
57545.455	0.021	0.009	1.0	0.4
57546.401	0.024	0.005	1.1	0.2
57550.131	0.032	0.005	1.5	0.2
57554.383	0.013	0.003	0.6	0.1
57718.041	0.022	0.003	1.0	0.1
57820.434	0.008	0.003	0.4	0.1
57821.966	0.015	0.003	0.7	0.1
57826.917	0.013	0.003	0.6	0.1
57828.568	0.014	0.005	0.7	0.2

Chapter 8

Conclusions

8.1 Comparison of synchrotron spectra

Throughout this thesis I have presented research in the area of radio transient astronomy, with a particular focus on relativistic outflows from transients containing a compact object. The systems discussed have been varied, and include accreting X-ray binaries, energetic γ-ray bursts caused by the death of massive stars, and tidal disruption events involving supermassive black holes. I believe it is interesting to spend some space discussing the similarities and differences between the outflows produced by these systems, and how different frameworks have been developed to analyse observations of these outflows. Despite the extremely varied systems producing sub-relativistic to relativistic outflows, the outflows themselves (as well as the signatures of their interaction with surrounding material) are similar. Fundamentally, all of the systems discussed in detail in this thesis produce collimated outflows created through a coupling to an accretion flow. Until recently the suggestion that *all* TDEs with radio emission are producing jets would have been controversial, however recent observations (including those in this thesis) have shifted the paradigm. The most compelling evidence is the discovery of radio emission resolved from the known location of the host black hole in the thermal TDEs ASASSN-14li and Arp 229. Due to the discovery of radio emission from TDEs being relatively new, I will primarily compare the outflows from XRBs and GRBs, but will also include properties of TDE outflows in cases where they are constrained.

While all three systems produce collimated outflows, the primary difference, at least as far as their analysis goes, is their outflow velocities. Despite being at much greater distances, and being almost impossible to resolve, the outflow velocities from GRBs are much better constrained than for BHXRBs. This is due to the previously mentioned compactness problem, which sets a strong lower limit on the bulk Lorentz factor of $\Gamma \gtrsim 100$ and implies

the produced shocks are relativistic. This has two major consequences, **a)** photons are blue shifted significantly in the observer frame, and **b)** the entirety of the electron population is assumed to be accelerated into the power-law distribution. This is supported by the observed broadband spectra of GRBs which, in the case where the minimum energy break is observed, clearly indicate electrons accelerated to high Lorentz factors, with a minimum Lorentz factor $\gg 1$ at early time (e.g. for GRB 130427A, GRB 171010A [455, 323], however the exact value of γ_m is difficult to infer due to uncertainties on the properties of the jet such as its velocity), which is the result of relativistic shocks. At later times the electron population will have cooled and, as the shell decelerates, the level of blue shift will be reduced. This is clearly in contrast to the spectra seen from e.g. the discrete ejections from BHXRBs which are also thought to be caused by shock acceleration of electrons, but likely from a significantly less relativistic outflows. A comparison to GRBs leads to some interesting conclusions. While it has been suggested, through considerations of the radio - X-ray correlation, that for BHXRBs the Lorentz factor of the compact jet is $\lesssim 2$, it has not been directly confirmed. Similarly, the discrete ejecta seem to be more relativistic, but due to the inherent difficulties of constraining the Lorentz factors when measuring superluminal motion they only have Lorentz factors constrained to be $\gtrsim 2$. The $\nu^{1/3}$ slope is never seen in either of these cases (and neither is the slope change from $5/2$ to 2 in the optically thick region), indicating the shock velocities were not sufficient to accelerate the entire populations as for GRBs. A similar paradigm could be applied to the thermal (or weakly jetted) and relativistic TDEs, with the latter showing clear evidence for the presence of a relativistic shock (e.g. ν_m is clearly observed in Swift J1644) whereas the former show the standard self-absorbed/optically thin spectrum with no indication that ν_m is seen [384]. Further studies of the forward and reverse shocks of GRBs, especially at early times, and their comparison with XRB radio spectra could provide interesting constraints on the outflow velocities. The AMI-LA is a uniquely suited telescope for this task, due to its ability to respond rapidly and automatically to triggers from the Burst Alert Telescope on board the *Swift* satellite, as well as having a wide bandwidth [172]. The AMI-LA response program does, however, have some drawbacks. Firstly the automatically triggered observations were/are limited to 2 h snapshots which, depending on the source elevation, can result in a rather poor image (due to poor (u, v) coverage and enhanced RFI when observing towards the horizon). Due to the rapid evolution at early times, longer triggered observations could provide important information on the early afterglow evolution. Such a rapid response is particularly interesting in the current era of gravitational wave astronomy, where multi-wavelength observations of double neutron star mergers (and the subsequent afterglow resulting from the short GRB) provide valuable constraints on the proposed jet

models for such sources. This response system is primarily activated due to γ-ray emission from GRBs (which is the primary source class that the *Swift* satellite was designed to detect) but also has the potential to trigger on e.g. relativistic jetted TDEs and hard state outbursting BHXRBs (e.g. for MAXI J1820+070, as seen in the first data point in Figure 4.4). The result of the 'first wave' of GRBs detected automatically at early times by the AMI-LA was recently presented in [350], demonstrating the ability of the AMI-LA to provide observations only minutes after a burst occurs (probing the early time afterglow emission) and has even secured detections as early as 9 h post burst [329]. With the renewed excitement in the field of GRBs, following their association with gravitational wave radiation, resuming the AMI-LA GRB response program (perhaps with longer initial observations) seems timely to better understand the early time evolution of neutron star mergers as well as long GRBs, outbursting XRBs, and relativistic TDEs.

8.2 BHXRB outbursts and the accretion - jet connection

In Chapter 5 I made some suggestions as to how we can better understand state transition radio flaring from BHXRBs, however there is clearly more to consider here. It appears that non-impulsive particle acceleration must play a role in a significant number of state transition flares from BHXRBs (all of the examples considered in Chapter 5), however the model presented can be made to be more physical. Firstly, while a polynomial particle injection function is mathematically convenient, it is far from the only kind of injection that might occur. Additionally, the phase of particle acceleration will not be indefinite, and must instead fall to zero eventually. This can be seen obviously from observations of optically thin flares, where the rise timescale clearly defines the period of particle acceleration and results in a turnover. The effect of finite particle acceleration on the thick flares can be more subtle. We saw in Chapter 5 that while particle acceleration could flatten the peak to peak spectral index compared to the model of van der Laan 1966 [258], it came at the cost of increasing the delay between peaks. This could be somewhat remedied by acceleration that stops or falls with time (i.e. as an exponential, or a rise/peak, as considered in [287]). Such an addition would lead to a compromise between flattening the peak to peak index and decreasing the time delay. It will also allow for non-self-similar evolution of flares at different frequencies to be explained. With these additions it would no longer be the case that the peak to peak index and time delay should be the same between all combinations of frequency, as the rate of injection and therefore the peak to peak index and delay will be a function of time. Higher frequency observations, which peak first, will therefore be more dominated by the inclusion of such particle acceleration. Such additions, combined with

the disambiguation of overlapping flare events using sub-mm observations (see e.g. the PITCH-BLACK project approved on the sub-mm array, of which I am a Co-I) should allow state transition radio flares to be properly modelled and their associated physical parameters extracted.

Our radio monitoring of MAXI J1820+070 has, in conjunction with public X-ray monitoring, allowed for the accretion - ejection connection to be probed in great detail (with approximately daily observations) over an entire outburst cycle, as well as for hard-state only re-flaring. The radio data is perhaps the most detailed available for a canonical BHXRB outburst. MAXI J1820+070 was shown to be another of the 'radio-loud' sources (although with an unusually flat correlation index) and to launch large scale and highly energetic ejections at a similar time to when dramatic alterations in the accretion properties were observed [190]. While this association is compelling (it is the best association made to date) the campaign to monitor the ejections was rather ad-hoc (involving different groups of observers initially working independently). It still led to extremely interesting conclusions - most notably the comparison between the energy from the state transition radio flare and from the discrete ejection using different angular resolution radio observations. The ThunderKAT large survey project on MeerKAT is taking a unique approach to observing outbursting BHXRBs, regularly monitoring sources with an RMS sensitivity of $\sim 20\,\mu$Jy. These regular observations, which revealed the large angular scale structure of the ejections from MAXI J1820+070, will likely find more sources displaying such ejections (e.g. Carotenuto *et al.* in prep.) that will allow for the launch times and energetics (when combined with other observations) to be inferred for other systems. The advent of the SKA has the potential to revolutionise such studies, with the phase one mid-frequency SKA promising access to $0.03''$-$1.4''$ angular scales, with exquisite sensitivity ($< 10\,\mu$Jy in a one hour observation), from a single instrument. This will significantly simplify previously complex observing campaigns involving multiple telescopes. To a lesser extent this will also be achieved with the addition of MeerKAT S-band receivers, and additional antennae providing baselines three times longer than those currently available (additions both currently being added to the telescope).

There is still additional analysis to be done on the MAXI J1820+070 data, particularly of the re-brightening events which show a surprising regularity in shape and recurrence time. While I have demonstrated the radio - X-ray correlation for these re-brightenings in Chapter 4, it will be particularly interesting to examine if the correlation changes as the decay rates of the re-flares changes (it does so in all three events seen so far, at a similar

flux). To properly probe the connection, higher time resolution X-ray observation will be required. However, given the apparently periodic nature of the re-brightening events, planning such an observing campaign should be possible. Finally, a complete AMI-LA radio light curve of MAXI J1820+070 should be published as a resource to the community, as there is a wealth of data to be contrasted with it.

8.2.1 Discrete ejections observed with sub-mm interferometers

In Chapter 4 I presented an extended analysis of discrete ejections from the BHXRB MAXI J1820+070 which involved observations with five different $\sim$ GHz frequency interferometers. Due to the optically thin spectrum of the ejecta ($F(\nu) \propto \nu^{-0.7}$) this is often the sensible choice for sensitivity reasons. However there is a significant (factor $\sim 10^7$) gap in frequency between these observations and the X-ray frequencies where the ejections can also be resolved. There is the additional consideration that, as I demonstrated in Chapter 4, there is a resolution dependence on the flux observed from these ejections due to the sensitivity of a particular interferometer to certain angular scales (higher resolution facilities resolve out some of the emission). Simultaneous observations with (sub-)mm and radio frequency arrays are essential for constraining the broadband SED of ejections, filling a gap in frequency space between radio and the occasionally observed X-ray synchrotron radiation [206]. Using MAXI J1820+070 as an example, ejections were observed with a flux of ~ 5 mJy at 1.28 GHz, corresponding to $\sim 150\,\mu$Jy at 163 GHz (the top end of ALMA band 4, where the loss of surface brightness sensitivity would be minimum for all but the most extended array configurations) for an optically thin synchrotron spectrum of -0.7. Such flux densities are detectable by ALMA over modest time intervals (with a 5-sigma detection achievable with ~ 30 min on source time with 30 antennas of the 12 m array). Such spatially resolved observations of BHXRB ejecta would provide the first ever detection at (sub-)mm frequencies, and provide additional constraints on their energy content and spectral shape.

8.3 The radio properties of TDEs

There are currently only a handful of radio emitting TDEs known, a small fraction of the total population of candidates discovered at optical and X-ray frequencies (with more promised to follow with surveys such as LSST on the horizon). The radio properties of these systems are diverse, and many models have been proposed to explain them. It is clear that some TDEs produce highly relativistic outflows, however it is still an unanswered question if all TDEs produce jets of some kind. While follow-up of candidates discovered through wide field surveys is an obvious pathway to expanding the number of radio detected TDEs,

it is becoming increasingly feasible to search for candidates directly at radio frequencies. This is being made possible through large field of view and high sensitivity arrays such as MeerKAT, and in future the SKA, which regularly revisit certain fields. Feeding these wide field images into transient discovery pipelines (e.g. [435]) has the potential to reveal transient radio sources varying over a range of timescales. It has been shown (e.g. [384]) that not only can wide field surveys discover new radio TDEs, but the discovery rate has implications for the properties of potential jets from them. In addition to discovering new events it is also important to follow them up with high cadence and multi-frequency radio observations, which best probe jet properties and the interactions of outflows with the surrounding medium. The AMI-LA is again well placed to assist in these follow-up campaigns, and has already contributed excellent monitoring for multiple TDEs [432, 403]. As with BHXRBs, TDEs exhibit rapid changes in accretion rate, and as such are excellent systems to probe the accretion - ejection connection.

There are a host of phenomena, with a vast range of initial conditions, that produce transient radio emission. Studying these sources with current and near-future interferometers promises to provide us insights into fundamental processes including, but not limited to, accretion, it's connection to jet production, and how jets influence their environment. These observations will surely additionally, as they have in the past, present novel methods for gaining insight into seemingly unrelated problems. There has been no better time to be in the business of studying transients, with multi-wavelength and multi-messenger facilities across the globe dedicated to understanding their properties.

Bibliography

[1] Michell, J. On the Means of Discovering the Distance, Magnitude, &c. of the Fixed Stars... . By the Rev. John Michell, B. D. F. R. S. In a Letter to Henry Cavendish, Esq. F. R. S. and A. S. *Philosophical Transactions of the Royal Society of London Series I* **74**, 35–57 (1784).

[2] Einstein, A. Die Feldgleichungen der Gravitation. *Sitzungsberichte der Königlich Preußischen Akademie der Wissenschaften (Berlin* 844–847 (1915).

[3] Schwarzschild, K. On the Gravitational Field of a Mass Point According to Einstein's Theory. *Abh. Konigl. Preuss. Akad. Wissenschaften Jahre 1906,92, Berlin,1907* **1916**, 189–196 (1916).

[4] Kerr, R. P. Gravitational Field of a Spinning Mass as an Example of Algebraically Special Metrics. Phys. Rev. Lett. **11**, 237–238 (1963).

[5] Chandrasekhar, S. The Maximum Mass of Ideal White Dwarfs. ApJ **74**, 81 (1931).

[6] Chandrasekhar, S. The highly collapsed configurations of a stellar mass (Second paper). MNRAS **95**, 207–225 (1935).

[7] Tolman, R. C. Static Solutions of Einstein's Field Equations for Spheres of Fluid. *Physical Review* **55**, 364–373 (1939).

[8] Oppenheimer, J. R. & Volkoff, G. M. On Massive Neutron Cores. *Physical Review* **55**, 374–381 (1939).

[9] Penrose, R. Gravitational Collapse and Space-Time Singularities. Phys. Rev. Lett. **14**, 57–59 (1965).

[10] Penrose, R. Gravitational Collapse: the Role of General Relativity. *Nuovo Cimento Rivista Serie* **1**, 252 (1969).

[11] Israel, W. Event Horizons in Static Vacuum Space-Times. *Physical Review* **164**, 1776–1779 (1967).

[12] Schmidt, M. 3C 273 : A Star-Like Object with Large Red-Shift. Nature **197**, 1040 (1963).

[13] Salpeter, E. E. Accretion of Interstellar Matter by Massive Objects. ApJ **140**, 796–800 (1964).

[14] Zel'dovich, Y. B. The Fate of a Star and the Evolution of Gravitational Energy Upon Accretion. *Soviet Physics Doklady* **9**, 195 (1964).

[15] Lynden-Bell, D. Galactic Nuclei as Collapsed Old Quasars. Nature **223**, 690–694 (1969).

[16] Paczynski, B. Mass of Cygnus X-1. A&A **34**, 161–162 (1974).

[17] Orosz, J. A. *et al.* The Mass of the Black Hole in Cygnus X-1. ApJ **742**, 84 (2011).

[18] Shahbaz, T. *et al.* The mass of the black hole in V404 Cygni. MNRAS **271**, L10–L14 (1994).

[19] Torres, M. A. P. *et al.* Dynamical Confirmation of a Black Hole in MAXI J1820+070. ApJ **882**, L21 (2019).

[20] Torres, M. A. P. *et al.* The binary mass ratio in the black hole transient MAXI J1820+070. *arXiv e-prints* arXiv:2003.02360 (2020).

[21] Hurley, D. J., Callanan, P. J., Elebert, P. & Reynolds, M. T. The mass of the black hole in GRS 1915+105: new constraints from infrared spectroscopy. MNRAS **430**, 1832–1838 (2013).

[22] Orosz, J. A. *et al.* An Improved Dynamical Model for the Microquasar XTE J1550-564. ApJ **730**, 75 (2011).

[23] Genzel, R., Pichon, C., Eckart, A., Gerhard, O. E. & Ott, T. Stellar dynamics in the Galactic Centre: proper motions and anisotropy. MNRAS **317**, 348–374 (2000).

[24] Schödel, R. *et al.* A star in a 15.2-year orbit around the supermassive black hole at the centre of the Milky Way. Nature **419**, 694–696 (2002).

[25] Graham, A. W. Populating the Galaxy Velocity Dispersion - Supermassive Black Hole Mass Diagram: A Catalogue of (M_{bh}, σ) Values. PASA **25**, 167–175 (2008).

[26] Abbott, B. *et al.* Gwtc-1: A gravitational-wave transient catalog of compact binary mergers observed by ligo and virgo during the first and second observing runs. *Physical Review X* **9** (2019).

[27] Event Horizon Telescope Collaboration *et al.* First M87 Event Horizon Telescope Results. I. The Shadow of the Supermassive Black Hole. ApJ **875**, L1 (2019).

[28] Narayan, R., Paczynski, B. & Piran, T. Gamma-Ray Bursts as the Death Throes of Massive Binary Stars. ApJ **395**, L83 (1992).

[29] Narayan, R., Garcia, M. R. & McClintock, J. E. Advection-dominated Accretion and Black Hole Event Horizons. ApJ **478**, L79–L82 (1997).

[30] Narayan, R., Mahadevan, R., Grindlay, J. E., Popham, R. G. & Gammie, C. Advection-dominated accretion model of Sagittarius A*: evidence for a black hole at the Galactic center. ApJ **492**, 554–568 (1998).

[31] Chen, W. *et al.* Evidence for event horizon in soft X-ray transients? In Holt, S. S. & Kallman, T. R. (eds.) *American Institute of Physics Conference Series*, vol. 431 of *American Institute of Physics Conference Series*, 347–350 (1998).

[32] Abramowicz, M. A., Kluźniak, W. & Lasota, J. P. No observational proof of the black-hole event-horizon. A&A **396**, L31–L34 (2002).

[33] King, A. R., Davies, M. B., Ward, M. J., Fabbiano, G. & Elvis, M. Ultraluminous x-ray sources in external galaxies. *The Astrophysical Journal* **552**, L109–L112 (2001).

[34] Pringle, J. E. Accretion discs in astrophysics. ARA&A **19**, 137–162 (1981).

[35] Balbus, S. A. & Hawley, J. F. A Powerful Local Shear Instability in Weakly Magnetized Disks. I. Linear Analysis. ApJ **376**, 214 (1991).

[36] Balbus, S. A. & Hawley, J. F. A powerful local shear instability in weakly magnetized disks. I - Linear analysis. II - Nonlinear evolution. ApJ **376**, 214–233 (1991).

[37] Shakura, N. I. & Sunyaev, R. A. Black holes in binary systems. Observational appearance. A&A **24**, 337–355 (1973).

[38] Rees, M. J., Begelman, M. C., Blandford, R. D. & Phinney, E. S. Ion-supported tori and the origin of radio jets. Nature **295**, 17–21 (1982).

[39] Abramowicz, M. A. & Fragile, P. C. Foundations of Black Hole Accretion Disk Theory. *Living Reviews in Relativity* **16**, 1 (2013).

[40] Ichimaru, S. Bimodal behavior of accretion disks: theory and application to Cygnus X-1 transitions. ApJ **214**, 840–855 (1977).

[41] Narayan, R. & Yi, I. Advection-dominated Accretion: A Self-similar Solution. ApJ **428**, L13 (1994).

[42] Piconcelli, E. *et al.* The XMM-Newton view of PG quasars. I. X-ray continuum and absorption. A&A **432**, 15–30 (2005).

[43] Page, K. L., Reeves, J. N., O'Brien, P. T. & Turner, M. J. L. XMM-Newton spectroscopy of high-redshift quasars. MNRAS **364**, 195–207 (2005).

[44] Fabian, A. C. *et al.* Properties of AGN coronae in the NuSTAR era. MNRAS **451**, 4375–4383 (2015).

[45] Belloni, T. M. & Motta, S. E. *Transient Black Hole Binaries*, 61–97 (Springer Berlin Heidelberg, Berlin, Heidelberg, 2016).

[46] Done, C., Gierliński, M. & Kubota, A. Modelling the behaviour of accretion flows in X-ray binaries. Everything you always wanted to know about accretion but were afraid to ask. A&A Rev. **15**, 1–66 (2007).

[47] Burlon, D. *et al.* Three-year Swift-BAT Survey of Active Galactic Nuclei: Reconciling Theory and Observations? ApJ **728**, 58 (2011).

[48] Dunn, R. J. H., Fender, R. P., Körding, E. G., Belloni, T. & Merloni, A. A global study of the behaviour of black hole X-ray binary discs. MNRAS **411**, 337–348 (2011).

[49] Shapiro, S. L., Lightman, A. P. & Eardley, D. M. A two-temperature accretion disk model for Cygnus X-1: structure and spectrum. ApJ **204**, 187–199 (1976).

[50] Patterson, J. The DQ Herculis Stars. PASP **106**, 209 (1994).

[51] Hoyle, F. & Lyttleton, R. A. The effect of interstellar matter on climatic variation. *Proceedings of the Cambridge Philosophical Society* **35**, 405 (1939).

[52] Jaffe, W., Ford, H. C., O'Connell, R. W., van den Bosch, F. C. & Ferrarese, L. Hubble Space Telescope Photometry of the Central Regions of Virgo Cluster Elliptical Galaxies. I. Observations, Discussion, and Conclusion. AJ **108**, 1567 (1994).

[53] Ferrarese, L., Ford, H. C. & Jaffe, W. Evidence for a Massive Black Hole in the Active Galaxy NGC 4261 from Hubble Space Telescope Images and Spectra. ApJ **470**, 444 (1996).

[54] Event Horizon Telescope Collaboration *et al.* First M87 Event Horizon Telescope Results. IV. Imaging the Central Supermassive Black Hole. ApJ **875**, L4 (2019).

[55] Event Horizon Telescope Collaboration *et al.* First M87 Event Horizon Telescope Results. V. Physical Origin of the Asymmetric Ring. ApJ **875**, L5 (2019).

[56] Burrows, C. J. *et al.* Hubble Space Telescope Observations of the Disk and Jet of HH 30. ApJ **473**, 437 (1996).

[57] Huang, J. *et al.* The Disk Substructures at High Angular Resolution Project (DSHARP). II. Characteristics of Annular Substructures. ApJ **869**, L42 (2018).

[58] ALMA Partnership *et al.* The 2014 ALMA Long Baseline Campaign: First Results from High Angular Resolution Observations toward the HL Tau Region. ApJ **808**, L3 (2015).

[59] Marsh, T. R. & Horne, K. Images of accretion discs - II. Doppler tomography. MNRAS **235**, 269–286 (1988).

[60] Snell, R. L., Loren, R. B. & Plambeck, R. L. Observations of CO in L 1551 : evidence for stellar wind driven shocks. ApJ **239**, L17–L22 (1980).

[61] Gallo, E., Fender, R. P. & Pooley, G. G. A universal radio-X-ray correlation in low/hard state black hole binaries. MNRAS **344**, 60–72 (2003).

[62] Miller-Jones, J. C. A., Fender, R. P. & Nakar, E. Opening angles, Lorentz factors and confinement of X-ray binary jets. MNRAS **367**, 1432–1440 (2006).

[63] Homan, D. C. Physical Properties of Jets in AGN. In *International Journal of Modern Physics Conference Series*, vol. 8 of *International Journal of Modern Physics Conference Series*, 163–171 (2012).

[64] Hovatta, T., Valtaoja, E., Tornikoski, M. & Lähteenmäki, A. Doppler factors, Lorentz factors and viewing angles for quasars, BL Lacertae objects and radio galaxies. A&A **494**, 527–537 (2009).

[65] Liang, E.-W. *et al.* Constraining Gamma-ray Burst Initial Lorentz Factor with the Afterglow Onset Feature and Discovery of a Tight Γ_0-E $_{\gamma,iso}$ Correlation. ApJ **725**, 2209–2224 (2010).

[66] Goldstein, A., Connaughton, V., Briggs, M. S. & Burns, E. Estimating Long GRB Jet Opening Angles and Rest-frame Energetics. ApJ **818**, 18 (2016).

[67] Pushkarev, A. B., Kovalev, Y. Y., Lister, M. L. & Savolainen, T. MOJAVE - XIV. Shapes and opening angles of AGN jets. MNRAS **468**, 4992–5003 (2017).

[68] Burbidge, G. R. On Synchrotron Radiation from Messier 87. ApJ **124**, 416 (1956).

[69] Mościbrodzka, M., Falcke, H. & Shiokawa, H. General relativistic magnetohydrodynamical simulations of the jet in M 87. A&A **586**, A38 (2016).

[70] Blandford, R. D. & Königl, A. Relativistic jets as compact radio sources. ApJ **232**, 34–48 (1979).

[71] Dougados, C., Cabrit, S., Lavalley, C. & Ménard, F. T Tauri stars microjets resolved by adaptive optics. A&A **357**, L61–L64 (2000).

[72] Coppejans, D. L. *et al.* Novalike cataclysmic variables are significant radio emitters. MNRAS **451**, 3801–3813 (2015).

[73] van den Eijnden, J. *et al.* An evolving jet from a strongly magnetized accreting X-ray pulsar. Nature **562**, 233–235 (2018).

[74] Pavlov, G. G., Teter, M. A., Kargaltsev, O. & Sanwal, D. The Variable Jet of the Vela Pulsar. ApJ **591**, 1157–1171 (2003).

[75] Blandford, R. D. & Znajek, R. L. Electromagnetic extraction of energy from Kerr black holes. MNRAS **179**, 433–456 (1977).

[76] Blandford, R. D. Black Holes and Relativistic Jets. *Progress of Theoretical Physics Supplement* **143**, 182–201 (2001).

[77] Narayan, R. & McClintock, J. E. Observational evidence for a correlation between jet power and black hole spin. MNRAS **419**, L69–L73 (2012).

[78] Russell, D. M., Gallo, E. & Fender, R. P. Observational constraints on the powering mechanism of transient relativistic jets. MNRAS **431**, 405–414 (2013).

[79] Sikora, M., Stawarz, Ł. & Lasota, J.-P. Radio Loudness of Active Galactic Nuclei: Observational Facts and Theoretical Implications. ApJ **658**, 815–828 (2007).

[80] Blandford, R. D. & Payne, D. G. Hydromagnetic flows from accretion disks and the production of radio jets. MNRAS **199**, 883–903 (1982).

[81] Henriksen, R. N. & Rayburn, D. R. Relativistic stellar wind theory: ' Near'zone solutions. MNRAS **152**, 323 (1971).

[82] Fender, R. *et al.* An ultra-relativistic outflow from a neutron star accreting gas from a companion. Nature **427**, 222–224 (2004).

[83] Fomalont, E. B., Geldzahler, B. J. & Bradshaw, C. F. Scorpius X-1: Energy Transfer from the Core to the Radio Lobes. ApJ **553**, L27–L30 (2001).

[84] Motta, S. E. & Fender, R. P. A connection between accretion states and the formation of ultrarelativistic outflows in a neutron star X-ray binary. MNRAS **483**, 3686–3699 (2019).

[85] Körding, E. G., Jester, S. & Fender, R. Measuring the accretion rate and kinetic luminosity functions of supermassive black holes. MNRAS **383**, 277–288 (2008).

[86] Hewish, A., Bell, S. J., Pilkington, J. D. H., Scott, P. F. & Collins, R. A. Observation of a Rapidly Pulsating Radio Source. Nature **217**, 709–713 (1968).

[87] Manchester, R. N., Hobbs, G. B., Teoh, A. & Hobbs, M. The Australia Telescope National Facility Pulsar Catalogue. AJ **129**, 1993–2006 (2005).

[88] Hulse, R. A. & Taylor, J. H. Discovery of a pulsar in a binary system. ApJ **195**, L51–L53 (1975).

[89] Kramer, M. *et al.* Tests of General Relativity from Timing the Double Pulsar. *Science* **314**, 97–102 (2006).

[90] Petroff, E., Hessels, J. W. T. & Lorimer, D. R. Fast radio bursts. A&A Rev. **27**, 4 (2019).

[91] Tendulkar, S. P. *et al.* The Host Galaxy and Redshift of the Repeating Fast Radio Burst FRB 121102. ApJ **834**, L7 (2017).

[92] Marcote, B. *et al.* A repeating fast radio burst source localized to a nearby spiral galaxy. Nature **577**, 190–194 (2020).

[93] Lorimer, D. R., Bailes, M., McLaughlin, M. A., Narkevic, D. J. & Crawford, F. A Bright Millisecond Radio Burst of Extragalactic Origin. *Science* **318**, 777 (2007).

[94] Pietka, M., Fender, R. P. & Keane, E. F. The variability time-scales and brightness temperatures of radio flares from stars to supermassive black holes. MNRAS **446**, 3687–3696 (2015).

[95] Stirling, A. M. *et al.* A relativistic jet from Cygnus X-1 in the low/hard X-ray state. MNRAS **327**, 1273–1278 (2001).

[96] Dhawan, V., Mirabel, I. F. & Rodríguez, L. F. AU-Scale Synchrotron Jets and Superluminal Ejecta in GRS 1915+105. ApJ **543**, 373–385 (2000).

[97] Mirabel, I. F. & Rodríguez, L. F. A superluminal source in the Galaxy. Nature **371**, 46–48 (1994).

[98] Corbel, S., Nowak, M. A., Fender, R. P., Tzioumis, A. K. & Markoff, S. Radio/X-ray correlation in the low/hard state of GX 339-4. A&A **400**, 1007–1012 (2003).

[99] Russell, T. D. *et al.* Disk-Jet Coupling in the 2017/2018 Outburst of the Galactic Black Hole Candidate X-Ray Binary MAXI J1535-571. ApJ **883**, 198 (2019).

[100] Bright, J. S. *et al.* An extremely powerful long-lived superluminal ejection from the black hole MAXI J1820+070. *arXiv e-prints* arXiv:2003.01083 (2020).

[101] Atri, P. *et al.* A radio parallax to the black hole X-ray binary MAXI J1820+070. MNRAS L10 (2020).

[102] Hjellming, R. M. & Johnston, K. J. An analysis of the proper motions of SS 433 radio jets. ApJ **246**, L141–L145 (1981).

[103] Miller-Jones, J. C. A. *et al.* A rapidly changing jet orientation in the stellar-mass black-hole system V404 Cygni. Nature **569**, 374–377 (2019).

[104] Coriat, M. *et al.* The twisted jets of Circinus X-1. MNRAS **484**, 1672–1686 (2019).

[105] Merloni, A., Heinz, S. & di Matteo, T. A Fundamental Plane of black hole activity. MNRAS **345**, 1057–1076 (2003).

[106] Coriat, M., Fender, R. P. & Dubus, G. Revisiting a fundamental test of the disc instability model for X-ray binaries. MNRAS **424**, 1991–2001 (2012).

[107] Dulk, G. A., Bastian, T. S. & Chanmugam, G. Radio emission from AM Herculis : the quiescent component and an outburst. ApJ **273**, 249–254 (1983).

[108] Richards, M. T., Waltman, E. B., Ghigo, F. D. & Richards, D. S. P. Statistical Analysis of 5 Year Continuous Radio Flare Data from β Persei, V711 Tauri, δ Librae, and UX Arietis. ApJS **147**, 337–361 (2003).

[109] Fender, R. P. *et al.* A prompt radio transient associated with a gamma-ray superflare from the young M dwarf binary DG CVn. MNRAS **446**, L66–L70 (2015).

[110] Driessen, L. N. *et al.* MKT J170456.2-482100: the first transient discovered by MeerKAT. MNRAS **491**, 560–575 (2020).

[111] Klebesadel, R. W., Strong, I. B. & Olson, R. A. Observations of Gamma-Ray Bursts of Cosmic Origin. ApJ **182**, L85 (1973).

[112] Ruderman, M. Theories of gamma -ray bursts. In Bergman, P. G., Fenyves, E. J. & Motz, L. (eds.) *Seventh Texas Symposium on Relativistic Astrophysics*, vol. 262, 164–180 (1975).

[113] Lamb, D. Q. The Distance Scale to Gamma-Ray Bursts. PASP **107**, 1152 (1995).

[114] Metzger, M. R. *et al.* Spectral constraints on the redshift of the optical counterpart to the γ-ray burst of 8 May 1997. Nature **387**, 878–880 (1997).

[115] Norris, J. P., Cline, T. L., Desai, U. D. & Teegarden, B. J. Frequency of fast, narrow γ-ray bursts. Nature **308**, 434–435 (1984).

[116] Kouveliotou, C. *et al.* Identification of Two Classes of Gamma-Ray Bursts. ApJ **413**, L101 (1993).

[117] Taylor, G. B., Frail, D. A., Berger, E. & Kulkarni, S. R. The Angular Size and Proper Motion of the Afterglow of GRB 030329. ApJ **609**, L1–L4 (2004).

[118] Mooley, K. P. *et al.* Superluminal motion of a relativistic jet in the neutron-star merger GW170817. Nature **561**, 355–359 (2018).

[119] Taylor, J. H., Fowler, L. A. & McCulloch, P. M. Measurements of general relativistic effects in the binary pulsar PSR1913 + 16. Nature **277**, 437–440 (1979).

[120] Abbott, B. P. *et al.* Observation of gravitational waves from a binary black hole merger. *Phys. Rev. Lett.* **116**, 061102 (2016).

[121] Abbott, B. P. *et al.* Multi-messenger Observations of a Binary Neutron Star Merger. ApJ **848**, L12 (2017).

[122] Kasen, D., Metzger, B., Barnes, J., Quataert, E. & Ramirez-Ruiz, E. Origin of the heavy elements in binary neutron-star mergers from a gravitational-wave event. Nature **551**, 80–84 (2017).

[123] Mooley, K. P. *et al.* A mildly relativistic wide-angle outflow in the neutron-star merger event GW170817. Nature **554**, 207–210 (2018).

[124] Rees, M. J. Tidal disruption of stars by black holes of 10^6-10^8 solar masses in nearby galaxies. Nature **333**, 523–528 (1988).

[125] Cenko, S. B. *et al.* Swift J2058.4+0516: Discovery of a Possible Second Relativistic Tidal Disruption Flare? ApJ **753**, 77 (2012).

[126] Metzger, B. D., Giannios, D. & Mimica, P. Afterglow model for the radio emission from the jetted tidal disruption candidate Swift J1644+57. MNRAS **420**, 3528–3537 (2012).

[127] van Velzen, S. *et al.* A radio jet from the optical and x-ray bright stellar tidal disruption flare ASASSN-14li. *Science* **351**, 62–65 (2016).

[128] Alexander, K. D., Berger, E., Guillochon, J., Zauderer, B. A. & Williams, P. K. G. Discovery of an Outflow from Radio Observations of the Tidal Disruption Event ASASSN-14li. ApJ **819**, L25 (2016).

[129] Bellm, E. C. *et al.* The Zwicky Transient Facility: System Overview, Performance, and First Results. PASP **131**, 018002 (2019).

[130] Hjorth, J. & Bloom, J. S. *The GRB-supernova connection*, 169–190. Cambridge Astrophysics (Cambridge University Press, 2012).

[131] Coppejans, D. L. *et al.* Jets in Hydrogen-poor Superluminous Supernovae: Constraints from a Comprehensive Analysis of Radio Observations. ApJ **856**, 56 (2018).

[132] Perley, D. A. *et al.* The fast, luminous ultraviolet transient AT2018cow: extreme supernova, or disruption of a star by an intermediate-mass black hole? MNRAS **484**, 1031–1049 (2019).

[133] Coppejans, D. L. *et al.* A Mildly Relativistic Outflow from the Energetic, Fast-rising Blue Optical Transient CSS161010 in a Dwarf Galaxy. ApJ **895**, L23 (2020).

[134] Ho, A. Y. Q. *et al.* The Koala: A Fast Blue Optical Transient with Luminous Radio Emission from a Starburst Dwarf Galaxy at z = 0.27. ApJ **895**, 49 (2020).

[135] Margutti, R. *et al.* An Embedded X-Ray Source Shines through the Aspherical AT 2018cow: Revealing the Inner Workings of the Most Luminous Fast-evolving Optical Transients. ApJ **872**, 18 (2019).

[136] Longair, M. S. *High Energy Astrophysics* (Cambridge University Press, 2011).

[137] Condon, J. J. & Ransom, S. M. *Essential Radio Astronomy* (Princeton University Press, 2016).

[138] Fermi, E. On the Origin of the Cosmic Radiation. *Physical Review* **75**, 1169–1174 (1949).

[139] Bell, A. R. The acceleration of cosmic rays in shock fronts - I. MNRAS **182**, 147–156 (1978).

[140] Bell, A. R. The acceleration of cosmic rays in shock fronts - II. MNRAS **182**, 443–455 (1978).

[141] Sari, R., Piran, T. & Narayan, R. Spectra and Light Curves of Gamma-Ray Burst Afterglows. ApJ **497**, L17–L20 (1998).

[142] Granot, J., Piran, T. & Sari, R. The Synchrotron Spectrum of Fast Cooling Electrons Revisited. ApJ **534**, L163–L166 (2000).

[143] Yost, S. A. *et al.* Optical Light Curve and Cooling Break of GRB 050502A. ApJ **636**, 959–966 (2006).

[144] Filgas, R. *et al.* GRB 091127: The cooling break race on magnetic fuel. A&A **535**, A57 (2011).

[145] Rhodes, L. *et al.* Radio Afterglows of Very High Energy Gamma-Ray Bursts 190829A and 180720B. *arXiv e-prints* arXiv:2004.01538 (2020).

[146] Spinks, M. J., Rees, W. G. & Duffett-Smith, P. J. How old is Cygnus A? Nature **319**, 471–473 (1986).

[147] Fanaroff, B. L. & Riley, J. M. The morphology of extragalactic radio sources of high and low luminosity. MNRAS **167**, 31P–36P (1974).

[148] Asada, K. & Nakamura, M. The Structure of the M87 Jet: A Transition from Parabolic to Conical Streamlines. ApJ **745**, L28 (2012).

[149] Falcke, H. & Biermann, P. L. The jet-disk symbiosis. I. Radio to X-ray emission models for quasars. A&A **293**, 665–682 (1995).

[150] Biretta, J. A., Sparks, W. B. & Macchetto, F. Hubble Space Telescope Observations of Superluminal Motion in the M87 Jet. ApJ **520**, 621–626 (1999).

[151] Ressler, S. M. & Laskar, T. Thermal Electrons in Gamma-Ray Burst Afterglows. ApJ **845**, 150 (2017).

[152] McClintock, J. E. & Remillard, R. A. *Black hole binaries*, vol. 39, 157–213 (Cambridge University Press, 2006).

[153] Esin, A. A., McClintock, J. E. & Narayan, R. Advection-Dominated Accretion and the Spectral States of Black Hole X-Ray Binaries: Application to Nova Muscae 1991. ApJ **489**, 865–889 (1997).

[154] Haardt, F. & Maraschi, L. X-Ray Spectra from Two-Phase Accretion Disks. ApJ **413**, 507 (1993).

[155] Meyer, F. & Meyer-Hofmeister, E. On the elusive cause of cataclysmic variable outbursts. A&A **104**, L10–L12 (1981).

[156] Mukai, K., Kinkhabwala, A., Peterson, J. R., Kahn, S. M. & Paerels, F. Two Types of X-Ray Spectra in Cataclysmic Variables. ApJ **586**, L77–L80 (2003).

[157] Galeev, A. A., Rosner, R. & Vaiana, G. S. Structured coronae of accretion disks. ApJ **229**, 318–326 (1979).

[158] Haardt, F. & Maraschi, L. A Two-Phase Model for the X-Ray Emission from Seyfert Galaxies. ApJ **380**, L51 (1991).

[159] Taylor, G. B., Carilli, C. L. & Perley, R. A. *Synthesis Imaging in Radio Astronomy II*, vol. 180 (Astronomical Society of the Pacific, 1999).

[160] Thompson, A. R., Moran, J. M. & Swenson, J., George W. *Interferometry and Synthesis in Radio Astronomy, 3rd Edition* (Springer, 2017).

[161] Ryle, M. & Hewish, A. The synthesis of large radio telescopes. MNRAS **120**, 220 (1960).

[162] Cotton, W. D. Fringe Fitting. In Zensus, J. A., Diamond, P. J. & Napier, P. J. (eds.) *Very Long Baseline Interferometry and the VLBA*, vol. 82 of *Astronomical Society of the Pacific Conference Series*, 189 (1995).

[163] Briggs, D. *High Fidelity Deconvolution of Moderately Resolved Sources*. Ph.D. thesis, New Mexico Institute of Mining and Technology (1995).

[164] Högbom, J. A. Aperture Synthesis with a Non-Regular Distribution of Interferometer Baselines. A&AS **15**, 417 (1974).

[165] Clark, B. G. An efficient implementation of the algorithm 'CLEAN'. A&A **89**, 377 (1980).

[166] Schwab, F. R. Relaxing the isoplanatism assumption in self-calibration; applications to low-frequency radio interferometry. AJ **89**, 1076–1081 (1984).

[167] Cornwell, T. J. Multiscale CLEAN Deconvolution of Radio Synthesis Images. *IEEE Journal of Selected Topics in Signal Processing* **2**, 793–801 (2008).

[168] Ryle, M. The 5-km Radio Telescope at Cambridge. Nature **239**, 435–438 (1972).

[169] Zwart, J. T. L. *et al.* The Arcminute Microkelvin Imager. MNRAS **391**, 1545–1558 (2008).

[170] Hickish, J. *et al.* A digital correlator upgrade for the Arcminute MicroKelvin Imager. MNRAS **475**, 5677–5687 (2018).

[171] Perrott, Y. C. *et al.* Comparison of Sunyaev-Zel'dovich measurements from Planck and from the Arcminute Microkelvin Imager for 99 galaxy clusters. A&A **580**, A95 (2015).

[172] Staley, T. D. *et al.* Automated rapid follow-up of Swift gamma-ray burst alerts at 15 GHz with the AMI Large Array. MNRAS **428**, 3114–3120 (2013).

[173] Mauch, T. *et al.* The 1.28 GHz MeerKAT DEEP2 Image. *arXiv e-prints* arXiv:1912.06212 (2019).

[174] Fender, R. *et al.* ThunderKAT: The MeerKAT Large Survey Project for Image-Plane Radio Transients. *arXiv e-prints* arXiv:1711.04132 (2017).

[175] Offringa, A. R., van de Gronde, J. J. & Roerdink, J. B. T. M. A morphological algorithm for improving radio-frequency interference detection. A&A **539**, A95 (2012).

[176] McMullin, J. P., Waters, B., Schiebel, D., Young, W. & Golap, K. CASA Architecture and Applications. In Shaw, R. A., Hill, F. & Bell, D. J. (eds.) *Astronomical Data Analysis Software and Systems XVI*, vol. 376 of *Astronomical Society of the Pacific Conference Series*, 127 (2007).

[177] Offringa, A. R., McKinley, B., Hurley-Walker *et al.* WSClean: an implementation of a fast, generic wide-field imager for radio astronomy. *MNRAS* **444**, 606–619 (2014).

[178] Offringa, A. R. & Smirnov, O. An optimized algorithm for multiscale wideband deconvolution of radio astronomical images. *MNRAS* **471**, 301–316 (2017).

[179] Thompson, A. R., Clark, B. G., Wade, C. M. & Napier, P. J. The Very Large Array. ApJS **44**, 151–167 (1980).

[180] Perley, R. *et al.* The Expanded Very Large Array. *IEEE Proceedings* **97**, 1448–1462 (2009).

[181] Gehrels, N. *et al.* The Swift Gamma-Ray Burst Mission. ApJ **611**, 1005–1020 (2004).

[182] Burrows, D. N. *et al.* Swift X-Ray Telescope. In Flanagan, K. A. & Siegmund, O. H. (eds.) Proc. SPIE, vol. 4140 of *Society of Photo-Optical Instrumentation Engineers (SPIE) Conference Series*, 64–75 (2000).

[183] Hill, J. E. *et al.* Laboratory x-ray CCD camera electronics: a test bed for the Swift X-Ray Telescope. In Flanagan, K. A. & Siegmund, O. H. (eds.) Proc. SPIE, vol. 4140 of *Society of Photo-Optical Instrumentation Engineers (SPIE) Conference Series*, 87–98 (2000).

[184] Barthelmy, S. D. Burst Alert Telescope (BAT) on the Swift MIDEX mission. In Flanagan, K. A. & Siegmund, O. H. (eds.) Proc. SPIE, vol. 4140 of *Society of Photo-Optical Instrumentation Engineers (SPIE) Conference Series*, 50–63 (2000).

[185] Barthelmy, S. D. *et al.* The Burst Alert Telescope (BAT) on the SWIFT Midex Mission. Space Sci. Rev. **120**, 143–164 (2005).

[186] Evans, P. A. *et al.* An online repository of Swift/XRT light curves of γ-ray bursts. A&A **469**, 379–385 (2007).

[187] Evans, P. A. *et al.* Methods and results of an automatic analysis of a complete sample of Swift-XRT observations of GRBs. MNRAS **397**, 1177–1201 (2009).

[188] Matsuoka, M. *et al.* The MAXI Mission on the ISS: Science and Instruments for Monitoring All-Sky X-Ray Images. PASJ **61**, 999 (2009).

[189] Kara, E. *et al.* The corona contracts in a black-hole transient. Nature **565**, 198–201 (2019).

[190] Homan, J. *et al.* A rapid change in X-ray variability and a jet ejection in the black hole transient MAXI J1820+070. *arXiv e-prints* arXiv:2003.01012 (2020).

[191] Gies, D. R. & Bolton, C. T. The Optical Spectrum of HDE 226868 = Cygnus X-1. III. A Focused Stellar Wind Model for He II lambda 4686 Emission. ApJ **304**, 389 (1986).

[192] Hellier, C. *Cataclysmic Variable Stars* (Springer-Verlag London, 2001).

[193] Chen, W., Shrader, C. R. & Livio, M. The Properties of X-Ray and Optical Light Curves of X-Ray Novae. ApJ **491**, 312–338 (1997).

[194] Gallo, E. *et al.* The radio/X-ray domain of black hole X-ray binaries at the lowest radio luminosities. MNRAS **445**, 290–300 (2014).

[195] Middleton, M. J. *et al.* Bright radio emission from an ultraluminous stellar-mass microquasar in M 31. Nature **493**, 187–190 (2013).

[196] Fender, R. P., Belloni, T. M. & Gallo, E. Towards a unified model for black hole X-ray binary jets. MNRAS **355**, 1105–1118 (2004).

[197] Markoff, S., Falcke, H. & Fender, R. A jet model for the broadband spectrum of XTE J1118+480. Synchrotron emission from radio to X-rays in the Low/Hard spectral state. A&A **372**, L25–L28 (2001).

[198] Markoff, S., Nowak, M. A. & Wilms, J. Going with the Flow: Can the Base of Jets Subsume the Role of Compact Accretion Disk Coronae? ApJ **635**, 1203–1216 (2005).

[199] Stiele, H. & Kong, A. K. H. The 2015 hard-state only outburst of GS 1354-64. MNRAS **459**, 4038–4045 (2016).

[200] Tetarenko, B. E., Sivakoff, G. R., Heinke, C. O. & Gladstone, J. C. WATCHDOG: A Comprehensive All-sky Database of Galactic Black Hole X-ray Binaries. ApJS **222**, 15 (2016).

[201] Williams, D. R. A. *et al.* The 2018 outburst of BHXB H1743-322 as seen with MeerKAT. MNRAS **491**, L29–L33 (2020).

[202] Homan, J. *et al.* Correlated X-Ray Spectral and Timing Behavior of the Black Hole Candidate XTE J1550-564: A New Interpretation of Black Hole States. ApJS **132**, 377–402 (2001).

[203] Belloni, T. M. *States and Transitions in Black Hole Binaries*, vol. 794, 53 (Springer, Berlin, Heidelberg, 2010).

[204] Fender, R. P. *et al.* MERLIN observations of relativistic ejections from GRS 1915+105. MNRAS **304**, 865–876 (1999).

[205] Tetarenko, A. J. *et al.* Extreme jet ejections from the black hole X-ray binary V404 Cygni. MNRAS **469**, 3141–3162 (2017).

[206] Corbel, S. *et al.* Large-Scale, Decelerating, Relativistic X-ray Jets from the Microquasar XTE J1550-564. *Science* **298**, 196–199 (2002).

[207] Corbel, S. *et al.* Moving relativistic large-scale X-ray jets in the microquasar XTE J1550-564. New A Rev. **47**, 477–480 (2003).

[208] Corbel, S. *et al.* Discovery of X-Ray Jets in the Microquasar H1743-322. ApJ **632**, 504–513 (2005).

[209] Fender, R. P. Uses and limitations of relativistic jet proper motions: lessons from Galactic microquasars. MNRAS **340**, 1353–1358 (2003).

[210] Muñoz-Darias, T. *et al.* Hard-state Accretion Disk Winds from Black Holes: The Revealing Case of MAXI J1820+070. ApJ **879**, L4 (2019).

[211] Fender, R. & Belloni, T. Stellar-mass black holes and ultraluminous x-ray sources. *Science* **337**, 540–544 (2012). URL `https://science.sciencemag.org/content/337/6094/540`.

[212] Narayan, R. & Yi, I. Advection-dominated Accretion: A Self-similar Solution. ApJ **428**, L13 (1994).

[213] Heinz, S. & Sunyaev, R. A. The non-linear dependence of flux on black hole mass and accretion rate in core-dominated jets. MNRAS **343**, L59–L64 (2003).

[214] Coriat, M. *et al.* Radiatively efficient accreting black holes in the hard state: the case study of H1743-322. MNRAS **414**, 677–690 (2011).

[215] Garcia, M. R. *et al.* New Evidence for Black Hole Event Horizons from Chandra. ApJ **553**, L47–L50 (2001).

[216] Motta, S. E., Casella, P. & Fender, R. P. Radio-loudness in black hole transients: evidence for an inclination effect. MNRAS **478**, 5159–5173 (2018).

[217] Corbel, S. *et al.* The 'universal' radio/X-ray flux correlation: the case study of the black hole GX 339-4. MNRAS **428**, 2500–2515 (2013).

[218] Tremou, E. *et al.* Radio & X-ray detections of GX 339-4 in quiescence using MeerKAT and Swift. MNRAS (2020).

[219] Gallo, E., Degenaar, N. & van den Eijnden, J. Hard state neutron star and black hole X-ray binaries in the radio:X-ray luminosity plane. MNRAS **478**, L132–L136 (2018).

[220] Casella, P. & Pe'er, A. On the Role of the Magnetic Field on Jet Emission in X-Ray Binaries. ApJ **703**, L63–L66 (2009).

[221] Meyer-Hofmeister, E. & Meyer, F. The relation between radio and X-ray luminosity of black hole binaries: affected by inner cool disks? A&A **562**, A142 (2014).

[222] Tomsick, J. A. *et al.* X-Ray Jet Emission from the Black Hole X-Ray Binary XTE J1550-564 with Chandra in 2000. ApJ **582**, 933–944 (2003).

[223] Migliori, G. *et al.* Evolving morphology of the large-scale relativistic jets from XTE J1550-564. MNRAS **472**, 141–165 (2017).

[224] Espinasse, M. *et al.* Relativistic X-Ray Jets from the Black Hole X-Ray Binary MAXI J1820+070. ApJ **895**, L31 (2020).

[225] Shappee, B. J. *et al.* The Man behind the Curtain: X-Rays Drive the UV through NIR Variability in the 2013 Active Galactic Nucleus Outburst in NGC 2617. ApJ **788**, 48 (2014).

[226] Kochanek, C. S. *et al.* The All-Sky Automated Survey for Supernovae (ASAS-SN) Light Curve Server v1.0. PASP **129**, 104502 (2017).

[227] Tucker, M. A. *et al.* ASASSN-18ey: The Rise of a New Black Hole X-Ray Binary. ApJ **867**, L9 (2018).

[228] Negoro, H. *et al.* The MAXI/GSC Nova-Alert System and results of its first 68 months. *Publications of the Astronomical Society of Japan* **68** (2016). S1.

[229] Kawamuro, T. *et al.* MAXI/GSC detection of a probable new X-ray transient MAXI J1820+070. *The Astronomer's Telegram* **11399**, 1 (2018).

[230] Kennea, J. A., Marshall, F. E., Page, K. L., Palmer, D. M. & Siegel, M. H. Swift detection of MAXI J1820+070. *GRB Coordinates Network* **22471**, 1 (2018).

[231] Kennea, J. A. & Siegel, M. H. MAXI J1820+070: Swift/UVOT counterpart correction. *The Astronomer's Telegram* **11404**, 1 (2018).

[232] Kennea, J. A. MAXI J1820+070: Errata and updated XRT Position. *The Astronomer's Telegram* **11406**, 1 (2018).

[233] Denisenko, D. Optical follow-up of MAXI J1820+070 and possible identity with ASASSN-18ey. *The Astronomer's Telegram* **11400**, 1 (2018).

[234] Baglio, M. C., Russell, D. M. & Lewis, F. Optical observations of MAXI J1820+070 suggest it is a black hole X-ray binary. *The Astronomer's Telegram* **11418**, 1 (2018).

[235] Russell, D. M. *et al.* Global optical/infrared-X-ray correlations in X-ray binaries: quantifying disc and jet contributions. MNRAS **371**, 1334–1350 (2006).

[236] Russell, D. M., Fender, R. P. & Jonker, P. G. Evidence for a jet contribution to the optical/infrared light of neutron star X-ray binaries. MNRAS **379**, 1108–1116 (2007).

[237] Gandhi, P., Rao, A., Johnson, M. A. C., Paice, J. A. & Maccarone, T. J. Gaia Data Release 2 distances and peculiar velocities for Galactic black hole transients. MNRAS **485**, 2642–2655 (2019).

[238] Shidatsu, M. *et al.* X-Ray and Optical Monitoring of State Transitions in MAXI J1820+070. ApJ **874**, 183 (2019).

[239] Homan, J. *et al.* A rapid state transition in MAXI J1820+070. *The Astronomer's Telegram* **11820**, 1 (2018).

[240] Curran, P. A. *et al.* Radio polarimetry as a probe of unresolved jets: the 2013 outburst of XTE J1908+094. MNRAS **451**, 3975–3985 (2015).

[241] Brocksopp, C. *et al.* XTE J1752-223 in outburst: a persistent radio jet, dramatic flaring, multiple ejections and linear polarization. MNRAS **432**, 931–943 (2013).

[242] Brocksopp, C., Miller-Jones, J. C. A., Fender, R. P. & Stappers, B. W. A highly polarized radio jet during the 1998 outburst of the black hole transient XTE J1748-288. MNRAS **378**, 1111–1117 (2007).

[243] Hannikainen, D. C. *et al.* Revisiting the relativistic ejection event in XTE J1550-564 during the 1998 outburst. MNRAS **397**, 569–576 (2009).

[244] Brocksopp, C. *et al.* The 2003 radio outburst of a new X-ray transient: XTE J1720-318. MNRAS **356**, 125–130 (2005).

[245] Negoro, H. *et al.* MAXI/GSC detection of a rapid increase in the hard X-ray flux of MAXI J1820+070. *The Astronomer's Telegram* **12057**, 1 (2018).

[246] Bright, J., Motta, S. & Fender, R. AMI radio detection of the black hole candidate MAXI J1820+070 during the soft to hard transition. *The Astronomer's Telegram* **12061**, 1 (2018).

[247] Motta, S. E., Bright, J. & Fender, R. Swift observes MAXI J1820+070 in transition from the soft to the hard-intermediate state. *The Astronomer's Telegram* **12064**, 1 (2018).

[248] Russell, D. M. *et al.* Testing the Jet Quenching Paradigm with an Ultradeep Observation of a Steadily Soft State Black Hole. ApJ **739**, L19 (2011).

[249] Rushton, A. P. *et al.* Disc-jet quenching of the galactic black hole Swift J1753.5-0127. MNRAS **463**, 628–634 (2016).

[250] Drappeau, S. *et al.* Dark jets in the soft X-ray state of black hole binaries? MNRAS **466**, 4272–4278 (2017).

[251] Foreman-Mackey, D., Hogg, D. W., Lang, D. & Goodman, J. emcee: The MCMC Hammer. PASP **125**, 306 (2013).

[252] Martí-Vidal, I., Vlemmings, W. H. T., Muller, S. & Casey, S. UVMULTIFIT: A versatile tool for fitting astronomical radio interferometric data. A&A **563**, A136 (2014).

[253] Rodríguez, L. F. & Mirabel, I. F. Repeated Relativistic Ejections in GRS 1915+105. ApJ **511**, 398–404 (1999).

[254] Hjellming, R. M. & Rupen, M. P. Episodic ejection of relativistic jets by the X-ray transient GRO J1655 - 40. Nature **375**, 464–468 (1995).

[255] Burbidge, G. R. Estimates of the Total Energy in Particles and Magnetic Field in the Non-Thermal Radio Sources. ApJ **129**, 849–852 (1959).

[256] Burbidge, G. R., Jones, T. W. & Odell, S. L. Physics of compact nonthermal sources. III. Energetic considerations. ApJ **193**, 43–54 (1974).

[257] Rushton, A. P. *et al.* Resolved, expanding jets in the Galactic black hole candidate XTE J1908+094. MNRAS **468**, 2788–2802 (2017).

[258] van der Laan, H. A Model for Variable Extragalactic Radio Sources. Nature **211**, 1131–1133 (1966).

[259] Fender, R. & Bright, J. Synchrotron self-absorption and the minimum energy of optically thick radio flares from stellar mass black holes. MNRAS **489**, 4836–4846 (2019).

[260] Hannikainen, D. *et al.* XTE J1550-564: a superluminal ejection during the September 1998 outburst. *Astrophysics and Space Science Supplement* **276**, 45–48 (2001).

[261] Wang, X. Y., Dai, Z. G. & Lu, T. External Shock Model for the Large-Scale, Relativistic X-Ray Jets from the Microquasar XTE J1550-564. ApJ **592**, 347–353 (2003).

[262] Casella, P., Belloni, T. & Stella, L. The ABC of Low-Frequency Quasi-periodic Oscillations in Black Hole Candidates: Analogies with Z Sources. ApJ **629**, 403–407 (2005).

[263] Ingram, A. & Motta, S. A review of quasi-periodic oscillations from black hole X-ray binaries: observation and theory. *arXiv e-prints* arXiv:2001.08758 (2020).

[264] Stella, L. & Vietri, M. Lense-Thirring Precession and Quasi-periodic Oscillations in Low-Mass X-Ray Binaries. ApJ **492**, L59–L62 (1998).

[265] Ingram, A. & Motta, S. Solutions to the relativistic precession model. MNRAS **444**, 2065–2070 (2014).

[266] Motta, S. E. *et al.* Geometrical constraints on the origin of timing signals from black holes. MNRAS **447**, 2059–2072 (2015).

[267] Soleri, P., Belloni, T. & Casella, P. A transient low-frequency quasi-periodic oscillation from the black hole binary GRS 1915+105. MNRAS **383**, 1089–1102 (2008).

[268] Miller-Jones, J. C. A. *et al.* Disc-jet coupling in the 2009 outburst of the black hole candidate H1743-322. MNRAS **421**, 468–485 (2012).

[269] Fender, R. P., Homan, J. & Belloni, T. M. Jets from black hole X-ray binaries: testing, refining and extending empirical models for the coupling to X-rays. MNRAS **396**, 1370–1382 (2009).

[270] Broderick, J. *et al.* LOFAR observations of MAXI J1820+070 (ASASSN-18ey) during its recent state transition. *The Astronomer's Telegram* **11887**, 1 (2018).

[271] Hjellming, R. M. & Johnston, K. J. Radio emission from conical jets associated with X-ray binaries. ApJ **328**, 600–609 (1988).

[272] de Gouveia dal Pino, E. M. & Lazarian, A. Production of the large scale superluminal ejections of the microquasar GRS 1915+105 by violent magnetic reconnection. A&A **441**, 845–853 (2005).

[273] Fender, R. P. & Pooley, G. G. Infrared synchrotron oscillations in GRS 1915+105. MNRAS **300**, 573–576 (1998).

[274] Fender, R. P. *et al.* Spectral, polarization and time-lag properties of GRS 1915+105 radio oscillations. MNRAS **330**, 212–218 (2002). `astro-ph/0110501`.

[275] Pacholczyk, A. G. *Radio astrophysics. Nonthermal processes in galactic and extragalactic sources* (W. H. Freeman, 1970).

[276] Yusef-Zadeh, F., Roberts, D., Wardle, M., Heinke, C. O. & Bower, G. C. Flaring Activity of Sagittarius A* at 43 and 22 GHz: Evidence for Expanding Hot Plasma. ApJ **650**, 189–194 (2006).

[277] Yusef-Zadeh, F. *et al.* Simultaneous Chandra, CSO, and VLA Observations of Sgr A*: The Nature of Flaring Activity. ApJ **682**, 361–372 (2008).

[278] Mooley, K. P. *et al.* Rapid radio flaring during an anomalous outburst of SS Cyg. MNRAS **467**, L31–L35 (2017).

[279] Fender, R., Bright, J., Mooley, K. & Miller-Jones, J. Late-outburst radio flaring in SS Cyg and evidence for a powerful kinetic output channel in cataclysmic variables. MNRAS **490**, L76–L80 (2019).

[280] Wheatley, P. J., Mauche, C. W. & Mattei, J. A. The X-ray and extreme-ultraviolet flux evolution of SS Cygni throughout outburst. MNRAS **345**, 49–61 (2003).

[281] Russell, T. D. *et al.* The reproducible radio outbursts of SS Cygni. MNRAS **460**, 3720–3732 (2016).

[282] Miller-Jones, J. C. A. *et al.* The First Accurate Parallax Distance to a Black Hole. ApJ **706**, L230–L234 (2009).

[283] Armstrong, R. P. *et al.* A return to strong radio flaring by Circinus X-1 observed with the Karoo Array Telescope test array KAT-7. MNRAS **433**, 1951–1957 (2013).

[284] Kardashev, N. S. Nonstationarity of Spectra of Young Sources of Nonthermal Radio Emission. Soviet Ast. **6**, 317 (1962).

[285] Peterson, F. W. Particle Injection in the Cygnus X-3 Radio Outburst. Nature **242**, 173–177 (1973).

[286] Pacholczyk, A. G. & Scott, J. S. Physics of compact radio sources. I. Particle acceleration and flux variations. ApJ **210**, 311–320 (1976).

[287] Peterson, F. W. & Dent, W. A. A Prolonged Injection Model for Variable Radio Sources. ApJ **186**, 421–432 (1973).

[288] Ling, Z., Zhang, S. N. & Tang, S. Determining the Distance of Cyg X-3 with its X-Ray Dust Scattering Halo. ApJ **695**, 1111–1120 (2009).

[289] McCollough, M. L., Corrales, L. & Dunham, M. M. Cygnus X-3: Its Little Friend's Counterpart, the Distance to Cygnus X-3, and Outflows/Jets. ApJ **830**, L36 (2016).

[290] Falcke, H., Körding, E. & Nagar, N. M. Compact radio cores: from the first black holes to the last. New A Rev. **48**, 1157–1171 (2004). `astro-ph/0409125`.

[291] Sanders, R. H. The reconfinement of jets. ApJ **266**, 73–81 (1983).

[292] Fender, R. P. *et al.* Cygnus X-3 in outburst: quenched radio emission, radiation losses and variable local opacity. MNRAS **288**, 849–858 (1997). `astro-ph/9612125`.

[293] Levan, A. *et al.* Gamma-Ray Burst Progenitors. Space Sci. Rev. **202**, 33–78 (2016).

[294] Galama, T. J. *et al.* Evidence for a Supernova in Reanalyzed Optical and Near-Infrared Images of GRB 970228. ApJ **536**, 185–194 (2000).

[295] Hjorth, J. *et al.* A very energetic supernova associated with the γ-ray burst of 29 March 2003. Nature **423**, 847–850 (2003).

[296] Della Valle, M. *et al.* An enigmatic long-lasting γ-ray burst not accompanied by a bright supernova. Nature **444**, 1050–1052 (2006).

[297] Fynbo, J. P. U. *et al.* No supernovae associated with two long-duration γ-ray bursts. Nature **444**, 1047–1049 (2006).

[298] Frail, D. A., Waxman, E. & Kulkarni, S. R. A 450 Day Light Curve of the Radio Afterglow of GRB 970508: Fireball Calorimetry. ApJ **537**, 191–204 (2000).

[299] van der Horst, A. J. *et al.* Detailed study of the GRB 030329 radio afterglow deep into the non-relativistic phase. A&A **480**, 35–43 (2008).

[300] Rees, M. J. & Meszaros, P. Unsteady Outflow Models for Cosmological Gamma-Ray Bursts. ApJ **430**, L93 (1994).

[301] Spruit, H. C., Daigne, F. & Drenkhahn, G. Large scale magnetic fields and their dissipation in GRB fireballs. A&A **369**, 694–705 (2001).

[302] Granot, J. Gamma-Ray Bursts from Magnetic Reconnection: Variability and Robustness of Light Curves. ApJ **816**, L20 (2016).

[303] Wijers, R. A. M. J., Rees, M. J. & Meszaros, P. Shocked by GRB 970228: the afterglow of a cosmological fireball. MNRAS **288**, L51–L56 (1997).

[304] Wijers, R. A. M. J. & Galama, T. J. Physical Parameters of GRB 970508 and GRB 971214 from Their Afterglow Synchrotron Emission. ApJ **523**, 177–186 (1999).

[305] Rhoads, J. E. How to Tell a Jet from a Balloon: A Proposed Test for Beaming in Gamma-Ray Bursts. ApJ **487**, L1–L4 (1997).

[306] Rhoads, J. E. The Dynamics and Light Curves of Beamed Gamma-Ray Burst Afterglows. ApJ **525**, 737–749 (1999).

[307] Goodman, J. Are gamma-ray bursts optically thick? ApJ **308**, L47 (1986).

[308] Krolik, J. H. & Pier, E. A. Relativistic Motion in Gamma-Ray Bursts. ApJ **373**, 277 (1991).

[309] Kocevski, D. & Butler, N. Gamma-Ray Burst Energetics in the Swift Era. ApJ **680**, 531–538 (2008).

[310] Meszaros, P. & Rees, M. J. Relativistic Fireballs and Their Impact on External Matter: Models for Cosmological Gamma-Ray Bursts. ApJ **405**, 278 (1993).

[311] Mészáros, P. & Rees, M. J. Optical and Long-Wavelength Afterglow from Gamma-Ray Bursts. ApJ **476**, 232–237 (1997).

[312] Piran, T. Gamma-ray bursts and the fireball model. Phys. Rep. **314**, 575–667 (1999).

[313] Granot, J. & Sari, R. The Shape of Spectral Breaks in Gamma-Ray Burst Afterglows. ApJ **568**, 820–829 (2002).

[314] Chevalier, R. A. & Li, Z.-Y. Wind Interaction Models for Gamma-Ray Burst Afterglows: The Case for Two Types of Progenitors. ApJ **536**, 195–212 (2000).

[315] van Eerten, H. J. & Wijers, R. A. M. J. Gamma-ray burst afterglow scaling coefficients for general density profiles. MNRAS **394**, 2164–2174 (2009).

[316] Granot, J. & Königl, A. Radiative Hydromagnetic Shocks in Relativistic Outflow Sources. ApJ **560**, 145–159 (2001).

[317] van der Horst, A. J. *Broadband view of blast wave physics : a study of gamma-ray burst afterglows*. Ph.D. thesis, University of Amsterdam (2007).

[318] Frontera, F. *et al.* Prompt and Delayed Emission Properties of Gamma-Ray Bursts Observed with BeppoSAX. ApJS **127**, 59–78 (2000).

[319] Nakar, E. & Piran, T. Early afterglow emission from a reverse shock as a diagnostic tool for gamma-ray burst outflows. MNRAS **353**, 647–653 (2004).

[320] Kobayashi, S. & Sari, R. Optical Flashes and Radio Flares in Gamma-Ray Burst Afterglow: Numerical Study. ApJ **542**, 819–828 (2000).

[321] Sari, R. & Piran, T. Hydrodynamic Timescales and Temporal Structure of Gamma-Ray Bursts. ApJ **455**, L143 (1995).

[322] Sari, R. & Piran, T. GRB 990123: The Optical Flash and the Fireball Model. ApJ **517**, L109–L112 (1999).

[323] Perley, D. A. *et al.* The Afterglow of GRB 130427A from 1 to 10^{16} GHz. ApJ **781**, 37 (2014).

[324] Kulkarni, S. R. *et al.* The afterglow, redshift and extreme energetics of the γ-ray burst of 23 January 1999. Nature **398**, 389–394 (1999).

[325] Akerlof, C. *et al.* Observation of contemporaneous optical radiation from a γ-ray burst. Nature **398**, 400–402 (1999).

[326] Kulkarni, S. R. *et al.* Discovery of a Radio Flare from GRB 990123. ApJ **522**, L97–L100 (1999).

[327] Berger, E., Soderberg, A. M., Frail, D. A. & Kulkarni, S. R. A Radio Flare from GRB 020405: Evidence for a Uniform Medium around a Massive Stellar Progenitor. ApJ **587**, L5–L8 (2003).

[328] Frail, D. A. *et al.* The Enigmatic Radio Afterglow of GRB 991216. ApJ **538**, L129–L132 (2000).

[329] Anderson, G. E. *et al.* Probing the bright radio flare and afterglow of GRB 130427A with the Arcminute Microkelvin Imager. MNRAS **440**, 2059–2065 (2014).

[330] Zou, Y. C., Wu, X. F. & Dai, Z. G. Early afterglows in wind environments revisited. MNRAS **363**, 93–106 (2005).

[331] Mészáros, P. & Rees, M. J. GRB 990123: reverse and internal shock flashes and late afterglow behaviour. MNRAS **306**, L39–L43 (1999).

[332] Yi, S.-X., Wu, X.-F. & Dai, Z.-G. Early Afterglows of Gamma-Ray Bursts in a Stratified Medium with a Power-law Density Distribution. ApJ **776**, 120 (2013).

[333] Laskar, T. *et al.* A Reverse Shock in GRB 160509A. ApJ **833**, 88 (2016).

[334] Laskar, T. *et al.* A Reverse Shock in GRB 130427A. ApJ **776**, 119 (2013).

[335] van der Horst, A. J. *et al.* A comprehensive radio view of the extremely bright gamma-ray burst 130427A. MNRAS **444**, 3151–3163 (2014).

[336] Alexander, K. D. *et al.* A Reverse Shock and Unusual Radio Properties in GRB 160625B. ApJ **848**, 69 (2017).

[337] Hickish, J. *et al.* A digital correlator upgrade for the Arcminute MicroKelvin Imager. MNRAS **475**, 5677–5687 (2018).

[338] Atwood, W. B. *et al.* The Large Area Telescope on the Fermi Gamma-Ray Space Telescope Mission. ApJ **697**, 1071–1102 (2009).

[339] Meegan, C. *et al.* The Fermi Gamma-ray Burst Monitor. ApJ **702**, 791–804 (2009).

[340] Poolakkil, S. & Meegan, C. GRB 171010A: Fermi GBM observation. *GRB Coordinates Network* **21992** (2017).

[341] Omodei, N., Vianello, G. & Ahlgren, B. GRB 171010A: Fermi-LAT detection. *GRB Coordinates Network* **21985** (2017).

[342] Chand, V. *et al.* AstroSat-CZTI Detection of Variable Prompt Emission Polarization in GRB 171010A. ApJ **874**, 70 (2019).

[343] Evans, P. A. GRB 171010A: Swift ToO observations. *GRB Coordinates Network* **21986** (2017).

[344] D'Ai, A. *et al.* GRB 171010A: Swift-XRT afterglow detection. *GRB Coordinates Network* **21989** (2017).

[345] Thorstensen, J. R. & Halpern, J. P. GRB 171010A: OT, spectrum, and possible host galaxy. *GRB Coordinates Network* **21987** (2017).

[346] Kankare, E. *et al.* GRB 171010A: ePESSTO NTT spectroscopic redshift. *GRB Coordinates Network* **22002** (2017).

[347] Spergel, D. N. *et al.* First-Year Wilkinson Microwave Anisotropy Probe (WMAP) Observations: Determination of Cosmological Parameters. ApJS **148**, 175–194 (2003).

[348] Wright, E. L. A Cosmology Calculator for the World Wide Web. PASP **118**, 1711–1715 (2006).

[349] Guetta, D. & Della Valle, M. On the Rates of Gamma-Ray Bursts and Type Ib/c Supernovae. ApJ **657**, L73–L76 (2007).

[350] Anderson, G. E. *et al.* The Arcminute Microkelvin Imager catalogue of gamma-ray burst afterglows at 15.7 GHz. MNRAS **473**, 1512–1536 (2018).

[351] Condon, J. J. *et al.* The NRAO VLA Sky Survey. AJ **115**, 1693–1716 (1998).

[352] Horesh, A. *et al.* GRB 171010A: A detection of a radio source by AMI. *GRB Coordinates Network* **22013**, 1 (2017).

[353] Evans, P. A. *et al.* The Swift Burst Analyser. I. BAT and XRT spectral and flux evolution of gamma ray bursts. A&A **519**, A102 (2010).

[354] Gehrels, N. *et al.* Correlations of Prompt and Afterglow Emission in Swift Long and Short Gamma-Ray Bursts. ApJ **689**, 1161–1172 (2008).

[355] Beuermann, K. *et al.* VLT observations of GRB 990510 and its environment. A&A **352**, L26–L30 (1999).

[356] Virtanen, P. *et al.* SciPy 1.0: Fundamental Algorithms for Scientific Computing in Python. *Nature Methods* (2020).

[357] van der Horst, A. J. *et al.* The Radio Afterglow of GRB 030329 at Centimeter Wavelengths: Evidence for a Structured Jet or Nonrelativistic Expansion. ApJ **634**, 1166–1172 (2005).

[358] Racusin, J. L. *et al.* Jet Breaks and Energetics of Swift Gamma-Ray Burst X-Ray Afterglows. ApJ **698**, 43–74 (2009).

[359] Chandra, P. & Frail, D. A. A Radio-selected Sample of Gamma-Ray Burst Afterglows. ApJ **746**, 156 (2012).

[360] Laskar, T. *et al.* A VLA Study of High-redshift GRBs. II. The Complex Radio Afterglow of GRB 140304A: Shell Collisions and Two Reverse Shocks. ApJ **859**, 134 (2018).

[361] Hascoët, R., Beloborodov, A. M., Daigne, F. & Mochkovitch, R. X-ray flares from dense shells formed in gamma-ray burst explosions. MNRAS **472**, L94–L98 (2017).

[362] Panaitescu, A. & Kumar, P. Analytic Light Curves of Gamma-Ray Burst Afterglows: Homogeneous versus Wind External Media. ApJ **543**, 66–76 (2000).

[363] Laskar, T. *et al.* First ALMA Light Curve Constrains Refreshed Reverse Shocks and Jet Magnetization in GRB 161219B. ApJ **862**, 94 (2018).

[364] Alexander, K. D. *et al.* An unexpectedly small emission region size inferred from strong high-frequency diffractive scintillation in grb 161219b. ApJ **870**, 67 (2019).

[365] Berger, E. *et al.* A common origin for cosmic explosions inferred from calorimetry of GRB030329. Nature **426**, 154–157 (2003).

[366] Lazzati, D., Rossi, E., Covino, S., Ghisellini, G. & Malesani, D. The afterglow of GRB 021004: Surfing on density waves. A&A **396**, L5–L9 (2002).

[367] Heyl, J. S. & Perna, R. Broadband Modeling of GRB 021004. ApJ **586**, L13–L17 (2003).

[368] Rees, M. J. & Mészáros, P. Refreshed Shocks and Afterglow Longevity in Gamma-Ray Bursts. ApJ **496**, L1–L4 (1998).

[369] Guetta, D. *et al.* The variable X-ray light curve of GRB 050713A: the case of refreshed shocks. A&A **461**, 95–101 (2007).

[370] Piran, T. The physics of gamma-ray bursts. *Rev. Mod. Phys.* **76**, 1143–1210 (2005).

[371] Phinney, E. S. Manifestations of a Massive Black Hole in the Galactic Center. In Morris, M. (ed.) *The Center of the Galaxy*, vol. 136 of *IAU Symposium*, 543 (1989).

[372] Guillochon, J., Manukian, H. & Ramirez-Ruiz, E. PS1-10jh: The Disruption of a Main-sequence Star of Near-solar Composition. ApJ **783**, 23 (2014).

[373] Mainetti, D. *et al.* The fine line between total and partial tidal disruption events. A&A **600**, A124 (2017).

[374] Kesden, M. Black-hole spin dependence in the light curves of tidal disruption events. Phys. Rev. D **86**, 064026 (2012).

[375] Merritt, D. Loss-cone dynamics. *Classical and Quantum Gravity* **30**, 244005 (2013).

[376] Magorrian, J. & Tremaine, S. Rates of tidal disruption of stars by massive central black holes. MNRAS **309**, 447–460 (1999).

[377] Arcavi, I. *et al.* A Continuum of H- to He-rich Tidal Disruption Candidates With a Preference for E+A Galaxies. ApJ **793**, 38 (2014).

[378] van Velzen, S. & Farrar, G. R. Measurement of the Rate of Stellar Tidal Disruption Flares. ApJ **792**, 53 (2014).

[379] Stone, N. C. & Metzger, B. D. Rates of stellar tidal disruption as probes of the supermassive black hole mass function. MNRAS **455**, 859–883 (2016).

[380] van Velzen, S. On the Mass and Luminosity Functions of Tidal Disruption Flares: Rate Suppression due to Black Hole Event Horizons. ApJ **852**, 72 (2018).

[381] Lin, D. *et al.* A luminous X-ray outburst from an intermediate-mass black hole in an off-centre star cluster. *Nature Astronomy* **2**, 656–661 (2018).

[382] Shen, R.-F. & Matzner, C. D. Evolution of Accretion Disks in Tidal Disruption Events. ApJ **784**, 87 (2014).

[383] Wu, S., Coughlin, E. R. & Nixon, C. Super-Eddington accretion in tidal disruption events: the impactof realistic fallback rates on accretion rates. MNRAS **478**, 3016–3024 (2018).

[384] van Velzen, S. *et al.* Optical Discovery of Probable Stellar Tidal Disruption Flares. ApJ **741**, 73 (2011).

[385] Berger, E. *et al.* Radio Monitoring of the Tidal Disruption Event Swift J164449.3+573451. I. Jet Energetics and the Pristine Parsec-scale Environment of a Supermassive Black Hole. ApJ **748**, 36 (2012).

[386] Gezari, S. *et al.* An ultraviolet-optical flare from the tidal disruption of a helium-rich stellar core. Nature **485**, 217–220 (2012).

[387] Blagorodnova, N. *et al.* The Broad Absorption Line Tidal Disruption Event iPTF15af: Optical and Ultraviolet Evolution. ApJ **873**, 92 (2019).

[388] Wevers, T. *et al.* Evidence for rapid disc formation and reprocessing in the X-ray bright tidal disruption event candidate AT 2018fyk. MNRAS **488**, 4816–4830 (2019).

[389] Holoien, T. W. S. *et al.* ASASSN-15oi: a rapidly evolving, luminous tidal disruption event at 216 Mpc. MNRAS **463**, 3813–3828 (2016).

[390] Blagorodnova, N. *et al.* iPTF16fnl: A Faint and Fast Tidal Disruption Event in an E+A Galaxy. ApJ **844**, 46 (2017).

[391] Chornock, R. *et al.* The Ultraviolet-bright, Slowly Declining Transient PS1-11af as a Partial Tidal Disruption Event. ApJ **780**, 44 (2014).

[392] Gezari, S. *et al.* Luminous Thermal Flares from Quiescent Supermassive Black Holes. ApJ **698**, 1367–1379 (2009).

[393] Gezari, S. *et al.* UV/Optical Detections of Candidate Tidal Disruption Events by GALEX and CFHTLS. ApJ **676**, 944–969 (2008).

[394] Gezari, S. *et al.* Ultraviolet Detection of the Tidal Disruption of a Star by a Supermassive Black Hole. ApJ **653**, L25–L28 (2006).

[395] Komossa, S. & Bade, N. The giant X-ray outbursts in NGC 5905 and IC 3599:() hfill Follow-up observations and outburst scenarios. A&A **343**, 775–787 (1999).

[396] Esquej, P. *et al.* Candidate tidal disruption events from the XMM-Newton slew survey. A&A **462**, L49–L52 (2007).

[397] Komossa, S. *et al.* A Huge Drop in the X-Ray Luminosity of the Nonactive Galaxy RX J1242.6-1119A, and the First Postflare Spectrum: Testing the Tidal Disruption Scenario. ApJ **603**, L17–L20 (2004).

[398] Saxton, R. D. *et al.* A tidal disruption-like X-ray flare from the quiescent galaxy SDSS J120136.02+300305.5. A&A **541**, A106 (2012).

[399] Maksym, W. P., Ulmer, M. P. & Eracleous, M. A Tidal Disruption Flare in A1689 from an Archival X-ray Survey of Galaxy Clusters. ApJ **722**, 1035–1050 (2010).

[400] Lin, D. *et al.* An Ultrasoft X-Ray Flare from 3XMM J152130.7+074916: A Tidal Disruption Event Candidate. ApJ **811**, 43 (2015).

[401] Saxton, R. D. *et al.* XMMSL1 J074008.2-853927: a tidal disruption event with thermal and non-thermal components. A&A **598**, A29 (2017).

[402] French, K. D., Wevers, T., Law-Smith, J., Graur, O. & Zabludoff, A. I. The Host Galaxies of Tidal Disruption Events. Space Sci. Rev. **216**, 32 (2020).

[403] Eftekhari, T., Berger, E., Zauderer, B. A., Margutti, R. & Alexander, K. D. Radio Monitoring of the Tidal Disruption Event Swift J164449.3+573451. III. Late-time Jet Energetics and a Deviation from Equipartition. ApJ **854**, 86 (2018).

[404] Lodato, G., King, A. R. & Pringle, J. E. Stellar disruption by a supermassive black hole: is the light curve really proportional to $t^{-5/3}$? MNRAS **392**, 332–340 (2009).

[405] Auchettl, K., Guillochon, J. & Ramirez-Ruiz, E. New Physical Insights about Tidal Disruption Events from a Comprehensive Observational Inventory at X-Ray Wavelengths. ApJ **838**, 149 (2017).

[406] Mummery, A. & Balbus, S. A. Evolution of relativistic thin discs with a finite ISCO stress - I. Stalled accretion. MNRAS **489**, 132–142 (2019).

[407] Wevers, T. *et al.* Black hole masses of tidal disruption event host galaxies. MNRAS **471**, 1694–1708 (2017).

[408] Loeb, A. & Ulmer, A. Optical Appearance of the Debris of a Star Disrupted by a Massive Black Hole. ApJ **489**, 573–578 (1997).

[409] Miller, J. M. *et al.* Flows of X-ray gas reveal the disruption of a star by a massive black hole. Nature **526**, 542–545 (2015).

[410] Metzger, B. D. & Stone, N. C. A bright year for tidal disruptions. MNRAS **461**, 948–966 (2016).

[411] Krolik, J., Piran, T., Svirski, G. & Cheng, R. M. ASASSN-14li: A Model Tidal Disruption Event. ApJ **827**, 127 (2016).

[412] Hayasaki, K., Stone, N. & Loeb, A. Finite, intense accretion bursts from tidal disruption of stars on bound orbits. MNRAS **434**, 909–924 (2013).

[413] Bonnerot, C., Rossi, E. M., Lodato, G. & Price, D. J. Disc formation from tidal disruptions of stars on eccentric orbits by Schwarzschild black holes. MNRAS **455**, 2253–2266 (2016).

[414] Guillochon, J. & Ramirez-Ruiz, E. A Dark Year for Tidal Disruption Events. ApJ **809**, 166 (2015).

[415] Evans, C. R. & Kochanek, C. S. The tidal disruption of a star by a massive black hole. ApJ **346**, L13–L16 (1989).

[416] Pasham, D. R. *et al.* Optical/UV-to-X-Ray Echoes from the Tidal Disruption Flare ASASSN-14li. ApJ **837**, L30 (2017).

[417] Alexander, K. D., Wieringa, M. H., Berger, E., Saxton, R. D. & Komossa, S. Radio Observations of the Tidal Disruption Event XMMSL1 J0740-85. ApJ **837**, 153 (2017).

[418] Nikołajuk, M. & Walter, R. Tidal disruption of a super-Jupiter by a massive black hole. A&A **552**, A75 (2013).

[419] Romero-Cañizales, C. *et al.* The TDE ASASSN-14li and Its Host Resolved at Parsec Scales with the EVN. ApJ **832**, L10 (2016).

[420] Lei, W.-H., Yuan, Q., Zhang, B. & Wang, D. IGR J12580+0134: The First Tidal Disruption Event with an Off-beam Relativistic Jet. ApJ **816**, 20 (2016).

[421] Yang, J. *et al.* No apparent superluminal motion in the first-known jetted tidal disruption event Swift J1644+5734. MNRAS **462**, L66–L70 (2016).

[422] Mattila, S. *et al.* A dust-enshrouded tidal disruption event with a resolved radio jet in a galaxy merger. *Science* **361**, 482–485 (2018).

[423] Tavecchio, F. Gamma rays from blazars. In *6th International Symposium on High Energy Gamma-Ray Astronomy*, vol. 1792 of *American Institute of Physics Conference Series*, 020007 (2017).

[424] Stein, R. *et al.* A high-energy neutrino coincident with a tidal disruption event. *arXiv e-prints* arXiv:2005.05340 (2020).

[425] Jose, J. *et al.* ASAS-SN Discovery of an Unusual Nuclear Transient in PGC 043234. *The Astronomer's Telegram* **6777** (2014).

[426] Voges, W. *et al.* The ROSAT all-sky survey bright source catalogue. A&A **349**, 389–405 (1999).

[427] Levan, A. J. *et al.* An Extremely Luminous Panchromatic Outburst from the Nucleus of a Distant Galaxy. *Science* **333**, 199 (2011).

[428] Burrows, D. N. *et al.* Relativistic jet activity from the tidal disruption of a star by a massive black hole. Nature **476**, 421–424 (2011).

[429] Zauderer, B. A. *et al.* Birth of a relativistic outflow in the unusual γ-ray transient Swift J164449.3+573451. Nature **476**, 425–428 (2011).

[430] Brown, G. C. *et al.* Swift J1112.2-8238: a candidate relativistic tidal disruption flare. MNRAS **452**, 4297–4306 (2015).

[431] Irwin, J. A. *et al.* CHANG-ES V: Nuclear Outflow in a Virgo Cluster Spiral after a Tidal Disruption Event. ApJ **809**, 172 (2015).

[432] Bright, J. S. *et al.* Long-term radio and X-ray evolution of the tidal disruption event ASASSN-14li. MNRAS (2018).

[433] Goad, M. R. *et al.* Accurate early positions for Swift GRBs: enhancing X-ray positions with UVOT astrometry. A&A **476**, 1401–1409 (2007).

[434] Davies, M. L. *et al.* Follow-up observations at 16 and 33GHz of extragalactic sources from WMAP 3-yr data: I - Spectral properties. MNRAS **400**, 984–994 (2009).

[435] Swinbank, J. D. *et al.* The LOFAR Transients Pipeline. *Astronomy and Computing* **11**, 25–48 (2015).

[436] Pasham, D. R. & van Velzen, S. Discovery of a Time Lag between the Soft X-Ray and Radio Emission of the Tidal Disruption Flare ASASSN-14li: Evidence for Linear Disk-Jet Coupling. ApJ **856**, 1 (2018).

[437] Brown, J. S. *et al.* The Long Term Evolution of ASASSN-14li. MNRAS **466**, 4904–4916 (2017).

[438] Becker, R. H., White, R. L. & Helfand, D. J. The FIRST Survey: Faint Images of the Radio Sky at Twenty Centimeters. ApJ **450**, 559 (1995).

[439] Smith, H. E., Lonsdale, C. J., Lonsdale, C. J. & Diamond, P. J. A Starburst Revealed—Luminous Radio Supernovae in the Nuclei of ARP 220. ApJ **493**, L17–L21 (1998).

[440] Parra, R. *et al.* The Radio Spectra of the Compact Sources in Arp 220: A Mixed Population of Supernovae and Supernova Remnants. ApJ **659**, 314–330 (2007).

[441] Batejat, F. *et al.* Resolution of the Compact Radio Continuum Sources in Arp220. ApJ **740**, 95 (2011).

[442] Prieto, J. L. *et al.* MUSE Reveals a Recent Merger in the Post-starburst Host Galaxy of the TDE ASASSN-14li. ApJ **830**, L32 (2016).

[443] Espinasse, M. & Fender, R. Spectral differences between the jets in 'radio-loud' and 'radio-quiet' hard-state black hole binaries. MNRAS **473**, 4122–4129 (2018).

[444] Merloni, A. & Heinz, S. Measuring the kinetic power of active galactic nuclei in the radio mode. MNRAS **381**, 589–601 (2007).

[445] Falcke, H., Körding, E. & Markoff, S. A scheme to unify low-power accreting black holes. Jet-dominated accretion flows and the radio/X-ray correlation. A&A **414**, 895–903 (2004). astro-ph/0305335.

[446] Zauderer, B. A. *et al.* Radio Monitoring of the Tidal Disruption Event Swift J164449.3+573451. II. The Relativistic Jet Shuts Off and a Transition to Forward Shock X-Ray/Radio Emission. ApJ **767**, 152 (2013).

[447] Miller, L., Peacock, J. A. & Mead, A. R. G. The bimodal radio luminosity function of quasars. MNRAS **244**, 207–213 (1990).

[448] Pasham, D. R. *et al.* A Multiwavelength Study of the Relativistic Tidal Disruption Candidate Swift J2058.4+0516 at Late Times. ApJ **805**, 68 (2015).

[449] Perlman, E. S. *et al.* Compact Resolved Ejecta in the Nearest Tidal Disruption Event. ApJ **842**, 126 (2017).

[450] Blanchard, P. K. *et al.* PS16dtm: A Tidal Disruption Event in a Narrow-line Seyfert 1 Galaxy. ApJ **843**, 106 (2017).

[451] Bower, G. C., Metzger, B. D., Cenko, S. B., Silverman, J. M. & Bloom, J. S. Late-time Radio Emission from X-Ray-selected Tidal Disruption Events. ApJ **763**, 84 (2013).

[452] van Velzen, S., Frail, D. A., Körding, E. & Falcke, H. Constraints on off-axis jets from stellar tidal disruption flares. A&A **552**, A5 (2013).

[453] Saxton, R. D. *et al.* XMMSL2 J144605.0+685735: a slow tidal disruption event. A&A **630**, A98 (2019).

[454] Planck Collaboration *et al.* Planck 2015 results. XIII. Cosmological parameters. A&A **594**, A13 (2016).

[455] Bright, J. S. *et al.* A detailed radio study of the energetic, nearby, and puzzling GRB 171010A. MNRAS **486**, 2721–2729 (2019).